A Dark Matter Detector Based on the Simultaneous Measurement of Phonons and Ionization at 20 mK

by

Thomas Alan Shutt

B.S. (Texas A&M University) 1986

A dissertation submitted in partial satisfaction of the

requirements for the degree of

Doctor of Philosophy

in

Physics

in the

GRADUATE DIVISION

of the

UNIVERSITY of CALIFORNIA at BERKELEY

Committee in charge:

Professor Bernard Sadoulet, Chair

Professor Eugene Commins

Professor Eugene. E. Haller

1993

Abstract

A Dark Matter Detector Based on the Simultaneous Measurement of Phonons and Ionization at 20 mK

by

Thomas Alan Shutt

Doctor of Philosophy

University of California at Berkeley

Professor Bernard Sadoulet, Chair

One of the most important issues in astrophysics and cosmology is understanding the nature of dark matter. One possibility is that it is made of weakly interacting subatomic particles created in the big bang, such as the lightest particle in supersymmetry models. These particles should scatter elastically of nuclei in a detector on earth at a rate of ≈events/kg/week, and will deposit energies of a few keV. Current attempts to detect these interactions are limited by a radioactive background of photons and beta particles which scatter on electrons.

We have developed a novel particle detector to look for dark matter based on the simultaneous measurement of ionization and phonons in a 60 g crystal of high purity germanium at a temperature of 20 mK. Background events can be distinguished by our detector because they produce more ionization per unit phonon energy than dark matter interactions.

The phonon energy is measured as a temperature change in the detector by means of neutron transmutation doped germanium thermistors attached to the crystal. The ionization measurement is accomplished by applying a bias to implanted contacts on the faces of the disk. Charge collection differs from the normal situation at 77 K in

that no thermally generated free charge exists in the crystal at 20 mK. The collection efficiency is good with an electric field of only ≈0.2 V/cm after the charged impurities in the crystal have been neutralized by free charge created by particle interactions from a radioactive source. For fields below this charge collection is poor, and affects the amount of phonon energy measured. We have modeled this in terms of charge trapping.

The r.m.s resolution of the detector is 800 eV in phonons and 600 eV in ionization. We have tested the background rejection capability of the detector by exposing it to neutrons from a ^{251}Cf source which scatter elastically on nuclei. The neutrons are distinguished at energies of a few keV, and the current background rejection power is at least 10:1.

4/26/93

The dissertation of Thomas Alan Shutt is approved:

[signature] 4/26/93

Chair Date

Eugene D. Commins 4-30-93

Date

[signature] 4/30/93

Date

University of California Berkeley

1993

Table of Contents

Acknowledgments

There are a great number of people who have made my time in graduate school enjoyable, and who have contributed to all I have learned -- about life, as well as physics. I feel truly fortunate to have worked in the Sadoulet group, both because of its people and because I find the project fascinating.

I would first of all like to thank my advisor Bernard Sadoulet. His enormous breadth of physics knowledge and keen intuition are the lifeblood of the project. Moreover, his concern for the people around him sets an example, I believe, that makes our group such an enjoyable environment. His was the project that truly fired my imagination when I was a starting graduate student, and I am thankful for the opportunity to have worked with him.

I would also like to thank Eugene Haller for the interest he has always had in my work and career. Besides his many insights into solid state physics and charge collection in our detectors, I will remember the times he has carefully corrected my poorly written papers. Ron Ross and Andrew Lange have also always been quite helpful and friendly, as has Blas Cabrera at Stanford. A special note of thanks goes also to Paul Luke for helping to orient my thinking about charge collection at low temperatures. Jeff Beeman constructed a number of our early devices, and has had many useful suggestions.

Though they undoubtedly will never see this thesis, I shall always be grateful to Fred Wellstood, John Schmidt, and Seamus Davis for teaching me the business of running a dilution refrigerator. Fred, in particular, answered all my nagging questions about the proper size of this pumping line or that.

I had in mind to write something personal about each of the many people who have worked on our project, but there have been too many. Jim Rich, Yannick Giraud-Héraud, Peter Weilhammer, and Dominique Yvon taught me much, and I feel fortunate to count them as friends. The same is true of Chris Stubbs, who is certainly one the people most responsible for making the measurements in this thesis possible. Ning Wang, in addition to being a friend, set the foundation for much of my work, and built the detector which gave me this thesis. Brett Ellman taught me much about a large number of topics in physics, and I wish him happiness in the future.

It is even harder to try to acknowledge all the people with whom I work now. I guess this is because I think of them more as friends than colleagues -- I would like to thank the entire Sadoulet group for providing a human space for science. I especially will remember hiking trips, long lunches, coffee rituals, philosophical discussions and occasional nights of attempted debauchery with the likes of Steve Weiss, Alan Cummings, Peter Barnes, Tim Edberg and Ann Parsons. It has been a pleasure to know Angela DaSilva and Jeff Wilkerson. Walter Stockwell and Storn White have provided me a fascinating glimpse of the mysterious civilization that exists in the southern half of this state. I have enjoyed getting to know Betty Young, and look forward to working with her and Dan Akerib. Garth Smith is as much a friend as he is an invaluable part of the team. This thesis would have been impossible without John Emes, who carefully and conscientiously built nearly all the devices we have tested.

The entire staff at the Center for Particle Astrophysics has been wonderful, and each person has helped me in one way or another. In particular I am grateful for having gotten to know Rose Sergeant, Ann Fitzgerald, and Valerie MacLean. It is my sincere hope that the Center succeeds in its mission both to build and strengthen ties between science and society, and to foster a healthier community within science.

I would also like to thank my parents for their support over the years. As the years pass, my understanding of them grows, and I better appreciate how fortunate I have been to have them.

Finally, I would like to thank Krysta for her love, support, kindness and humor.

Chapter 1: The story of dark matter

1.1) Evidence for dark matter

The nature of dark matter is a central question in modern astrophysics and cosmology (1). Dark matter is a term for mass whose existence is inferred from the gravitational dynamics of various astrophysical systems, but which exceeds the total mass of luminous stars, gas and dust observed in these systems. This "missing" mass may in fact play the dominant role in determining the spacetime geometry of the universe - whether it will recollapse at some distant time, or whether it will expand forever.

There is evidence for dark matter on several length scales (2, 3). Perhaps the best known are measurements of angular velocity as a function of radius for objects (mostly gas clouds) orbiting spiral galaxies (4). These "rotation curves" indicate that the luminous parts of galaxies are embedded in spherical halos of matter with at least ten times the mass of the visible stars, and which extend far beyond the visible edge of the galaxy. About thirty times more mass still is found on larger scales in clusters of galaxies. These are systems of thousands of galaxies believed to be in equilibrium, thus the mass density can be inferred from both the velocity distribution of the galaxies (5, 6) and from measurements of the temperature and density distribution of x-ray emitting gas permeating the clusters (5, 6, 7). The mass of a number of clusters has also been estimated from gravitational lensing of distant objects behind the clusters (8). Even larger scales have been probed by mapping the distribution of peculiar velocities of galaxies (motion which deviates from the over-all Hubble flow), and comparing these to fluctuations in the mean number density of galaxies (9, 10). These methods yield several times as much mass as for clusters, but are less certain.

It is convenient to describe mass measurements in terms of a cosmological quantity. If the universe is isotropic and homogeneous on large enough scales (the

Friedmann-Robertson-Walker cosmology), then its possible spacetime geometries are "open", "closed" and "flat". A closed universe recollapses, an open universe expands forever, and a flat universe expands at a rate which asymptotically vanishes in the infinite future. A given mass density, ρ, can be described by the ratio $\Omega=\rho/\rho_c$, where ρ_c is the critical density that gives a flat geometry. This critical density varies with time and depends on the expansion rate of the universe, which is described by the Hubble constant. Figure 1.1 summarizes the amount of mass in the universe inferred from various methods in terms of Ω (2). The mass in each system refers to the total mass in the universe estimated from the sum of all such systems.

It is possible, at least in principle, to determine Ω by measurements of distant objects that directly probe the geometry of the universe. One example is the brightness or number density of distant galaxies as a function of redshift. Unfortunately the faintness of very distant objects, and uncertainties in how galaxies have evolved in time prevent these measurements from being very useful so far. Recently, efforts have begun which measure distant objects, such as type IA supernovae (11), whose intrinsic brightness is thought to be well understood theoretically.

There are two strong arguments that Ω=1. The first is that if Ω is bigger than one (closed universe) or less than one (open universe), then as time evolves Ω very rapidly approaches either infinity or zero, respectively. Only Ω=1 is stable. Remarkably, direct measurements (figure 1.1) indicate that in fact Ω is currently of order one. If Ω is not exactly one today, then when the universe was 1 sec old Ω- differed from 1 by only about one part in 10^{16} (1). This problem of the "fine tuning" of Ω at early times can be avoided only if Ω=1. The other argument comes from the theory of inflation, which strictly requires that Ω be one (12, 13, 14).

A final important point is that the age of the universe is specified by Ω and the value of the Hubble constant, which is known to within about a factor of 2. With Ω=1, this age is consistent with the age of the universe estimated from primordial radioactive

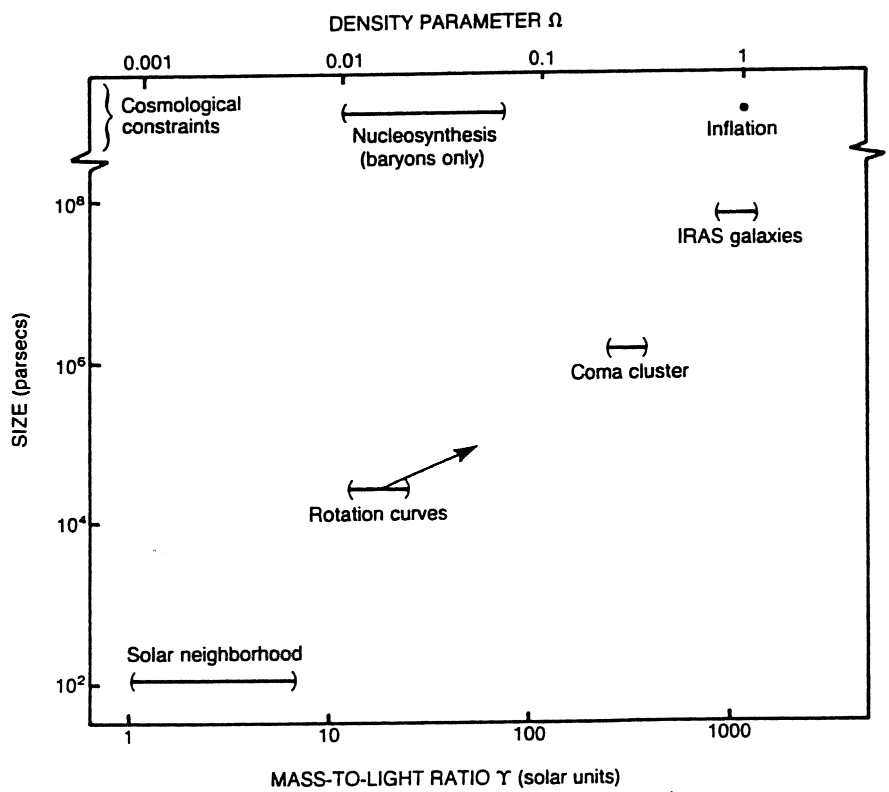

Figure 1.1 Values of Ω deduced by different methods on various distance scales, from (2).

isotopes, but may be too young to be consistent with the ages of the oldest stars as deduced by stellar evolution theory.

1.2) The nature of dark matter

Interestingly, particle physics and cosmology offer some clues as to what dark matter may be. As the early universe cooled below the binding energy of nuclei, the lightest elements were formed. The cross-sections for the relevant nuclear interactions are well known, and the abundances of the elements and their isotopes can be calculated as a function of the mass density of the universe in baryons, or Ω_B. The theoretical values agree remarkably well with the measured primordial abundances (15, 16, 17), provided that $\Omega_B=(0.016\pm0.002)/h^2$. Here h describes the indeterminacy in the Hubble constant, H_o, via $H_o=100h$ km/s/Mpc, and $0.5<h<1$. Note that even the lowest possible value implies that at least some of the dark matter in galaxies is baryonic. This may be in the form of brown dwarfs - planet like objects with insufficient mass to begin nuclear burning. Experimental searches for such objects have begun, and should be able to detect them if they constitute a significant fraction of the halo of the Milky Way (18, 19). On the other hand, the upper limit to Ω_B seems smaller than the mass measured for all scales greater than galaxies. If these results are confirmed, then we may be forced to accept the fact that at least 80% of the universe is non-baryonic.

If dark matter if it is not baryonic, then it may be made of neutrinos, or perhaps new particles not described by the standard model of particle physics. A powerful constraint can be placed on the amount of any elementary particle left over from the big bang if this species was once in thermal equilibrium with the other constituents of the hot plasma of the early universe (20). Thermal equilibrium here means that the number density of this particle, δ, and its antiparticle, $\overline{\delta}$, is maintained via interactions of the type $\delta\overline{\delta} \leftrightarrow X\overline{X}$ where X represents all other particles in equilibrium. If, at a given point in time, the temperature of a particle in equilibrium is greater than its mass, the particle is then relativistic and has a number density which is independent of its mass. As the temperature of the universe cools below this mass, the particle becomes non-relativistic and the number density of the particle drops exponentially because only the reaction $\delta\bar{\delta} \rightarrow X\bar{X}$ remains energetically favorable. However because the universe is expanding and the gas is becoming dilute, it is possible for the interactions maintaining thermal equilibrium to "freeze out", fixing the number of the particles.

Particles that freeze out when they are relativistic are called "hot" dark matter, an example of which is neutrinos with a mass on the order of electron volts. Because the number density of hot dark matter particles is independent of their mass, they have a mass density proportional to their mass.

Particles that are non-relativistic when they freeze out are called "cold dark" matter, and have a number density today, Ω_δ, that depends on the expansion rate of the universe and the cross section for the annihilation reaction $\delta\bar{\delta} \rightarrow X\bar{X}$ at the freeze out energy. If there is an initial asymmetry between the number of particles and anti-particles, this value of Ω_δ is a lower limit. Note that protons, neutrons and electrons, interact so strongly that none would be left today in any region of the universe where there was not an initial particle-antiparticle asymmetry. However particles with weaker interactions could still be around with large abundances. In fact particles with mass near a proton mass will have Ω_δ=1 if their annihilation cross-sections are roughly equal to those of weak interactions. This intriguing fact may be a simple numerical coincidence, or it could be a hint of a much deeper connection, namely that such weakly interacting massive particles, or WIMPs, are the dominant constituent of the universe.

Since dark matter is the major gravitational constituent of the universe it plays a major role in how the structures of galaxies we see today on large scales grew gravitationally from small initial density perturbations in the mostly isotropic early universe. These initial perturbations have recently been measured on large angular scales by the COBE satellite via their affect on the cosmic microwave background (21). Given this starting point, it is easy to calculate the growth when the perturbations are small. N-body simulations including fluid dynamics are needed when the gravitational dynamics become non-linear. In these calculations hot and cold dark matter give rise to different types of growth. Relativistic hot dark matter, for example, tends to damp out growths on small scales.

This study of the large scale structure of the universe is a rapidly changing field, and many conclusions are hotly debated. For a recent overview, see, for example, (22). It seems that the structures seen today cannot have grown from the initial perturbations measured by COBE without some dark matter present. Models based upon Ω=1 that include only cold dark matter roughly fit the data, but have trouble in many details. This has been used to argue for the "death of cold dark matter", or for other models such as ones that include both hot and cold dark matter. Better surveys of galaxy redshifts should help in the near future to better measure the current large scale structure; at the same time better measurements of anisotropies of the microwave background may also tell us more about the spectrum of initial density perturbations.

If, as much of the above discussion suggests, an as yet undiscovered particle dominates the mass of the universe, it is reasonable to ask where it fits into a particle physics view of the world. Neutrinos exist, of course, and could either be hot or cold dark matter. From the freeze-out argument it turns out that in fact neutrinos give Ω=1 if they have a mass of about 25 eV. The electron neutrino is too light to have a cosmologically significant relic abundance, but the muon and tau neutrinos masses could lie in the required range. As discussed in chapter 2, dark matter in the halo of our galaxy will occasionally interact in a detector on Earth. Unfortunately, though, a light neutrino will only impart an energy on the order of 10^{-9} eV in an elastic interaction with an electron in a detector, making it very difficult to detect.

Cold dark matter could be a very heavy neutrino, or it could be the axion, a particle well motivated by theory. Because axions would be created athermally in a phase transition in the early universe, the freeze out argument does not apply to them. For a certain range of parameters, axions could exist in large numbers, however, and some may be directly detectable via their coupling to photons in a microwave resonance cavity. Current searches have placed no cosmologically significant limits on them (23, 24), though more ambitious experiments have been proposed. Finally, many supersymmetry (SUSY) theories predict the existence of a stable particle remarkably similar to WIMPs that would have been in thermal equilibrium in the early universe. Searches for supersymmetric particles at CERN place their likely mass at or above a few tens of GeV.

Chapter 2: Detection of WIMP dark matter

2.1) Indirect detection

If WIMP dark matter exists and is the dominant component of the universe then it may have detectable signatures other than its enormous gravitational effect. In what follows we focus our attention on dark matter in the halo of our galaxy. Most of the information is taken from several good review articles on dark matter searches (25, 26, 27).

One class of dark matter experiments is to look for the products of WIMP particle-antiparticle annihilation reactions. Balloon-borne experiments, for example, have searched for antiprotons in cosmic rays from $\delta\overline{\delta} \rightarrow p\overline{p}$ reactions, but have not set cosmologically significant limits. Another technique is to look for neutrinos from $\delta\overline{\delta} \rightarrow \nu\overline{\nu}$ annihilations (93). The largest rates should come from WIMPs that have been trapped gravitationally in the Sun or the Earth. Because weak interaction rates are so small, WIMPs typically pass through the Earth or Sun unmolested. If their interaction cross sections on ordinary matter are large enough, however, a significant number of them can lose part of their galactic orbital energy through elastic scattering and become trapped.

These trapped WIMPs can in principle alter the behavior of the Sun. The cosmion, for instance, is a hypothetical type of WIMP that interacts just strongly enough to carry heat from the center of the sun to the outer layers, thereby cooling the inside. The model has been constructed so that this change in the core temperature solves the problem of the deficit of ^{8}B solar neutrinos. The cosmion has been essentially ruled out, however, by experiments discussed below (28).

2.2) Direct detection

Another way to search for WIMPs in the galactic halo is to look directly for their interactions in a particle detector (29). The rate of such interactions can be calculated as follows (25). The dark matter halo is usually assumed to be spherically symmetric and have a density of the form

$$\rho(r) = \rho_o \frac{r_c^2}{r^2 + r_c^2},$$

where r is the radial distance, r_c the radius of core the halo, and ρ_o the central core density. Typical values are $r_c \approx 5.6$ kpc and $\rho_o \approx 1.0$ GeV/cm^3. The particles are assumed to be in orbit about the center of the galaxy and to have a Maxwellian distribution of speeds given by

$$\frac{dn}{d\dot{v}} = A \frac{n_o v^2}{\sigma_H^3} e^{-\frac{v^2}{\sigma_H^2}}, \qquad 2.1$$

where $\sigma_H \approx 210$ km/sec, or 0.7×10^{-3} c. A is a dimensionless constant of order unity that depends on the relationship between σ_H and the galactic escape velocity. With these assumptions, 1 GeV WIMPs have a flux on earth on the order of 10^5 s^{-1}cm^{-2}. Because weak interaction cross sections are so small, however, most would pass through the earth without interacting. Occasionally, though, there will be interactions that might be seen in a detector. Of the various types of process that can occur, most attention has been given to elastic scattering events on nuclei. These occur at a much higher rate than inelastic nuclear interactions for these low energy WIMPs, and, as discussed below, give much greater recoil energies than elastic interactions with electrons.

Elastic scattering is isotropic in the center of mass frame, with the recoil energy of the struck nucleus given by

$$E_r = \frac{m_N m_\delta}{\left(m_N + m_\delta\right)^2} m_\delta v^2 \left(1 - \cos(\theta^*)\right) \qquad 2.2$$

where m_N is the mass of the nucleus, m_δ and E_δ are the WIMP mass and energy, and θ^* is the center of mass scattering angle. Note that the recoil energy is largest when the masses of the WIMP and target nuclei are equal. For halo WIMPs with mass $\approx$10 GeV and a germanium target nuclei, the recoil energy is several keV.

The spectrum of recoil energies is found by convolving the velocity distribution, equation 2.1, with recoil energy, equation 2.2. Account must be taken of the solar system's galactic orbital velocity with respect to the velocity of the WIMPs in the stationary halo. With the parameters of the halo specified, the shape of recoil energy spectrum is a function of the WIMP and target masses only. The rate is determined by the interaction cross section and by the number of WIMPs in the halo. For a given halo mass density the number of WIMPs is inversely proportional to their mass. The cross section is calculable for a given WIMP model, though in practice exact results are difficult to obtain because the compton wavelengths of these low energy WIMPs are large enough that they interact with the entire nucleus instead of a single quark. Thus the rate for a given WIMP depends on the detector material. Some WIMPs, in fact, couple only to spin and thus have appreciable cross sections only for nuclei with large net spin.

Recoil energy spectra for several WIMP masses in germanium are shown in figure 2.1. The shape is quasi-exponential with the highest rates lying at lowest energies. Heavier WIMPs give flatter spectra and larger average recoil energies, but lower overall rates than lighter WIMPs. An approximate relationship between the average recoil energy and the WIMP and nuclear masses is

$$\langle E_r \rangle = 5.8 \frac{4 m_N m_\delta}{\left(m_N + m_\delta\right)^2} \left(\frac{m_\delta}{10\ \mathrm{GeV}}\right) \left(\frac{v_{\delta,rms}}{300\ \mathrm{km} \cdot \mathrm{sec}^{-1}}\right)^2 \mathrm{keV}. \qquad 2.2$$

The scattering rates for supersymmetry WIMPs are quite model dependent, but in germanium are typically on the order of 0.01 cnt/kg/day, or less. For a more complete discussion of WIMP rates in various materials, see (25).

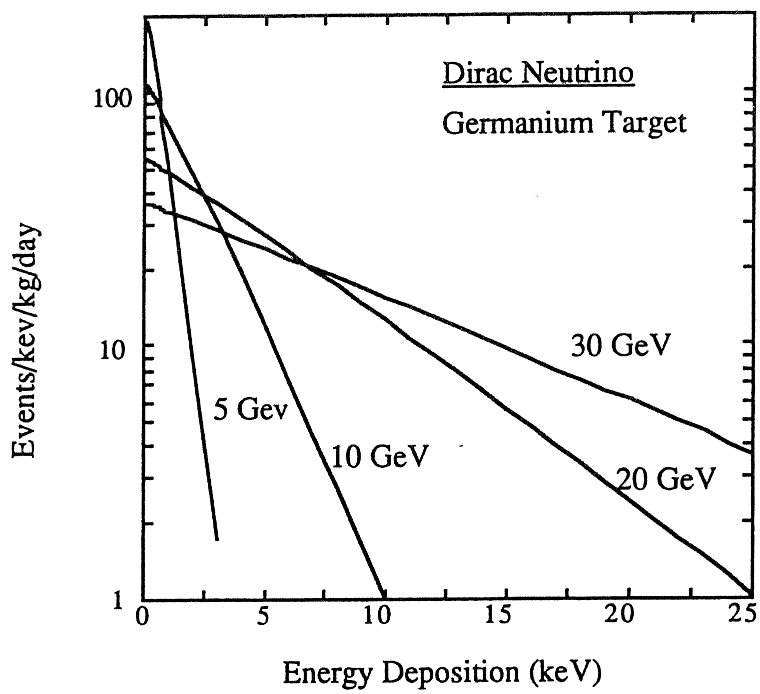

__Figure 2.1__ Expected energy deposition spectrum in germanium for a heavy neutrino WIMP with various masses.

The experimental challenge is clear. A detector with mass on the order of at least 1 kg is needed to obtain signals at the rate of events/week. To see the signal, the radioactive background must be held below this limit. Further, the energies are in the keV range, near the resolution limits of conventional detectors of this mass. Despite these difficulties, several experiments have in fact been carried out (30, 31, 32). Germanium and silicon solid state detectors are placed in carefully designed low radioactivity shields in an underground site. An energy spectrum is taken which is dominated by a background of both line sources and a somewhat flat continuum. With the lines identified, the background spectrum is fit and a limit is obtained to the amount of an additional WIMP spectrum that can be present. This is illustrated in figure 2.2. As discussed above, each WIMP spectrum is determined entirely by the mass of the WIMP and the interaction cross section. An exclusion plot in mass-cross section space can thus be mapped out in this way. Figure 2.3 shows the state of the art limit.

2.3) Simultaneous ionization and phonon measurement

There are two ways to improve upon these results. The first is to reduce the threshold of the detector, which means increasing its resolution. For a given WIMP mass this improves the limit on cross sections somewhat since the interaction rate increases at low energies. More importantly, it improves the lower mass limit since light WIMPs deposit less energy. Indeed, much of the early enthusiasm for using cryogenic detectors to detect dark matter arose from the possibility of having very low threshold detectors. Lately, however, this enthusiasm has waned because lighter mass WIMPs have been made less favorable by CERN experiments.

An alternate approach is to somehow reduce the background. It will probably be quite difficult to significantly reduce the actual amount of radioactive background present. The current experiments have already gone to extraordinary lengths to shield the detector

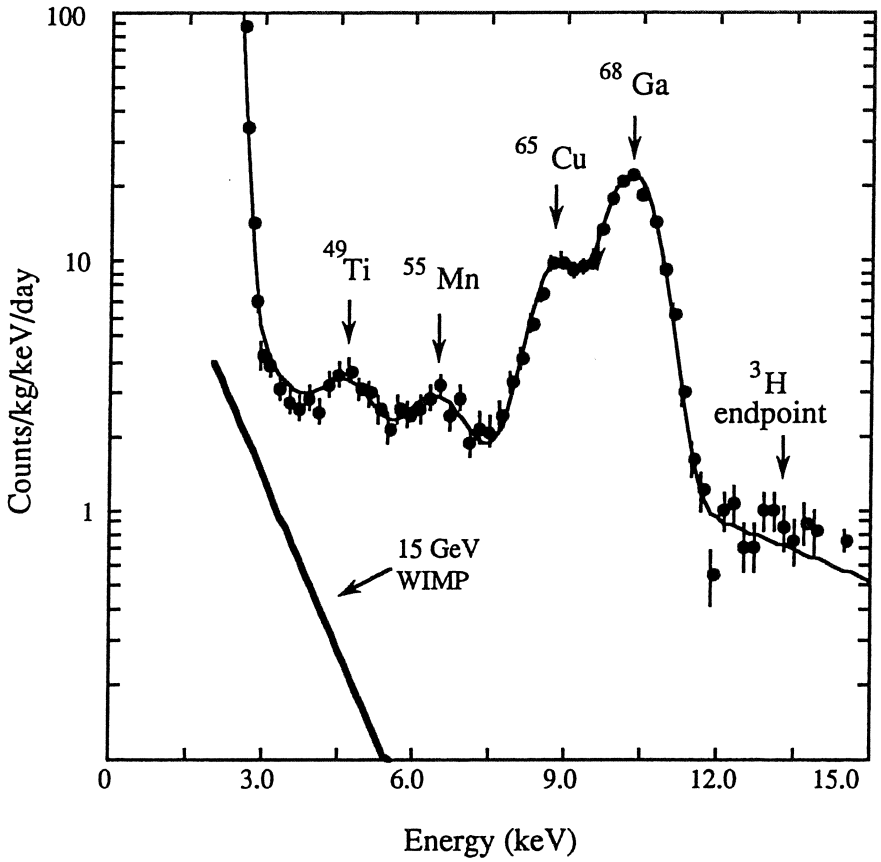

__Figure 2.2__ Measured spectrum from a germanium detector in the UCSB/LBL/UCB experiment at Oroville, representing 3509 kg hr of counting. The data has been fit to the identified radioactive background lines using the known detector resolution. The expected spectrum from a WIMP with a mass of 15 Gev is also shown, and can be ruled out at the rate shown because of the small error it causes in the fit at low energies.

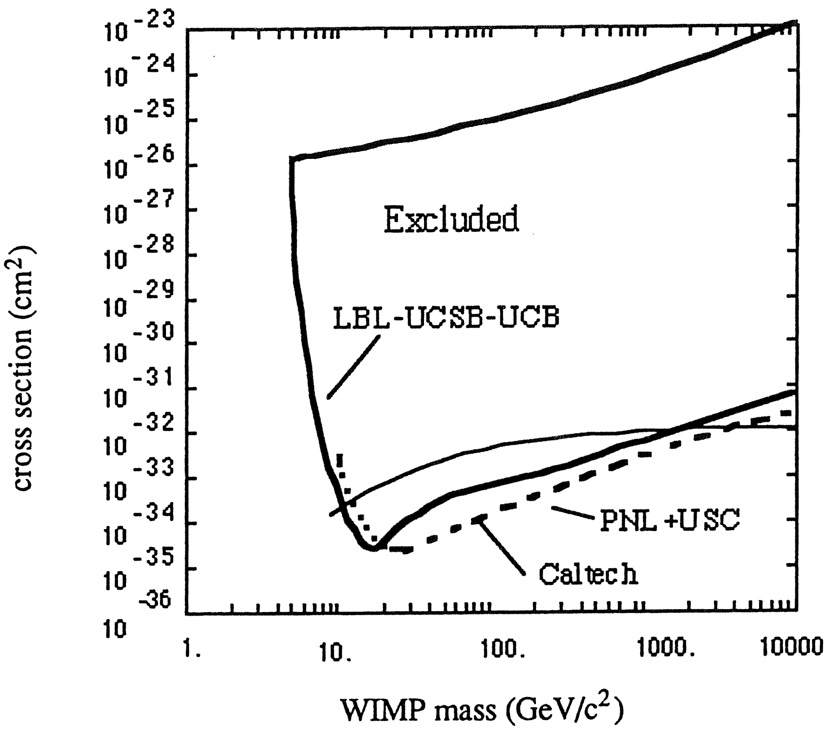

__Figure 2.3__ Current exclusion plot from three experiments using conventional ionization detectors.

from external radioactivity and cosmic rays, and to remove radioactive impurities from the detector and its immediate surroundings. Most of remaining background, in fact, comes from radioactivity in the detector itself. A much better option is to distinguish the signal and the background intrinsically within the detector. This may be possible for one simple reason: the signature of dark matter is recoils of nuclei, while the dominant background in existing experiments is caused by photons and betas, both of which give recoiling electrons.

There are several techniques that can distinguish recoiling electrons and nuclei. One idea that has been proposed is to use a gas filled time projection chamber in which recoils of electrons and nuclei are recognized by their different tracks in a magnetic field (33). A drawback to this approach is that low gas pressures are needed and so a detector of reasonable mass will have a very large volume. Shielding from radioactivity and cosmic rays would then be extremely expensive. A more general technique is to find a material which has several measurable excitation modes (e.g., scintillation, ionization, and heat.) Recoils of nuclei and electrons can be distinguished if the recoil energy is partitioned differently into the various modes for the two types of events.

Perhaps the most important excitation mode to measure is heat, since in many systems most of the recoil energy eventually becomes heat. At room temperature or 77 K this microscopic amount of energy is difficult, if not impossible, to measure in a detector of macroscopic size. At temperatures near absolute zero, however, "cryogenic" detectors can actually measure the thermal energy produced by individual particle interactions.

Other excitations modes that exist at higher temperature are still present at low temperatures in many materials. There are also additional excitation modes such as quasiparticles in a superconductor or rotons in superfluid helium. Heat itself is better thought of as phonons at low temperatures, and the spectrum of phonons created by events may reflect the nature of the interaction.

Of the many possibilities for discrimination of electronic and nuclear recoils at low temperature, our group has chosen to focus first on perhaps the most straightforward detector approach. We simultaneously measure the ionization charge and phonons from events in a semiconductor; recoils of nuclei are distinguished from recoils of electrons because they are less efficient at producing ionization. The phonon measurement is accomplished, essentially, by attaching a thermometer to a large semiconductor crystal operated at a temperature of 0.02 K. Ionization created by an event in the semiconductor is drifted out the crystal in a manner similar, but not identical, to the way standard ionization detectors work at 77 K.

In figure 2.4 we anticipate the result of making a series of such measurements for simulated spectra of background photons and WIMPs. As is done for conventional ionization measurements, the axes are defined in terms of electron equivalent energy. This means that both measurements are calibrated in terms of the energy of a recoiling electron that would give this same signal. A 20 keV photon totally absorbed in the crystal has 20 keV of "equivalent ionization energy" and 20 keV of "equivalent phonon energy" in this scheme. A nucleus recoiling with 20 keV of energy after being struck by a WIMP has less than 20 keV of equivalent ionization energy and more than 20 keV of equivalent phonon energy.

Photons thus appear at a slope of one, while the line at higher slope is due WIMPs. The relative partitioning of energy into phonons and ionization for electronic and nuclear recoils is taken from a calculation performed in the 1960's by Lindhard and his collaborators (34). The resolution of both measurements is taken to be 500 eV. The absolute calibration of phonon energy and the number of charge pairs created by events is discussed in subsequent chapters.

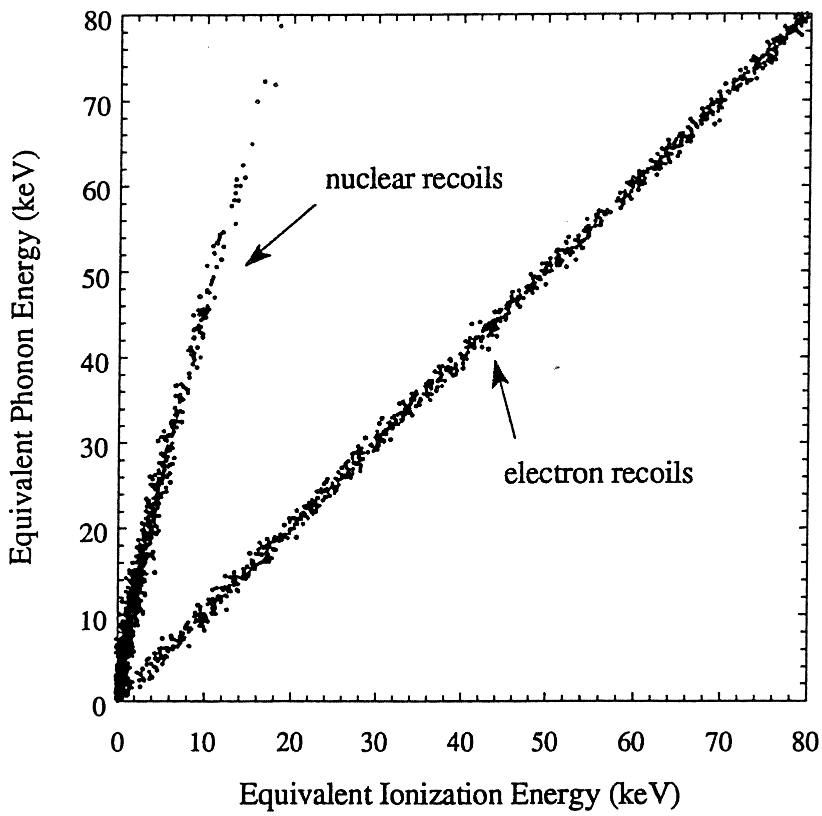

Figure 2.4 Gedanken experiment where both ionization and phonons have been measured for recoils of both electrons and nulcei. The experimental resolution on each measurement is taken to be 0.5 keV

2.4) Low voltage ionization measurement

The hypothetical result shown in figure 2.4 ignores one important detail. As N_Q charges are drifted out of the crystal under a voltage V, they deposit an energy $E=eN_QV$ in the form of phonons in the crystal. In germanium, for example, a charge pair is produced for every 3 eV of photon energy; thus at a 3 V bias this drift energy is equal to the total recoil energy from the initial interaction. At the thousand volts or so bias needed in conventional detectors at 77 K the drift heat would dwarf the recoil energy. Paul Luke has in fact suggested using this "thermal amplification" of the ionization signal to achieve high mass, high resolution detectors (35). It has also been observed by one other group (36). Unfortunately, this large amplified phonon signal is really just another measurement of the ionization charge, and cannot be used to distinguish nuclear and electron recoils. The charge must therefore be collected with a relatively small bias, the maximum value of which depends on the resolution of both the phonon and ionization measurements.

When a bias, V, is used to collect charge, the total measured phonon energy, E_m becomes $E_m=E_\phi+eN_QV$ where E_ϕ is phonon energy created by the initial interaction. As we show in chapter 5, $E_\phi=E_r$, where E_r is the recoil energy. (In general one might expect that $E_\phi<E_r$ if all the recoil energy is not converted to phonons.) Figure 2.5 shows the actual values of E_m and N_Q for recoils of electrons and nuclei with $V=0$ and $V>0$. The axes differ from the electron equivalent energy convention used in figure 2.4 only by a rescaling factor. For clarity the lines are shown without simulated errors. Clearly as V is increased the two lines move closer together.

We define ε as amount of recoil energy required to create a charge pair so that $N_Q=E_r/\varepsilon$. For electron recoils $\varepsilon=\varepsilon_e\approx3$ eV and for nuclear recoils $\varepsilon=\varepsilon_N\approx10$ eV. The measured phonon energy can be written (using $E_\phi=E_r$) as $E_m=N_Q(\varepsilon+eV)$. The distance in

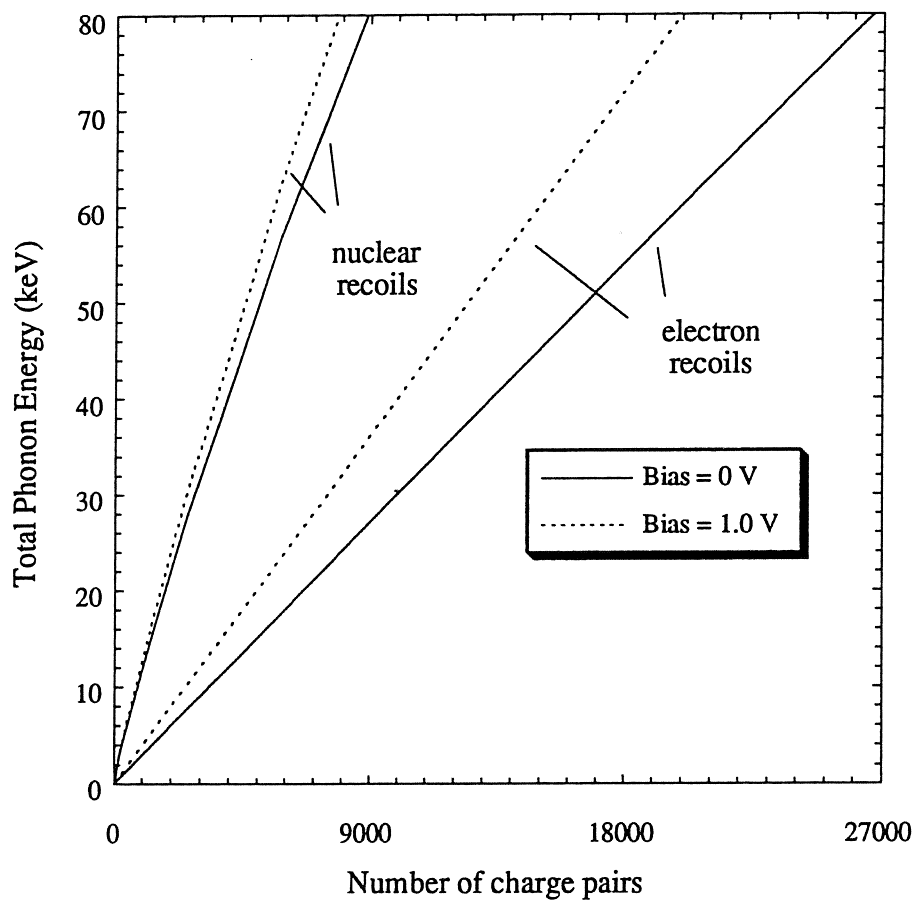

Figure 2.5 Total phonon energy and number of charge pairs for nuclear and electron recoils, with no charge collection bias, and with a bias of 1.0 V.

the vertical (phonon energy) direction between points on the two lines with equal N_Q is given by

$$\Delta E_m = N_Q(\varepsilon_N - \varepsilon_e),$$

which is independent of bias. This is because for a given value of N_Q the same amount of drift heat is added to each line. However the distance in the horizontal (number of charges) direction between a point on the nuclear recoil line with phonon energy E_ϕ to the point on the electron recoil line with the same measured phonon energy, E_m, (but not equal E_ϕ) is

$$\Delta N_Q = E_\phi \frac{\varepsilon_N - \varepsilon_e}{\varepsilon_N(\varepsilon_e + eV)},$$

which decreases like $1/V$ for large bias. The two lines will not be resolved if this distance becomes comparable to the width of lines as determined by the resolution of the detector.

Another way of looking at the situation is to explicitly subtract out the drift heat term, eN_QV, from the measured phonon energy. The recoil energy $E_r = E_\phi$ is then plotted on the vertical axis and the position of the lines is independent of bias. The uncertainty in the charge measurement, σ_N, however, leads to an uncertainty $\sigma_N eV$ in the energy that is subtracted from both lines. The measured resolution in phonons, $\sigma_{E,m}$, is given by the quadrature sum of this variance and intrinsic variance of the phonon measurement, σ_E. Expressing the variance in the ionization measurement in terms of equivalent electron energy we finally find that

$$\sigma_{E,m}^2 = \sigma_E^2 + \left(\sigma_N \frac{eV}{\varepsilon_e}\right)^2.$$

Currently in our 60 gm detector the resolution in both measurements is about 700 eV equivalent electron energy. The bias for which $\sigma_{E,m}$ increases by $\sqrt{2}$ is thus 3 V. This is illustrated graphically in figure 2.6, where simulated measurements with the drift heat term subtracted out are shown for several bias voltages and with an r.m.s. resolution in each measurement of 500 eV. The axes here are once again defined in terms of electron equivalent energy.

To close this section, it is worth noting that it may be possible to get around this problem if the phonons created by the drifting charges have a quite different energy spectrum than the phonons from the initial event. However it will be necessary to have phonon sensors that are sensitive to this difference, and the small amount of energy from the initial recoil must be measured in the face of the larger, though distinct, drift energy.

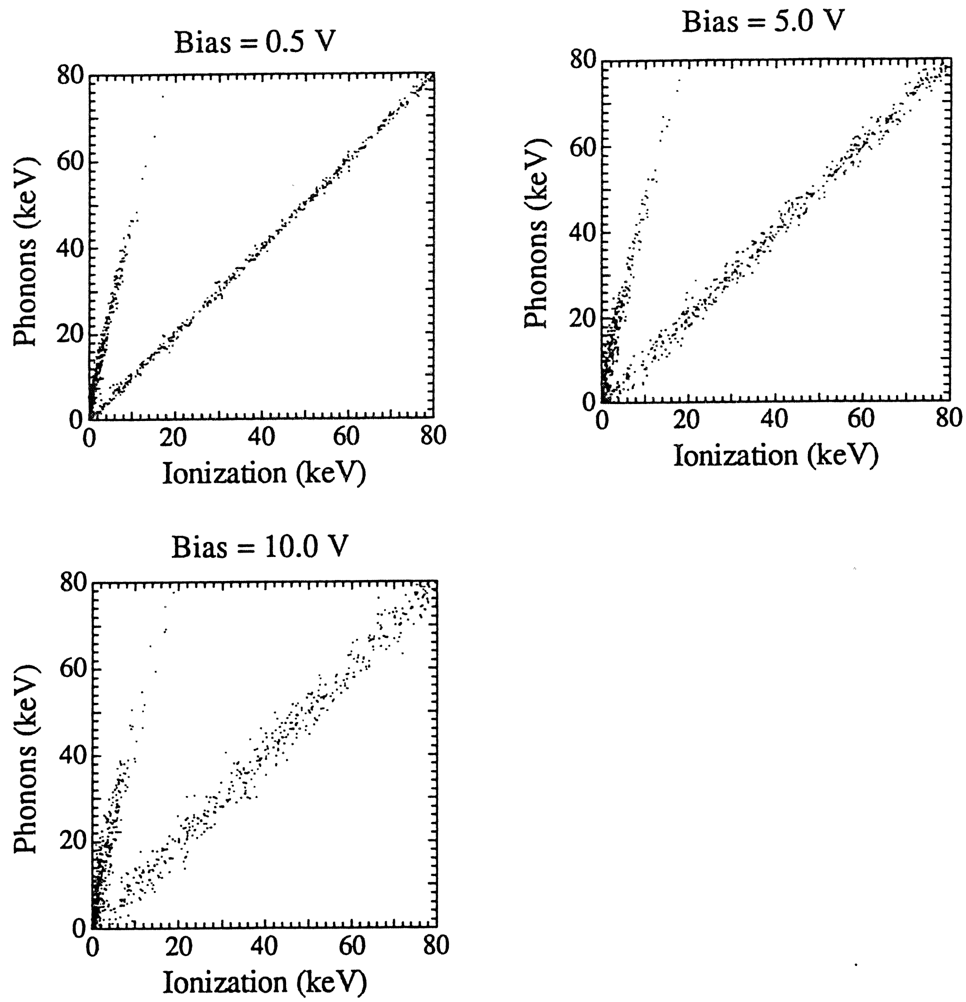

Figure 2.6 Simulated measurement with the drift heat subtracted from the phonon energy at three different charge collection biases.

Chapter 3: Experimental Setup

3.1) Cryogenics

The measurement of the thermal energy created by individual particle interactions can only be achieved at temperatures well below 1 K, as will be discussed in chapter 4. We have therefore cooled our devices in a Model 75 dilution refrigerator made by Oxford Instruments. The base temperature of the refrigerator was ≈15 mK before wiring was installed and has been ≈18 mK thereafter. I spent much of my first two years of work with this group installing and learning to operate this refrigerator. Appendix A lists an operating procedure for the refrigerator that I wrote.

The temperature of devices can be varied by adding electrical heat directly to the coldest point in the refrigerator, which raises its temperature. Most of the results described here were obtained near the base temperature of the refrigerator. Because temperature controllers do not work well near the base temperature, we typically adjusted this power manually.

We use two methods to determine the temperature. One elegant and powerful method is to measure the degree to which thermal energy randomizes the spins of nuclei in an ordered crystal of ^{60}Co in the presence of a known magnetic field. This randomness is a direct probe of the absolute temperature as defined by statistical mechanics. It is a cumbersome technique to actually use, however, and is most sensitive at temperatures below about 25 mK. Because of this, for normal use we calibrated several neutron transmutation doped, or NTD, Ge thermometers (described in greater detail in chapter 4) against the ^{60}Co method and against a commercially produced thermometer at temperatures above 50 mK (Lakeshore GRT 200). These NTD Ge thermometers have excellent long-term stability, and high temperature sensitivity, but unfortunately tolerate less than 10^{-12} W of power at 20 mK before self-heating, and hence are difficult to read out using a conventional conductance bridge. We usually measure the resistance of our thermometers by taking IV curves by hand using low noise voltage amplifiers (PAR model 113) as described in detail in Ning Wang's thesis (37).

3.2) Cryogenic wiring

There are two systems of wiring installed on the refrigerator. One is a set of 18 unshielded, moderate resistance ($\approx 200\Omega$) wires with ≈ 4 nF of stray capacitance to ground per wire. This capacitance makes them unsuitable in most situations for all but the slowest signals, and hence they were used mainly for thermometry and to set DC bias voltages. For more details about wiring and heat sinking, see appendix C.

The other system is used for the primary signals from the detectors, and is designed for low noise and high speed. We make two basic measurements: a voltage measurement for the phonon sensors, and a charge measurement for the ionization. Simply bringing wiring out of the refrigerator to commercial amplifiers is not an attractive option for either of these measurements. The cables used would be nearly 2 m long, and thus, if made of typical coaxial cable, would have roughly 200 pF of capacitance to ground each. This is about ten times higher than the intrinsic capacitance of the thermistor in the voltage measurement and of the detector in the ionization measurement. Extra capacitance means a loss of speed in the voltage measurement, and a decrease of the signal to noise in the charge measurement. In addition, long cables increase the susceptibility to microphonics noise and to interference from external electromagnetic waves.

Another option is to bring part or all of the amplifiers into the refrigerator as close as possible to the detector. There are two problems with this approach: the power dissipated by the amplifiers is now located in the refrigerator and must be either removed or minimized; and not all electronic components can work at low temperatures. We chose to separate out the "front end" JFETs of our amplifiers and to place them in the inner vacuum chamber of the cryostat. They are housed in a 4K environment (where their several mW of power dissipation can be tolerated) and heated to a temperature of roughly 140 K. Mechanical constraints in the refrigerator force this housing to be about 36 cm away from the detector at 20 mK.

This arrangement gives us a relatively open space between the detector and the FET housing. In this space we have constructed "vacuum coax" wires running directly from the 20 mK detector to the 4 K FET housing. As discussed in appendix D, these wires have low capacitance, and also a greatly reduced sensitivity to microphonics noise as compared to standard coaxial or unshielded cables. Another advantage of this arrangement is that we are able to operate the FETs at any temperature above 4 K. The noise of these silicon junction FETs in fact depends on their temperature and so we are able to operate them where the noise is a minimum, which is roughly 140 K.

There are six such wires, each connected to the gate of an FET. The source and drain of each FET are connected with coaxial cables to the room temperature cards that complete the voltage and charge amplifiers. These cards are discussed briefly in appendix E, and are described in detail in a paper by D. Yvon (38). In addition to the sensitive signal wires and FETs, there are a number of coaxial cables running from room temperature to the experimental region that allow such things as biasing and pulsing of circuits, and for the feedback loop in the charge measurement circuit. Between room temperature and 4 K all the coaxial lines are cryogenic coaxial cables from Lakeshore Cryogenics. Most have stainless steel inner and outer conductors (Lakeshore model S1), though a few have copper inner and outer conductors (Lakeshore model C1). Between 4 K and the base temperature region we installed coaxial cables made by Cooner (part number AS421) that have stainless steel outer conductors and superconducting inner conductors.

3.3) Devices

Nearly all of the results presented in this thesis were obtained with the first large detector produced by our group, a 60 g device called E2. Most of the groundwork for the design and production of this detector was work of Ning Wang, who has described it in detail in her doctoral thesis (37). For the sake of completeness I will briefly describe it again here.

The detector consists of a 58.4 g disk of single crystal ultra-pure germanium, 3.8 cm in diameter and 0.96 cm thick, which serves as the "target" for events. Electron-hole pairs created by events are collected and measured in the target, and six sensors attached to the target measure the phonons. The detector is shown schematically in figure 3.1.

The sensors are 1.3x1.3x.0.33 mm^3 pieces of neutron transmutation doped (NTD) germanium, which serve as a temperature sensitive resistors, or thermistors. The characteristics of the NTD germanium used on E2 (NTD 12) are discussed in more detail in chapter 4. A degenerately-doped contact layer is made on the top and bottom surfaces of the thermistors by implanting them with boron ions to a depth of about 2000Å with a total flux of about $3x10^{14}cm^{-2}$. A thin layer of palladium (≈200 Å thick) is deposited on this contact, and serves to help gold stick to the germanium. Several thousand Å of gold are sputtered onto the palladium layer, and wires for thermal and electrical contact are ultra-sonically wedge bonded to the gold layer.

Separate electrical connections are made to the gold contact pads on the top and bottom of each sensor. The connections to the bottom surfaces are made to gold pads on the target crystal to which the thermistors have been attached. All electrical connections are made with very thin (≈17.5 μm Ø) superconducting aluminum wires that have negligible heat conductivity and heat capacity at 20 mK.

The primary thermal link between the detector and the refrigerator is made with three copper wires glued with a silver-filled epoxy to the deposited gold on top of the

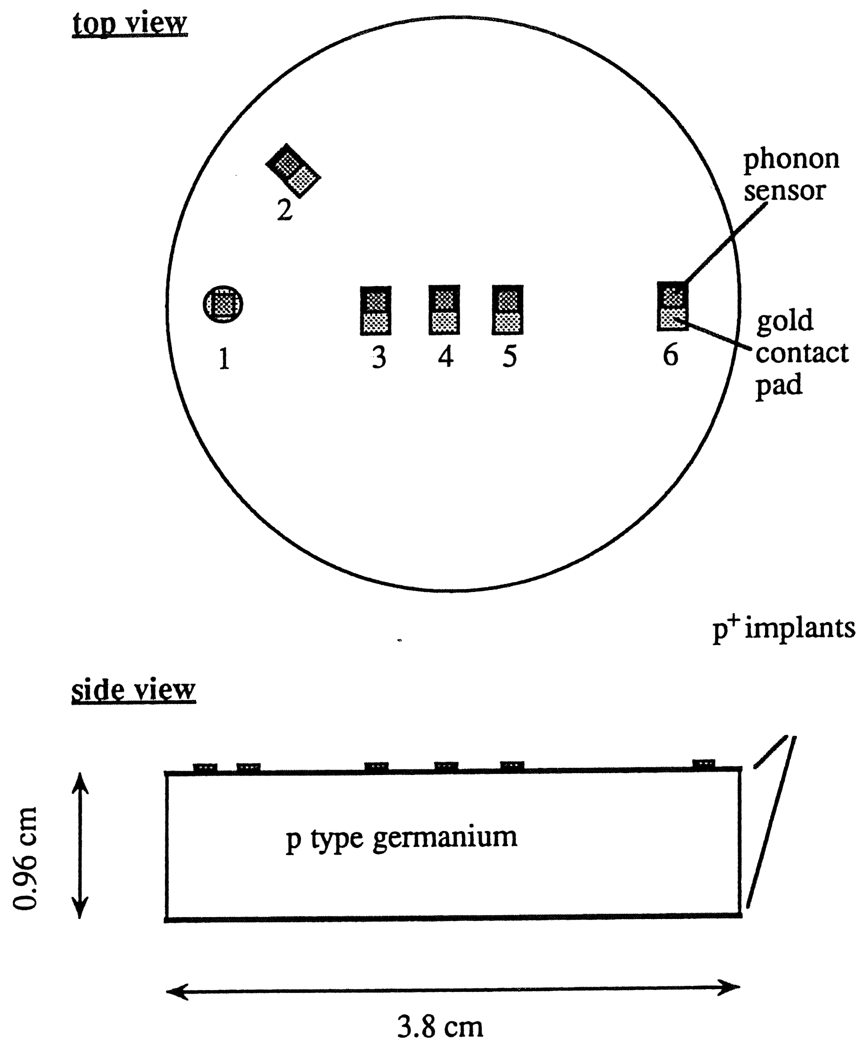

Figure 3.1 The 60 gm detector, E2. The scale is 2:1, and the numbers next to the sensors are referred to in chapter 4.

three sensors in the center of the detector. These wires are glued with the same epoxy to electrically insulating heat sinks made of copper-kapton-copper sandwiches on the refrigerator. The dominant thermal impedance in this arrangement in fact is the boundary resistance between the germanium in the sensors and the gold deposition on top of the sensors.

A key issue for the phonon measurement is the degree to which high energy (≈meV) nonequilibrium phonons are able to travel into the sensors across the interface layer used to attach the sensors to the target crystal. Previous tests with a smaller device had shown that bonds made with a metal-semiconductor eutectic interface are more transmissive for high energy phonons than bonds made with a glue. Eutectic bonding is a technique based upon the fact that a mixture of germanium and gold will melt into a liquid phase, called a eutectic, at a temperature (356 °C) well below the melting temperature of either element alone. For more details on this technique, see (37). Four of the sensors on E2 were attached with this eutectic technique, and two others were attached with a thin layer (≈25 μm) of silver-filled epoxy.

The large target crystal functions as an ionization detector. The disk is p-type germanium, with a net dopant concentration $(n_a - n_d) \approx 2\times10^{11}\mathrm{cm}^{-3}$. The top and bottom faces of the disk have identical p^+ contacts made with boron implants like those on the thermistors. These implanted regions serve as conductive planes, no additional gold layer is deposited on top of them. A bias is applied between these surfaces, drifting charges to the implanted contacts. The physics of this charge collection is the subject of chapter 5. Note that the top surface of the detector serves electrically both as one of the charge collection planes, and as the voltage at the bottom of each sensor. The wires attached to the bottoms of the sensors are in fact used to define the charge collection voltage on this surface. Electrical connection to the other side of the target crystal is made with an aluminum wire attached to a small gold pad.

Finally, in addition to E2, we constructed a simpler detector consisting of a 1 cm x 1 cm square of p-type germanium 1 mm thick glued directly to a copper heat sink. The ionization collection contact on one of the 1 cm^2 surfaces is a p^+ boron implant like those on E2, while on the other side there is an n^+ phosphorous implant. A thermistor similar to those on E2 was glued to the p^+ surface.

3.4) Voltage and charge measurements

Figure 3.2a shows the circuit used to measure the phonon signal in a thermistor, and figure 3.2b shows the circuit used to make a charge measurement. Typical values of various circuit components are shown in table 3.1. The amplifiers themselves consist of a FET in the cryostat connected to a board outside, and are discussed in greater detail in appendix D. The FETs we use are silicon junction FETs from InterFET corporation. The complete electronics chain includes other modules following the amplifiers shown, and is discussed in section 3.6.

The phonon circuit allows a relatively straightforward voltage measurement. Electronically, the phonon sensor acts as a resistor (with a parallel capacitance) whose resistance changes when its temperature changes, i.e., a thermistor. To the extent that the load resistor is much bigger than the phonon sensing resistor, $R_b \gg r$, the current through the sensor is approximately constant, $I=V_b/R_b$, and a change in the sensor resistance, δr, due to an event is measured as $\delta v=I\cdot\delta r$. The actual form of $\delta r(t)$ and hence $\delta v(t)$, and the choice of bias voltage are discussed in chapter 4. Because δr is negative for a positive change in temperature, the signals are usually inverted when digitized.

It is important to note that the signal speed is limited by the time it takes to charge the capacitors C_r and C_p indicated in figure 3.2*a*. The relevant time constant is $\tau_r=r_{//}\cdot C_{//}$, where $r_{//}^{-1}=R_b^{-1}+r^{-1}$, $C_{//}=C_r+C_p$, and C_p is the parasitic capacitance from the gate wire

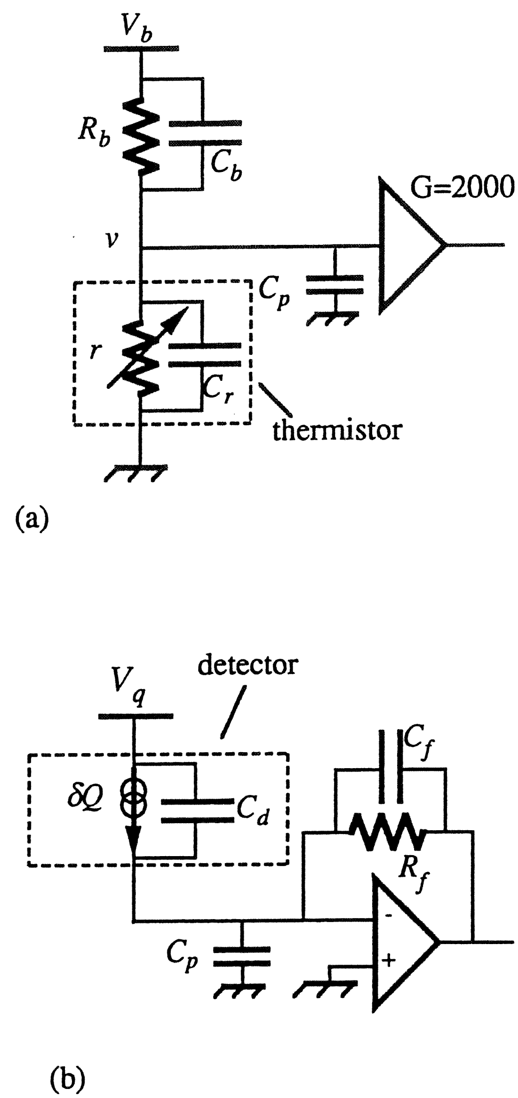

Figure 3.2 Circuits for (a) the voltage measurement of the phonon sensor, and (b) the charge measurement.

Table 3.1 Values of various circuit elements

Voltage measurement	R_b	10 MΩ
	C_b	3 pF
	C_p	≈30-50* pF
	r	≈0.1 - 5 MΩ
	FET	2N6453
charge measurement	R_b	10 MΩ
	C_b	3 pF
	R_f	100 MΩ
	C_f	0.4 pF
	C_c	5000 pF
	C_d	16 pF
	C_p	≈70-100* pF
	FET	NJ450L

*These values are estimates, and have large uncertainties.

and FET. In most of the work described in this thesis, however, $R_{//} \approx r \approx 500$ kΩ, $C_{//} \approx 80$ pF, giving $\tau_r \approx 40$ μsec, much faster than the 0.5 msec rise and 50 msec fall times of typical pulses. Another comment is that the amplifier has as a very large input impedance, and thus, except for the capacitance it adds, merely senses the voltage v and amplifies it by a gain.

The charge measurement, whose circuit is shown in figure 3.2*b*, is quite different from the voltage measurement. The amplifier acts through a feedback network to keep its negative input at a "virtual" ground. This virtual ground acts with the bias on the other side of the detector to create an electric field that drifts electrons and holes created by events to the implanted contacts. The amplifier supplies image charge to the bottom plane of the detector to maintain the ground voltage as the charge drifts out, and the bias supplies image charge to hold the top contact at a constant voltage. The output of the amplifier has to change in order to drive this image current through the feedback network, and this change is the signal measured. Simply speaking, the charge produced in an event is integrated on the feedback capacitor, C_f.

The actual mechanism of this process on time scales short compared to R_fC_f is worth clarifying. Negative charge is supplied to the output side of the feedback capacitor, inducing an equal amount of positive charge to build up on the other side, and an equal amount of negative charge to flow to the bottom of the detector. The input terminal of the amplifier supplies no charge itself, and the input side of the circuit remains strictly at ground. The negative charge on the bottom of the detector exactly cancels the positive charge Q drifting out of the detector from the event. An instant after the event, then, the feedback capacitor has $+Q$ and $-Q$ on its input and output sides, respectively, and the output of the amplifier is therefore at a voltage $-Q/C$. This charge on both sides of the capacitor then flows through the feedback resistor discharging the capacitor. The voltage at the output is thus

$$\delta v(t) = -\frac{Q}{C_f} e^{-\frac{t}{R_f C_f}}.$$

Note that the capacitance of the detector does not play a role in the signal. However it does play a major role in the noise, as described below.

The rise time is assumed to be infinite here, but in reality is limited by the slower of the time it takes for the charges to drift to the contacts and the amplifier's rise time. We have implicitly assumed an ideal amplifier with infinite gain, while in reality the gain of the amplifier is attenuated at high frequencies. It is this attentuation that determines the amplifier rise time. Charge amplifiers can have rise times of several nanoseconds, but we had to limit ours to about 1 μsec because phase shifts in the ≈2 m long cables between the FET and room the temperature card cause oscillations at higher frequencies. This risetime does not depend explicitly on any of the circuit elements shown. The fall time, $R_f C_f$, with the circuit values of table 3.1 is ≈40 μsec.

It is inconvenient to combine the phonon and charge measurements on the same device when each is configured exactly as shown in figure 3.2. One contact of the detector must serve as the ground (or at least a fixed voltage) for the phonon measurement while at the same time helping to define the bias voltage for ionization collection. If ionization is collected on this surface, then changes in the current through a thermistor during an event will also be measured in the charge circuit. Our solution to this problem is shown in figure 3.3. The ionization amplifier is coupled through a capacitor to the side of the detector that is biased for ionization. Charge flowing to the detector on time scales faster than the rolloff time constant of the bias circuit, $\tau = R_b C_c \approx 5$ msec, passes through C_c to the amplifier circuit and is measured without distortion. Signals slower than this pass across the bias resistor and are not measured.

Working at low temperatures places certain constraints on electrical circuit elements. Resistors made of such materials as carbon or metal-oxides have a resistance that increases dramatically at temperatures below 1 K. Metal film resistors have nearly the same resistance at milliKelvin temperatures as at room temperature, but are not readily available in the standard solderable form for resistances larger than 2.2 MΩ. When we need resistances larger than this, we use 10 MΩ NiCr chip resistors (MiniSystems, part number MSTF 4-S-N-10M) that unfortunately require wedge-bonding for connections. Each of these resistors has a parallel stray capacitance of about 3 pF. In the feedback of the charge circuit this stray capacitance serves as the feedback capacitor, with no other capacitor explicitly added. When we do need a capacitor at low temperature, it too must be carefully selected. The dielectric constants of many materials, especially those with large dielectric constant, change dramatically with temperature. We have only used silver-mica capacitors, and have thus been limited to capacitances less than 10,000 pF.

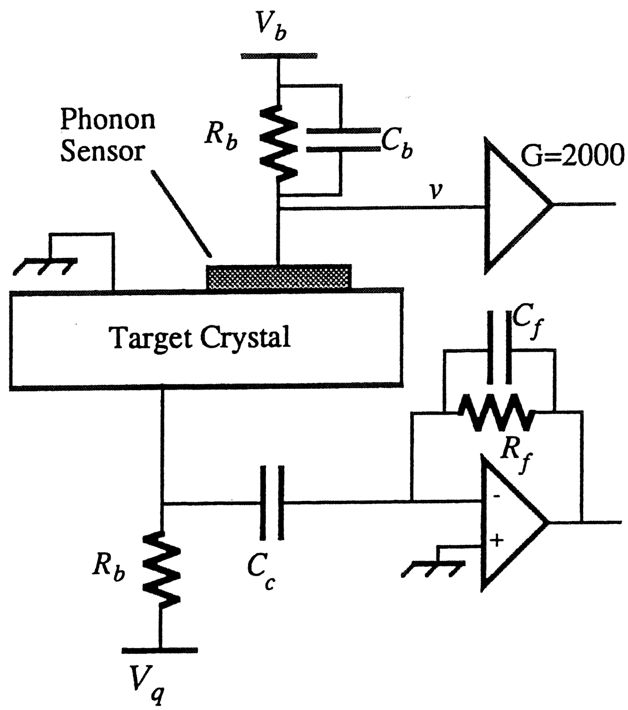

__Figure 3.3__ The combined phonon and ionization measurement circuits connected to the detector

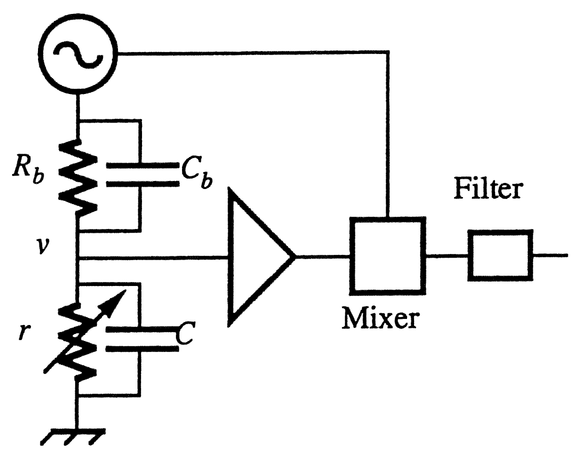

__Figure 3.4__ The AC voltage measurement scheme.

3.5) Noise

One of the more important experimental challenges we face is achieving the lowest possible electronic noise. Because light WIMPs deposit small amounts of energy, reducing noise to maximize sensitivity allows a more comprehensive test of the possible WIMP mass range. Although noise reduction is a somewhat standard subject treated in many books (see, for example, 39), there are certain problems and opportunities unique to cryogenic electronics. A more detailed discussion of this subject, which consumed a great deal of my time in graduate school, is found in appendices D and E. Here I briefly discuss the most important results.

The dominant noise sources in the phonon measurement are the voltage noise of the FET, the Johnson noise from the thermistor and microphonics pickup in the gate wire. The voltage noise of our FETs is currently about 1.5 $nV/Hz^{1/2}$ at frequencies above a few hundred Hz, though it is possible to obtain FETs with a noise that is about half this value, or even lower. The Johnson noise of a $\approx$1 MΩ thermistor at 20 mK is also about 1 $nV/Hz^{1/2}$, a tiny fraction of the 130 $nV/Hz^{1/2}$ it has at room temperature. Both of these voltage noise sources appear at the input to the amplifier, thus they compete directly with the signal. Microphonics, on the other hand, is a source of current injected directly onto the gate wire input to the amplifier. It is caused by microscopic vibrations of the wire and its surroundings. This current noise, δI, flows across the thermistor giving a voltage noise $\delta I\, r$ that competes with the signal. The measured "power spectral density" of the noise as it appears at the input to the amplifier in the voltage circuit is shown in figure E.2 of appendix E. Below 500 Hz the noise is mostly microphonic (though there is some 60 Hz pickup) and above 500 Hz it is dominated by the frequency independent, or "white", FET noise.

The noise in the charge measurement is also dominated by the FET noise and microphonics, but is a bit more subtle to understand. Microphonically generated current at the gate flows through the feedback network, giving a voltage drop $\delta I \cdot Z_f$ across the feedback network whose impedance is Z_f. Because the input to the amplifier is at virtual ground, this voltage appears at the output. The voltage noise of the FET will also push current through the feedback network, but only to the extent this current can also flow to ground on the input side of the feedback network through the detector capacitance, C_d, and the parasitic capacitance of the FET and gate wire, C_p. Calling the total input impedance due to these capacitances Z_i, the FET noise e_n causes an output noise e_o in the frequency domain given by $e_o=e_n(1+Z_i/Z_f)$.

This noise can be roughly understood by noting that at high frequencies it reduces to $e_o \cong e_n \cdot (C_i/C_f)$ where $C_i=C_d+C_p$, and C_f is the feedback capacitance. Since the pulse height scales like $1/C_f$, the signal to noise ratio scales like the inverse of the input capacitance. Figure E.5 of appendix E shows the voltage noise of the charge circuit, this time as it appears at the *output* of the amplifier. (For the charge measurement it does not make sense to talk about the voltage noise at the input.) Just as in the phonon measurement, the noise is dominated by microphonics at low frequencies. At frequencies above a few kHz it is $\approx$200 nV/Hz$^{1/2}$, consistent with $e_o \cong e_n \cdot (C_i/C_f)$ where $e_n \approx 1$ nV/Hz$^{1/2}$, $C_i \approx 80$ pF, and $C_f \approx 0.4$ pF.

3.6) AC phonon measurement

As is clear from the voltage noise measurement shown in figure E.2 of appendix E, $1/f$ noise, microphonics and 60 Hz are an order of magnitude larger than the FET noise at frequencies less than about 500 Hz. Unfortunately this is precisely where most of the phonon signal lies. To circumvent this problem we often use an AC biasing scheme (40) shown in figure 3.4. The thermistor is biased with a sinusoidal voltage. If, for the moment, we ignore the capacitances and assume $R_b \gg r$, then the current is $I(t)=I_o\cos(2\pi f_o t)$, where $I_o=V_b/R_b$, and the total voltage at the thermistor is

$$v(\mathrm{t})=I_o r(\mathrm{t})\cos(2\pi f_o t)+e_n(t)$$

where $e_n(t)$ is the noise. This signal is then mixed with (i.e., multiplied by) a reference signal of frequency f_o in phase with the bias. The mixing process, which is performed with a PAR 128 lock-in amplifier, affects the signal part of $v(t)$ and the noise differently.

After the first stage amplification and mixing, the signal portion of the "output" voltage, referred to the input of the amplifier (i.e., with the gain G of the first stage amplifier divided out), is given by

$$\begin{aligned} v_{out}(t) &= I_o r(t)\cos^2(2\pi f_o t) \\ &= I_o r(t)\frac{1}{2}\left(1+\cos(4\pi f_o t)\right). \end{aligned}$$

Half of the signal appears at its normal frequency, and half appears as the amplitude of a $2f_o$ signal. A steep filter (8 pole Bessel) with a cutoff frequency higher than changes of interest in $r(t)$, but well below $2f_o$, is then used to remove the $2f_o$ term, so that the final signal is

$$v_o(t)=\frac{1}{2}I_o r(t)I.$$

Thus the event is recovered intact, but reduced by a factor of 2.

The noise, however, is not affected by the sinusoidally varying bias. The mixing then effectively separates the noise into a component at $f+f_o$ and a component at f-f_o. The noise at low frequencies after mixing is therefore the sum of the noise just above and just below the reference frequency before mixing. The bias frequency can be picked to be outside the frequency range where microphonics noise dominates, and so the noise after mixing at low frequencies is basically the flat noise of the amplifier near 1 kHz.

Figure 3.5 shows the noise referred to the input of the amplifier obtained after mixing at 1 kHz. For clarity the thermistor is unbiased, otherwise there would be a large signal at $2f_o$=2 kHz. The overall decrease in the noise with frequency is due to a slight rolloff in the mixing circuit. The low frequency noise can be clearly seen on both sides of

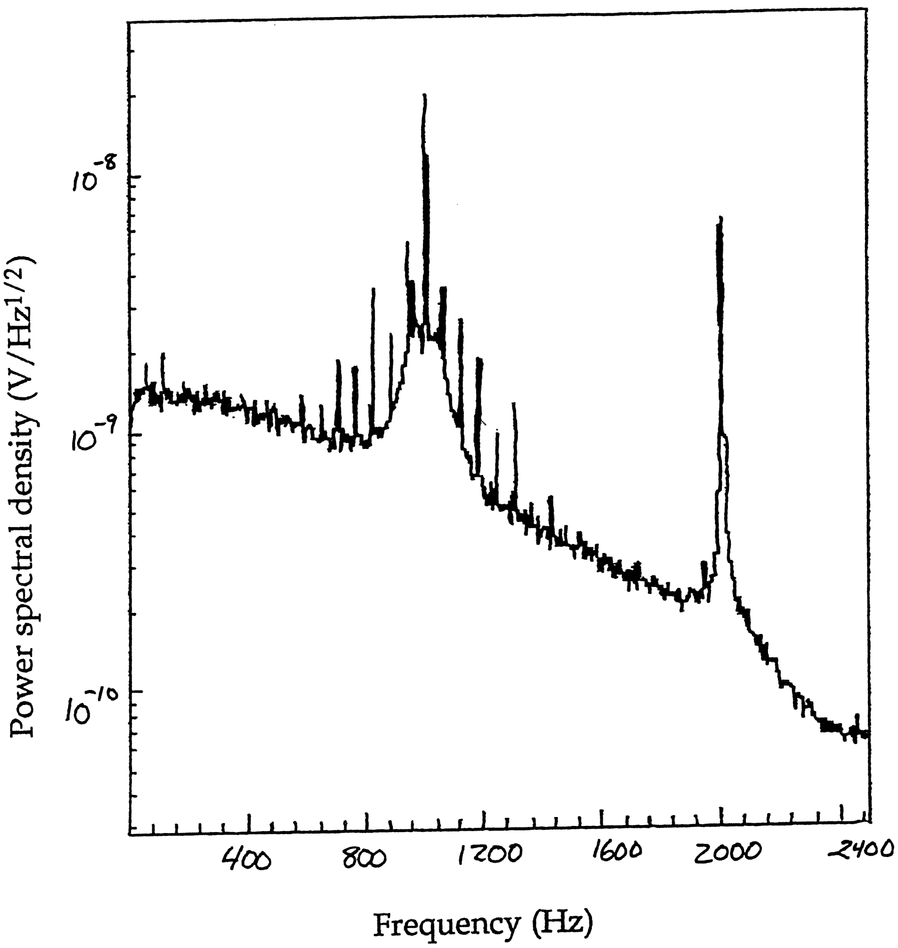

Figure 3.5 The noise in the phonon measurement after mixing at 1 kHz. When taking data we employ a steep low-pass filter with a 200 Hz corner frequency to remove the noise at higher frequencies.

1 kHz, and the noise below 500 Hz is just the flat noise from the FET and the Johnson noise of the thermistor.

This technique works only because the dominant microphonic noise physically originates on the gate wire and is unaffected by the sinusoidal current bias on the thermistor. If the dominant noise were a 1/f fluctuation in the thermistor resistance, for instance, this noise would appear at f_o after biasing, and then be mapped back down to low frequencies by the mixing process along with the signal.

There are several factors that constrain the bias frequency besides the basic requirement that it be faster than changes of interest in $r(t)$. The most stringent limitations are that the frequency be higher than the microphonics noise, or well above ≈500 Hz, and yet well below the roll-off frequency of the thermistor. This roll-off frequency is $f_r = 1/(2\pi r_{//} C)$, where $C = C_r + C_p + C_B \approx 80$ pF, $r_{//}^{-1} = r^{-1} + R_B^{-1}$, and r is both bias and temperature dependent. This presents a problem in that the signal size roughly increases with r, but f_r decreases with increasing r. Typically $r \approx 1$ MΩ, for which $f_r \approx 2$ kHz. We usually pick $f_o = 1$ kHz. If $f_o > f_r$, it is easy to show that the measured signal is divided by a factor $\sqrt{1 + (\omega_o R_{//} C_{//})^2}$ where the parallel sums $R_{//}$ and $C_{//}$ are defined in section 3.4.

Two other constraints turn out to be less severe. One is that f_o be smaller than the roll-off frequency of the bias network, $f_b = 1/(2\pi R_b C_b) \approx 5$ kHz. Another is that f_o exceed the electron-phonon decoupling frequency within a thermistor, which is typically ≤200 Hz. This decoupling is discussed in chapter 4.

3.7) Signal Processing and data acquisition

The full data acquisition system used when simultaneous measuring ionization and the signal from one thermistor is shown in figure 3.6. The basic scheme consists of digitizing the voltage versus time traces from both signals and digitally fitting them to

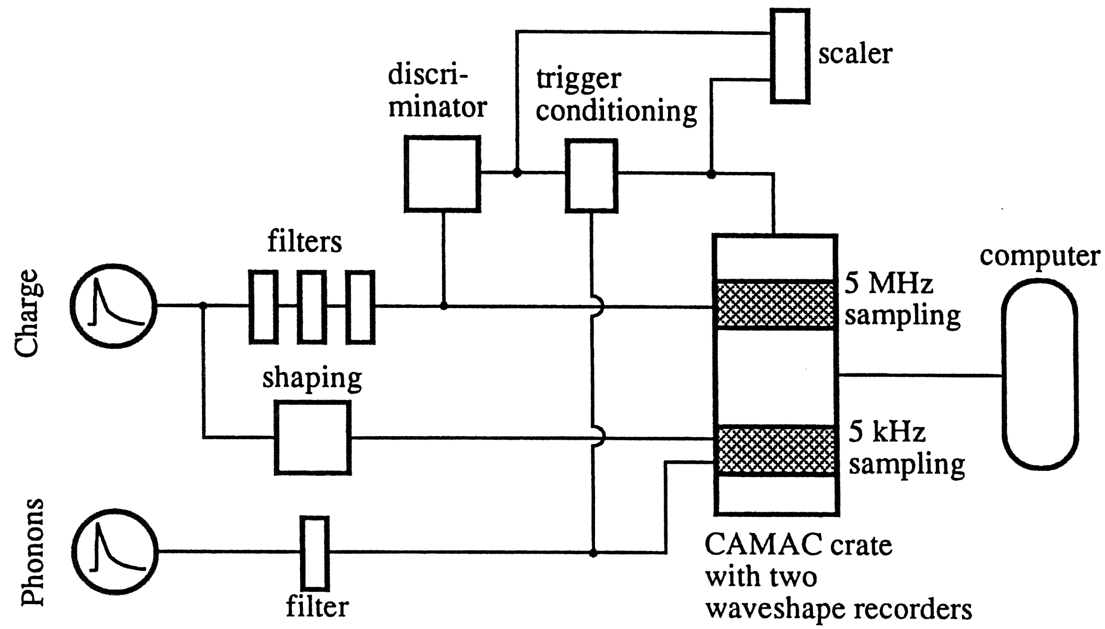

Figure 3.6 The data acquisition system.

obtain estimates of the phonon energy and number of charges for each event. The ionization is used for a trigger because it is much faster than the phonon signal.

An important result from Fourier transform theory (the Nyquist theorem) is that only information at frequencies at or below half the sampling frequency is correctly measured in the digitization process. Any noise at frequencies above half the sampling frequency, even if well above the relevant signal frequencies, will be "aliased" down to lower frequencies during digitization, and cannot be removed after the fact; it must be filtered out beforehand. We employ steep (6 or 8 pole) anti-aliasing filters whenever digitizing signals. We use Chebychev filters when looking at noise in systems, since these have a sharp corner frequency and fairly good flatness in the frequency domain. For pulses we use Bessel filters because they are minimally distorting in the time domain. When the AC bias technique is used on the phonon signal, the filter that removes the carrier frequency also serves as the anti-aliasing filter.

In addition to these filters, a high pass filter with a corner frequency of $\approx$400 Hz is used on the ionization signal to remove the low frequency microphonics seen in figure E.5. A notch filter is also used to remove cross-talk from the AC biasing of the thermistor.

For convenience, a digital scope is used as a discriminator to obtain trigger signals from the ionization pulses. Events are digitized with LeCroy model 8192 waveshape recorders in a CAMAC crate, and read out by a VAX model 3100 workstation. Each recorder has several inputs, but samples all of them at the same rate. We digitize the phonon signal in one module at a typical rate of 5 kHz, and the ionization in another, typically at 5 MHz. Both signals are fit online in the time domain against a template made from the average of many events carefully selected to have no pile-up. This fitting is discussed in appendix F. Either the entire event, or just the fit results, are then saved on disk. The documentation for the data taking code, which I wrote, is included in appendix H.

All the other elements of the data acquisition system are designed to cope with pile-up in the phonon signal, which is illustrated in figure 3.7. Here the phonon signal in E2, which is proportional to the temperature, is seen for a typical three sec time interval when exposed only to the room background with no source present. For reference, a 60 keV photon gives about a 2.5 μV signal under the same conditions. There are several problems associated with this pileup. One is simply that often a second event follows a good event within the time window of the fit, thereby distorting the fit results. These events are discarded by cutting on the chi-square of the fit.

A more serious problem is that large events significantly heat the crystal, so that events following just after are distorted by the fact that the thermal system has been driven into a non-linear regime. The fitting of the phonon signals includes a variable amplitude falling exponential term that accounts for a previous event; distorted events can be removed by examination of this amplitude. Practically speaking, though, data taking is slowed considerably if all triggers are digitized and examined, since the majority of events suffer from this problem. We built a module that examines the level of the phonon signal at the trigger time, and inhibits the trigger if the voltage is outside a window near the quiescent level. This "trigger conditioner" is shown in figure 3.6. Both the raw and conditioned trigger rates are recorded by a scaler.

A final, and more subtle, pileup problem results from the fact that currently our ionization and phonon signals have vastly different time scales. The phonon signals have a 1-2 msec rise and 50 msec fall, while the ionization signals have a 2 μsec rise and 40 μsec fall. If a second event happens after the ionization digitization has stopped, but within the first ≈msec of a trigger, it is difficult to distinguish this double event structure in the phonon signal alone. The original event then appears to have a higher phonon energy to ionization ratio than a photon, possibly mimicking a dark matter signal. One way to deal with this is to continue to digitize the ionization for more than a millisecond for each event, but this involves processing an inconveniently large number of samples.

Instead we built a shaping amplifier that slows the ionization signal down enough so that events can be seen when sampled at the same speed as the phonon signal. This is also shown in figure 3.6. Unfortunately this reshaped signal has a poorer signal to noise ratio than the raw signal, and therefore is not a good substitute for the primary ionization measurement.

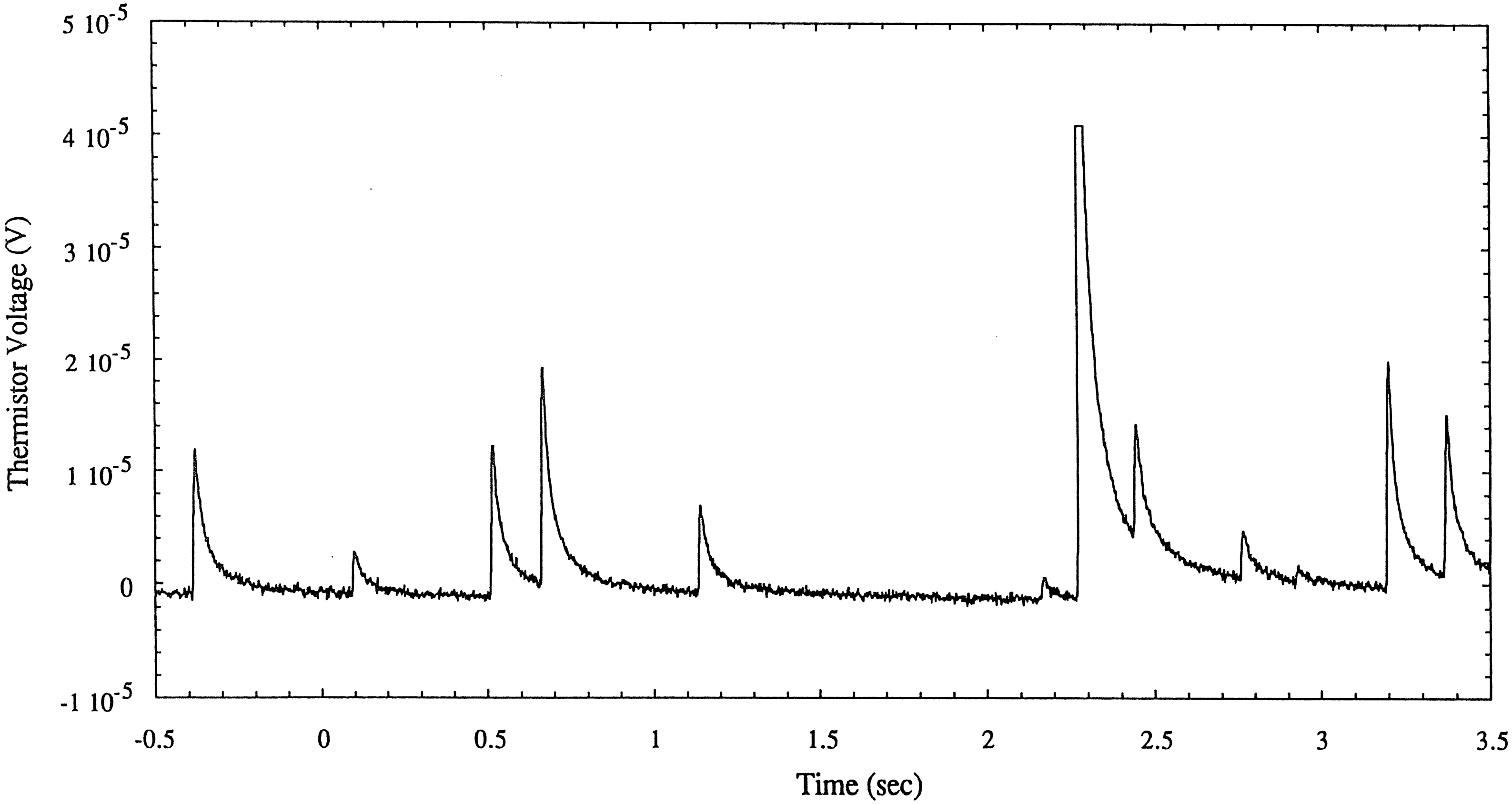

Figure 3.7 A long time trace of the phonon signal taken at a temperature of ≈25 mK. All the pulses seen are created by photons from the radioactive background in the room. For scale, 60 keV photons have a pulse height of ≈2 μV.

Chapter 4: Physics of the phonon measurement

The physics of the phonon measurement, though in many ways the most interesting aspect of our detector, has not been the main subject of my work. Neutron transmutation doped (NTD) thermistors have been used extensively at temperatures greater than about 300 mK (41, 42), and studied more recently at temperatures near 100 mK (43). Their basic behavior at 20 mK was first studied by Ning Wang, who developed a "hot electron" model in which the electrons in the sensor thermally decouple from the phonons in the sensor (37, 44). Another interesting and potentially quite important aspect of the measurement is the degree to which we can measure high energy, non-equilibrium phonons. As mentioned in the last chapter, the eutectic bonds employed on E2 were designed to maximize the transmission of these phonons into the sensors (37).

For completeness, the basic ideas of the hot electron model are presented in this chapter, and the expected pulses within the hot electron model are worked out it detail in appendix G. Experimentally, however, we have not had time to continue the initial careful study of the phonon measurement until quite recently. In the meantime the electronics noise in the system has been reduced considerably, and the current measurements are more sensitive than previous ones. The discussion of the experimental results, then, is essentially a status report of work in progress. The goal is to help clarify what measurements have been made, what is understood, and what is not.

4.1) Thermistor behavior and the hot electron model

A typical current vs voltage (I-V) curve for an NTD thermistor on E2 is shown in figure 4.1. As the current is increased the resistance drops, due to the heating of both the thermistor and E2 as the power is increased. The power at any point on the curve is just

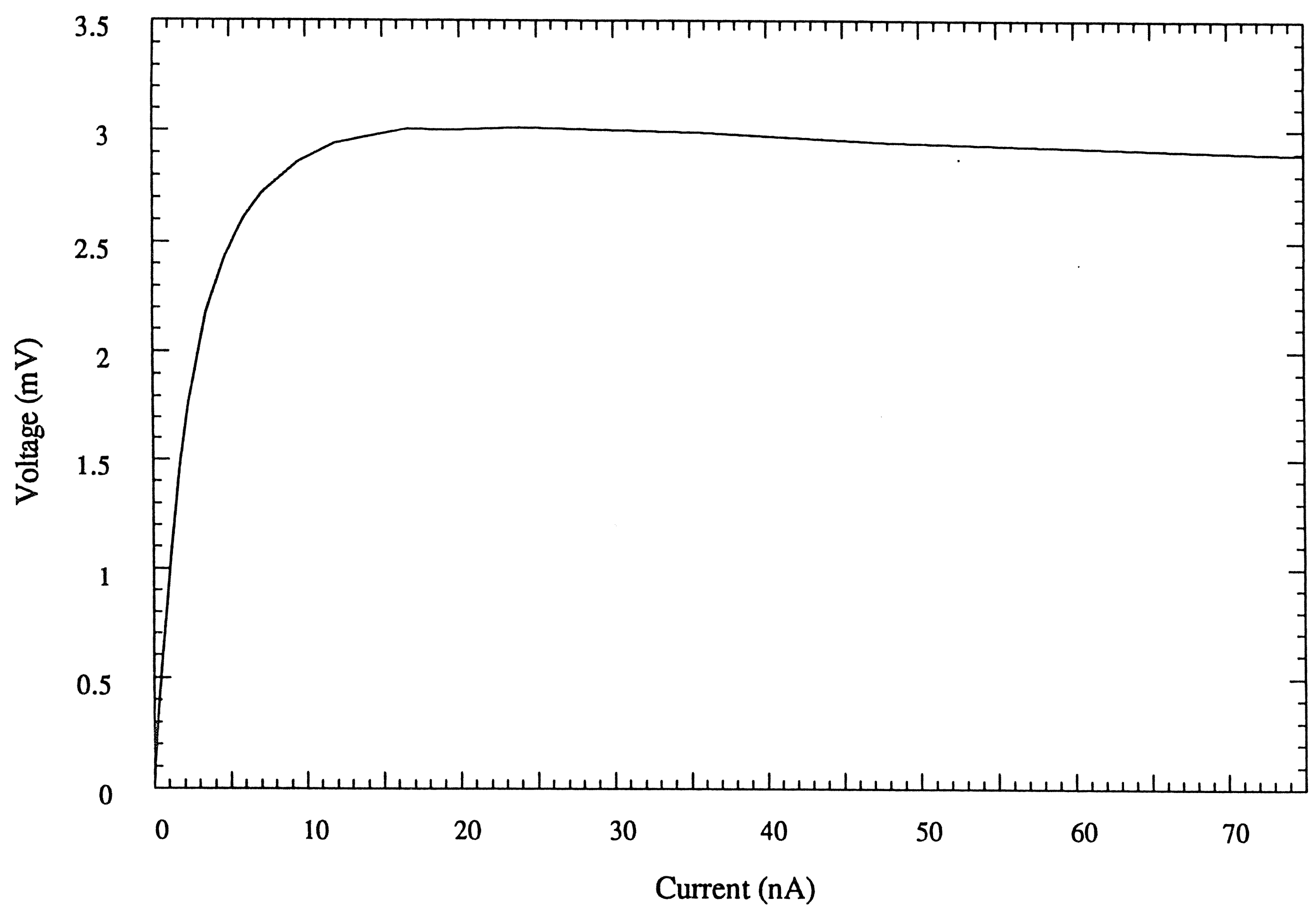

Figure 4.1 IV curve of sensor 6 taken at ≈22 mK

IV. This non-linearity is a fundamental feature of the phonon measurement, and limits the size of signals from events.

The resistance at the origin of the I-V curves (zero power) for NTD thermistors is found to depend on the temperature of the device as

$$R = R_o e^{\sqrt{\frac{\Delta}{T}}}. \qquad 4.1$$

The conduction mechanism at low power is known as variable range thermally assisted hopping conduction (45). Charges tunnel between impurity sites, a process which depends strongly on their thermal energy. A recent calibration of the zero power resistance of the thermistors on E2 is shown in figure 4.2, and is well described by equation E.1. Although this data set only extends in temperature to ≈50 mK, the resistances are a few MΩ at 20 mK, and that they change by about 4 orders of magnitude between 20 mK and 100 mK.

Certainly part of the non-linearity in figure 4.1 is due to the fact that E2 heats up above the temperature of the refrigerator, thus T in equation 4.1 increases. However, as described in (44), there is more of a decrease in resistance than can simply be accounted for by the change in the temperature of E2. At temperatures as low as a few hundred mK in NTD germanium (43) this is well described by the "electric field effect" (46), which arises because the charge carriers acquire energy from the electric field during the hopping process. However the electric field model does not appear to explain the behavior seen in NTD germanium at 20 mK.

In the "hot electron" model the electrons in the thermistor are assumed to thermally decouple from the phonons in the thermistor when power is applied to the electron system, as represented in figure 4.3. This power can be both electrical and, we believe, from high energy phonons created by particle interactions. Also shown in the figure is the decoupling of the phonons from the heat sink due to the thermal boundary resistance discussed in appendix B. The electron-phonon decoupling occurs because the

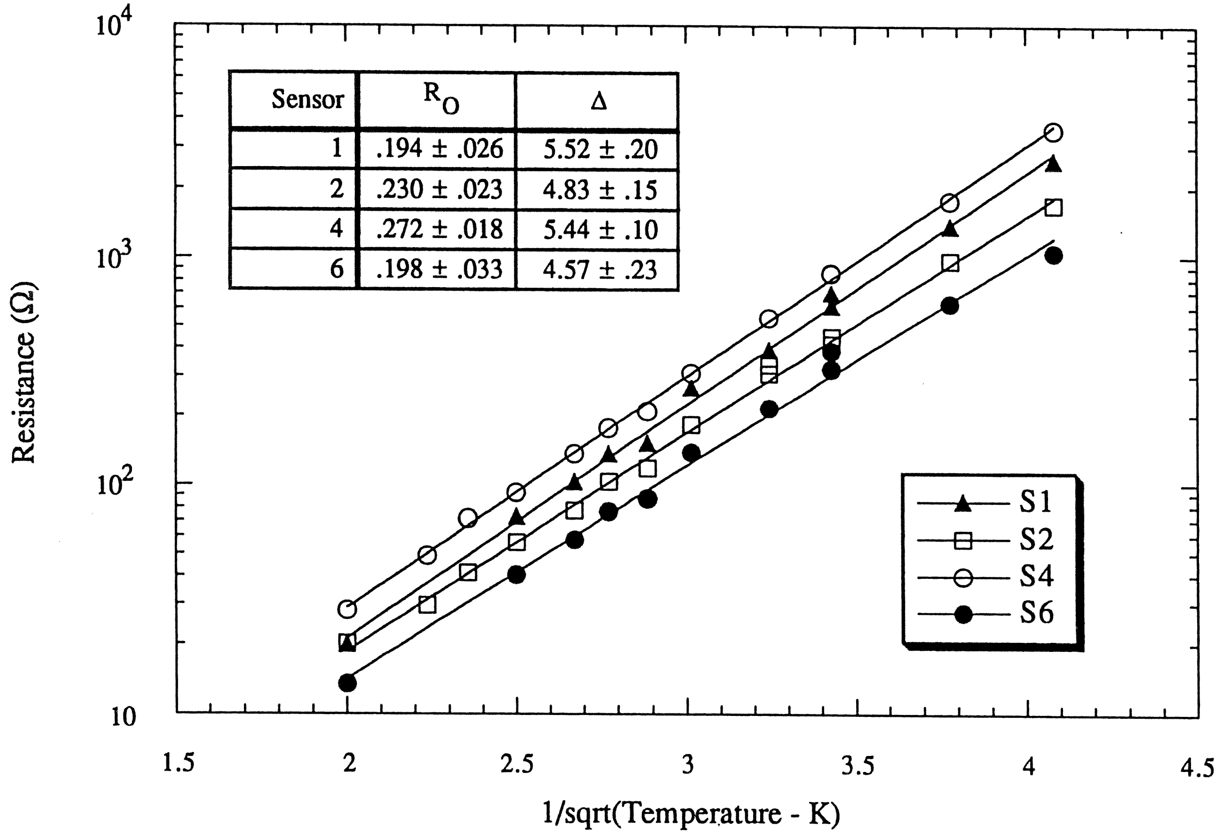

Figure 4.2 Calibration of sensors on E2 (against Lakeshore thermometer), Run 87. (Note: this recent calibration was used to check previous results, and was not used in the data analysis discussed in this thesis.)

Thermal circuit Electrical circuit

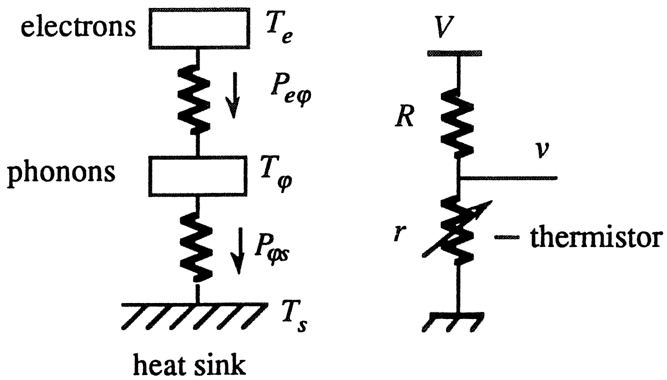

Figure 4.3 Thermal and electrical circuits for electron phonon decoupling.

density of states of phonons and electrons decreases at low temperature, and hence the rate of phonon-electron interactions which couple the two systems also drops.

Such an effect is well established in metals at temperatures near 20 mK. With a power, P, applied to the electrons and then flowing to the phonons, the system comes to an steady state where the electron temperature T_e and the phonon temperature T_φ are related to P by

$$P = g(T_e^5 - T_\varphi^5).$$

This is somewhat analogous to a thermal boundary resistance. The parameter g is an extensive quantity, and scales like 1/volume. Thus the decoupling is smaller, for a given power, in a larger sample. Note also that the power that can flow for a given temperature difference increases very rapidly with temperature. The effect is thus only noticeable at temperatures that are low on a scale defined by the parameter g.

In contrast to the case of metals where the electrons can be well approximated by a free-electron gas, it is much less clear how to describe the charges from impurities in NTD germanium. For instance, how valid is it to assign a temperature to the electrons undergoing hopping, and what phase space is available to these electrons? Because of these difficulties, the theory has not yet been worked out to our knowledge, and we do not have an analytical expression like that for metals. Instead we write empirically

$$P = g_{e\varphi}(T_e^{\alpha} - T_{\varphi}^{\alpha}). \qquad 4.2$$

where the parameters α and $g_{e\varphi}$ are to be found from experiment. An I-V curve like that in figure 4.1 is then analyzed by presuming that at each point equation 4.1 is still valid, but that the temperature is the *electron* temperature, which is given by equation 4.2. The electrical power at a voltage v and current i is just iv. The temperature of the phonons must be determined separately, as discussed below. N. Wang found that for NTD 12 thermistors, the I-V curves are well described with α=6.

The main argument for the hot electron model is that it predicts a time dependence in the decoupling of electrons and phonons, as we discuss in detail below and calculate in appendix G. Experimentally we find that if the phonon system is suddenly heated, the electron temperature rises exponentially with a time constant on the order of 1 msec. The mere observation of this decoupling time is strong evidence for something like the hot electron model. In the electric field model there is no explicit discussion of a time scale, but if one exists it seems reasonable that it would be related to the hopping time, which is presumably much faster than 1 msec.

N. Wang also tried to explain our static measurements at low temperature using only the electric field model. When she did so (44) she deduced an electron hopping length that does not have the temperature dependence predicted by the theory of variable range hopping . Moreover, in measurements with a device that is heated to a fixed temperature with the refrigerator operating at different base temperatures, the deduced hopping length seems to depend on the refrigerator temperature. In our understanding of the measurement such a dependence is unphysical.

4.2) Static thermal behavior of E2

4.2a) Basic thermal picture

In principle E2 should be described by a much more complicated thermal picture than the one in figure 4.3*a*. There are six sensors attached to the main crystal, and the heat sinks are made to the tops of three of these sensors, not to the crystal itself.

However we usually model the system as looking much like figure 4.3, though with a separate electron system representing each sensor. In so doing, we make the basic assumption that the phonons in each sensor are in very intimate thermal contact with the phonons in the bulk. For the eutectically bonded sensors this is probably appropriate. Ideally we would like to know the thermal conductance of the interface, but it cannot be measured on E2 because we cannot independently measure the phonon temperature in a sensor which is being heated electrically. This can be done in differently configured devices though we have not yet made such a measurement.

However in a separate test with a eutectically bonded sensor on a small (0.1 g) crystal we observe phonon pulses with a few μsec rise time (37). Within our hot electron model which predicts ≈msec rise times, this can only be understood if the eutectic bond transmits high energy, i.e., non-thermal, phonons. Moreover, the transmission of phonons should be related to the ratio of the phonon wavelength to the thickness of the interface. Thermal phonons have a wavelength on the order of microns, while the meV-type phonons we suspect we see across the eutectic interface have a wavelength on the order of 100 Å. Thus we expect in quite general terms for the interface to be quite transmissive of thermal phonons. If the thermal conductance of this interface is quite large compared thermal conductance due to phonons across both the sensor and E2, then our treatment of the electrons in a thermistor as being connected to one unified phonon system dominated by the bulk is appropriate.

The heat sinking of E2 physically consists of three copper wires glued with silver filled epoxy to the top of the three central thermistors. The thermal conductance of the wires (calculated using an average value of the conductivity of copper) is very large compared to the boundary conductance between the thermistors and the gold metalization on top of them. As discussed in appendix B, this boundary is expected to be described by

$$P = g_{\varphi s}(T_\varphi^4 - T_s^4) \qquad 4.3$$

where T_s is the heat sink temperature. In principle there is also a thermal connection between the electrons in the gold metalization and the charge carriers in the thermistor. Because the resistance of the thermistors is on the order of 1 MΩ, however, this thermal link is presumably not important. We thus treat E2 like figure 4.3, with the phonon system, and not the electron system, being attached to the heat sink.

It is worth pointing out that for the thermistors that have been glued down this approximation of one phonon system is probably not appropriate. The silver-filled epoxy is highly thermally conductive, but we have two glue-germanium interfaces, each of which should be similar to the interface between the germanium and the gold metalization on the main heat sinks. The glued thermistors should thus be roughly as well coupled to the bulk as the whole detector is to the heat sink. Again, however, we cannot measure *in situ* the conductance of the glue joints for the thermistors on E2.

We usually analyze the behavior of a given sensor by ignoring the presence of the other sensors. As we will show below, this is justified because the heat capacities of the sensors are very small compared to the heat capacity of the bulk crystal. The behavior of each sensor is then basically determined by the behavior of that sensor alone and the bulk crystal.

4.2b) Measurement of the conductance to ground

Experimental verification of the conductance described by equation 4.3 is complicated by the fact that the temperature of E2 is somewhat uncertain near 20 mK. The resistance of the thermistors has been calibrated against the temperature of the refrigerator at higher temperatures, as indicated in figure 4.1. When the refrigerator is near 20 mK, this calibration consistently indicates that E2 is several millikelvin warmer, and is slowly cooling on a time scale of weeks. After about a month of running with the refrigerator near 18 or 19 mK, E2 cools to ≈21 mK. This means there is some external power source on the detector, perhaps from heat stored in the plastic ball and screw assemblies used to hold the detector, or perhaps from epoxy used in several places on the crystal. Part of this power may also come from radio frequency electromagnetic radiation that leaks into the cryostat.

It is important to note that at the time of N. Wang's thesis, there was an additional heat load on E2 that prevented it from cooling below about 30 mK. We eventually discovered that this was due to a thermoelectric current caused by attaching the grounds underneath two separate sensors to two separate wires made of different metals that come out to room temperature. Breaking this loop immediately caused the detector to cool.

We measure the conductance between E2 and the heat sink by dissipating electrical power in the crystal, and then measuring the zero power resistance on a sensor. Electrical power is put into E2 by passing current between the gold pads on the bottom of two different sensors. The current thus flows through the thin implanted contact. We used this technique not only for slow measurements like the one described here, but also to inject short bursts on energy to simulate particle events. The resistance between various sensors was measured with a 4-wire technique and an Elektronikka model AVS-46 conductance bridge. The resistance was stable to better than 0.05 % over several different cool-downs, and is independent of the measurement current up to at least 30 μA.

In table 4.1 we list the value of resistance between three different combinations of sensors that we commonly use.

Table 4.1 Resistance of heating paths on implant of E2. S2 means sensor 2, etc. Sensors 4,5 and 6 were connected together.

sensor combination	R (Ω)
S2-(S4,S5,S6)	159.08±0.05
S3-(S4,S5,S6)	67.00±0.05
S2-S3	146.05±0.05

Because of the excess power discussed above that prevents the crystal from cooling to the base temperature of the refrigerator, the power in equation 4.3 is the sum of the electrical power, P_{ele}, and the external power, P_{ext}, whose value is not known *a priori*. We then write

$$P_{ele} + P_{ext} = g_{\varphi s}(T_{\varphi}^{4} - T_{s}^{4}).$$

In figure 4.4 we plot the sum of these powers vs T_{φ}^4-T_s^4. The external power has been adjusted by hand to obtain a straight line, and is equal to 2 5 pW. The measured value of $g_{\varphi s}$ is quite close to the value N. Wang measured, and is given in Table 4.2.

4.2c) Measurement of the thermistors

All that we can learn of the static thermal behavior of the sensors is contained in the I-V curves like that of figure 1.1, provided we also independently know the temperature of the phonons in the sensors at every point. Within the hot electron model we expect this measurement to be characterized by equation 4.2. For the eutectically bonded sensors, as explained above, we believe that the phonon temperature in the sensor, even when being heated, is the same as the phonon temperature in the bulk on

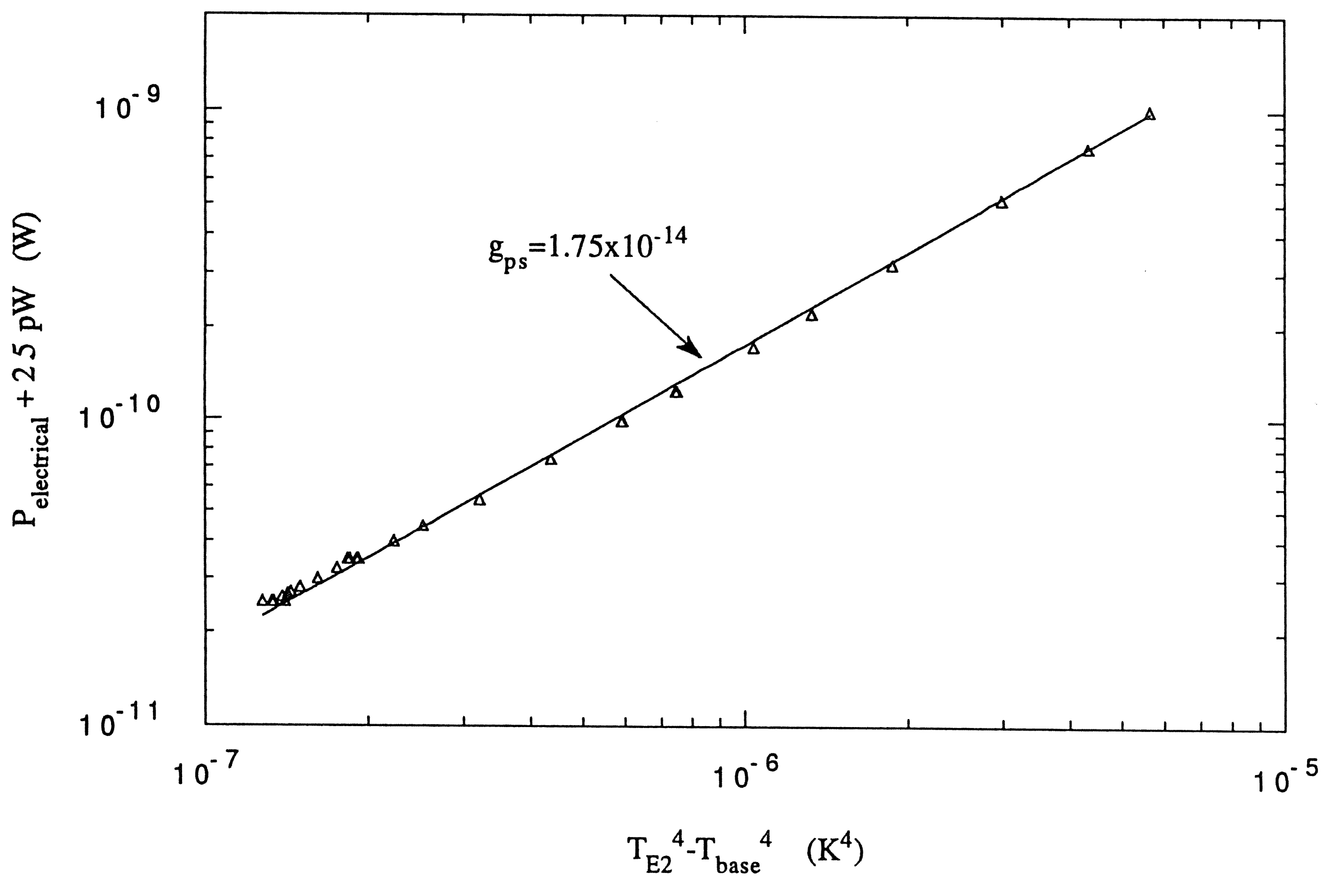

Figure 4.4 Measurement of the conductance between the crystal and the heat sink. An extra power of 2 5 pW was added to obtain a straight line, as discussed in the text.

Table 4.2 Various parameters of E2.

$g_{\varphi s}$		1.75×10^{-4}
$g_{e\varphi}$	S2	0.03*
$g_{e\varphi}$	S4	0.0034
$g_{e\varphi}$	S6	0.040

*The measurement of $g_{e\varphi}$ for sensor 2 has some uncertainties, as discussed in the text.

E2. We can then determine the temperature of the phonons in the sensor by measuring the zero power resistance of a separate sensor.

This has been done for sensors 4 and 6, and the results for sensor 6 are plotted in figure 4.5 in terms of power versus T_φ^6-T_e^6. The discrepancy in the figure between the two different base temperatures is not fully understood, but may result from a small parasitic heat lead due, perhaps, to radio frequency radiation. The curve is fit to extract $g_{e\varphi}$, as defined in equation 4.2. We can perform the same measurement on sensor 2, which is glued, but must bear in mind in this case that the phonon temperature in the sensor is probably not strictly equal to the phonon temperature measured in a separate sensor. The values of $g_{e\varphi}$ found from these curves are shown in table 4.2. Note that the new value for sensor 4 is a factor of ≈ 10 below the previous measurement by N. Wang.

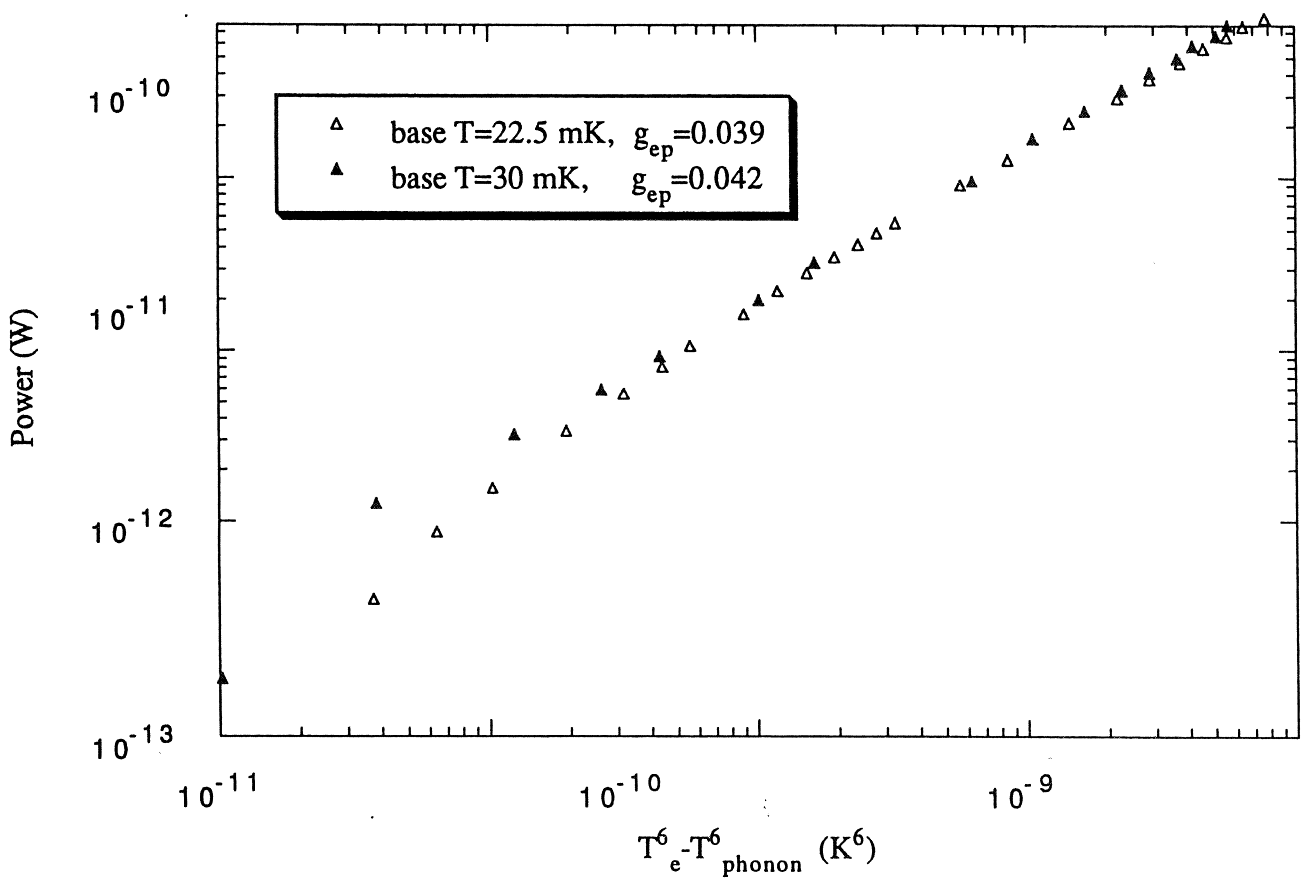

Figure 4.5 Power versus electron and phonon temperatures for sensor 6, measured at two different refrigerator temperatures.

4.3) Expected pulse shapes

4.3a) Simple calorimetry

Before discussing the phonon pulses in E2, which are rather complicated, let us first consider the simple case of an energy E_o being deposited in a crystal. If this energy is small enough to cause only a small perturbation to the system we can write

$$\delta T = \frac{E_o}{C} \tag{4.4}$$

where C is the heat capacity of the detector. The smaller the heat capacity, the bigger the temperature change we measure for a given E_o. The heat capacity of a pure semiconductor is dominated by the phonon system, and at low temperatures is well approximated by the Debye law

$$C = c_o \frac{M}{A}\left(\frac{T}{\theta}\right)^3$$

where c_o=1946 J/K/mole, M is the mass of the crystal, A is the atomic weight and θ is the Debye temperature. This T^3 dependence is the reason for cooling our detector to 20 mK. For germanium, with θ=374 K, we find

$$C = 5.1\times10^{-7}\left(\frac{T}{\mathrm{K}}\right)^3\left(\frac{M}{\mathrm{g}}\right)\frac{\mathrm{J}}{\mathrm{K}}. \tag{4.5}$$

For E2 at 20 mK this gives 2.5x10^{-10} J/K. Using this value, a 60 keV photon at 20 mK causes a temperature change of δT=38 μK, while at 30 mK δT=11 μK.

After this initial temperature rise energy flows to the heat sink and the crystal cools. The thermal connection between the crystal and the heat sink is described by equation 4.3. Dropping the subscripts for clarity, the power flowing *out* of the crystal is

$$\delta P = 4gT^3\delta T \equiv G\delta T .$$

The temperature change of the crystal, $dT/dt \equiv \dot{T}$, is related to the total power flowing *into* the crystal by

$$\delta P = C\delta\dot{T} .$$

Combining these two equations we get

$$C\delta\dot{T} = -G\delta T$$

which has as a solution

$$\delta T(t) = \frac{E_o}{C} e^{-\frac{t}{\tau}} \qquad 4.6$$

where

$$\tau = \frac{C}{G}. \qquad 4.7$$

This time constant is completely analogous to an RC time in an electrical circuit. Note that in an actual measurement of δT, the power dissipated by the measurement circuit represents a "thermal feedback" that alters the time constant in equation 4.7 somewhat. This is calculated in detail in appendix G.

Even if we could measure T directly, there is a limit to how well E_o is estimated. A basic result from thermodynamics is that a system with a heat capacity C undergoes energy fluctuations that, at a given point in time, have a value, σ_E^2, given by

$$\sigma_E^2 = kT^2C.$$

This fluctuation in E2 at 20 mK is 7.3 eV.

In reality, though, the thermal sensor is usually not sensitive enough for this "noise" to dominate other electronics noise in the measurement. If we apply a current i to the thermistor, we measure a voltage change δv given by

$$\delta v = i\frac{\partial r}{\partial T}\delta T.$$

For many types of sensors $\partial r/\partial T$ decreases as the temperature increases. For instance in NTD germanium, by equation 4.1,

$$\frac{\partial r}{\partial T} = -\frac{1}{2}\sqrt{\frac{\Delta}{T^3}}R_o e^{\sqrt{\frac{\Delta}{T}}}.$$

We would like to increase i to increase δv compared to whatever noise we have, but as we do so the device heats up and $\partial r/\partial T$ drops. Thus δv does not simply increase linearly with i, and there is a trade off between increasing the bias current and heating. Note that this will happen even if there is no electron-phonon decoupling, since the detector itself will heat as the electrical power is increased.

Because of this, the measurement circuit must be taken into account when calculating the theoretical resolution of the detector. The techniques involved in this calculation are discussed breifly in appendix F. Moseley and collaborators have treated the situation where there is no electron-phonon decoupling, and where the dominant noise sources are thermal fluctuations and Johnson noise in the thermistor (47, 48). They find that the lowest achievable r.m.s. resolution is

$$\sigma_{E,m} = \xi\sqrt{kT^2C}$$

where ξ depends on the details of the sensor, and is on the order of, but somewhat larger than unity.

4.3b) Calorimetry in a minimal model of E2 with hot electrons

In appendix G we calculate the expected pulse shapes in a detector within the full thermal model that includes electron-phonon decoupling. In the case of pure calorimetry, which means that the energy from an interaction promptly becomes a temperature rise in the phonon system, the voltage at the sensor is given by equation G.25, or

$$\delta v(t) = i\frac{R_{\|}}{r}\frac{\partial r}{\partial T}\frac{E_o}{C_e}\frac{G_{\varphi e}}{C_\varphi}\frac{1}{s_1 - s_2}\left\{e^{-s_2 t} - e^{-s_1 t}\right\} \qquad 4.9$$

where s_1 and s_2 are given by equations G.19.

Because there are two thermal components in the model, namely electrons and phonons, there are two time constants in equation 4.9, τ_1=1/s_1 and τ_2=1/s_2. To understand these two time constants, it is useful to define two basic thermal time constants analogous to equation 4.7. The first is the electron-phonon decoupling time (equation G.11),

$$s_e = \frac{1}{\tau_e} = \frac{G_{e\varphi}}{C_e}\left(1 - \frac{R-r}{R+r}\frac{P_{ele}}{G_{e\varphi}}\frac{1}{r}\frac{\partial r}{\partial T}\right). \tag{4.10}$$

where C_e is the heat capacity of the electrons, and $G_{e\varphi}$ is the conductance between the electrons and phonons. The term in parenthesis is a modification of the bare time constant due to thermal feedback: as the resistance changes in response to temperature changes, the electrical power also changes, which in turn affects the thermal system. The other time constant is the time constant of the detector (equation G.13)

$$s_\varphi = \frac{1}{\tau_\varphi} = \frac{G_{\varphi s}}{C_\varphi} \tag{4.11}$$

where $G_{\varphi s}$ is the small signal conductance between the crystal and the heat sink, and C_φ is the heat capacity of the phonon system. The two time constants that actually appear in equation 4.9, τ_1 and τ_2, are closely related to τ_e and τ_φ. As we show in equations G.21, if $\tau_e \ll \tau_\varphi$ (which is usually the case), then $\tau_1 \approx \tau_e$ and $\tau_2 \approx \tau_\varphi$.

With the identification $\tau_1 \approx \tau_e$ and $\tau_2 \approx \tau_\varphi$, equation 4.9 shows that the signal rises with the electron-phonon decoupling time and falls with the detector time constant. It is important to note (see appendix G) that even if some of the initial energy from the event goes directly into the electron system (which is not what we assumed above), there are still only two time constants to the pulses, provided that this energy is deposited promptly.

4.3c) Pulses with long-lived high energy phonons

One of our long term goals is to measure the high energy phonons created by a particle interaction before the total energy from the event simply becomes a temperature change of the detector. The full spectrum of phonons created by a particle interactions, and what happens this spectrum in time is the subject of much current interest (49, 50). It has been proposed that there is an initial "fireball" consisting of a high density of high energy optical phonons. The phonons in this region rapidly down-convert to lower energy phonons, and the ball expands. For acoustic phonons that have cooled to the linear part of the dispersion curve, the decay rate is proportional to ω^5 where ω is the phonon frequency. Thus they live longer at lower energies, and near 1 meV (equivalent to $\approx$10 K) are expected to live as long as many msec. (Note that this does not imply that a thermal distribution of phonons cannot cool below $\approx$1 meV. Inelastic phonon-phonon interactions allow phonons to maintain thermal equilibrium at any temperature. At low temperatures, however, there are no 1 meV thermal phonons, and so a low density of high energy, non-equilibrium phonons created by processes such as particle interactions can be long-lived.)

The $\approx$1 meV phonons move with the phonon group velocity of $\approx$3 km/sec, or 1 cm in $\approx$3 μsec, and propagate preferentially along the so-called "phonon-focusing" directions. In germanium, however, they scatter frequently because of the different isotopes in the crystal. It is not clear how the phonons eventually lose energy and become thermal, though presumably down-conversion occurs in interactions at the surface of the crystal or at the sensors. To the extent that the down conversion process is slow, the crystal can perhaps be thought of as a "mirrored box" with a gradually dissipating dilute gas of high energy phonons.

The purpose of the eutectically bound thermistors is to have as many of these high energy phonons as possible transmitted into the thermistor. In separate tests with 60 keV photons interacting directly in a thermistor, we have observed pulses with electronics-limited rise-times of $\approx$2 μsec. This is much faster than the electron-phonon decoupling time in the hot electron model. We believe this short rise time is due to high-energy phonons in NTD germanium coupling directly to the electrons.

A simple way to model the response of the detector to long-lived high energy phonons is to consider the energy from the event to consist of two components: a power on the electron system from high energy phonons, and a power on the phonon system from thermalized phonons. In appendix G we treat the case of high energy phonons decaying away exponentially with a time constant $\tau_h=1/s_h$. If these phonons dump a fraction η of their power into the electron system and the rest into the phonon system, the resulting pulse is (equation G.27)

$$\delta v(t) = i\frac{R_{\parallel}}{r}\frac{\partial r}{\partial T}\left\{\frac{s_o - s_2}{(s_1 - s_2)(s_h - s_2)}e^{-s_2 t} + \frac{s_h - s_o}{(s_h - s_2)(s_1 - s_h)}e^{-s_h t} - \frac{s_1 - s_o}{(s_1 - s_2)(s_1 - s_h)}e^{-s_1 t}\right\}\frac{\eta E_o s_h}{C_e}. \qquad 4.12$$

where s_1 and s_2 are the same as in equation 4.9. Note that the phonon lifetime direcly appears in the pulse shape, so that there are three time constants.

4.4 Comparison with experiment

4.4a) Basic pulse shape

In figure 4.6 we show the signals in sensors 2, 4 and 6 for a background photon which deposited ≈1.3 MeV in the detector. These signals are quite typical of what we see for all events. In order to measure the phonon signal without distortion, we did not use the AC bias technique discussed in chapter 3, and we modified the amplifiers discussed in appendix E to have a low-frequency roll-off well below 1 Hz. This meant that we suffered from the low frequency noise visible in figure E.2. We can barely detect 60 keV photons in this arrangement, and so had to measure events that are quite large. As a final note, we carefully checked that the electrical time constant was roughly 50 μsec or less, and so did not affect the signals significantly.

The signals in the three sensors have fairly different shapes, and somewhat different pulse heights. They can be quite well fit in the time domain to a sum of three exponentials with arbitrary time constants and amplitudes. The results are listed in the table included in the figure. It is quite apparent to the eye that sensors 4 and 6 have more

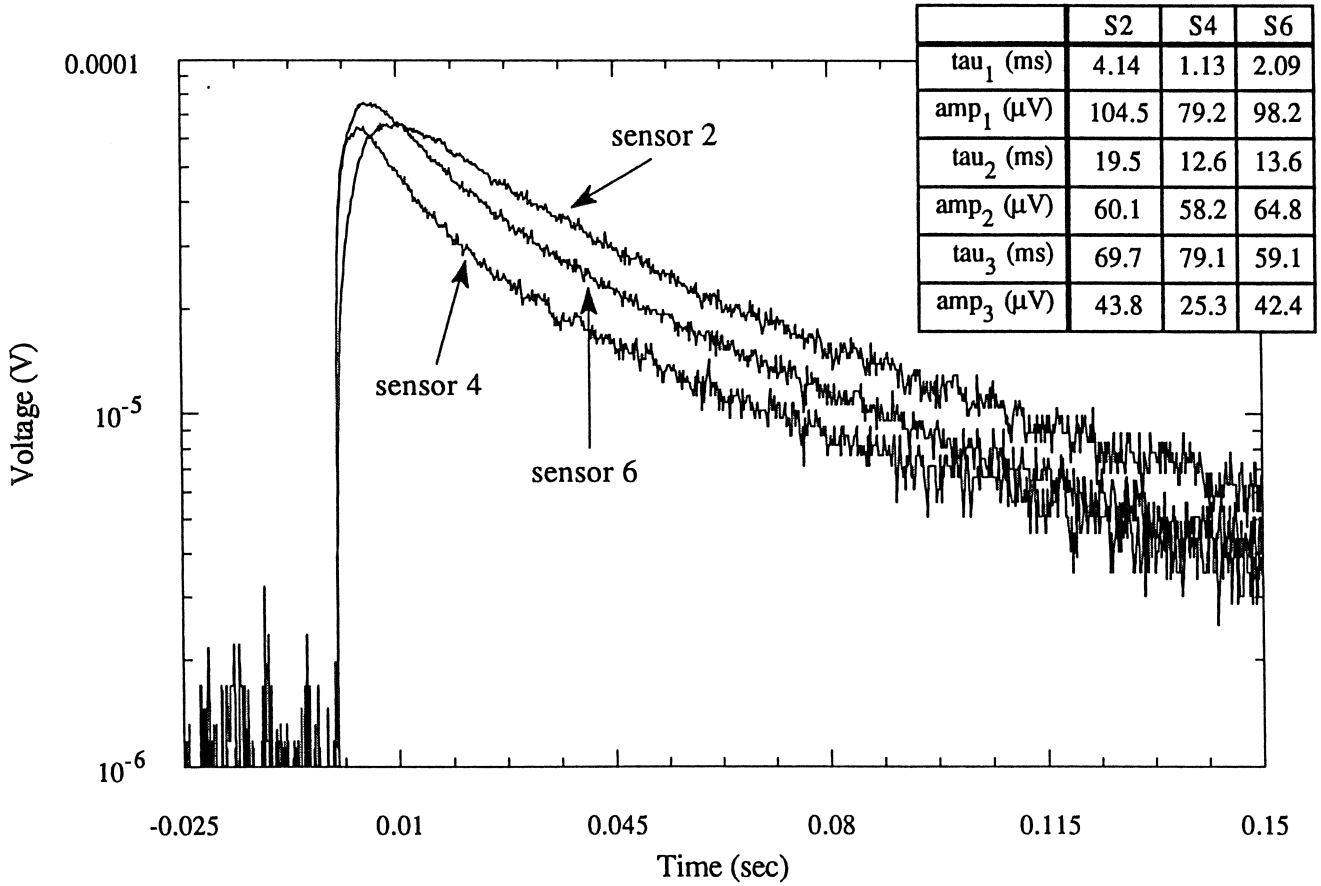

	S2	S4	S6
tau_1 (ms)	4.14	1.13	2.09
amp_1 (μV)	104.5	79.2	98.2
tau_2 (ms)	19.5	12.6	13.6
amp_2 (μV)	60.1	58.2	64.8
tau_3 (ms)	69.7	79.1	59.1
amp_3 (μV)	43.8	25.3	42.4

Figure 4.6 Pulses from a gamma at a base temperature of about 22.5 mK. The bias on all sensors is 1 nA.

than one fall time, while for sensor 2 this feature seems less pronounced. For some time we had taken this as being due to the fact that sensor 2 is glued while 4 and 6 are eutectically bound. However it is clear from the fit results that the signal in sensor 2 also has three components, and the amplitudes of these components have roughly the same ratios between them as those for sensors 4 and 6. The primary difference between the sensors for this event is that the time constants are fastest for sensor 4, slower for sensor 6, and slowest for sensor 2.

We would of course ultimately like to quantitatively understand this pulse in terms of one of the models discussed above, but we have not yet progressed to this point. Instead, let us first consider these three time constants in general terms. It seems reasonable that the long time constant is basically the time constant of the crystal given in equation 4.11, assuming that mixing between the time constants is small. Using the heat capacity of E2 from equation 4.5 and the measured value of $G_{\varphi s}$ from above, we predict τ=44 msec. Note that since both $G_{\varphi s}$ and C_{φ} scale like T_{φ}^3, this time constant is independent of temperature. The values in figure 4.6 range between 60 and 80 msec. A very general explanation for a time constant exceeding 44 msec is that something on the detector (e.g., epoxy) adds an extra capacity that is significant especially at the lowest temperatures. Measurement of a time constant shorter than 44 msec would be much more difficult to explain.

We also expect that one time constant must be the electron-phonon decoupling time given by equation 4.10. Unfortunately we have no *a priori* knowledge of the electron heat capacity from theory, so we cannot predict this time constant even though $G_{e\varphi}$ has been fairly well determined. However, as we discuss below, from an independent electrical measurement, it seems likely that the rise time is this time constant. We can thus deduce the electron heat capacity from the rise time.

This leaves us with the first fall time in the pulses of figure 4.6. Within the minimal hot electron model discussed above, there are only two time constants unless the phonons are long lived and couple directly to the electrons in a sensor. It would be quite exciting if this is actually what we are seeing. One hallmark we might expect of these ≈meV energy phonons is that their lifetime should be insensitive to small changes in the temperature of the crystal and sensors. This means the time constant should be independent of the bias. Moreover, the lifetime of the phonons should basically be determined by whatever object(s) it is that most efficiently down converts the phonon energies. This implies that all the sensors should see the same time constant. This is not what is observed in figure 4.6. It also seems unlikely that sensor 2, which is glued to the crystal, would see the high energy phonons.

4.4b) Electrical measurement of the time constants

An independent method to test the above ideas is to probe the dynamic response of the thermistors electrically. We did this by adding a small square wave to the normal DC bias current in a sensor. This has two effects. If δI is the change in current, and r is the resistance of the thermistor, then to zeroth order the voltage across the thermistor simply changes by an amount $\delta v = \delta I r$. However the electrical power also changes in this process, and so the thermistor comes to a new thermal equilibrium. In appendix G we show that in fact the voltage changes to its new value basically on the time scale of the electron-phonon decoupling, with a smaller variation occurring with the detector time constant.

The electron-phonon decoupling time is very easy to see, but the signal due to the crystal time constant is quite difficult to measure, both because it is a small part of the signal, and because of large noise at low frequencies. This is a problem because the measured value of the electron-phonon time constant is affected by the value of the second time constant. In addition, the measurement has to be corrected for low frequency roll-off of the amplifier.

In our first analysis of the measurements we found that the inferred time constant of the crystal was much shorter than 40 msec, which seems to be in error. Because we see an extra time constant in pulses, it seems reasonable to add another time constant to the fit of the electrical measurement. Note that this additional time constant is not required by the quality of the fit, which is fairly good with only two time constants. Moreover, because of the poor signal to noise at low frequencies, with three time constants the fit essentially has too many free parameters, and the results are erratic. We analyzed the data, then, by fitting the results to three exponentials with all the amplitudes and two of the time constants free. The third time constant was fixed at the value of the detector time constant as measured from pulses. With this method we achieve fairly good agreement between the electrically measured electron-phonon decoupling time and the rise time of events, and between the electrically measured extra time constant and the first fall time of events.

In figure 4.7 we show these two time constants, called τ_1 and τ_2, as a function of the amplitude of the corresponding exponential component of the signal. The data is for sensor 6 only, which was biased at 200 mV. The detector base temperature is ≈22mK. We also show the time constants measured from photon events, and from "pulser events". These are events that we generate by putting 10 µsec current pulses through sections of the implanted contact between various sensors. The current paths are described above in section 4.2b in the context of dissipating a constant power. The pulses generated this way seem to be essentially identical to photon events.

The discrepancies between the various time constants in figure 4.7 are puzzling. Note that for that the first time constant especially, the value is clearly related to the amplitude of the excitation. However even at a constant amplitude, there are differences between the time constants from the various types of pulses. We do not yet understand the reason for this. It is important to realize that the measurement of τ_2 is quite sensitive to low frequency noise, and there are also some reliability problems with the fitting.

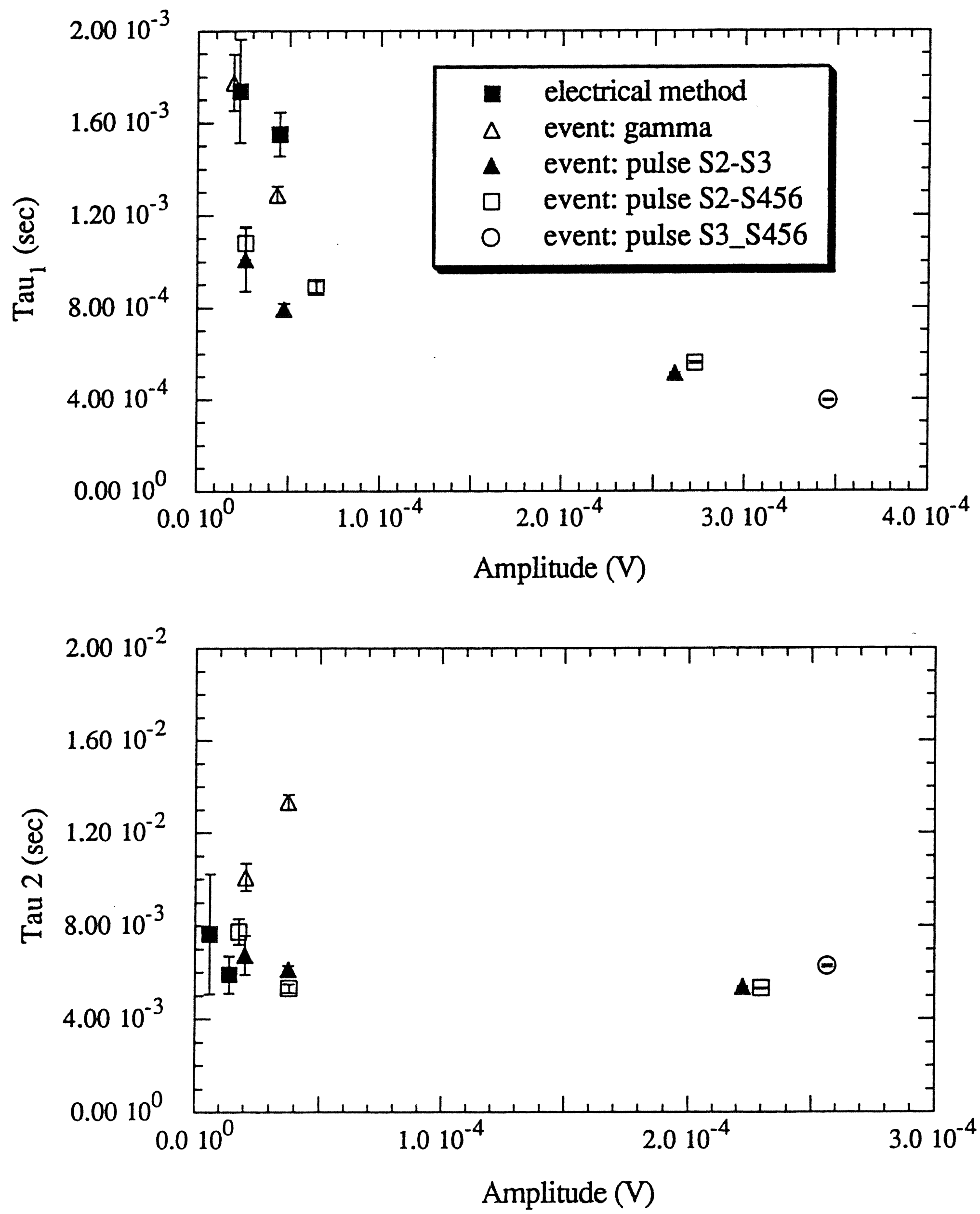

Figure 4.7 Time constants plotted as a function of the their amplitudes. The symbols are the same in both plots

However the rough consistency between the time constants deduced from electrical measurements and from events is a is a strong indication that the time constants in each case arise from the same phenomena.

4.4c) Temperature dependence of time constants

The other important test for the time constants is to see how they vary with temperature. In figure 4.8*a* we show the rise time and first fall time for events (generated by both gammas and the pulser method) as a function of electron temperature. The pulser events are all about 500 keV in energy, and the photons are near this energy. The base temperature of the detector before biasing is ≈22 mK, and the electron temperature is changed only through the bias. In figure 4.8*b* we plot the first fall time and the second fall time as a function of the temperature of the crystal. The events are the same as those in figure 4.8*a*, and we replot the first fall time because it is unclear which temperature it should be associated with. The detector temperature, like the electron temperature, changes only because of the power from the bias.

This measurement is difficult enough so that definitive conclusions are hard to reach. It is somewhat troubling that the time constants all seem to be correlated in the same way with temperature. This could be a result of problems with the fits. The error bars shown are estimated by a crude analysis that does not correctly account for correlations between the time constants. Further analysis will be needed to clarify this point. In addition, the measured value of the second fall time is very sensitive to event pileup and low frequency noise. In the data set shown, "bad" events were painstakingly removed by hand. This process can easily bias the value obtained for the second fall time, which in turn can affect the fit results for the other time constants. Finally, it is important to keep in mind that in the model of appendix G, the observed time constants are mixtures of the time constants given by equations 4.10 and 4.11. If the first fall time

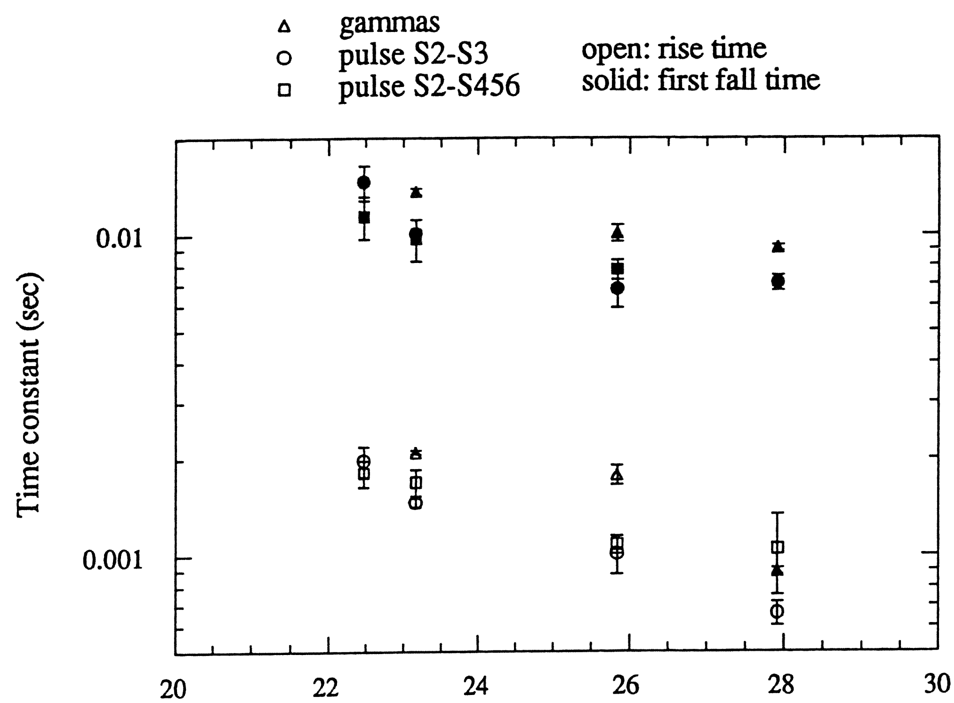

(a)

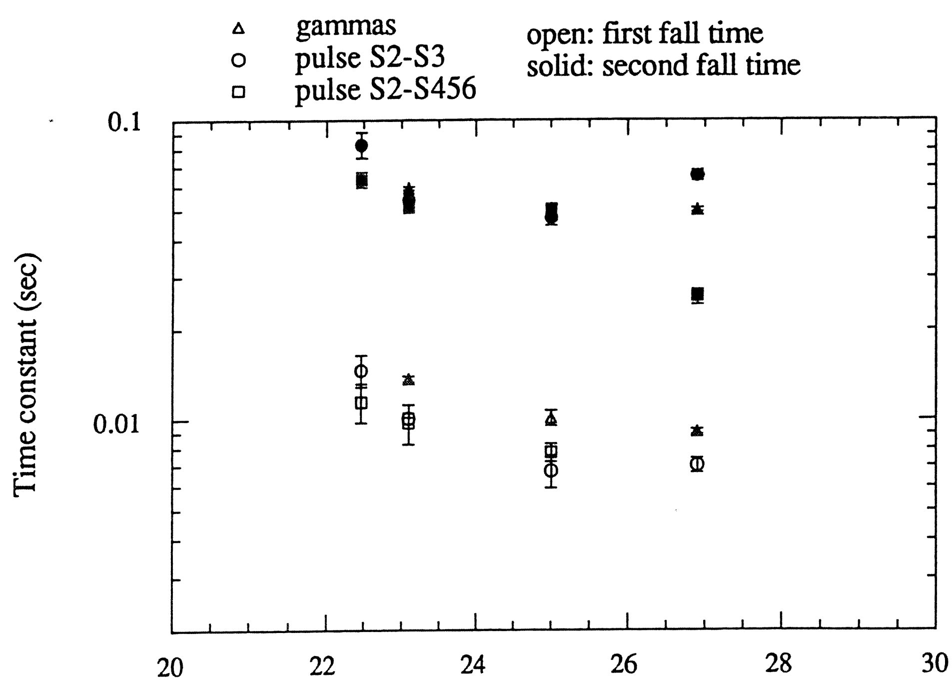

(b)

Figure 4.8 Time constants as a function of electron temperature (a), and phonon temperature (b) for sensor 6. The base temperature of the detector is ≈22 mK, and the temperature rises are only due to biasing. Potential errors in the measurements are important and are discussed in the text.

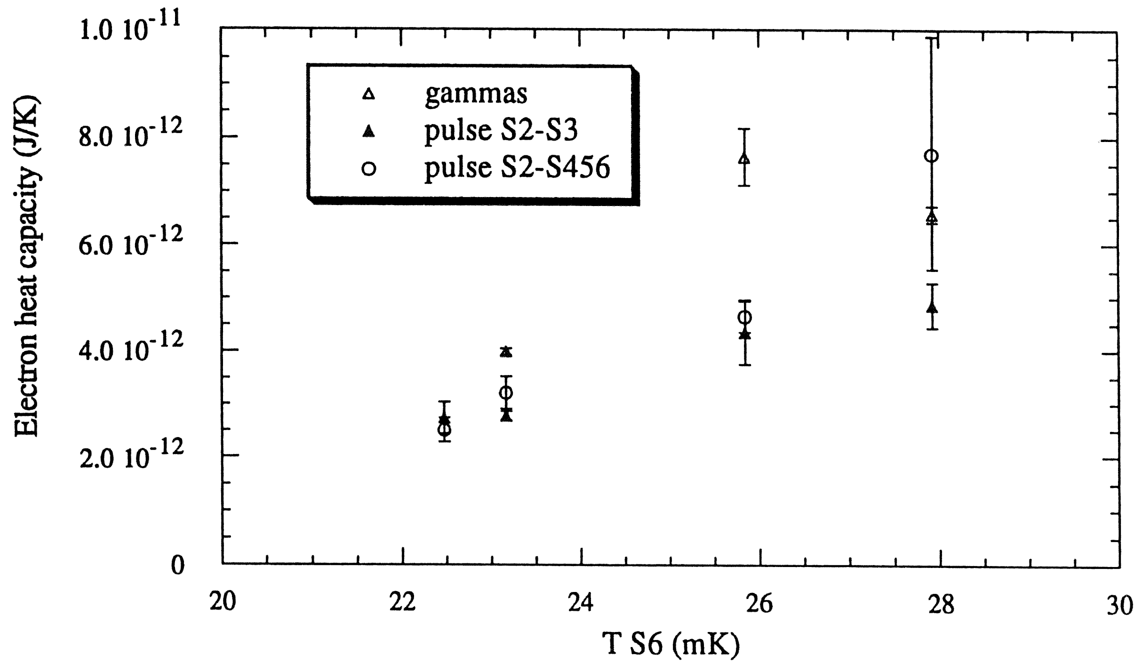

Figure 4.9 Electron heat capacity in sensor 6, obtained from the data set in figure 4.8.

is due to high energy phonons, then it should not mix with the other time constants. However if the data is explained by adding another thermal element to the model in appendix G, then mixing might account for the some of the apparent correlation between time constants.

With these caveats in mind, there does indeed appear to be a correlation between all three time constants and temperature. Of the three time constants, we have a prediction only for the third, namely that it should be independent of temperature. If the second is due to high energy phonons, it seems unlikely that it would vary over this temperature range. The electron-phonon time constant depends on the electron heat capacity, which is unknown expect from measurements like this. In figure 4.9 we show the heat capacity of the electrons in sensor 6 derived from this measurement and equation 4.10.

4.5) Conclusions

Clearly the phonon measurement exhibits a very complex phenomenology. It is important for us to remember that apart from the inherent physics interest in this new condensed matter system, the main reason to study the pulses in detail is to be able to predict ways to make the detector more sensitive. So far the optimal conditions for operating the detector have been found empirically by measuring the pulse heights in each of the sensors as a function of current and temperature. In figure 4.10 we show the results at 24 mK (which is essentially the optimal condition) and 31 mK for sensor 2, 4 and 6.

There are significant differences between the sensors, and it is important to pick the correct bias current and temperature. At the moment, however, our theoretical understanding of how to do this is limited. As we discussed in section 4.3, it is not clear how two interpret the three time constants we see in our pulses. Moreover, the minimum hot electron calorimetric model (equation 4.9) predicts a pulse height of $\approx 6\mu V$ in sensor 6 at 22 mK and at the optimum bias. In reality we observe a 2.4 μV pulse height, and roughly of this is due to the first fall time component whose origin is uncertain. The calorimetric part of our signal is presumably the other half of the signal, or only ≈1.2 μV, which is about one fifth of the prediction.

On the other hand it is quite suggestive that sensor 4 has both the smallest value of $g_{e\varphi}$ (table 4.2) and the smallest pulse height at low temperatures (figure 4.10), despite the fact that it has the largest resistance (figure 4.2). This is probably also related to the very strong bias dependence for sensor 4 seen in figure 4.10. Sensor 6, with a large value of $g_{e\varphi}$ on the other hand, has the largest pulse height despite its small resistance. It seems as though electron-phonon decoupling is the dominant effect in determining the pulse height.

This points to another direction of future effort, namely trying to better understand and control the important parameters of the thermistors. It is not clear why the resistances and values of $g_{e\varphi}$ vary for the different sensors on E2. We know that the doping of the NTD germanium is very uniform, and at higher temperatures other groups have found good reproducibility from sample to sample. It may be that there are problems associated with the stress of gluing or eutectically bonding the sensors. Alternatively, it may be that statistical variations in the number of conduction paths are important at very low temperatures where few charges participate in the hopping process.

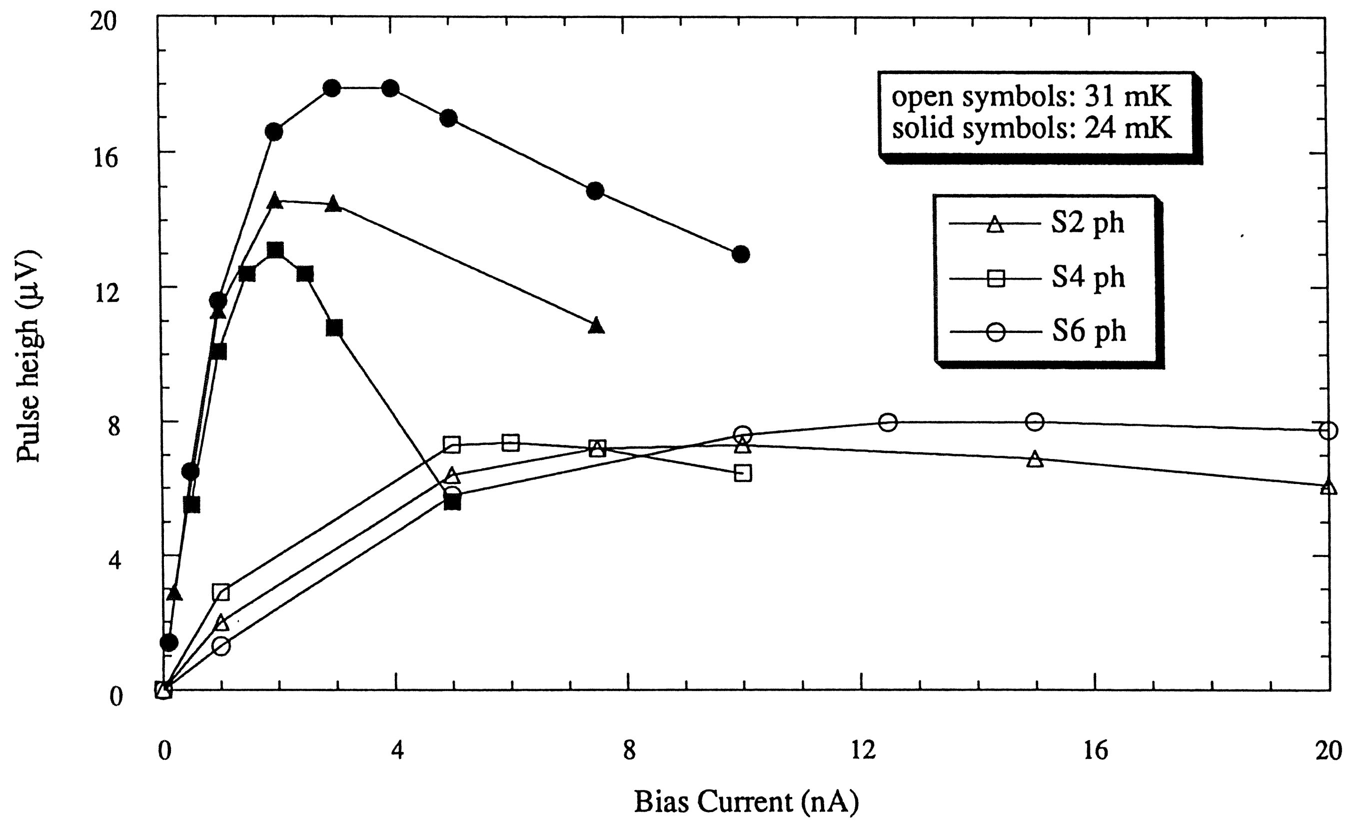

Figure 4.10 Pulse height versus bias for sensor 2, 4 and 6 at 24 mK and 31 mK. The events were generated with the pulser method and have an energy of about 420 keV. The measurements were made with the AC bias technique at 1 kHz.

Chapter 5: Physics of the ionization measurement

5.1) Overview of the ionization measurement

Measurement of charges created by particle interactions in a semiconductor at sub-Kelvin temperatures is an essentially new phenomenon. Although at least two other groups have reported seeing it (51, 52, 53) (and one of these (52) preceded our first observation), to our knowledge there is not a detailed, published discussion of the physics involved.

To some extent our detector acts like a standard diode ionization detector operated at 77 K (54). Microscopically, however, the picture is entirely different, as all the impurities are "frozen out" at our low temperature. This means that holes in a p-type material, for example, are not thermally excited from acceptors to the valence band. At 77 K thermally excited holes from acceptors form a sea of free-charge which must be removed, or "depleted", by the application of a large external electric field. At low temperatures there is no free charge and thus "depletion region" and "depletion voltage" are not applicable concepts, though they have been used in the literature to describe this situation (51).

In many respects our detector is much more like an infrared photo-conductor operated at 4 K (55, 56). Photo-conductors are used to detect a steady flux of infrared photons which, in p-type material for example, excite holes into the valence band. At 4 K there are only a small number of thermally generated free charges, and thus the holes created by the external photons can be collected by applying a small external electric field. This is similar to our situation in that most impurities are frozen out, but different in that holes and fixed A^- sites are created by the infrared photons, in contrast to the electron-hole pairs created by high energy photons or particles in our detector. Photo-conductors are often configured as p^+-p-p^+ devices, as is E2, and the energy bands at 4 K are probably only slightly different than at 20 mK (57). Many of the charge transport processes that may be important in our device, such as scattering, trapping, and impact ionization are discussed in the literature of photo-conductors (58, 59). These papers are helpful, but not completely applicable, because the thermal phonons that play a significant role at 4 K are not an important factor at 20 mK.

5.2) Phenomenology of the charge measurement

Most of the results described in this chapter were obtained by exposing the detector to photons from a ^{241}Am source as shown in figure 5.1. The photons are collimated to strike a small (≈200 μm Ø) spot in the center of the face of the crystal opposite the thermistors, at a rate of a few Hz. Though ^{241}Am emits a series of X-rays and γ-rays, the X-rays were filtered by a 0.15 mm thick sheet of copper so that only the 59.54 keV γ-rays reach the detector. These 60 keV photons are primarily photo-electrically absorbed, with an exponential attenuation length of ≈0.86 mm, thus the events are fairly well localized. There is also a comparable rate of background events, which are presumably originate from the Compton scattering of 1.45 MeV photons from ^{40}K in the walls of the room. They have a roughly flat spectrum up to several hundred keV. (A typical ionization signal in response to a 60 keV photon is shown in the next chapter, figure 6.1)

Charge collection in our detector exhibits a wide variety of behavior. When the detector is first cooled to base temperature, collection of the charge created by photons is very poor. Pulses are seen when the charge collection bias is first turned on, but the amount of charge collected is much less than the full charge created by the photons. On a time scale of about a minute the pulses became smaller and less numerous and finally cease altogether. Over time, however, the spectrum improves. We finally determined that grounding the detector (i.e., connecting both implanted contacts to ground) while exposing the crystal to a fairly high rate of high energy photons "fixes" the charge collection in about two days. This process does not need to be repeated as long as the temperature of the detector is kept below about 4 K.

With the detector in this final state, we have calibrated the charge measurement and find that nearly all charges are collected for drift fields greater than about 200 mV/cm. However after the detector has been biased for about one hour, the spectrum of the 60

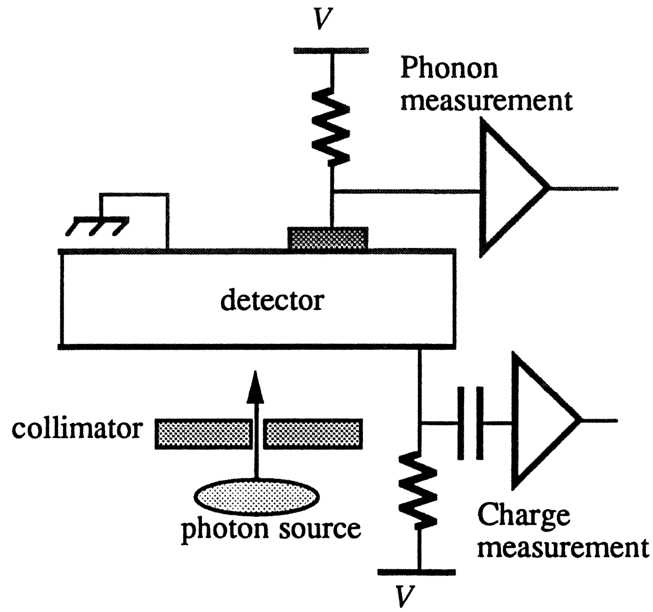

Figure 5.1 Arrangement used to measure the response of the detector to photons from a ^{241}Am source.

keV photons develops a significant low charge collection tail. Grounding the bias for a few minutes restores the quality of spectrum. Additionally, if the detector is suddenly grounded after having been biased for some time, pulses of both polarities (i.e., events for which the charges drift in both directions in the crystal) are observed for a short time.

The variety of these phenomena has for a long time made it difficult for us to understand the basic physics involved. A priori we might be observing trapping of charge, recombination of electron-hole pairs, effects due to space charge, impact ionization, or perhaps diffusion of charges. We also do not know how many infrared photons from room temperature "leak" into the coldest stage of our cryostat. A flux of such photons on the detector can ionize neutral impurities, creating free charge in the crystal. Most of our understanding is now based upon a measurement of both the ionization and phonons created by the 60 keV photons as a function of the charge collection bias. At small biases charge collection is incomplete, and, perhaps surprisingly, the measured phonon energy depends on the amount of charge collected. We have developed a model for this process in terms of charge trapping, and have come to understand much of the other observed behavior in terms of trapping as well.

5.3) Equilibrium state of the crystal and neutralization

We first consider the equilibrium state of the crystal. For a an introductory reference see Kittel (60), and for a general reference see Sze (61). A cartoon of the energy levels is shown in figure 5.2. A neutral donor, or d^o, has an "extra" electron which is bound to the donor site by a shallow, approximately hydrogenic potential $\approx$10 meV deeper than the conduction band minimum. If the electron is removed, the site becomes a positively charged ionized donor, or d^+. A neutral acceptor, or a^o, has an extra hole bound in a potential well $\approx$10 meV deeper than the valence band edge. If the hole is removed the site becomes a negatively charged ionized acceptor, or a^-. In E2 there are more acceptors than donors, thus it is p-type material. The net dopant concentration, n_a-n_d, has been measured and varies from 2.2×10^{11} cm^{-3} to 0.6×10^{11} cm^{-3} from one face of the crystal to the other, as shown in figure 5.3.

It is energetically favorable for each donor to lose its electron to an acceptor, and so in equilibrium all donors are ionized and n_d of the acceptors are ionized. At 77 K most holes on the n_a-n_d neutral acceptors are thermally ionized to the valence band. However at 20 mK all these acceptors remain neutral, as we show below.

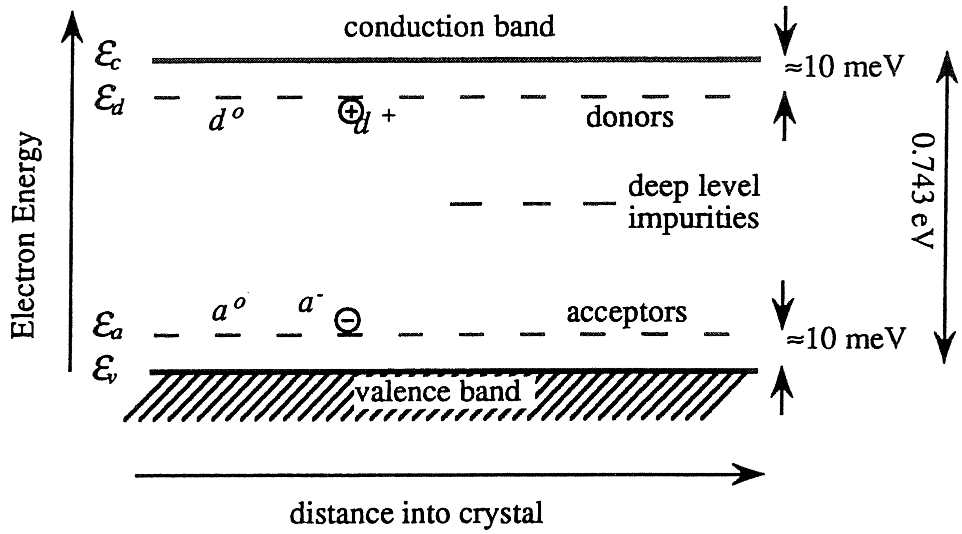

Figure 5.2 Diagram of energy bands and energy levels in the bulk of the detector

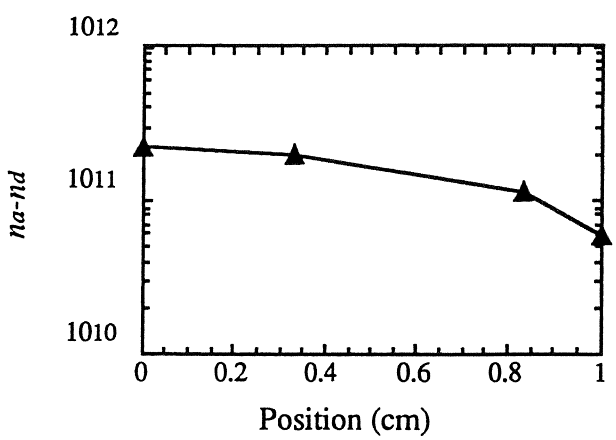

Figure 5.3 Net dopant concentration as a function of depth into E2. The thermistors are on the surface of the detector that is on the right in this figure.

This same information is contained in the Fermi energy level, μ, which is found by requiring that the crystal be electrically neutral. In general, the number density electrons in the conduction band is given by

$$n_e = \frac{1}{V}\int_{\mathcal{E}_c}^{\infty} f_{FD}(E)D(E)dE.$$

Here $f_{FD}(E)$ is the Fermi-Dirac occupation probability,

$$f_{FD}(E) = \frac{1}{1+e^{\frac{E-\mu}{kT}}},$$

and $D(E)$ is the density of states in the conduction band,

$$D(E) = \frac{V}{2\pi^2}\left(\frac{2m_e^*}{\hbar}\right)^{3/2}(E-\mathcal{E}_c)^{\frac{1}{2}}.$$

Note that this is the standard expression for the density of states in a free electron gas, but with the effective electron mass in the conduction band, $m_e^*=0.56m_e$, replacing the bare electron mass, and with the energy defined relative to the energy at the edge of the conduction band, $\mathcal{E}_c$.

Since, as we shall show, the Fermi level is not near the conduction band edge, $E-\mu \gg kT$ and

$$f_{FD}(E) \cong e^{-\frac{E-\mu}{kT}}.$$

In this case the integral for n_e can be easily evaluated, and gives

$$n_e = N_c e^{-\frac{\mathcal{E}_c-\mu}{kT}} \qquad 5.1$$

where N_c is known as the effective density of states in the conduction band, and is given by

$$N_c = 2\left(\frac{m_e^* kT}{2\pi\hbar^2}\right)^{\frac{3}{2}}.$$

At 20 mK $N_c=5.8\text{x}10^{12}$ cm^{-3}, and, since μ is in fact very close to the acceptor energy, by equation 5.1 n_e is negligibly small.

By similar reasoning, the hole density in the valence band is

$$n_h = N_v e^{-\frac{\mu-\mathcal{E}_v}{kT}} \qquad 5.2$$

where

$$N_v = 2\left(\frac{m_h^* kT}{2\pi\hbar^2}\right)^{\frac{3}{2}}$$

is the effective density of states in the valence band edge and $m_h^*=0.35m_e$ is the effective hole mass. At 20 mK, $N_v=2.9\text{x}10^{11}$ cm^{-3}, and n_h is negligibly small.

The number of ionized acceptors is given by

$$n_a^- = n_a \frac{1}{1+2e^{\frac{\varepsilon_a-\mu}{kT}}} \qquad 5.3$$

and the number of ionized donors by

$$n_d^+ = n_d \frac{1}{1+2e^{\frac{\mu-\varepsilon_d}{kT}}}. \qquad 5.4$$

The condition that the crystal be neutral is

$$\rho = e\left(n_h - n_e + n_d^+ - n_a^-\right) = 0.$$

Since $n_e=n_h=0$, this means $n_a^-=n_d^+$. With μ close to $\mathcal{E}_a$, by equation 5.4 all the donors are ionized, and so

$$n_a \frac{1}{1+2e^{\frac{\varepsilon_a-\mu}{kT}}} = n_d.$$

This is easily solved for μ,

$$\mu = \mathcal{E}_a - kT\ln\left(\frac{n_a-n_d}{2n_d}\right). \qquad 5.5$$

At 20 mK, kT=1.7 μeV, and so μ is very nearly just $\mathcal{E}_a$, as previously stated. Equation 5.3, with μ from equation 5.5, simply gives $n_a^-=n_d=n_d^+$. Thus the Fermi energy is just different enough from the acceptor energy so that the occupation number at the acceptor energy reflects the impurity density in the crystal. Finally, with $\mu=\mathcal{E}_a$, the number of free holes (equation 5.2), is on the order of 10^{-2500} - the crystal truly has no thermally generated free charge.

Particle interactions in the crystal excite electrons from the valence band to the conduction band, creating an equal number holes in the valence band. Because there are

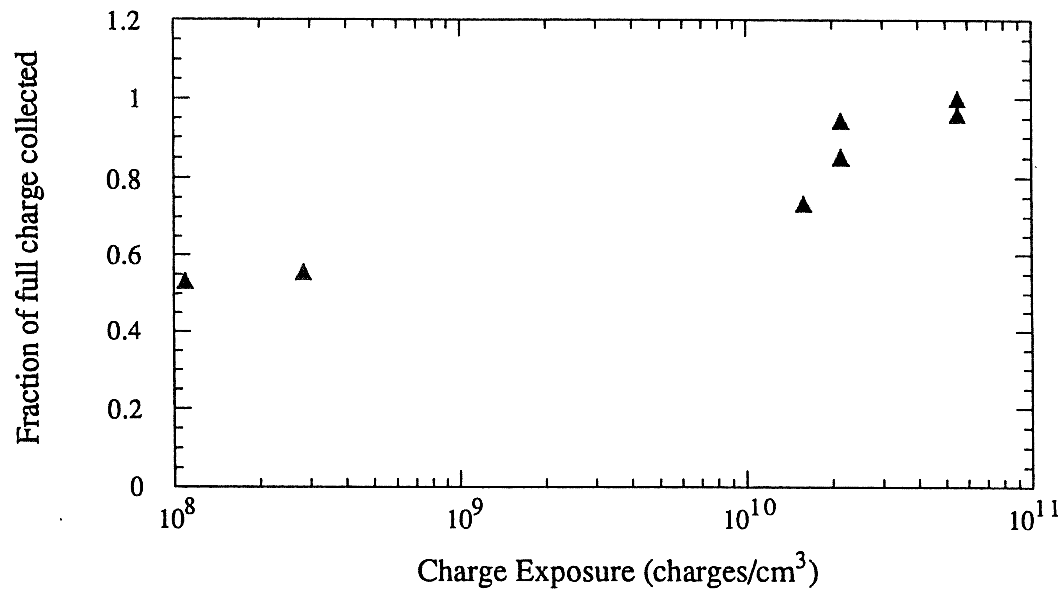

Figure 5.4 Fraction of total charges collected for 60 keV events as a function of the total exposure of the detector to free charge created by energy photons. The charge exposure estimate is uncertain by a factor of perhaps two. Also, the spectra at low exposure were not good, and the points may have large errors. For the two highest exposures, collection for both positive and negative biases is shown.

no thermally generated free carriers, these events can change the crystal to a new steady but non-equilibrium state. For instance, electrons excited to the conduction band by events can fall onto d^+ sites and the resulting d^o states cannot be thermally excited back to d^+ and free electrons. Similarly, valence band holes can neutralize the normally ionized acceptors. We believe, in fact, that it is this process that occurs when the crystal is exposed to a radioactive source after it is first cooled down. The initially charged ionized donors and acceptors trap electrons and holes, respectively, eventually neutralizing all the impurities. After the crystal is neutralized there are still possible trapping mechanisms, but the cross-sections for trapping on neutral impurities are a few order of magnitude smaller than on charged impurities.

In figure 5.4 we show the fraction of the total charge collected for 60 keV photons just after cooldown. In between data points the detector was exposed to a ^{252}Cf source which produces a broad spectrum of photons up to about 2 MeV. The total charge exposure, which is plotted in units of charge pairs/cm^3, is estimated from the measured spectrum in the detector when exposed to this source. Unfortunately this data was not obtained under ideal conditions, and the numbers in the figure, especially on the charge exposure axis, are only accurate to within a factor or 2. However the fact that full collection is obtained when the total charge created is roughly equal to the number of dopants strongly supports the picture of neutralization of the crystal.

5.4) Charge collection and phonon energy

Figure 5.5 shows the amount of charge collected and the total absolute phonon energy measured as a function of the applied bias across the 0.96 cm thick device (62). Each point represents the mean value of a gaussian fit to a spectrum; the statistical errors on each measurement are quite small. The sign of the bias refers to voltage between the charge measurement side of the detector and the thermistor side, which is held at ground.

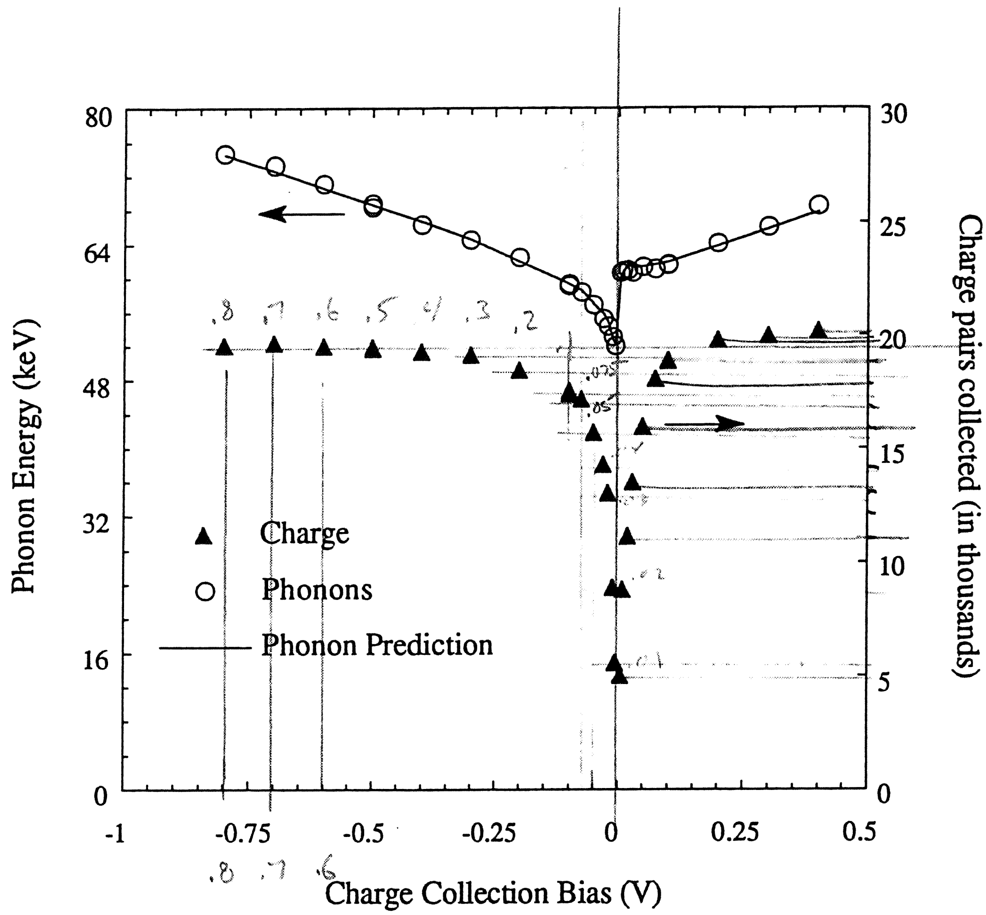

Figure 5.5 Absolute phonon energy and number of charge pairs collected for 60 keV photons as a function of the charge collection bias.

The maximum voltage was limited by breakdown of the detector, which is discussed in section 5.8

5.4a) Calibration of the charge measurement

The calibration of the number of charges is worth discussing because it is not easy and may suffer from systematic errors. As discussed in chapter 3, the signal consists of a voltage step followed by an exponential decay. The amplitude of the step is Q/C_f where Q is the charge from the event and C_f is the value of the capacitor in the feedback network. The difficulty is that C_f is difficult to measure precisely when configured in the circuit at low temperatures because it is small enough that stray capacitances can affect it, and it probably is different cold than at room temperature. In principle it can be estimated from the fall time of the pulse which is equal to $R_f C_f$, if R_f is also well known at low temperature. Unfortunately R_f is not easy to measure when the entire circuit is configured for the charge measurement. This method would also require careful characterization of all stages of the data acquisition chain. A different approach is to add an extra capacitor through which charges can be injected. However the capacitance will not a-priori be known at low temperatures and must be measured separately. Further, if this capacitor is made large enough so that stray capacitances are not a factor when it is configured in the circuit, then it will increase the parasitic capacitance to ground of the circuit, and thus increase the noise, as discussed in appendix E.

Though these problems are not insurmountable, we instead used the detector itself as a capacitor to pulse the circuit. The statistical error from this calibration is very small. A larger uncertainty may come from the capacitance of the detector, which is determined by the geometry of the detector and the dielectric constant of germanium at 20 mK. The geometry is measured accurately, and the correction due to the fact that it is does not consist of infinite planes is tabulated (63). There seems to be some confusion in the literature as to the exact dielectric constant near absolute zero, with some authors using 15.4 (64) and others using 16 (65). In figure 5.5 we have used 16.0.

The number of charge pairs created by a photon is given by $N_Q=E_r/\varepsilon$ where E_r is the recoil energy and ε is a band gap dependent number. At liquid nitrogen the accepted value of ε is 2.97 eV. A model has been proposed (66) for ε that matches this value at 77 K and predicts 3.0 at zero K where the band gap is different than at 77K. Adopting this value, the average number of charges created by the 59.54 keV photons from ^{241}Am is 19,850.

5.4b) Model of trapping and phonon energy

As is clear from figure 5.5, essentially all of the charge is collected for large positive biases, and slightly less than this for large negative biases. For smaller biases charge collection drops dramatically. The phonon energy, as discussed in chapter 4, is the sum of the energy from the interaction, and the energy created by the drifting charges. When charge collection is not complete, however, the phonon energy is clearly also affected by the polarity of the charge collection bias.

We have developed a model, based on trapping of drifting charges, that explains both the deficit of collected charge at low biases and the asymmetry in the phonon energy between small positive and negative bias. This asymmetry at first sight seems puzzling since the crystal is configured as a symmetric p^+-p-p^+ device. However it comes about because the photons only travel a short distance into the crystal.For positive bias holes drift the far distance across the detector and suffer a greater amount of trapping than electrons, while for negative bias the situation is reversed. We show this in figure 5.6.

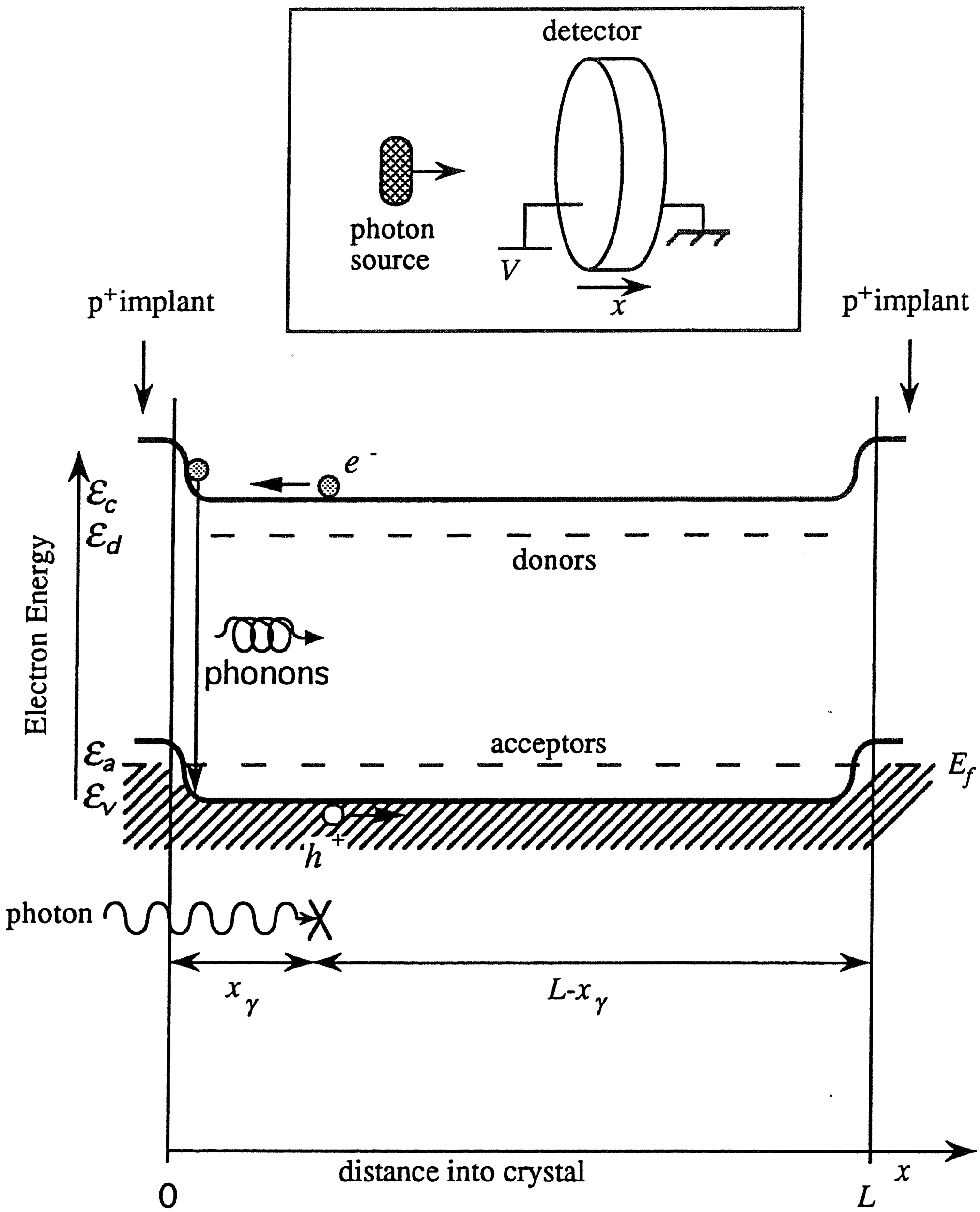

Figure 5.6 Diagram of processes involved in the trapping model of section 5.4 of the text. The shaded region represents the sea of electrons inthe valence band. The inset shows the definition of the dimension labeled x.

We had originally assumed that the total phonon energy is equal to the sum of initial energy from the particle interaction and the drift heat energy, minus the amount of energy that goes into the creation of electron hole pairs. That is,

$$E_m = E_r + eN_Q V - N_Q \mathcal{E}_{gap},$$

where E_m is the measured energy and E_r is the energy of the recoiling electron or nucleus. However if that drift to the edge of the detector "relax" to the valence band edge in the contact region, then the measured energy is instead

$$E_m = E_r + eN_Q V.$$

In retrospect it is highly probable that this should happen since the contact is a reservoir of holes.

Now if an electron is trapped on a donor (which we assume, for the moment, is ionized) before reaching the contact, the band gap energy $\mathcal{E}_{gap}$ will be "lost", while the much smaller energy $\mathcal{E}_c$-$\mathcal{E}_d$ is instead released as phonons. If a hole is trapped on an (ionized) acceptor, the small energy $\mathcal{E}_a$-$\mathcal{E}_v$ will be released as phonons. However this is precisely the same amount of energy released by a hole that relaxes to the Fermi level in the contact since the Fermi energy is equal to $\mathcal{E}_a$. Thus trapped electrons represent a "loss" of energy, while trapped holes do not. The phonon measurement in figure 5.5 is then explained by the fact that for negative bias electrons drift the far distance across the crystal and suffer more trapping than holes, while for positive biases holes drift further and are trapped more. We consider below what happens if other trapping mechanism are important besides the two discussed here.

5.4c) Calculation of number of charges trapped

The number of charges trapped can be deduced from the charge measurement as follows. We first need an expression for the measured signal in terms of the drifting charge in the detector. Consider a charge that drifts a distance l in a detector with a thickness L that is biased at a voltage V. The electrical circuit, as described in chapter 3, consists of the bias voltage connected to the contact on one side of the detector, and the charge measurement circuit connected to the contact on the other. The electric field in the detector is V/L, and so this charge acquires an energy $eV(l/L)$ from the electrical circuit, which it dissipates as phonons. The circuit generates this energy by supplying image charges to both contacts on the detector. Since the crystal remains neutral, the charge supplied to each contact is equal in magnitude. The voltage across the detector is fixed at V, and so the energy needed to supply a charge Q to either side of the detector is QV. This charge Q is the signal measured in the circuit (see the discussion in chapter 3), and so by equating these energies we find $Q=el/L$. If $l=L$, $Q=e$, as we expect.

If we sum over all the N_Q charges created in the particle interaction, the measured charge signal, Q_m, is given by

$$Q_m = e\frac{1}{L}\sum_i l_i. \qquad 5.6$$

Electrons and holes must be considered separately in the evaluation of equation 5.6. For an event at a depth x_γ with a positive bias, the holes will drift a distance L-x_γ and the electrons a distance x_γ. If no charges are trapped, equation 5.6 is evaluated as

$$Q_m = e\frac{1}{L}N_Q\{(L-x_\gamma)+x_\gamma\} = eN_Q.$$

When trapping is present the calculation is a bit more complicated. Consider, at first, just one species of charge drifting the entire distance across the crystal. The total signal comes from the charges that are trapped and those that are not. For the charges that are trapped, equation 5.6 can be written as

$$Q_m = e\frac{1}{L}\int_0^L \frac{dN_t}{dx}x\,dx,$$

where dN_t/dx is the number of charges trapped in an interval dx at a the point x. With a "trapping length" λ,

$$\frac{dN_t}{dx} = \frac{N_Q}{\lambda}e^{-\frac{x}{\lambda}} \quad ,$$

the trapped charge gives a signal

$$Q_m = eN_Q\left(\frac{\lambda}{L} - \frac{\lambda + L}{L}e^{-\frac{L}{\lambda}}\right).$$

The number of charges not trapped is simply

$$N = N_Q e^{-\frac{L}{\lambda}}$$

and since they drift a distance L, by equation 5.6 give a signal

$$Q_m = e\frac{1}{L}\left(L \cdot N_Q e^{-\frac{L}{\lambda}}\right) = eN_Q e^{-\frac{L}{\lambda}}.$$

The total signal from trapped and untrapped charge is then

$$Q_m = eN_Q\frac{\lambda}{L}\left(1 - e^{-\frac{L}{\lambda}}\right). \qquad 5.7$$

At a given bias, λ can be found from Q_m using equation 5.7, and the number of charges trapped is then found by integrating dN_t/dx over the width of the crystal to yield

$$N_t = N_Q\left(1 - e^{-\frac{L}{\lambda}}\right).$$

In the actual case where the event occurs at a depth x_γ equation 5.7 is modified as

$$Q_m = eN_Q\frac{1}{L}\left\{\lambda_1\left(1 - e^{-\frac{L-x_\gamma}{\lambda_1}}\right) + \lambda_2\left(1 - e^{-\frac{x_\gamma}{\lambda_2}}\right)\right\},$$

where λ_1 is the trapping length for the species that drifts from $x = x_\gamma$ to $x = L$, and λ_2 is for the species that drifts from $x = x_\gamma$ to $x = 0$. The measured spectrum of charge from photons is found by averaging over the distribution of event depths,

$$\frac{dN_\gamma}{dx} = \frac{1}{\lambda_\gamma}e^{-\frac{x}{\lambda_\gamma}}.$$

The resulting expression is

$$Q_m = eN_Q\frac{1}{L}\left\{\lambda_1\left(1 - \frac{\lambda_1}{\lambda_1 - \lambda_\gamma}e^{-\frac{L}{\lambda_1}}\right) + \lambda_2\left(1 - \frac{\lambda_2}{\lambda_2 + \lambda_\gamma}\right)\right\}. \qquad 5.8$$

where we have used the fact that $L \gg \lambda_\gamma$. The number of trapped charges of each species is similarly found as

$$N_{t1} = N_Q\left(1 - \frac{\lambda_1}{\lambda_1 - \lambda_\gamma} e^{-\frac{L}{\lambda_\gamma}}\right) \qquad 5.9a$$

and

$$N_{t2} = N_Q\left(1 - \frac{\lambda_2}{\lambda_2 + \lambda_\gamma}\right). \qquad 5.9b$$

Equation 5.8 relates two unknown trapping lengths to the one measured quantity. The data in figure 5.5 is taken at pairs of biases with opposite polarities but equal magnitudes. Thus for positive bias $\lambda_1=\lambda_h$ (the hole trapping length), and $\lambda_2=\lambda_e$ (the electron trapping length). For negative bias $\lambda_1=\lambda_e$ and $\lambda_2=\lambda_h$. Provided we know eN_Q from the calibration of the measurement, equation 5.8 can then be solved numerically for λ_e and λ_h if we assume that they are independent of the bias polarity. This assumption is probably a reasonable approximation, but ignores the fact that the net dopant concentration, n_a-n_d, varies with depth in the crystal. Figure 5.7 shows the resulting trapping lengths, and the fraction of electrons and holes trapped for both polarities of bias. Note that according to our calibration we collect essentially all the charge for large positive biases, and so the estimated hole trapping length diverges.

5.4d) Trapping mechanisms and fit of the phonon data

With the number of holes and electrons trapped known, the phonon energy can be predicted. However under the assumption that electrons only trap on donors and holes only on acceptors, this predicted phonon energy does not match the measurement. If indeed the crystal is completely neutral, then we might not expect holes to trap preferentially on acceptors and electrons on donors. To achieve a good fit to the data we have in fact had to consider other trapping processes.

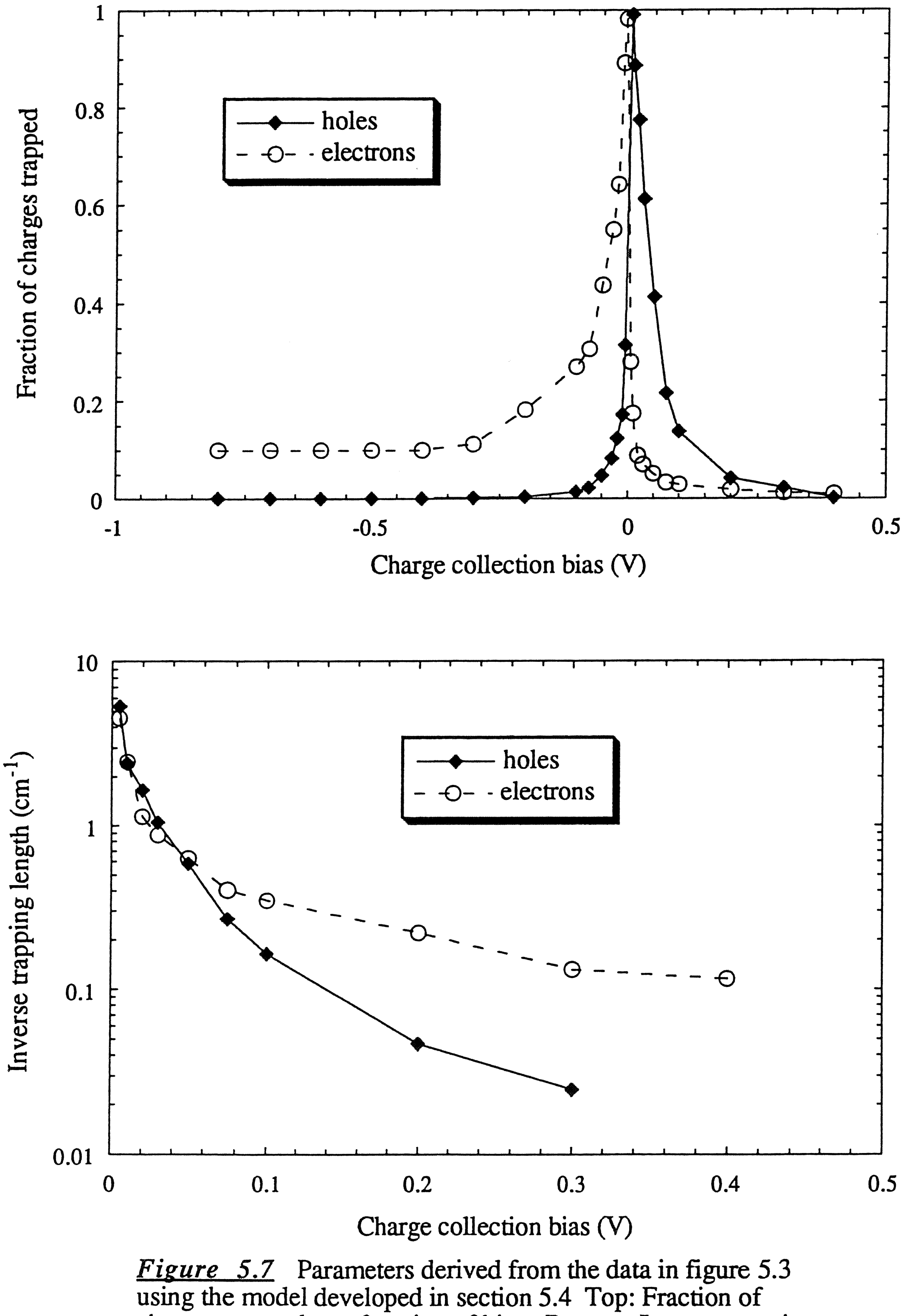

Figure 5.7 Parameters derived from the data in figure 5.3 using the model developed in section 5.4 Top: Fraction of charges trapped as a function of bias. Bottom: Inverse trapping length as a function of bias.

Unfortunately there does not seem to be a great deal of literature about trapping at our very low temperatures to guide us. One approach is to simply consider all those trapping mechanisms that are energetically allowed. If the crystal is not completely neutral, then electrons can trap on ionized donors, $e^{-}+d^{+}\rightarrow d^{o}$, and holes can trap on ionized acceptors, $h^{+}+a^{-}\rightarrow a^{o}$. Neutral impurities can also be trapping sites. Electrons and holes might trap across the band, $e^{-}+a^{o}\rightarrow a^{-}$ and $h^{+}+d^{o}\rightarrow d^{-}$. Additionally, "overcharged" impurity states, analogous to overcharged hydrogen, H^{-}, are known to exist in semiconductors and have binding energies of 1-3 meV (67, 68). At 20 mK they should be stable. Thus the processes $e^{-}+d^{o}\rightarrow d^{-}$ and $h^{+}+a^{o}\rightarrow a^{+}$ may be important. Moreover, if a large number of d^{-} and a^{+} states exist, then we can have $h^{+}+d^{-}\rightarrow d^{o}$, and $e^{-}+a^{+}\rightarrow a^{o}$. Finally, though they are presumably fewer in number, there are deep level impurities that may also serve as trapping and recombination sites.

An electron trapping on either a neutral or a charged donor releases a very small amount of phonon energy compared to an electron falling across the band gap and trapping on a neutral (or overcharged) acceptor. The same is true for holes trapping on acceptors versus donors. The phonon data can thus be fit by treating the number of holes and electrons that trap on shallow or deep (i.e., across the band) levels as parameters. The total number of trapped charges is known for each bias, so at each bias one free parameter for both holes and electrons describes the partitioning onto deep and shallow sites for holes and electrons, respectively. The partitioning in reality is probably a function of bias, but for simplicity we have considered it an overall constant. We also ignore the possibility of trapping onto deep level impurities.

The final measured energy is then

$$E_m(V) = E_r + e\frac{V}{L}\sum_i l_i - N_{te}(V)\mathcal{E}_{gap}$$
$$+ N_{th}(V)\{(1-d_h)\mathcal{E}_{sh} + d_h\mathcal{E}_{dh}\} \qquad 5.10$$
$$+ N_{te}(V)\{(1-d_e)\mathcal{E}_{se} + d_e\mathcal{E}_{de}\}$$

where:

V is the bias voltage

E_r is the energy deposited in the event

$e\frac{V}{L}\sum_i l_i$ = The drift heat from events. By equation 5.6 this is equal to VQ_m.

$N_{te}(V)$ is the number of trapped electrons, as determined by equation 5.9

$N_{th}(V)$ is the number of trapped holes, as determined by equation 5.9

d_h is the fraction of trapped holes that trap on deep sites, as found by the fit

d_e is the fraction of trapped electrons that trap on deep sites, as found by the fit

$\mathcal{E}_{sh}$ and $\mathcal{E}_{dh}$ are the shallow and deep trap energies for holes

$\mathcal{E}_{se}$ and $\mathcal{E}_{de}$ are the shallow and deep trap energies for electrons

Note that for simplicity we have taken the trapping to occur only on ionized donors and acceptors, so that, for example, $\mathcal{E}_{sh}$=$\mathcal{E}_a$-$\mathcal{E}_v$, and so on for $\mathcal{E}_{dh}$, $\mathcal{E}_{se}$, and $\mathcal{E}_{de}$. The resulting phonon energy would be very little changed if we instead consider trapping on neutral impurities.

The other unknown quantity is the calibration of the raw phonon signals. Equation 5.10 predicts this energy when the trapping fractions are known. We thus fit the entire phonon data set with three parameters: a calibration of the phonon energy scale, and the partitioning fractions for trapped holes and for trapped electrons. The measured phonon energy in figure 5.5 uses this calibration, and the predicted energy in the figure comes from equation 5.10 and the result of the fit. We find that the fraction of electrons that traps on acceptors (d_e) is 45 %, and on donors (1-d_e) is 55 %; the fraction of holes that traps on donors (d_h) is 20 % and on acceptors is (1-d_h) 80 %.

These fractions give us the trapping cross sections if the density of charged and uncharged donors and acceptors is known. Unfortunately we can only make an assumption about the charge state, and for our crystal only the net dopant concentration, n_a-n_d, has been measured. For a given value of n, the cross section $\sigma=1/(n\lambda)$ can be extracted from the measurement of the trapping length, λ, in figure 5.7. Using a benchmark value of $n=1\text{x}10^{11}$ cm^{-3}, we deduce cross-sections between 10^{-13} cm^2 and a few 10^{-11} cm^2. In section 5.6 we briefly discuss these results in terms of measurements of trapping made at 4 K.

The quality of the fit in figure 5.5 is fairly good, though not perfect. Clearly there are many more sophisticated treatments of the trapping that we could explore. For instance we could relax the assumption that the fractions are universal constants, or we could include mid-band level band trapping states. However it probably makes more sense for us to first try to understand the cross sections found from this simple model in terms of fundamental physics. On the experimental side, an obvious idea is to vary the doping levels and see if this changes the trapping as expected.

5.4e) Calibration of the phonon energy

Our model predicts the phonon energy, and thus affords a calibration of the measured phonon signals. Since we fit the trapping at the same time, it would be nice to obtain an independent estimate of the phonon energy. We have done so by two different methods. The first is that in the high bias regime where trapping is small, the slope of the phonon energy versus charge bias is simply eN_Q. This slope can be seen in figure 5.5. The raw phonon signals can in principle be calibrated by matching this prediction with the measured slope. In fact the trapping has a significant, if small, effect on both N_Q and the measured phonon energy, even at high bias. We have therefore approached the problem slightly differently. We have repeated the fit for the calibration and trapping fractions, but also include the deposited energy, E_r, as a fit parameter in equation 5.10. The resulting value of E_r is primarily determined by the drift heat term and depends directly on the charge calibration, as discussed above. If the dielectric constant is taken to be 16.0, then the fit value of E_r is 57.9 keV; if ε=15.4, E_r=54.4 keV. The fact that this "recoil energy" is close to 60 keV confirms that the first calibration is probably fairly good.

The other method of calibrating the phonon signal is to put an electrical pulse of energy through three different sections of the implanted contact, as discussed in chapter 4. We have checked that these "pulser" events produce no measurable ionization signal. We find that the energy measured in a sensor using this method has $\approx$5 % variations depending on the relative position of the phonon sensor and heating path used. These variations may be due to either non-linearities in the sensors, or variations in the amount of heat lost to epoxy or sensors on the surface of the crystal. When we calibrate the phonon signals against the pulser events, we deduce that the phonon energies in figure 5.5 should actually about 3 % to 9 % (depending on the pulsing path used) *higher* than shown. This discrepancy seems to be roughly consistent with the inherent errors in the method. Moreover, if anything, it strongly supports the conclusion that when little trapping is present the *full* energy from the event is recovered as phonons.

5.5) Other possible mechanisms

5.5a) Diffusion

There are perhaps other mechanisms that affect the behavior of the detector, including the results shown in figure 5.5. One possibility is that diffusion of the charges competes with the drift induced by the electric field. The diffusion constant is related to the mobility by the Einstein relation, (69)

$$D = \frac{kT}{e}\mu .$$

We have not found data for the mobility at very low temperatures, though at 10 K mobilities in the range of 10^6 cm^{2}V^{-1}sec^{-1} have been measured (70).

In our case the rise time of pulses measured with a drift field of 0.01 V/cm is faster than the electronics limit of 2 μsec, indicating mobilities *at least* as big as 5x10^7 cm^{2}V^{-1}sec^{-1}. The distance a charge moves by diffusion in a time t is given by $l_D^2=Dt$, while under the influence of an electric field, E, it moves a distance $l_E=\mu Et$. The ratio of diffusion to drift distance is then

$$\frac{l_D}{l_E} = 1.8\times10^{-5}\left(\frac{\frac{\mathrm{V}}{\mathrm{cm}}}{E}\right)\left(\frac{5\times10^{7}\,\frac{\mathrm{cm}^2}{\mathrm{V\cdot sec}}}{\mu}\right)^{\frac{1}{2}}\left(\frac{\mathrm{sec}}{t}\right)^{\frac{1}{2}}.$$

and it would seem that even at the lowest biases diffusion is negligible after a few 10^{-9} sec. In fact, as discussed in section 5.6, we have reason to believe that the carriers are accelerated to the saturation velocity by even very modest fields. If so, the velocity cannot be described by a mobility and the above argument is not applicable, but diffusion is certainly negligible.

5.5b) Space charge

If trapping occurs, at different rates for holes and electrons in a given location, then an excess of positive or negative charge will be created. This "space charge", by Poisson's equation, creates an electric field that can affect the charge collection process. Space charge is thus related to trapping, but is a distinct phenomenon. It is difficult to determine what state the crystal is actually in, and we have not had time to study the issue deeply. What follows is a discussion in simple terms of what qualitative effects space charge can have.

In figure 5.8 we schematically show the potential energy of electrons, U_e, and the electric field, E_x, in a detector with an external bias and with and without space charge. For simplicity, the contact regions are not shown. Note that U_e, the electron energy, is related to the electrostatic potential, ϕ, by U_e=-$e\phi$. The electric field is related to ϕ by E_x by E_x=-$d\phi/dx$, so that U_e=$ed\phi/dx$. The energy for holes, U_h, is given by U_h=-U_e. The externally bias, V_{ext}, is applied to the x=0 edge of the crystal with the x=L side at ground.

With no space charge the external potential produces a constant electric field and a linearly increasing potential energy. We then include space charge confined to a region of width w and extending across the detector in the other two dimensions. We treat this charge distribution as an infinite plane. Clearly much more complicated space charge structures can actually exist. The electric field due to the space charge in this simple geometry points away from its center and has a magnitude outside of the space charge region

$$E_x = \frac{en_{sc}w}{2\varepsilon\varepsilon_o}$$

where n_{sc} is the charge density. If the density is high enough, the total electric field can be zero to the left of the space charge, and double the value of the external field to the

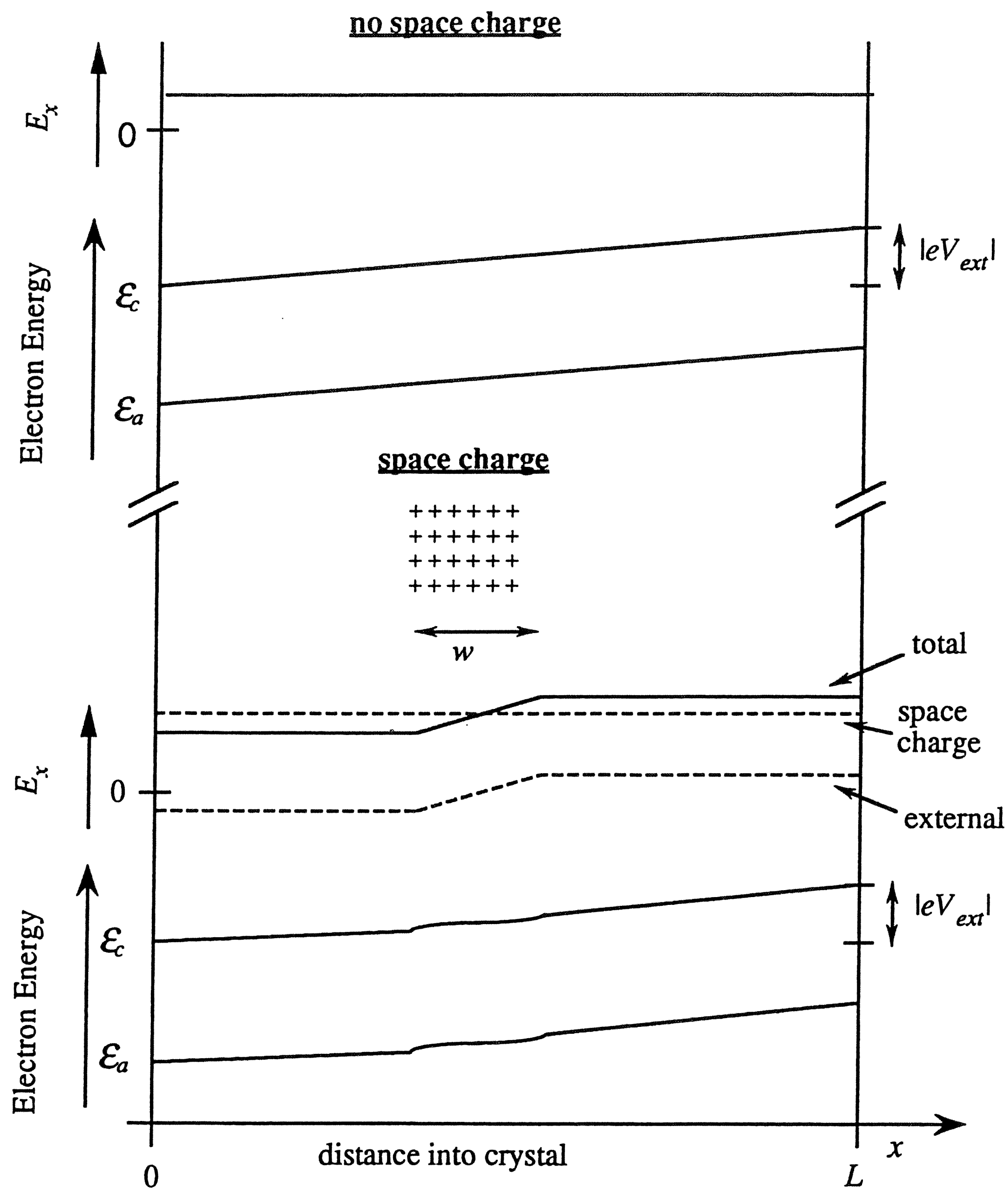

Figure 5.8 Energy for electron ($=-e\phi$, where ϕ is the electric potential) and electric field in x direction for detector externally biased, with and without space charge.

right of the charge. The space could thus cause a large portion of the detector to be inactive. A field of 0.4 V/cm, for example, will be created by a space charge region 1 mm thick with a density of only 7×10^7 charges/cm^3.

One strong piece of evidence we have that some space charge exists in our detector is that when the detector is grounded after having been biased for some time, pulses of due to charge flowing in both directions in the crystal are observed for a short time, but then die out. This is seen quite easily in figure 5.8 where if the external field is removed, negative charges will be pulled to the center and positive charges will flow to the contacts. Events on either side of the space charge will produce signals in the amplifier of different polarities; and as electrons from events accumulate in the center they will eventually eat away the space charge.

5.6 Comparison with other measurements

Unfortunately there does not seem to be much literature on charge transport in semiconductors at temperatures as low as 20 mK. The literature on photoconductors at 4 K (58, 59) is somewhat applicable to our case. The mobility of holes and electrons at 4 K is limited in high purity crystals by scattering with thermal phonons, with a temperature dependence $\mu \propto T^{-3/2}$. At 20 mK this should be negligible. Scattering on ionized impurities is also important at 4 K and gives a mobility proportional to $T^{3/2}$, thus it should be even more important at 20 mK if our crystal is not neutral. This in fact may well be what prevents charge collection until the crystal is neutralized, as discussed in section 5.3. Scattering on neutral impurities is temperature independent, and should be negligible for our high purity material.

What is very different between 4 K and 20 mK is that of the three processes above, only scattering on phonons is inelastic, and it should be negligible in our case. Thus whether or not the crystal is neutralized, the electrons must lose energy they acquire from the electric field in some other way. We expect that this energy loss occurs through the emission of phonons, which limits the drift velocity to the "saturation" velocity of $\approx 1 \times 10^7$ cm/sec. In this case the electrons will not have a thermal energy distribution at T=20 mK, but will have considerably higher energies.

Trapping on charged impurities has been measured at temperatures down to a few K and has cross sections on the order of 10^{-11} cm^{-2} at 4 K (71). Theory suggests that this trapping depends on temperature as T^{-3} (72). Spread in the data makes it difficult to extrapolate the measurements to lower temperatures, though it does appear that the cross sections will be somewhat higher than those we deduce in section 5.4. This would be consistent with the expectation that trapping on charged sites is stronger than trapping on neutral sites. However we clearly need to better understand the energy distributions of the charge carriers in our crystal before we can begin to compare our results to theory.

5.7 Near contact region

A full description of the implanted contacts on the on the top and bottom surfaces (x=0 and x=L in the above discussions) of the detector is a topic beyond the scope of this thesis. They have been described in some detail by Ning Wang in her thesis (37), and a more general discussion can be found in (61). Basically, though, the doping level in the implanted regions is so high that all the potential wells of the impurity atoms overlap and an energy band is formed. This is called degenerate doping. The band is wide enough that it in facts overlaps with the original valence band edge, so that the valence band edge is effectively raised in the implanted region. Since each acceptor impurity acts as a site for an electron, but does not supply an electron, the acceptor sites can be considered to be occupied by holes. Thus in the contact there is a sea of holes, and the Fermi level lies beneath the valence band edge.

There is a transition region between the implanted region and the undoped bulk material, described in detail for a device at 4 K by N. Haegel (57). If, somehow, the valence band edges in the implanted and bulk regions were to line up, then it would be energetically favorable for holes from the valence band to spill into the undoped region and fall onto ionized acceptors (a^-). For each neutralized hole there is a positively charged donor, or d^+, and so a region of positive space charge with a density n_d is built up in the undoped bulk. Very near the contact there is a region where free holes "spill over" into the bulk, driven by the enormous concentration gradient of holes between the implanted region and the bulk. Finally, there is also a very thin high density region of negative charge in the implant where the holes have left. These space charge regions create an electric field which opposes further flow of holes into the undoped region. The potential, ϕ, created by this field bends the band edges and energy levels so that it is no longer energetically favorable for the holes to fall onto acceptor sites. Another statement of this is that in the final thermal equilibrium state the Fermi energy must be the same in all parts of semiconductor. Figure 5.9 shows the transition region, with the edge of the implanted region taken to be infinitely sharp.

The equations 5.1-5.4 can be used to describe the region beyond the region near the contact with free holes. To do so we replace the fixed electron energy levels by $\mathcal{E}(x)=\mathcal{E}_b+e\phi(x)$ where $\mathcal{E}_b$ is the value in the bulk far from the contact. As is clear from figure 5.9 in the transition region the Fermi level lies below the acceptor energy $\mathcal{E}_a=\mathcal{E}_{ab}+e\phi(x)$, but well above the valence band energy, $\mathcal{E}_v=\mathcal{E}_{vb}+e\phi(x)$. Except for a tiny regions at x=0 and at the end of the transition region, then, $\mathcal{E}_a-\mu \gg kT$ and $\mu-\mathcal{E}_v \gg kT$, and so n_h=0 and n_a^-=0 by equations 5.2 and 5.3. The space charge density in this region is thus constant and equal to $n_d^+=n_d$. Poisson's equation,

$$\nabla^2\phi = -\frac{\rho}{\varepsilon\varepsilon_o},$$

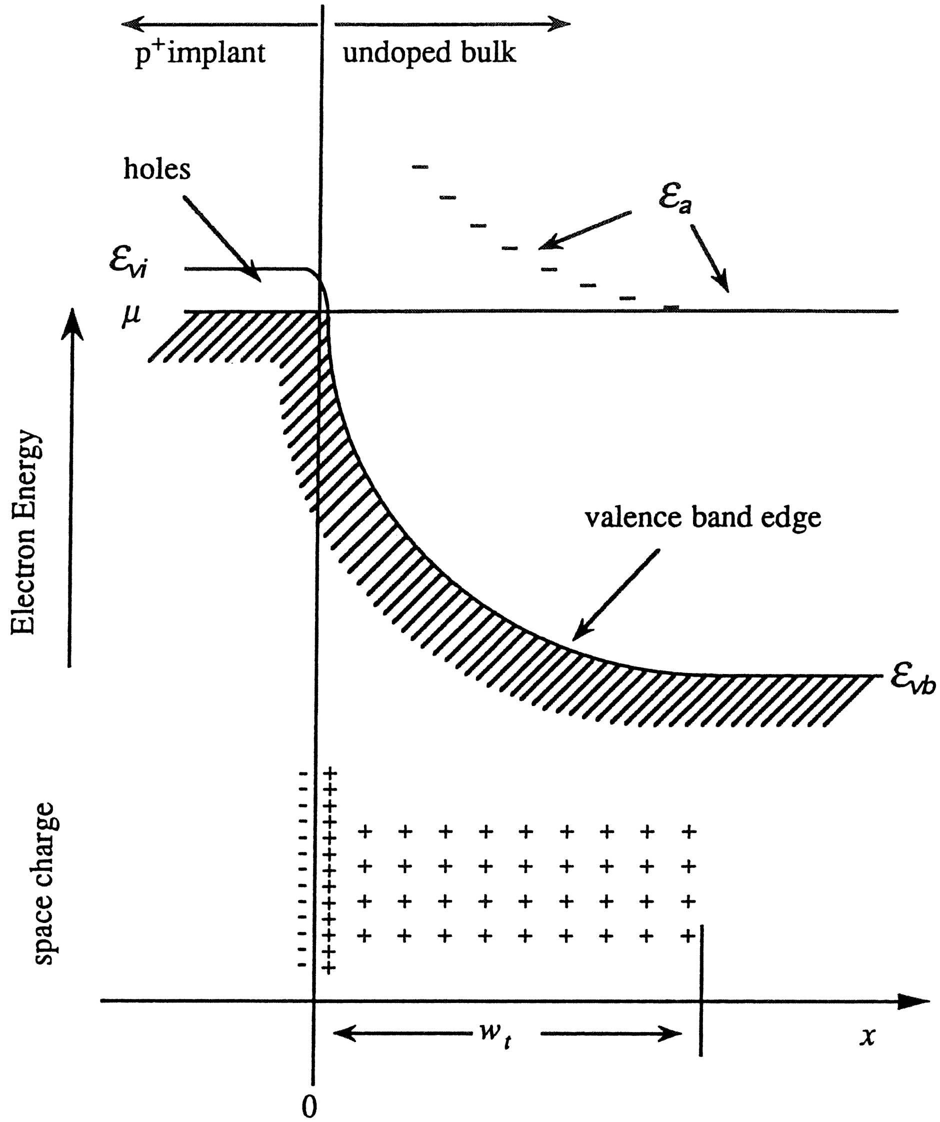

__Figure 5.9__ Diagram of implanted contacts and transition to the undoped bulk. The valence band edge, and acceptor energy levels are bent by the built in electrostatic potential created by space charge. The Fermi level, by contrast, is constant throughout the structure.

can be immediately integrated to find w_t, the width of the transition region with a charge density n_d. This gives

$$w_t = \sqrt{\frac{2\varepsilon\varepsilon_o(\mathcal{E}_a - \mathcal{E}_{vb})}{e^2 n_d}}. \qquad 5.11$$

where $\mathcal{E}_{vb}$ is the valence band energy far from the implant. Taking n_d=1x10^{11} cm^{-3} (although in reality we have only measured n_a-n_d for E2), we find w_t=13 μm. The electric field varies with position in the space charge region as

$$E = \frac{en_d}{\varepsilon\varepsilon_o}x, \qquad 5.12$$

starting at a value of 15 V/cm at the left edge of this region and decreasing to zero at the right edge of the space charge zone.

The region near x=0 is a bit more complicated. Until the valence band edge dips below the Fermi level, there is a region in the bulk material with a very high density of free holes. There is also a region in the implanted contact with a high density of negative charge where the holes have left. The free charge in the bulk is driven by the gradient between the hole density in the implanted contact and the vanishing free hole density in the bulk. Resisting the diffusion is the electric field created by the space charge. In equilibrium, then, there is a balance between a diffusion current and an electric-field driven current. N. Haegel (57) calculates the width of this region at 4 K and finds that it extends only a fraction of a micron. It also scales as $T^{1/2}$ and so should be a few hundred Å at 20 mK, which is quite small compared to w_t.

It is important to realize that this equilibrium situation, just like the equilibrium state of the bulk crystal, is not the only stable state. In particular, the equilibrium state is based upon the fact that is energetically favorable for holes from the implant to sit on acceptors in the bulk to a depth of w_t. However in figure 5.9 it is clear that to get to these acceptor sites they first have to overcome an energy barrier of as much as $\mathcal{E}_a$-$\mathcal{E}_v$≈10 meV. At temperatures as low as 4 K there are always some thermally generated holes that have overcome this barrier, but once again, because 20 mK is equivalent to 1.7 μeV, this should not happen in our case. If electrons from events fall onto the neutralized acceptors in the transition region, the resulting ionized acceptors should make the band edges and Fermi energy discontinuous. It is not clear, then, what the actual near contact region looks like when we are running. It may be in fact that the free carriers constantly generated by events tend to maintain the equilibrium situation.

There is one piece of experimental information that is probably directly related to the above discussion. Charges created by 13.9 keV and 17.6 keV photons from a ^{241}Am source are not well collected, as seen in figure 6.2. The penetration depths of these X-rays are ≈15 μm and ≈30 μm respectively, thus many of these photons interact in the transition region. It is not clear exactly what happens in this region, since while the space charge may decrease the mobility and cause trapping, this is also a region of a strong electric field. For a negative external voltage on a given contact, this internal field is in the same direction as the external field and decreases from 15 V/cm near the contact to 0 at $x=w_t$. The maximum external field is about 0.5 V/cm thus one might expect quite good collection of the low energy X-rays for negative biases, and poor collection for positive biases. Experimentally, however, charge collection for both bias polarities is essentially equivalent and quite poor. A more complete understanding of this phenomena will probably require greater knowledge of the mobilities and trapping cross sections.

5.8 Current-voltage characteristics of the detector

When a voltage is applied across the crystal to collect charge, a small amount of current flows. For small biases the current depends linearly on the voltage, with a temperature dependent resistance of approximately 5×10^{10} Ω at 20 mK. If the voltage is increased beyond a certain point, the detector "breaks down" into a low resistance state. Once the breakdown voltage has been passed, the high current behavior can only be stopped by returning the voltage to a value well below the critical value. This critical voltage is not the same for both directions of bias, and is largest soon after cooldown of the device from room temperature. Over a period of many days it settles to just over 0.3 V in the positive direction and just over 0.5 V in the negative direction.

We have not had time to try to understand this behavior in fundamental terms. However, from the above discussions it would seem that no current should flow under ideal conditions until a substantially higher bias is applied. There are no thermally generated free carriers, and the holes at the contacts have a barrier many times greater than kT to overcome before they can enter the bulk. The built in electric field restraining these hole at the contacts is estimated above to be $\approx$15 V/cm. Further, since the contacts are in principle the same, there should not be an asymmetry between the two directions of bias. In reality, however, one of the contacts has the eutectically bonded thermistors, while the other contact was created after this heating process. Small structures of gold created during the eutectic could serve as high field regions that inject holes into the bulk. Finally, if current does flow through the bulk, then how does the crystal remain neutral, as we believe it does from the discussion in section 5.3?

It could also be that infrared photons from room temperature leak into the coldest part of the cryostat and excite electrons and holes from impurities into the bands, causing conduction. We have also not investigated this carefully, however note that at a bias of 0.5 V we have a current of 6×10^7 charges/sec. If this comes entirely from charge generated by photons in the bulk (i.e., no charge flows in from the contacts), then the crystal will become completely ionized in about 1 hour, contradicting our view of the neutralization of the crystal. Moreover, why should this current be linear in voltage, and why should the resistance be temperature dependent?

Another possibility is that we have current flowing along the edges of the detector. The time evolution might then reflect changes in the charge state of the outer edge of the detector. If this is the case, though, it is somewhat puzzling that over many cooldowns the breakdown voltages have tended to the same long-term values.

5.9 Tests of a p-p-n device

In addition to the tests of E2 that are the focus of this thesis, we have run a smaller detector that has a p^+-p-n^+ contact structure and one thermistor. This device is described briefly in chapter 3. We exposed it to a ^{241}Am source on the side with the n^+ contact. The ionization spectrum obtained when the detector is reverse biased at -0.5 V (reverse bias means the n^+ contact is held at a higher voltage that the p^+ contact) is shown in figure 5.10. The complex of low energy X-rays from the source, including the 14 keV and 18 keV lines, are well resolved. (There is an additional line at ≈7.5 keV, perhaps due to the escape of $K_{\alpha 1}$ 9.8 keV X-rays from the crystal after the photo-absorption of 18 keV X-rays from the source.)

This result is intriguing. The transition region between the n^+ contact and the p-type bulk is similar in structure to the transition between the p^+ contact and p-type bulk in E2. A much larger energy difference drives this process however: electrons fall onto otherwise neutral acceptors until the built-in voltage is $(\mathcal{E}_d\text{-}\mathcal{E}_a)/e$=0.72 V. The density of negative space charge is n_a-n_d, and, by equation 5.11, extends over roughly 100 μm.

If the crystal is actually in this equilibrium state, then all the low energy X-rays interact in space charge region. The maximum internal field in this case is 125 V/cm, much larger than for the p^+-p transition. Presumably this overcomes the scattering and/or trapping due to the space charge. Note that for forward bias the low energy X-rays are not resolved. This improved charge collection is fortunate, and may be essential in detectors for the actual dark matter experiment.

Finally, we have made a rough measurement of the simultaneous phonon and ionization energy as a function of charge bias, just like the measurement discussed in section 5.4. The result is shown in figure 5.11. Note that both measurements are uncalibrated and are presented in terms of raw pulse height. The voltage is defined from the p^+ to n^+ contact, thus positive voltages are forward bias in the standard terminology of

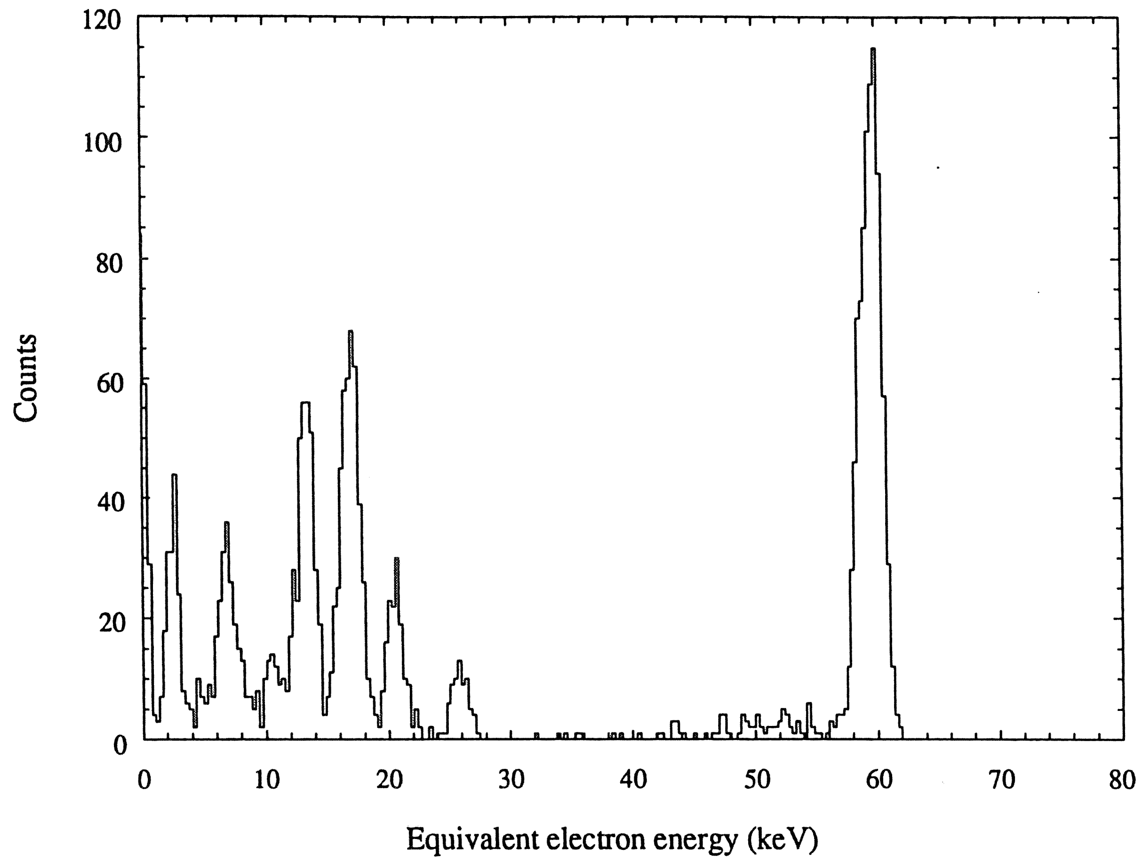

Figure 5.10 Spectrum of ionization created by photons from ^{241}Am in the p^+-p-n^+ device.

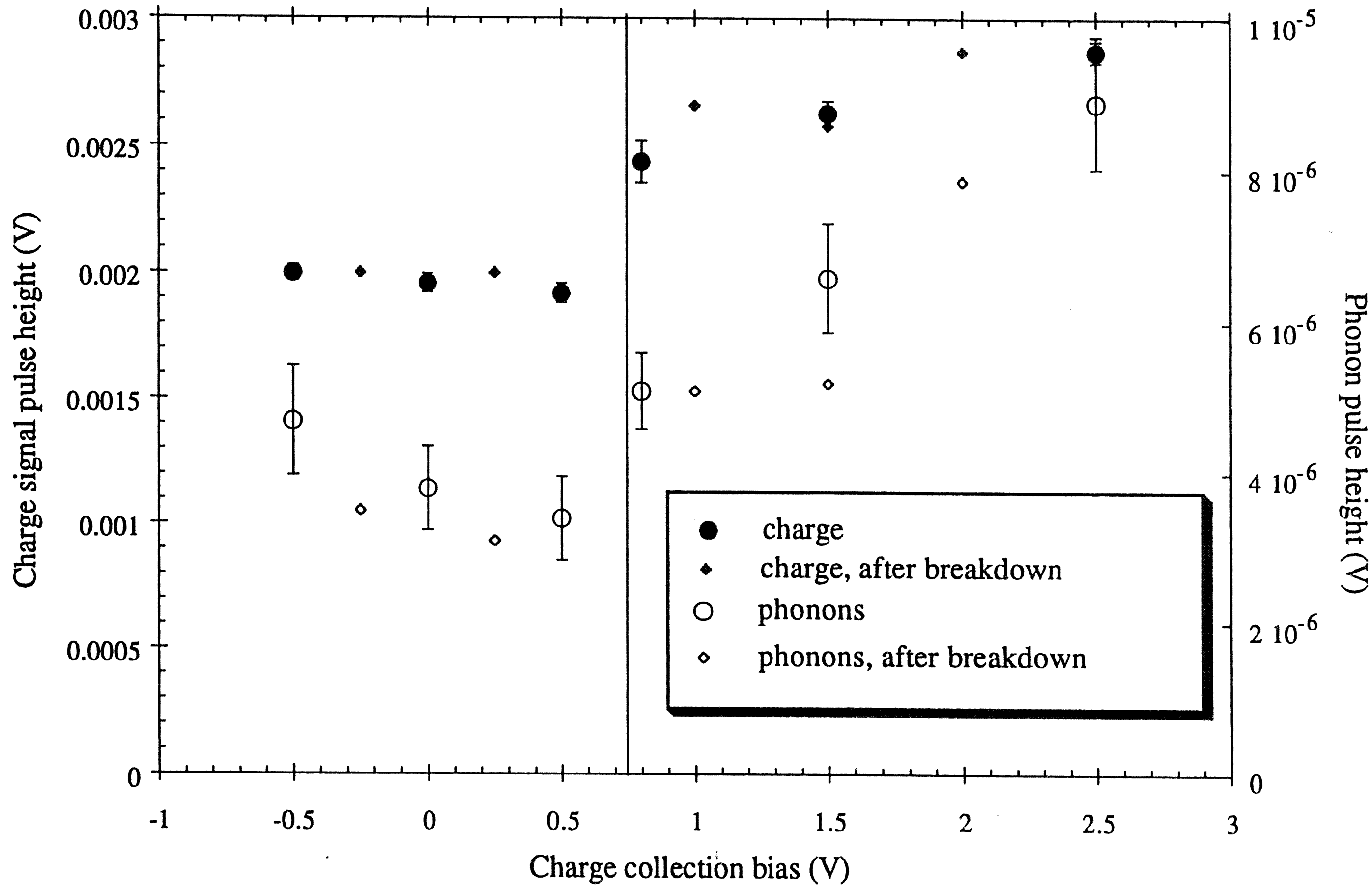

Figure 5.11 Charge collected and phonon energy measured in the small p-p-n device. Note the shift in behavior after the voltage across the detector broke down. Error bars are omitted for for clarity from the post-breakdown data for clarity, but are comparable to the other errors.

p-n junctions. Negative biases and positive biases less than about +0.7 V give the same polarity charge pulses. Voltages more positive than this give pulses of the opposite polarity, presumably because the external voltage exceeds the built-in potential. At biases near +0.72 volts, pulses of both polarities are often seen, and the detector behavior is erratic.

There are a number of interesting features in the figure. Both the phonon energy and charge collection are discontinuous at the band gap voltage. Unlike figure 5.5 for E2, however, in this case the electric field is fairly large for all data points since the device is only 1 mm thick. Trapping in undoped bulk regions is presumably not an important effect. Also, after the data points at +2.5 V bias were taken, the detector broke down into a high current mode. It was returned to ground for a while, and data collection was resumed. A pronounced shift in the behavior of the detector is seen after this, especially for positive bias. This may be a reflection of the fact that the n^+-p transition region is not in its equilibrium state, and that causing the detector to break down changes its state.

5.10 Conclusions

The ionization measurement is essential to the success of our background rejection scheme. Though the physics of the ionization measurement is interesting in its own right, in terms of a dark matter experiment we can be more utilitarian. We need only to know how much charge is created by an event, and we must obtain this estimation with a fairly low bias, as discussed in chapter 2. In this respect the results discussed in section 5.4 are quite reassuring. We have shown that in a moderately pure crystal we can collect essentially all the charge from events that occur deep in the crystal with a small bias voltage. However, there is one outstanding issue which we discuss in chapter 6, namely there are a number of events for which charge collection seems not to be good. Some of these events are related to the near contact region, while the others may be caused by a build up of charge at the edges of the detector. It will be imperative for us to minimize these problems.

As a final note, if the basic ideas in model presented in section 5.4 prove to be correct, then simultaneous ionization and phonon measurements could prove to be a powerful tool for studying impurity states in semiconductors.

Chapter 6: Performance of the Detector

6.1) Resolution

The resolution of E2 has been tested by exposing it to photons from a ^{241}Am source, using the same setup indicated in figure 5.1. The primary photons from this source are 60 keV gammas and 14 and 18 keV X-rays. The data acquisition system, and the treatment of the signals are described in section 3.7. The pulses in the ionization and phonon measurement for a 60 keV photon are shown in figure 6.1. These signals are fit as described in appendix F, and the result is shown in figure 6.2. As in section 2.3, the axes are defined in terms of electron equivalent energy, with the scale set by hand so that the 59.54 keV line appears at this energy in both measurements.

The data set includes a number of events which were triggered "randomly" by the computer. They are fit just like the other events, and appear in the peak at zero energy. The width of this "baseline" is a measure of the electronic noise. Note that after the fit, hardware noise triggers also show up in this baseline and not at the trigger threshold. In addition, the fit smears the trigger threshold somewhat.

The 60 keV peak and baseline have been fit to a Gaussian and the standard deviation, σ, (=FWHM/2.36) is shown in table 6.1. In appendix F we compare the baseline resolution to that expected based on the electronic noise level. The resolution on the 60 keV peak exceeds the baseline by a small amount in both measurements. In the charge this is presumably due to trapping and/or space charge, perhaps in conjunction with the small ($\approx$1mm) spread in the depth into the crystal of events. As discussed in chapter 5, the phonon signal is somewhat dependent on charge collection, both because of drift heat and through the release of energy stored in the electron-hole pairs. Thus the excess width in the phonon measurement may well be related to the excess width in the charge measurement. However we have not studied this idea in any detail.

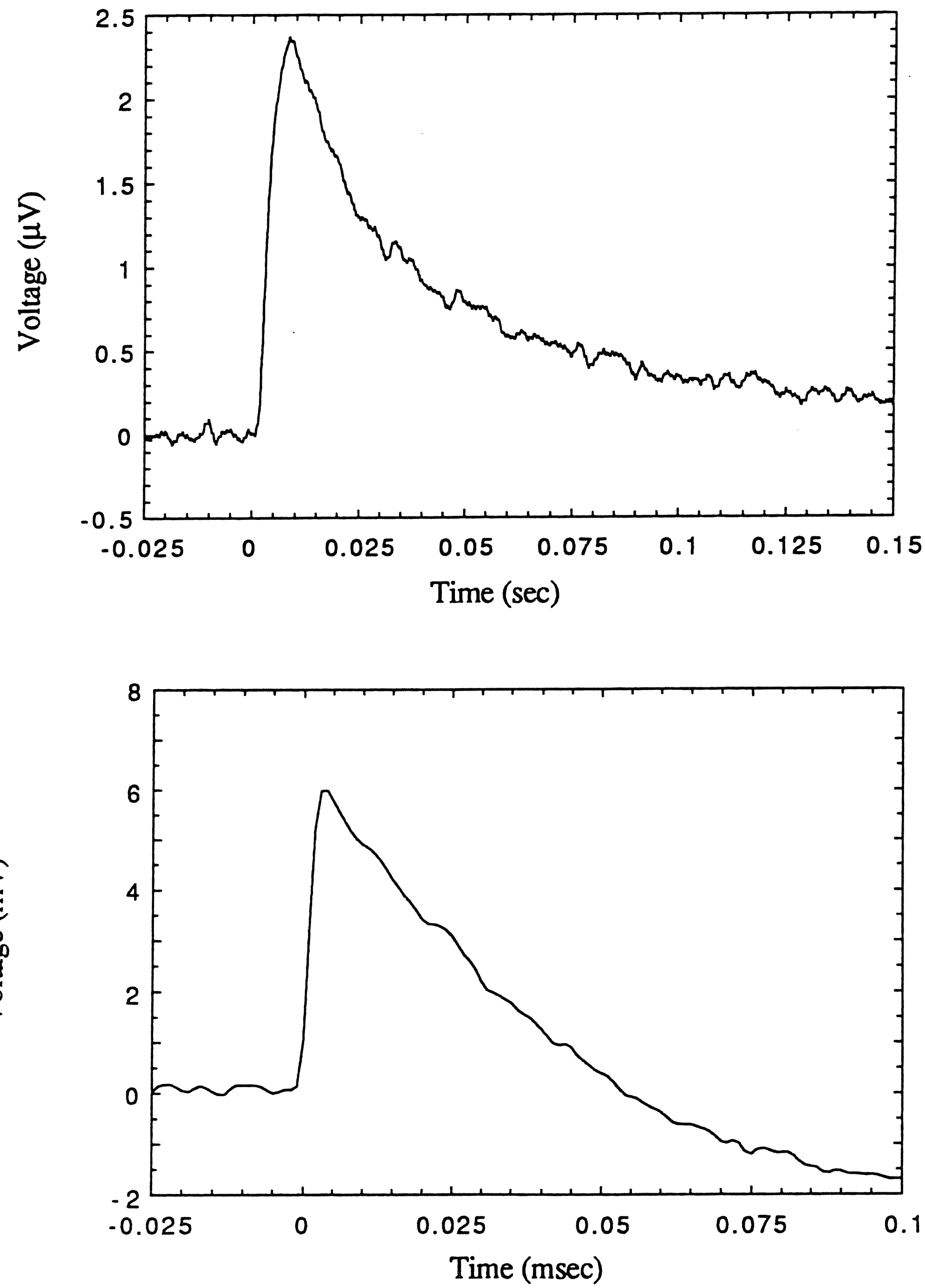

Figure 6.1 Pulses created by 60 keV photons in E2. The top is the signal in the phonon measurement, the bottom is the signal in the charge measurement. The treatment of the signals is described in section 3.7. Note in particular that the undershoot in the charge signal is caused by the steep 400 Hz high pass filter employed to remove low frequency microphonics.

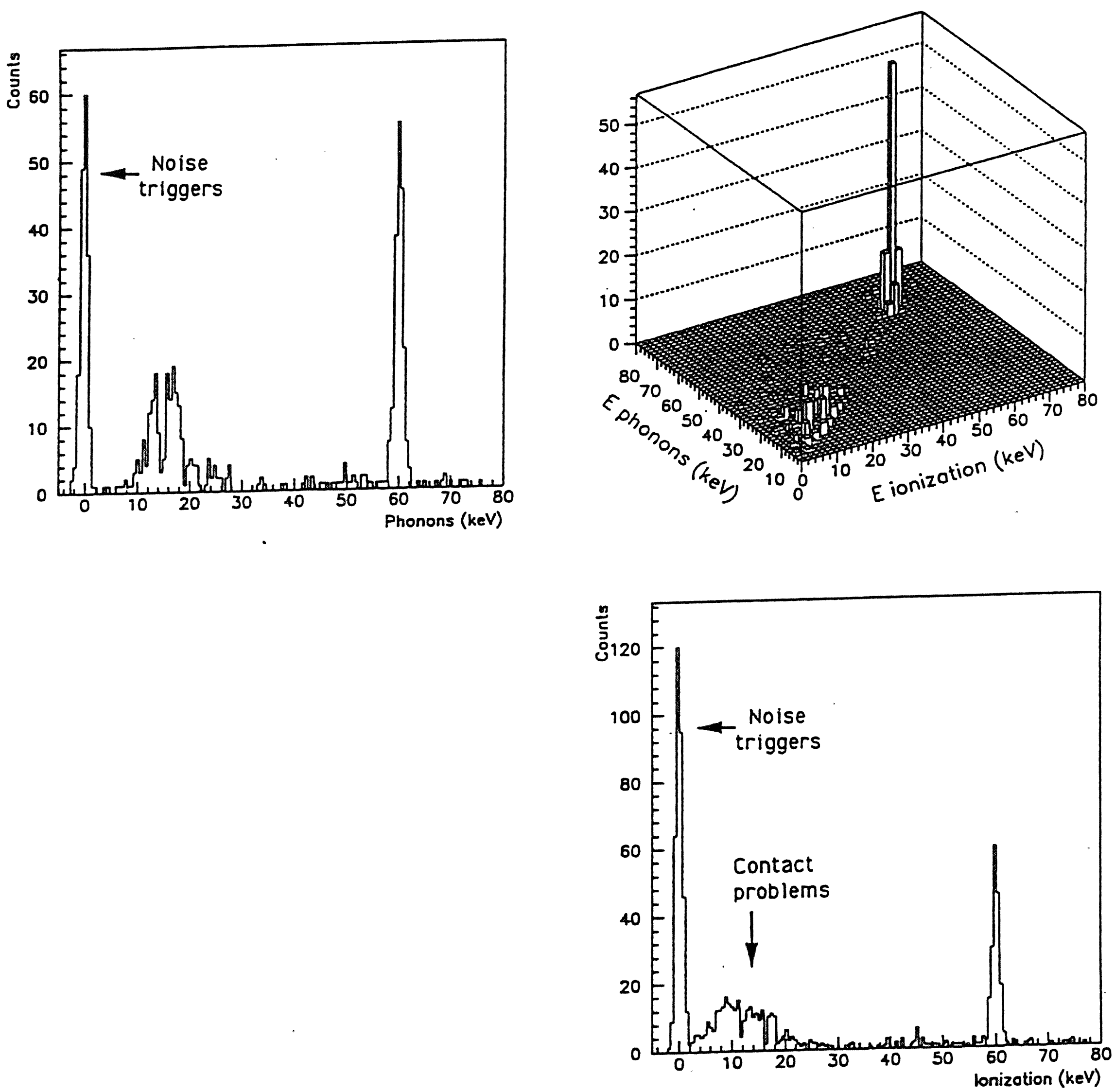

Figure 6.2 Lego plot of the phonons and ionization created by photons from a ^{241}Am source in E2, and projections onto both axes.

Table 6.1 The r.m.s. resolution, σ, in eV, measured from the spectra in figure 6.2.

	60 keV	baseline
phonons	820±50	730±50
ionization	600	500

Our sensitivity is currently limited entirely by noise unrelated to the signal size. In this case it is appropriate to speak in terms of r.m.s resolution/detector mass in order to compare results obtained with different detectors. The results in figure 6.2 currently have the best resolution per detector mass of all groups working with cryogenic detectors.

6.2) Discrimination of nuclear and electronic recoils

6.2a) Measurement of neutrons and photons

We have tested the ability of the detector to discriminate electronic and nuclear recoils by exposing it first to photons alone, and then to both photons and neutrons from a ^{252}Cf source (73). This source decays by both alpha emission and spontaneous fission, producing broad spectra of neutrons and photons. The neutron energy spectrum is not known to high precision, but has a mean energy of about 2 MeV and a high energy tail to roughly 8 MeV (74). The photons are emitted at a rate that is higher than the neutron emission rate, but have a somewhat lower mean energy. Neutrons with a few MeV of energy scatter predominantly elastically on nuclei in the target, giving signals that are identical to elastic scatters of WIMPs on nuclei. There are also a number of inelastic resonances for neutrons scattering on germanium, but we did not make use of them.

The phonon and ionization scatter plot obtained for photons alone is shown in figure 6.3*a*. Here we have used the ^{241}Am source, just as in section 6.1, but with ≈150 μm of copper blocking the lower energy X-rays. The axes are once again defined in terms of electron equivalent energy, with the energy scales set by the clearly visible 60 keV photons. The ionization collection bias is +0.3 V, but the drift heat energy has *not* been subtracted from the phonon measurement. Besides the 60 keV photons there is a roughly flat spectrum of background photons. Independent tests with a NaI detector indicate these are mostly Compton-scatters of 1.45 MeV gammas from ^{40}K in the walls of the room. These events, unlike the 60 keV photons, are presumably spatially distributed more or less uniformly throughout the detector.

Next, we repeated this measurement under essentially identical conditions, but with the ^{252}Cf source placed underneath the cryostat. A lead shield 28 cm thick was used to reduce the rate of photons from the source. The charge collection bias is now -0.5 V. The results are shown in figure 6.3*b*. The neutrons are clearly distinguished as a second line at higher slope, i.e., less ionization per unit phonon energy, than the photons. Their energy spectrum roughly agrees with a very simple Monte Carlo estimate (note, by equation 2.2, that a 1 MeV neutron can deposit at most 53 keV in germanium).

The neutrons can be distinguished from the photons at all energies, even down to the trigger threshold of 2 keV equivalent energy in ionization. One other group has reported a similar measurement with a 0.25 g silicon detector (53). Their energy resolution is much worse than ours, however, and they were only able to distinguish neutrons from photons at energies above ≈50 keV.

6.2b) The "Lindhard ratio"

The amount of ionization produced by recoils of nuclei measured in figure 6.3*b* is interesting in its own right. As mentioned in chapter 2, Lindhard and his collaborators

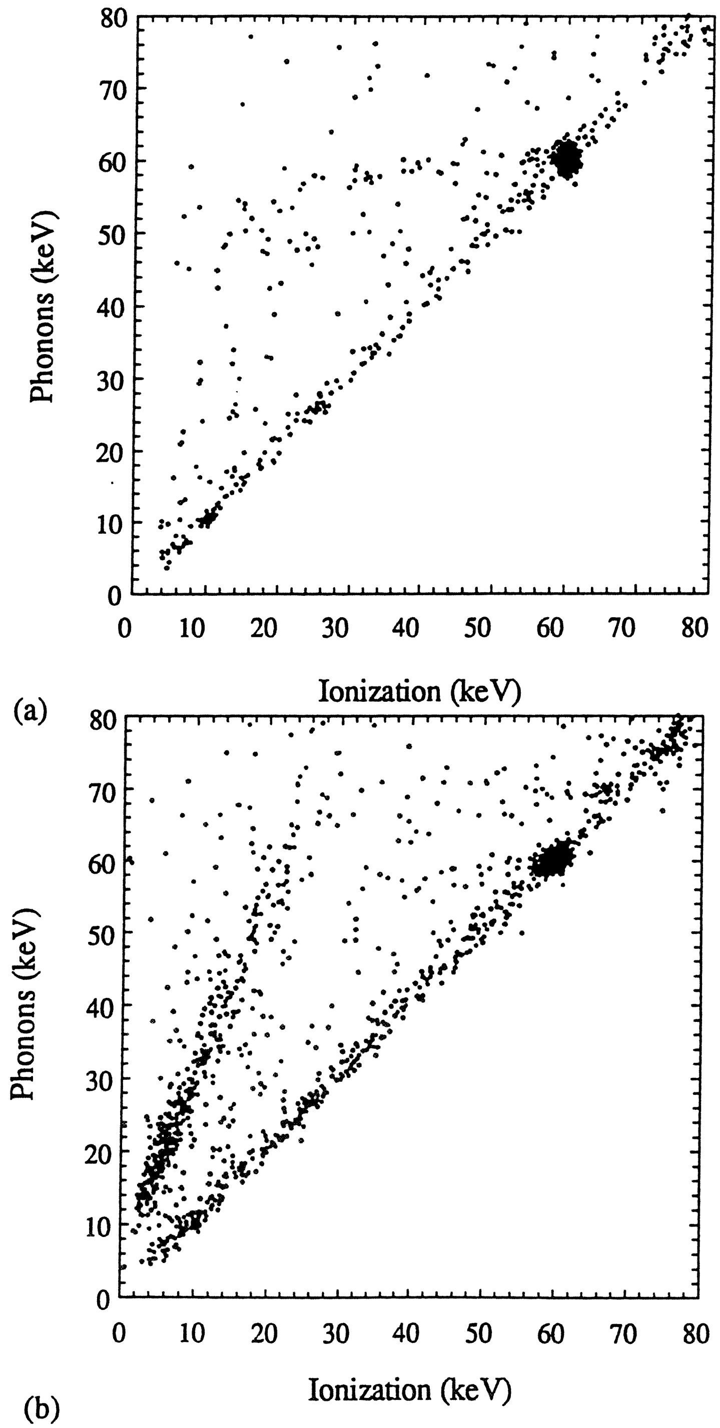

Figure 6.3 Measurement of phonons and ionization when the detector is exposed (a) to photons only and (b) to photons and neutrons. Note that both axes are defined in terms of electron equivalent energy.

calculated this quantity in the 1960's, and it was measured around that time by a number of groups using conventional silicon and germanium ionization detectors (75, 76, 77). With only the ionization measured, the recoil energy is determined kinematically by using a mono-energetic neutron beams from an accelerator, and, in some cases, by identification of nuclear excited states. These measurements are hampered by large backgrounds of photons and multiply scattered neutrons in the accelerator environment. With the recent interest in dark matter searches similar measurements have recently been made in silicon detectors by several groups (78, 79).

What is usually plotted is the ratio of amount of ionization produced by nuclear recoils to the amount produced by electronic recoils for a given recoil energy, E_r, or

$$R = \frac{N_{Q,N}(E_r)}{N_{Q,\gamma}(E_r)}. \qquad 6.1$$

This number is sometimes referred to as the Lindhard ratio, and can be readily extracted from the data in figure 6.3*b* as follows.

As we discuss in detail in chapter 5, the recoil energy, E_r, is related to the measured phonon energy, E_m, by

$$E_m = E_r + eN_Q V + \{\text{trapping terms}\}. \qquad 6.2$$

Here V_Q is the charge collection bias and N_Q is the number of charges collected as estimated from the ionization measurement. Though the axes in figure 6.3*b* are defined in terms of electron equivalent energy, the absolute calibration of both E_m and N_Q are known (see chapter 5). The trapping term is given by equation 5.11 and amounts to about a 1 % correction at -0.5 V bias. E_r can thus be found from E_m in figure 6.3.

Following the discussion in chapter 2, the number of charges created by recoils of nuclei is given by

$$N_{Q,N} = \frac{E_r}{\varepsilon_N} \qquad 6.3a$$

while the number of charges created by recoils of electrons is

$$N_{Q,e} = \frac{E_r}{\varepsilon_e}. \qquad 6.3b$$

The Lindhard ratio is hence

$$R = \frac{\varepsilon_e}{\varepsilon_N}.$$

Now the electron equivalent ionization energy, E_{eeQ}, used in figure 6.3 is related to N_Q by $E_{eeQ}=\varepsilon_e N_Q$. To obtain our measured value of R we form the ratio

$$\eta \equiv \frac{E_{eeQ}}{E_r}. \qquad 6.4$$

Using the definition of E_{eeQ} and equations 6.4a and 6.4b, $\eta=1$ for electron recoils. For nuclear recoils $\eta=\varepsilon_e/\varepsilon_N=R$. If we take the data in figure 6.3 and plot η vs E_r for each point, the neutron events will lie along the measured $\eta(E_r)=R(E_r)$. We show the result of this in figure 6.4. We then bin the recoil energy and fit the neutron data within each bin to a Gaussian. The results are listed in table 6.2 and shown in figure 6.5 along with earlier measurements and the calculation of Lindhard.

Table 6.2 Measured Lindhard ratio

E_r (keV)	R	counts
15-20	0.251 ± 0.01	49.5
20-25	0.277 ± 0.006	65.5
25-30	0.284 ± 0.006	51
30-40	0.316 ± 0.004	67
40-50	0.315 ± 0.006	40
50-60	0.33 ± 0.01	25
60-80	0.34 ± 0.01	50

The error bars shown are 1σ errors from the fit, and are quite small. Systematic errors are harder to estimate but potentially much more important. An error in the

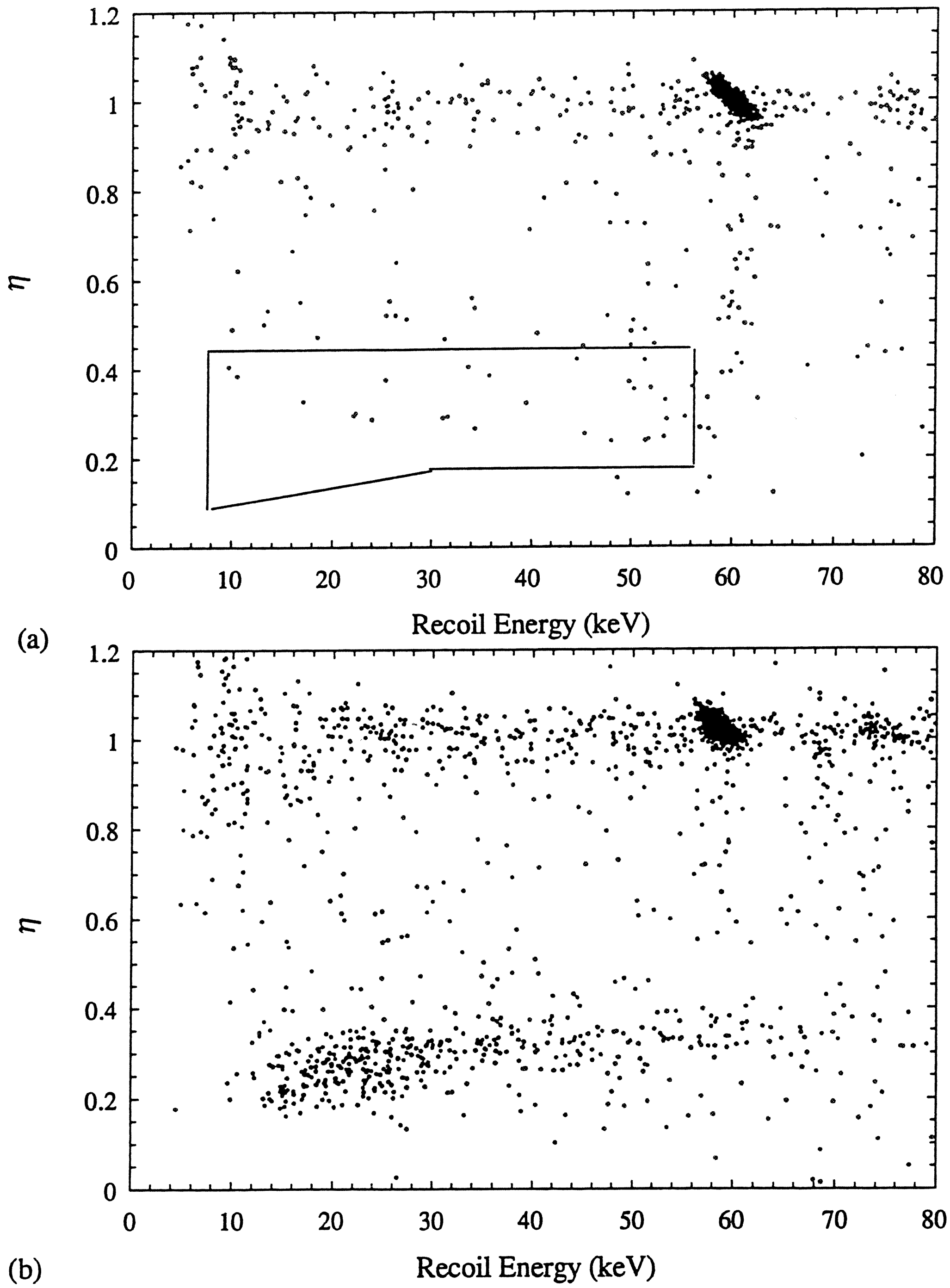

Figure 6.4 The measurements of figure 6.3, reploted in terms of $\eta = E_{eeQ}/E_r$ and E_r, as described in text. The window drawn in figure a is used to estimate the background rejection efficiency.

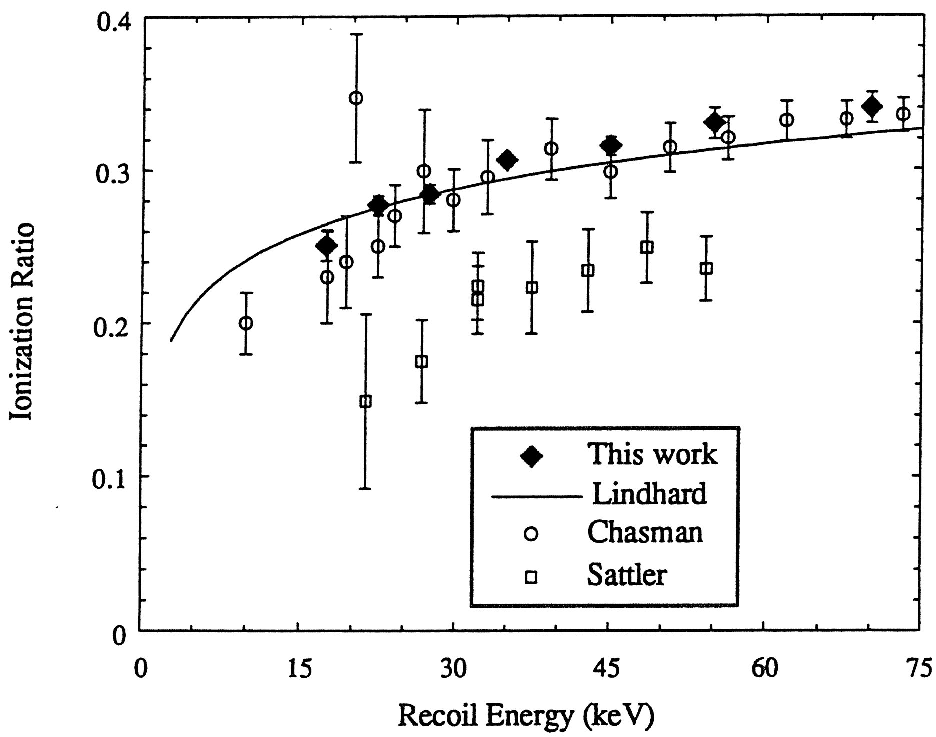

Figure 6.5 The Lindhard ratio, as measured by us and others

calibration of the phonon energy, E_m, does not cause a systematic error in the ratio, but does affect the horizontal axis in figure 6.5 directly. If our model of charge trapping presented in section 5.4 is correct, then the error in the phonon calibration is probably at most on the order of a few %, and stems primarily from the uncertainty in the charge calibration via equation 6.2. If the model is not correct the error could be greater, though the independent calibration of the phonon signal obtained by electrically pulsing the crystal (discussed in chapters 5) suggests that the calibration is off by less than 10 %.

Errors in the charge calibration affect the ratio since the drift heat term in equation 6.2 is much larger for electron recoils then nuclear recoils. With N_q mis-estimated, E_r will not be the same in the numerator and denominator of equation 6.1. At -0.5 V bias, however, it is easy to show that this causes an error in the ratio that is only 10% of the error in the charge calibration. The charge calibration is probably accurate to better than 5%, thus this effect is less than about 0.5%.

Another potential systematic effect is that our estimate of the recoil energy does not account for energy lost by recoiling nuclei when atoms are displaced from their sites in the lattice. These crystal defects are known as Frenkel pairs. To the extent that this energy loss is large, our estimate of R is distorted because E_r is not the same in the numerator and denominator of equation 6.1. The horizontal axis in figure 6.5 will also be incorrect.

The measurements with conventional detectors, on the other hand, determine the full recoil energy kinematically, and thus are not sensitive to this energy loss. The good agreement between our results and those of Chasman seems to indicate that this loss is small. Note finally that neither measurement alone can actually measure the energy lost to defects, but that in principle a comparison of the two measurements can. A better method still is to combine the two methods by using one of our detectors in a neutron beam. Such an effort is currently being carried out by collaborators at Saclay, France.

6.2c) Measured discrimination ability and limitations

The neutrons fall within a defined region of the η-E_r space of figure 6.4*b*. The window drawn in figure 6.4*a* corresponds to the region in figure 6.4*b* in which most of the neutrons lie. Note that although nearly all the events in figure 6.4*a* are from photons or betas, a large number do lie in the neutron window. A measure of the background rejection power of our detector is the ratio, ε_b, of photon events in the neutron window to the total number of photon events. As can be seen in figure 6.4*a*, some of the events in the neutron window seem to be related to the 60 keV photons, while the others do not. In table 6.3 we show ε_b separately for 55 keV$<E_r<$65 keV and for $E_r<$55 keV. The rejection is even better above 65 keV, but this energy range, by equation 2.2, is interesting only for very heavy WIMPs.

Table 6.3 Background rejection efficiency, ε_b, estimated from figure 6.4*a*

E_r	ε_b
$55<E_r<65$ keV	0.008
$E_r<55$ keV	0.15

A priori there are a number of possible explanations for the photon events in the neutron window. One is that for these events, somehow, an excess number of phonons are created. Given that we believe we recover the entire recoil energy in events as phonons, this seems fairly unlikely. Another possibility is that some sort of timing problem causes us to incorrectly identify the simultaneous signals. In fact we have worked fairly hard to prevent this from occurring, as discussed in section 3.7, and from a careful examination of individual events do not believe this to be the case. More likely, charge collection is simply not complete for these events. As we discussed in chapter 5, there are a number of mechanisms that could be responsible for this.

Accepting this hypothesis, the tail of low η for 60 keV photons in figure 6.4*a* is then presumably caused by the "dead layer" just underneath the implanted contact. We know this dead layer exists because of the poor collection for 14 and 18 keV X-rays in figure 6.2. This dead layer is related to the transition region between the implanted contact and the high-purity bulk material. In chapter 5 we estimate that this region, if the crystal is in an equilibrium state, should be only about 13 μm deep. About 1.5 % of the 60 keV photons, with their 0.86 mm attenuation length, stop in 13 μm. In fact 5 % of the 60 keV photons lie in the region of η<0.8 in figure 6.4*a*. The transition region may be wider than the estimate, or perhaps the collection is affected by a build up of space charge beyond the calculated transition region.

It is important to realize that the danger of a surface dead region is not only overall loss of fiducial volume. At 10 micron thick layer in an E2 size detector represents only 2 parts in 10^3 of the volume. A bigger issue is that all low energy photons from external sources will interact in this layer. The extent to which this is a problem will depend on the nature of the radioactive background in the final experiment.

There may be ways to solve this problem. As discussed in chapter 5, preliminary results show that an n^+-p contact structure provides good charge collection even for very low energy photons that penetrate a very short distance into the crystal. It remains to be seen, however, if there are obstacles to using such a structure on at least one side of a detector. It may also be possible to make the transition region between the implant and the bulk very thin by intentionally doping the transition region. In an n^+-p structure, for instance, the number of p-dopants just under the contact could be increased. By equation 5.11 this reduces the width of the transition region.

The other population of events with poor charge collection appear to come from the Compton-scattered photons that interact throughout the detector. These events do not go away if the detector is grounded and exposed to a hot radioactive source for a very long time, as described in chapter 5, and are present even at a bias of -0.8 V.

Our current hypothesis is that these events occur at the periphery of the detector (i.e., at the outer radius.) It is known that charges on untreated surfaces can create local electric fields that severely degrade ionization collection (80). When building E2, we took no special precautions to treat this surface. Further, between the time of its fabrication and when these measurements were taken, the detector had been exposed to air, off and on, for well over a year. If this is indeed the explanation then it is reasonable to assume that charge collection problems will occur to a depth comparable to the thickness. The number of background (non-60 keV) events in figure 6.4*a* for which charge collection is poor is ≈30% of the total, while the outer 30 % of the volume of the detector lies in the outer 4 mm. We are currently performing tests of this hypothesis with the 60 keV and/or other sources in various locations. We are also testing guard rings and field shaping structures to try to minimize this effect if our explanation proves correct.

6.3 Projected performance in a dark matter experiment

In the final experiment we will presumably construct a plot much like figure 6.4*b* and a WIMP exclusion plot like figure 2.3 will be obtained by simultaneous fitting the measured events to the sum of the expected signal from WIMPs and the background. The spectrum of background photons and charged particles in the neutron window will be well characterized.

Even without performing such a careful analysis, however, we can roughly estimate the improvement to the exclusion plot that we can expect with our detector. Typical WIMP energy deposition spectra are shown in figure 2.1. The rate depends on the interaction cross-section between WIMPs and the target nuclei, and is highly model dependent. The shape is roughly exponential, and, for a given target nucleus, depends only on the mass of the WIMP. If the data is plotted in terms of η versus E_r, the WIMP spectrum will be similar to the neutrons in figure 6.4*b*. We can construct the normalized distribution of WIMPs on this plot, $n(E_r,\eta,m_\delta)$, from the measured Lindhard ratio $R(E_r)$ and the measured responses of both the phonon and ionization measurements.

For an exponential energy deposition spectrum, we can take the region in E_r in which the WIMPs lie to extend to twice the average energy, or $2\langle E_r\rangle$. If the total WIMP interaction rate is Γ_s, then the measured rate is $\varepsilon_s\Gamma_s$, where

$$\varepsilon_s = \int_{E_{th}}^{2\langle E_r\rangle} dE_r \int n(E_r,\eta,m_\delta)d\eta . \qquad 6.5$$

E_{th} is the recoil energy threshold of the detector, and the integral over η will be restricted to a window similar to the one in figure 6.4*a*. Note that ε_s depends on m_δ, E_{th}. The number of events measured after a counting time t is just

$$N_s=\varepsilon_s\Gamma_s t. \qquad 6.6$$

Suppose now there are background electron recoil events (photons or betas) in the WIMP window. Let the total background rate be Γ_b, and let the rejection efficiency (as estimated in section 6.2c) be ε_b. Note that the value of ε_b will vary with WIMP mass because the window in E_r depends on the WIMP mass. We expect to have $\varepsilon_b\Gamma_b t$ background events in the WIMP window, but by postulate cannot distinguish them from WIMPs on an event by event basis. Since ε_b is small, most of the background events lie outside the window and the total number of background events, $\Gamma_b t$, is large and well estimated. We can then subtract $\varepsilon_b\Gamma_b t$. events from WIMP window. However since this number is small, it will have 1σ fluctuations of $\sqrt{\varepsilon_b\Gamma_b t}$. If we require that the signal exceed this fluctuation by a factor n_σ, then we will only be sensitive to WIMPs whose rate satisfies

$$\Gamma_s \geq \frac{n_\sigma}{\varepsilon_s}\sqrt{\frac{\varepsilon_b\Gamma_b}{t}} . \qquad 6.7$$

The sensitivity of the experiment thus increases as the square root of the counting time.

If, on the other hand, the number of photons in the nuclear recoil window (as seen in figure 6.4*a*) can be eliminated by improvements to the detector, then we will be sensitive to all the events given by equation 6.6. In this case the sensitivity of the experiment increases linearly with time. Note that even if we do improve the detector to eliminate most of the photon background, at the lowest energies the neutron and photon regions will always merge as the recoil energy becomes comparable to the resolution in both measurements. At best, then, we can expect that at low energies the sensitivity will increase with the square root of counting time, while at higher energies it increases linearly with time.

If the background is dominated by neutrons, the situation is much more grim, since the WIMP rate we can measure will be directly limited by the neutron rate. Indeed, if we see any signal at all, our first task will be to prove that it is *not* neutrons. Possible strategies for doing this are well beyond the scope of this thesis. However, two general methods may be useful. We can add neutron moderator, or change the amount of moderator present, in order to test if a given component of the spectrum is from neutrons. We can also use both silicon and germanium detectors. With two different target masses and enough events, the mass and velocities of the signal particles can in principle be determined.

To close, in figure 6.6 we show calculations by Kim Greist (81) of expected WIMP event rates for a variety of SUSY models. The calculations include constraints from cosmology and particle physics experiment. The measured rate has been taken equal to the total rate for simplicity (i.e., we integrate equation 6.5 over all η with E_{th}=0, so that ε_s=1), and the target crystal is taken to be isotropically pure ^{73}Ge, which enhances the rate for spin-dependent interactions. We have 800 g of this material, and plan to construct detectors out of it.

Also included in figure 6.6 is the current exclusion limit from figure 2.3, and projected exclusion curves calculated by a simultaneous fit of both the WIMP spectrum and the background, as described at the beginning of this section. We have assumed that the detectors can be operated in a state-of-the-art low background environment, so that the background spectrum is ≈2 event/kg/keV/day, similar to figure 2.2. The counting time is taken to be 100 kg·days (e.g., 10 E2 type detectors for 160 days), and the rejection efficiencies indicated are equal to $1/\varepsilon_b$.

We can roughly understand these curves from equation 6.7. For a 50 GeV WIMP with $<E_r>=20$ keV, the background expected over $0<E_r<40$ keV is ε_bx(40 keV)x(2 events/kg/day/keV)x(100 kg·days)=ε_bx8000 events. For 99 % rejection $\varepsilon_b=0.01$, and with $n_\sigma=1.64$ we are sensitive to 9 events by equation 6.7, or a rate of 0.15 events/kg/day. This is roughly what we see in the figure. For $\varepsilon_b=0.001$ the rate is $\approx 10^{1/2}$ times lower. I conclude this thesis by noting that we should be able to see WIMPs in a number of SUSY models!

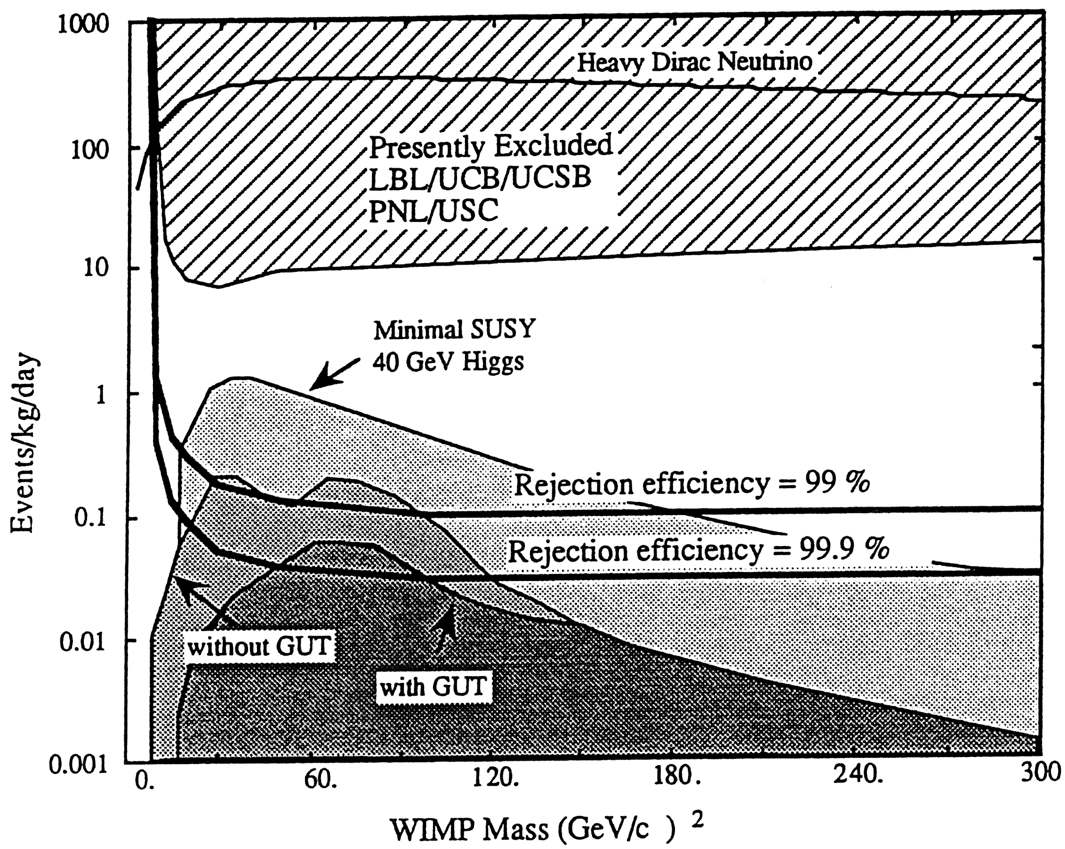

Figure 6.6 WIMP exclusion plot showing current limits and expected rates under three different SUSY scenarios. Also shown are results anticipated with detectors made of ^{73}Ge counting for 100 kg·days, and with the rejection efficinecies indicated.

Appendix A: Refrigerator running procedure

The running procedure for the dilution refrigerator which I wrote is presented verbatim in this appendix. I include it to give some sense of what is involved in working at 20 mK. Note that this document in and of itself cannot possibly be used to *learn* how to run the refrigerator. Such a manual would be quite long. This is instead intended to be more like a checklist for people who already know how to operate the refrigerator, and hence is admittedly not particularly comprehensible to the non-specialist.

REFRIGERATOR RUNNING PROCEDURE

Before you start checklist:

- LHe
- turbo pump
- Adequate thermometers

At room temperature

- check experimental wiring, thermometers
- install shields, vacuum can
- start turbo pump, turn on leak detector
- close needle valve, pump out pot
- do throughput test, record time to 1mm on still. (~5min)
- leak check VC after ≥ 20 minutes of pumping:
    - Indium O-ring, pipes, electronics box
    - pot, by filling to 2-3 p.s.i. with He
    - dilution unit

- When throughput test is finished, close keg to back of pump, equalize still and condensor pressures to do more sensitive leak check. Return mix to keg.

- stop check, put at least 500 μm H_2 in can

- put 20 liters LN in dewar, raise slowly. Leave large value on top of dewar open.

- fridge should reach 77K (as measured by thermometers) in ~3hrs.

At 77 K

- start pumping VC, start leak detector.

- bring pot to 2-3 p.s.i. He, blow LN out of dewar with N2 (~30 minutes).

- After LN quits coming out of dewar, pump dewar to ≤ ~5mm with pot pump, having closed pot line to pot at top of fridge, (and making sure the pot pump is open to air on its exhaust). Begin leak checking, then fill dewar to 1 atm with He.

- do throughput test *through a cold trap* (~45sec), then leak check as at RT.

- Pump pot to ≤1mm (with He gas in bath), then fill to atm while leak checking.

- Valve off VC, fill to 500-800 μm with H2.

- Shut down leak detector

Initial Transfer:

- Start with normal (fast) transfer (~ 3 p.s.i. in storage dewar) until VC pressure is 200-300μm.

- Below ~200μm, gently pressurize storage dewar via gas panel, so that temp as read by resistors (Still and Cold Plate are best) slowly drops and gas is steadily returned to chemistry (~4 turns/min). This is "slow transfer." Monitor pressure in VC after putting He in storage dewar, don't let H_2 freeze out. Continue this at least until resistors reach their nominal 14 K values - the colder you get during slow transfer, the quicker condensing goes. Then transfer normally until dewar is full.

- Slow transfer advice: Don't be in too much of hurry, a successful transfer lasts 1.5 - 2 hours. You don't need to watch the temp constantly if you are conservative enough that you do not freeze out - freezing out is almost never worth any time saved by transferring quickly. I try to do something else while I transfer, otherwise I become impatient, fiddle too much and freeze out. *However, do not become engrossed in something else and neglect the transfer*, ten minutes of mismanagement can turn the transfer into an ordeal.

<u>Condensing and running:</u>

- First fill the pot as follows. When the dewar is ≥ ~20% full, pump on pot, then open a needle valve (or both) 4 or 5 *full* turns. The pot pressure should go to ~ -28 " Hg quickly, then stabilize. After a few minutes the pressure should begin to rise fairly quickly. Close the valves, the pot is now full. The pot should cool quickly to ~ 1 K. (Caution: if there is not enough LHe in the dewar to fill the pot, you will get confusing pressure behavior, and the pot will not cool to 1 K.)
- Do a throughput test through a cold trap, then begin circulating, but with Keg 1 open to the back of the pump.
- When you like, close the keg to the back of the pump, and open it partially to the still line. *Do not let the condensor line pressure get above ~ -6 " Hg*. Continue in this way until you can fully open the keg to the still line (~ 20 min.) This is the final running mode.
- Apply 1-3 mW to the still. While warm, more is better; when cold 1 mW or less typically needed. When cold, one should shoot for 60-100 μm pressure in the still, *regardless* of power.

- The fridge should reach 20 mK in about 2 hours.

Warm up:

Remove the mix: Close the last valve before the condensor, and begin pumping the mix into the keg through a cold trap. You can stop pumping on the pot, and vent it to chemistry return, however be certain that the return system is not vented to air somewhere. Begin to gingerly add heat to the still, then the mixing chamber. (Use only a couple of volts for the first few minutes: $2V \approx 10mW$). You will first get the 3He out, then the still pressure may well go to a very low value, say 10-20 μm, at which point I often get a bit more earnest with the heat, say 7V. Anytime you increase the heat, watch the still pressure for a minute or so afterwards - there are long time constants in the system.

In about 20 minutes the mix will all be out, change the pumping mode to evacuate the entire panel and the condensor. Check that the keg has as much mix as you started with. Keep pumping for a few more hours, or overnight.

Dropping the dewar and beyond: Not much to say here, just check the following: The pot is empty, either because it is well above 4K, or because you've pumped it dry. It is best to look at the V.C. when dropping the dewar, so change the plumbing if you just pumped the dewar. Make sure you don't have the plumbing attached to the dewar in any case. Finally, attach the counterweights *before* removing the bolts.

You can drop the dewar as soon as the mix is out and the pot is dry. However, do not open the vacuum can until all parts of the fridge have come to room temperature. Remove the In O-ring as soon as you drop the V.C., if you let it sit for a week it tends to stick for some reason and is a pain.

REFRIGERATOR SAFETY COMMENTS

Mixture circulation system

- Never turn on circulation pump without thinking about how much gas is in the still line, and where it will go when you turn on the pump.

-If you get a plug in condensor, pump out mix, drop dewar slowly while pumping plug from both still and condensor. If there is a lot of material in the plug, be prepared to pump it to air instead of back to circulation system.

Vacuum can (V.C.) system

- Never open valve(s) to vacuum can while at LHe.
- Never pump on VC with turbo pump unattended unless you remove and blank off turbo pump vent valve.
- Only He and H_2 gas are allowed in V.C. below LN2 temp. Remember that H_2 is flammable.

1K Pot system

- Avoid pumping on pot when dewar does not have He in it, otherwise you can plug the needle valves.

Dewar handling (transferring):

- Always make sure dewar has a vent path - either to air or chemistry return - before putting LN or LHe in it. Never let dewar pressure rise above 3-4 p.s.i..
- Try not to let storage dewar get above 6 p.s.i..
- Only put He in a dewar once it has LHe.

Weight system for raising/lowering dewar:

- Be careful not to damage ropes with snags on sharp objects.
- Think twice before either unbolting dewar from frame, or disconnecting weights from dewar. Make sure you won't drop the dewar.
- Never use an open flame or the heat gun anywhere near the support ropes.

Pre-run checklist

- LHe
- Use of turbo pump
- Correct thermometers
- Parasitic tests

Post-run checklist

- Note final pressure in keg 1. Clean cold trap, unless otherwise agreed upon, in which case fill LN dewar for trap. Turn off water.
- Leave storage dewar in reasonable state: if it will go dry before others can reasonably fill it, then you should fill it.
- Put away all cables, boxes, etc.
- Drop dewar, open can, remove In o-ring, remove sample holder can (keep track of your own washers/spacers for SHC)
- Clean up all papers, graphs, etc.
- Note, and arrange to fix any broken equipment

Appendix B: Thermal conductance at low temperatures

This appendix containes a simplified discussion of thermal conductance at very low temperatures (at or below a few kelvin). Although everything here can be found elsewhere, I decided to write this section because a few simple arguments essentially explain all the important ideas involved in the mechanical aspects of the experiment such as wiring and mounting. These same ideas also underlie the much of the physics of the phonon measurement.

B.1 Bulk conductivity

The power, P, that flows through an area A in an object with a thermal gradient in one direction (such as in a wire) is related to the thermal gradient, dT/dX, by

$$P = \kappa A \frac{dT}{dX} \qquad \text{B.1}$$

where κ is the thermal conductivity. The thermal conductivity contains all the information about the material, and in general is temperature dependent.

Microscopically, the conductivity is thought of as heat being transported by thermal "carriers". In metals both electrons and phonons serve as carriers; in insulators only phonons can be carriers since the electrons cannot move freely. It turns out that the transport process is fairly well described by the following simplistic argument (69). Consider a carrier moving randomly with an average velocity v, that at one instant happens to be moving in the direction of the thermal gradient. Between successive scattering events it transports an energy $\delta E = c\,\delta T$ where c is the carrier heat capacity and δT is the temperature change in the travel distance. The distance traveled is the average scattering length, λ. Roughly 1/6 of the carriers move in the direction of the gradient at any time, thus the total flux in this direction is $1/6nv$, where n is the carrier density and v

the carrier velocity. An equal number travel in the opposite direction, transporting an energy $E=-c\delta T$ from the cold region to the hot. The total heat transported along the gradient through an area A per unit time, then, is $dE/dt=P=1/3nvcA\delta T$. Comparing this to the definition of thermal conductivity in equation B.1, and with $dT/dX=\delta T/\lambda$, the conductivity is

$$\kappa = \tfrac{1}{3} v \lambda C \qquad \text{B.2}$$

The product nc has been written as C, the bulk heat capacity of the thermal carriers. The behavior of κ with temperature is in general complicated , since v, λ, and C can depend on temperature. At very low temperatures, however, the situation is a bit simpler.

The velocity of phonons is a function of the lattice stiffness. Although the stiffness of a material can change when first cooled below room temperature, at low temperatures it is essentially temperature independent, and hence so is v. The heat capacity is the product of the specific heat, $dE/dT \alpha d(kT)/dT \approx k$, and the number density of phonons, which is proportion to T^3 at low temperatures. Thus $C \alpha T^3$. (This result that $n \alpha T^3$ is the same as for photons in a blackbody. In both cases the energy density u is the energy, kT, times the density of states n, so $u \alpha T^4$.) The scattering length at high temperatures is dominated by phonon-phonon scattering, but at low temperatures this process is negligible since the number of phonons drops off like T^3. Scattering occurs on impurities and defects in a material, or the boundaries of the material. Some of these scattering processes depend on the phonon wavelength and thus are temperature dependent, some do not. If λ were independent of T then $\kappa \alpha T^3$. In practice for many insulators κ is proportional to T to a power between 1 and 3.

Electrons also scatter mainly on phonons at high temperatures and on impurities, defects and boundaries at low temperatures. Because only electrons with the Fermi velocity are important, the scattering length λ and the velocity v in equation B.2 are independent of temperature. The heat capacity of the electron system is proportional to number of electrons near the Fermi energy that can change their energy level, which is proportional to T. Thus for electrons $\kappa \alpha T$.

Since at low enough temperatures T is much larger than T^3, electrons dominate the thermal conductivity of metals, and metals have a much larger conductivity than insulators. The electrons in a superconductor are bound in Cooper pairs and cannot change their energy, thus they cannot serve to transport heat. Below the transition temperature some electrons are still in the normal state, but their number drops off exponentially. Well below the transition, then, only phonons can conduct heat, and the superconductor behaves like an insulator in terms of thermal conductivity.

Unfortunately not much data exists for thermal conductivity of various material at very low temperatures. For many years, figure C.1, from the well-known book by Lounasmaa (82), was one of the few large data sets. Additional values can be found in the new book by Pobell (83).

B.2 Wiedemann-Franz Law

The thermal conductivity of a metal is related to its electrical conductivity since electrons act as carriers of heat as well as charge. The electrical conductivity, σ, is defined via $j=\sigma E$ where E is the applied electric field and j is the current density. This density is env_d, where e is the electrical charge and v_d is the drift velocity due to the electric field. The drift velocity is given by the acceleration times the average scattering time τ, or $v_d=(eE/m)\tau$ where E is the electric field and m the electron mass. The scattering time is the scattering length v divided by the Fermi velocity, so that

$$\sigma = \frac{e^2 n\lambda}{mv} \tag{B.3}$$

The ratio of thermal to electrical conductance is then, from B.2 and B.3

$$\frac{\kappa}{\sigma} = \frac{\pi^2}{3}\left(\frac{k}{e}\right)^2 T \tag{B.4}$$

where the scattering length has scaled out, and the Fermi velocity is written in terms of fundamental quantities. This result is known as the Wiedemann-Franz law. The T term comes from the thermal conductivity, and the coefficient of T, known as the Lorentz number, has a value of 24.5 nΩ/W/K^2.

The Wiedemann-Franz law is not always valid. In poor conductors the lattice can contribute appreciably to the thermal conductivity. Also, at temperatures below the Debye temperature of the material, electrons undergo small angle scattering which has little effect on the electric current, but which impedes the thermal current. Thus the actual thermal conductivity can be substantially less than given by equation B.4. At temperatures near the Debye temperature of a material (which is often about room temperature), however, energetic phonons cause large angle scattering and Wiedemann-Franz is valid. It is also usually accurate at our very low temperatures, since in this case inelastic scattering on impurities dominates both the thermal and electrical current flow. However see the warning in Pobell (83)about its use at low temperatures.

B.3 Thermal conduction at a boundary between materials

Another important phenomenon in low temperature experimental work is heat flow across the boundary between two materials (84). The conduction due to phonons results from both objects acting essentially as blackbody phonon emitters. The power that flows through an area A from an object with a temperature T_h to an object at T_c with $T_h > T_c$ is

$$P = aA(T_h^4 - T_c^4). \qquad \text{B.5}$$

The constant a is the product of the Stephan-Boltzmann constant and a term describing phonon emission from the lattice of each material. Note that for a small temperature difference, $T_h = T_c + \delta T$, this becomes $P = 4aAT_c^3\delta T$, and the situation can be described by a thermal conductance that varies as T^3, just like phonon heat flow within a material.

Numerous measurements by our group have established that between germanium and glue the constant a is approximately 4×10^{-5} W/K^4/mm^2.

Finally, If there is an electrical connection between the materials, an approximate estimate of the thermal conduction from electrons can be made using the Wiedemann-Franz law, equation B.4.

Appendix C: Wiring and heat sinks

C.1 Wiring heat loads

The basic equation that governs one dimensional heat flow, as discussed in appendix B, is

$$P = \kappa A \frac{dT}{dX} \qquad \text{C.1}$$

where P is the power that flows through an area A when driven by a thermal gradient dT/dX. The conductivity, κ, depends on temperature and also position since the temperature depends on position. If a piece of material has only a small temperature difference over a distance L, then equation C.1 can be written as $P=G\Delta T$. G, the thermal conductance is given by

$$G = \kappa \frac{A}{L},$$

and κ is evaluated at the average temperature. When the temperature difference is large, we use the fact that the power flow is constant along the wire. Rearranging equation C.1 and integrating,

$$P\int_0^L dX = A\int_{T_c}^{T_h} \kappa dT,$$

so that

$$P = \frac{A}{L}\int_{T_c}^{T_h} \kappa dT \qquad \text{C.2}$$

where L is the length of the wire, and the hot and cold ends are at temperatures T_h and T_c, respectively. This equation gives P directly, but can also be used, with P known, to find the temperature profile $L(T)$.

For normal (non-superconducting) metals at temperatures below about 10 K, $k=gT$, where the value of g can be extracted from a plot such as the one in figure C.1. In this case

$$P = g\frac{A}{L}\frac{1}{2}\left(T_h^2 - T_c^2\right).$$

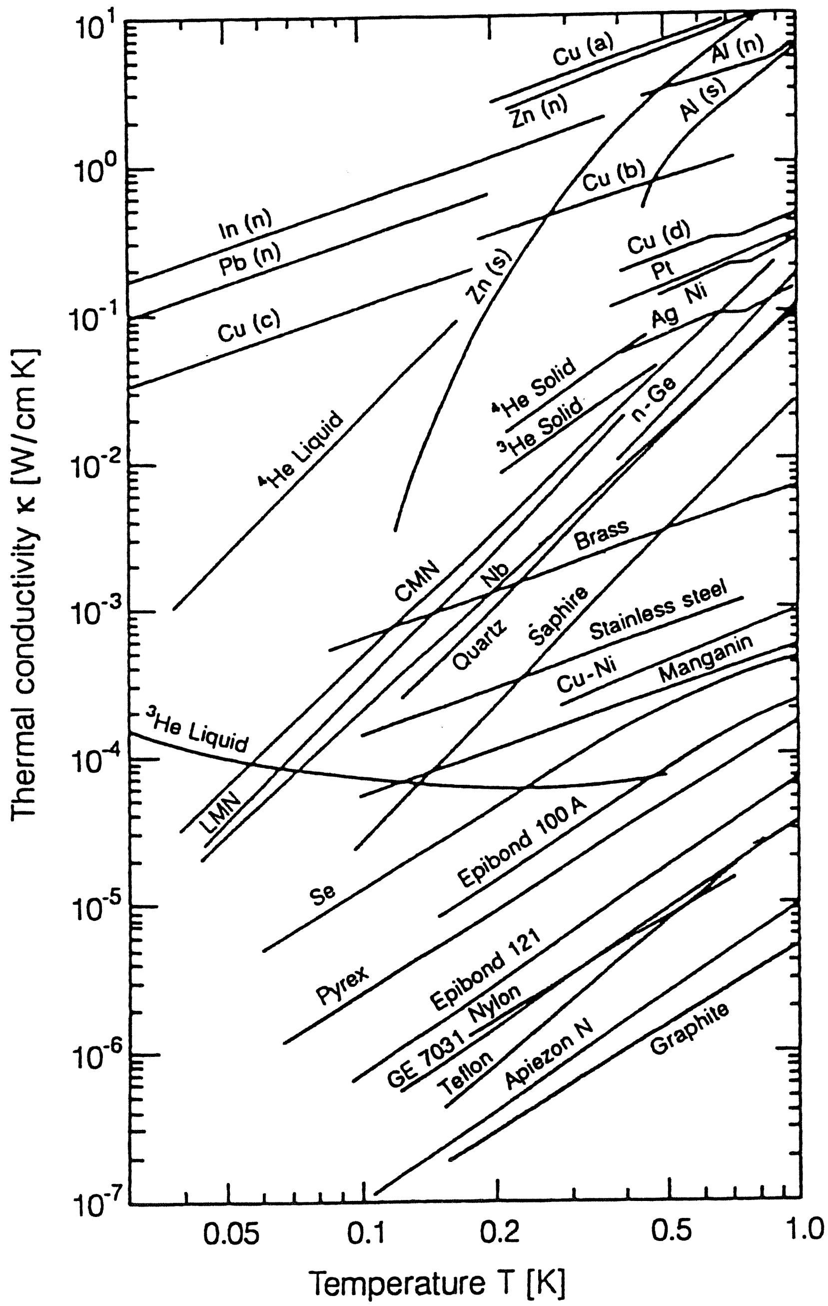

Figure C.1 Thermal conductivity of various materials below 1 K from (82).

Unless the two temperatures are very close the lower temperature term is usually negligible, and dropping it introduces errors that are much smaller than the typical uncertainties in g. Finally,

$$P = \tfrac{1}{2} g \frac{A}{L} T_h^2 .$$

In terms of practical units for a wire of diameter $\emptyset$ (where 1 mil=0.001 inches), this is

$$P \approx 3\ \mathrm{nW} \times \left(\frac{g}{0.5\ \mathrm{W/K/m^2}}\right)\left(\frac{\emptyset}{5\ \mathrm{mil}}\right)^2\left(\frac{10\ \mathrm{cm}}{L}\right)\left(\frac{T_h}{\mathrm{K}}\right)^2 .$$

Alternatively, the Wiedemann-Franz law relates gA/L to the electrical resistance R at low temperatures, so that

$$P \approx \tfrac{1}{2}\ \mathrm{nW} \times \left(\frac{25\ \Omega}{R}\right)\left(\frac{T_h}{\mathrm{K}}\right)^2 .$$

The power flow at temperatures above about 10 K can in principle be found from equation C.2 if $\kappa(T)$ is known. For many common materials the integral of $\kappa(T)$ between room temperature to 77 K and between 77 K and 4 K is tabulated. A starting reference for these values is White (85).

Typically in a cryostat there are a number of intermediate temperature stages of some sort between room temperature and base temperature. For example many liquid helium (4 K) systems have a liquid nitrogen (77 K) stage, and in many dilution refrigerators there are stages at the temperature of pumped helium (≈1.2 K), at 0.6 K, and at 50-100 mK, in addition to the coldest stage. The amount of power that each of these stages can accept without warming significantly increases dramatically with the temperature of the stage. Table C.1 lists the heat loads tolerable on each temperature stage of the model 75 dilution refrigerator used for this thesis. Because the power carried by a wire basically depends only on the temperature of the hot end, this means that it is advantageous (in terms of heat load at least) to bring the wire to an intermediate temperature stage between desired end points. The intermediate stage can always more easily handle the power dumped on it than can the cold stage, and the resulting power on the cold stage is always less than if the intermediate stage were bypassed. A final comment is that in super-insulated dewars that have no liquid nitrogen, wires running from room temperature to 4 K are often designed to be cooled by the vapor of boil-off gas from the liquid helium bath. In this case the vapor effectively acts as an intermediate temperature stage. For low resistance current-carrying wires used for magnets this technique can be essential.

Table C.1 Approximate powers tolerable at various temperatures in the dilution refrigerator without sacrificing refrigerator performance.

T (K)	Tolerable Power (W)
4	0.03=1 liter of liquid He/day
1.2	order of 0.01
0.6	0.5×10^{-3}
0.1	5×10^{-6}
0.02	0.5×10^{-6}

C.2 Heat sinking "theory"

Installing the wiring on a cryostat is typically much more of an art than a science. While a number of ideas for wiring heat sinks can be found the standard low temperature references mentioned above, and especially in Richardson and Smith (86), there is not always a careful discussion of the performance of heat sinks. This may be because of large uncertainties in the bulk thermal conductivities of materials and in the thermal properties of boundaries between materials. Heat sink design often seems to consist merely of copying someone else's working system. This is in fact how I wired our apparatus, stealing ideas from the groups of John Clarke and Dick Packard in our department.

However we do not have this luxury in the full scale experiment we are now beginning to build, since we will have a great many wires and will need to understand in more detail where power is going. For this reason I decided to write down a few ideas about heat sinking that I have had over the last few years. What follows is not a well developed theory, and may have serious deficiencies. Hopefully, though, it can be of some use.

A wire is heat sunk by mechanically connecting it to a heat reservoir (usually made of copper) with a thin electrical insulator in between. This is shown in figure C.2*a* where power flowing in the wire from some distant point at high temperature enters the heat sink at point A. The goal is to have the wire at the same temperature, T_s, as the heat sink when it exits at point B. The temperature profile of the wire can be found exactly by using the three dimensional analog of equation C.1. The conductivities of the metals and the insulator in principle vary with temperature and hence position, and the boundary resistances between the insulator and wire and between the insulator and reservoir must also been taken into account. Given the typical uncertainties in the material properties, however, an exact calculation is often not warranted.

A simpler approach is to consider a linear approximation appropriate for small temperature differences. The system is taken to consist of a thermal resistance R_w along the wire and a resistance R_s between the wire and heat sink, as shown in figure C.2*b* Both resistances are calculated assuming the material is at the heat sink temperature T_s. The resistance between point A and the reservoir has been labeled R_x, which is not in general equal to R_s because of the fact that R_s is distributed along R_w. Following the heat sink at point B is a resistance R_f, which represents the continuation of the wire and whatever else it is ultimately attached to. The end point temperature on the other side of R_f, T_e, may in general be a lower temperature than T_s.

The input point A sees a resistance to T_s that depends on the relationship between R_s and R_x. In many cases, the "wire" in the heat sink region is made of a very good

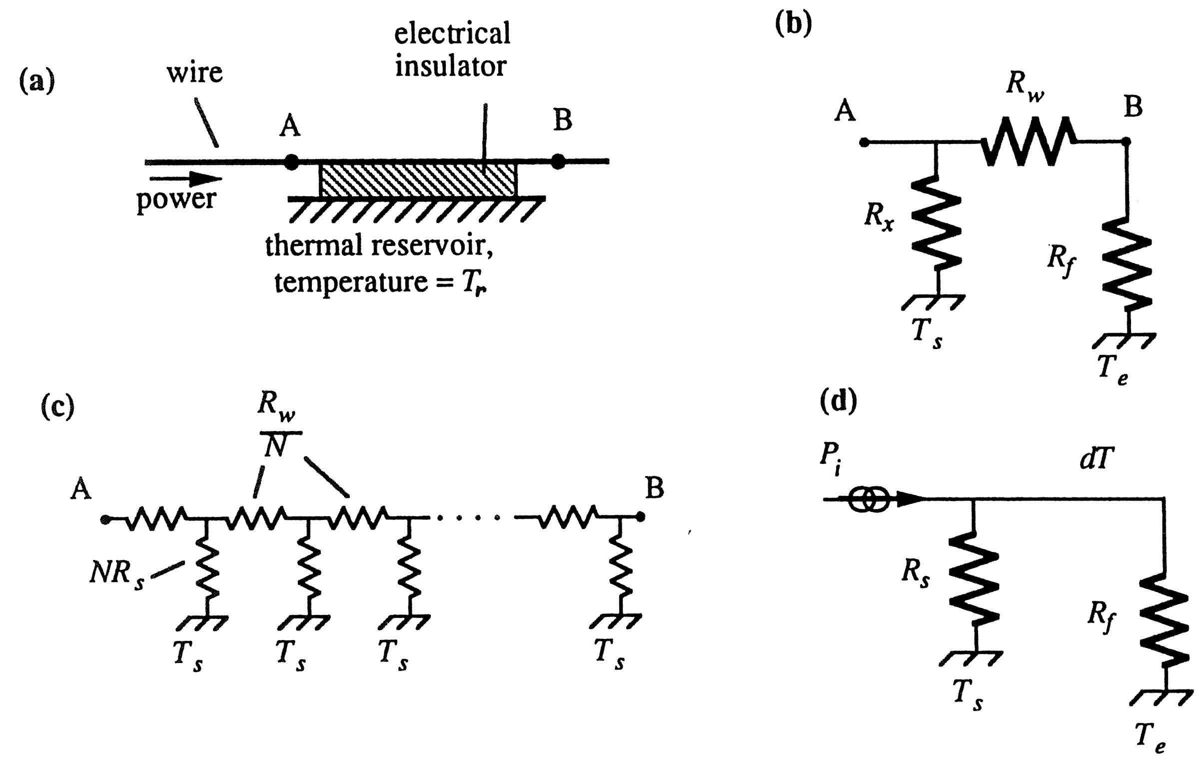

Figure C.2 A heat sink for a wire (a) and three approximate representations of it discussed in the text (b), (c), (d).

electrical and thermal conductor, such as copper metalization on circuit board. In this case R_w is very small, and R_x=R_s. The heat sinking then relies on R_f being large.

On the other hand, if R_w and R_s are comparable, the value of R_x can be found by conceptually breaking the heat sink into a large number of segments, as shown in figure C.2*c*. Each segment has a small wire resistance, R_w/N, and a large resistance to the reservoir, NR_s, where N is the number of sections. For N very large, R_x is the sum of R_w/N and the parallel resistance combination of NR_s and R_x itself. Symbolically,

$$R_x = \frac{R_w}{N} + \frac{NR_sR_x}{NR_s + R_x},$$

or

$$R_x^2 = \frac{R_w}{N}R_x + R_sR_w.$$

Letting $N \to \infty$, this becomes

$$R_x = \sqrt{R_sR_w},$$

reminiscent of the electrical impedance of a coaxial cable. If $R_s \ll R_w$, then this formulation is probably not correct.

The heat sink resistance, R_s, is the sum of the resistance of the insulator, R_i, and the thermal boundary resistances, R_b, in the system. The insulator's resistance is decreased by making the it as thin as possible. However the electrical capacitance between the wire and the thermal reservoir (which is usually at electrical ground) is thereby increased. Indeed, the electrical capacitance of the heat sink, C, and the thermal conductance of the insulator have the same geometrical dependence so that

$$\frac{G_i}{C} = \frac{\kappa}{\varepsilon},$$

where ε is the dielectric constant of the insulator, and $G_i \equiv 1/R_i$. In principle the insulating material should be selected for large κ/ε; in practice the insulator is usually a glue picked for mechanical properties and for which neither κ nor ε is well known a sub-kelvin temperatures. Finally, since R=$2R_b$+R_i, (where the 2 reflects the fact that there are two boundaries) the capacitance can be minimized by increasing the thickness of the insulator until R_i is on the order of $2R_b$.

The heat sink works when the input power at point A, P_i, is diverted to the heat sink instead of continuing along the wire. If $R_w \ll R_s$, then the circuit can be simplified as shown in figure C.2*d*. If the end point temperature, T_e, is equal to T_s (for instance, if this is the last heat sink), then the "leakage" power that continues past the heat sink along the wire is

$$P_l = P_i \frac{R_s}{R_s + R_f}. \qquad \text{C.3}$$

We must have $R_f \ll R_s$ in order for P_l to be small. In addition, the wire in the heat sink will be warmer than T_s by an amount

$$\delta T = P_i \frac{R_f R_s}{R_s + R_f}. \qquad \text{C.4}$$

If this temperature rise is not small, then the calculation of the conductances at the temperature T_s will not be valid. If $T_e < T_s$, then the situation is a bit more complicated because even in the absence of the input power, P_i, there is a power flow across R_f driven by the difference between T_s and T_e. It is easy to show, however, that in addition to this inevitable power flow there will be a leakage of any input power, P_i, again given by equation C.3, and a temperature rise given by C.4.

In the case that the conductor in the heat sink has an impedance comparable to R_s, then R_f in equation C.3 is replaced by the sum of R_f and R_w, and R_s is replaced by R_x.

C.3 Wiring on our apparatus

There are three systems of wires on our cryostat. The first is a set of unshielded manganin wires used mainly for thermometry. Because of the large capacitance these wires have between each other and to ground they are only useful at low frequencies, and hence are referred to as "DC" wires. The section between 1.2 K and room temperature was installed by the refrigerator manufacturer, we installed the wiring below this. The heat sinks are made by gluing a copper heat sink to copper traces on a printed circuit board with a piece of rolling paper in between to prevent electrical shorts. The glue used, stycast 1266 epoxy, has a very low viscosity and soaks through the paper to form a fairly solid insulating layer about as thick as the paper, or 50 μm. Connectors are soldered onto the edges of the printed circuit board, and high-resistance manganin wires run between the temperature stages. Each copper strip is 1 inch x0.05 inch, which gives a capacitance of 17 pF per wire per heat sink. Because of the large wire-to-wire capacitance, however, the total capacitance of any wire to ground has been measured to be ≈4 nF.

A full calculation of the properties of the wires below 1.2 K is given in Worksheet C.1*a*, which was created with a software package called MathCad. The power loads from the wires are quite low compared to the powers of ≈1 mW, ≈10 μW, and ≈0.5 μW that the refrigerator can tolerate at 600 mK, 100 mK, and 20 mK temperature stages, respectively. All the heat sinks also work well in terms of having low leakage power and a small temperature rise. The leakage power at 20 mK, $\approx 2 \times 10^{-13}$ W is about an order of magnitude lower than what is just noticeable in most of our experiments. It is clear, however, that heat sinking becomes increasingly difficult at the lowest temperatures. Note also that the boundary resistance dominates the heat sinking at all but the highest temperature. A more optimal design would have increased the insulator thickness to decrease the capacitance.

There is also a set of coaxial cables on the refrigerator with stainless steel outer conductors and superconducting inner conductors. The thermal properties of this system is shown in worksheet C.1*b*. The cables are heat sunk by mechanically holding them against a sheet of copper and liberally covering both the cable and copper with a silver-filled paint. This forms a very intimate electrical connection between the braids and copper sheet. The sheet of copper is actually one side of a copper-kapton-copper composite that electrically isolates the outer conductors from the refrigerator in order control the grounds in the system. The surface area of the copper-kapton boundary is ≈1 inch^2, so that the braid is very well heat sunk. The inner conductor is heat sunk through the cable dielectric. At and above 4 K the coaxial cables are no longer superconducting, but the heat sinking at 4 K is done in the same way as for the superconducting cable.

The most critical wiring involves the signal wires which run from the experiment to the gates of the FETs which serve as the input of the amplifiers. The thermal properties are calculated in worksheet C.1*c*. These wires were designed to reduce both microphonics noise and capacitance, and are discussed further in appendix D. I note here only that the heat sinks used have a thick insulator which optimizes the trade-off between capacitance and thermal conductance, as discussed above.

C.4) FET installation

The FETs are installed in a brass housing box which is thermally anchored to 4 K. The system in our refrigerator was designed and first tested by Carol Stanton, who described it in her undergraduate thesis (87), though the technique has been widely used elsewhere. I will describe it briefly here for the sake of completeness. The FET noise is minimized at a temperature of ≈140 K. This is achieved by mounting the FET atop a fiberglass post 0.5 inches tall, 0.075 inches in diameter, and with a 0.0065 inch wall thickness. Manganin (0.003 inches Ø) wires run from the drain, source and gate of the FET to connectors in the body of the box. Two more manganin wires run to a resistor attached to the FET which is used as a heater. The thermal conduction along these wires and the fiberglass post is such that, ideally, the operating power of the FET maintains the FET at 140 K with the box at 4 K.

Worksheet C.1a. (page 1)

DC wires on the 75 Fridge (All units MKS)

Temperatures: $T_1 := .02$ $T_4 := 1.2$ $T_2 := .1$ $T_5 := 4$ $T_3 := .6$ $i := 1..4$

Wire heat loads

$rwire := \frac{1}{2} \cdot .006 \cdot 25.4 \cdot 10^{-3}$ $Lwire := 0.1$ $Awire := \pi \cdot rwire^2$ $Awire = 1.82 \cdot 10^{-8}$

$gwire := 5.2 \cdot 10^{-2}$ $Pi_i := \frac{Awire}{Lwire} \cdot \frac{gwire}{2} \cdot \left[(T_{i+1})^2 - (T_i)^2 \right]$

$\kappa wire_i := gwire \cdot T_i$

Pi_i (W)	T_i
$4.55 \cdot 10^{-11}$	$2 \cdot 10^{-2}$
$1.66 \cdot 10^{-9}$	$1 \cdot 10^{-1}$
$5.12 \cdot 10^{-9}$	$6 \cdot 10^{-1}$
$6.91 \cdot 10^{-8}$	1.2

This is fine

Heat sinks:

$As := (1 \cdot 25.4 \cdot 10^{-3}) \cdot (.05 \cdot 25.4 \cdot 10^{-3})$ $d := .002 \cdot 25.4 \cdot 10^{-3}$ $As = 3.23 \cdot 10^{-5}$

$\varepsilon := 3$ $Cs := \varepsilon \cdot 9 \cdot 10^{-12} \cdot \frac{As}{d}$ $Cs = 1.71 \cdot 10^{-11}$

$\kappa glue_i := 0.049 \cdot (T_i)^{1.98}$ $a := 1.43 \cdot 10^3$

$Gglue_i := \frac{As}{d} \cdot \kappa glue_i$ $Gboundary_i := As \cdot a \cdot (T_i)^3$

$Gs_i := \left[(Gglue_i)^{-1} + 2 \cdot (Gboundary_i)^{-1} \right]^{-1}$ $Gwire_i := \frac{Awire}{Lwire} \cdot \kappa wire_i$

$Pl_i := \frac{\left[(Gwire_i)^{-1} + (Gs_i)^{-1} \right]^{-1}}{Gs_i} \cdot Pi_i$ $\delta T_i := Pi_i \cdot \frac{\left[(Gwire_i)^{-1} + (Gs_i)^{-1} \right]^{-1}}{Gs_i \cdot Gwire_i}$

__Worksheet C.1a__ (page 2)

Results: (G in W/K, P in W, T in K)

$Gglue_i$	$Gboundary_i$	Gs_i	$Gwire_i$	Pl_i	δT_i	T_i
$1.35\cdot 10^{-5}$	$3.69\cdot 10^{-7}$	$1.82\cdot 10^{-7}$	$1.9\cdot 10^{-10}$	$4.74\cdot 10^{-14}$	$2.5\cdot 10^{-4}$	$2\cdot 10^{-2}$
$3.26\cdot 10^{-4}$	$4.61\cdot 10^{-5}$	$2.15\cdot 10^{-5}$	$9.49\cdot 10^{-10}$	$7.31\cdot 10^{-14}$	$7.71\cdot 10^{-5}$	$1\cdot 10^{-1}$
$1.13\cdot 10^{-2}$	$9.96\cdot 10^{-3}$	$3.46\cdot 10^{-3}$	$5.69\cdot 10^{-9}$	$8.43\cdot 10^{-15}$	$1.48\cdot 10^{-6}$	$6\cdot 10^{-1}$
$4.46\cdot 10^{-2}$	$7.97\cdot 10^{-2}$	$2.11\cdot 10^{-2}$	$1.14\cdot 10^{-8}$	$3.73\cdot 10^{-14}$	$3.28\cdot 10^{-6}$	1.2

The heat sinks work well

Heat sink conductances

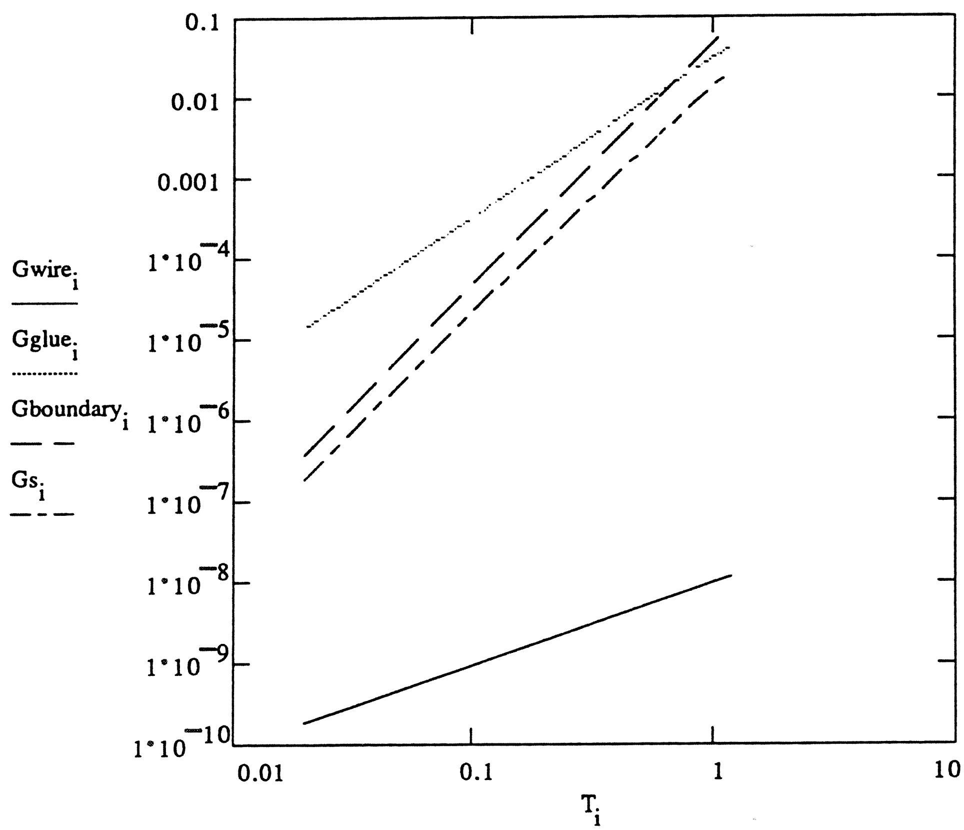

Worksheet C.1b (page 1)

Coaxial cables on 75 fridge (All Units MKS)

Temperatures: $T_1 := .02$ $T_4 := 1.2$

$T_2 := .1$ $T_5 := 4$ $i := 1..4$

$T_3 := .6$

Braid heat loads

$Lbraid := 0.1$ $Rbraid := 7.3 \cdot Lbraid$ $gbraid := \frac{24.5 \cdot 10^{-9}}{Rbraid}$ $Pi_i := \frac{gbraid}{2} \cdot \left[(T_{i+1})^2 - (T_i)^2 \right]$

This is using Wiedemann-Franz

Pi_i (W)	T_i
$1.61 \cdot 10^{-10}$	$2 \cdot 10^{-2}$
$5.87 \cdot 10^{-9}$	$1 \cdot 10^{-1}$
$1.81 \cdot 10^{-8}$	$6 \cdot 10^{-1}$
$2.44 \cdot 10^{-7}$	1.2

This is fine for fridge

Heat sinking of braids:

$As := (25.4 \cdot 10^{-3}) \cdot (25.4 \cdot 10^{-3})$ $d := .002 \cdot 25.4 \cdot 10^{-3}$ $As = 6.45 \cdot 10^{-4}$ $a := 1.43 \cdot 10^3$

$\kappa insulator_i := 0.03 \cdot (T_i)^2$ This is for nylon, I don't know the value for kapton $Gboundary_i := As \cdot a \cdot (T_i)^3$

$$Ginsulator_i := \frac{As}{d} \cdot \kappa insulator_i$$

$$Gs_i := \left[(Ginsulator_i)^{-1} + 2 \cdot (Gboundary_i)^{-1} \right]^{-1}$$ $Gbraid_i := gbraid \cdot T_i$

$$Pl_i := \frac{\left[(Gbraid_i)^{-1} + (Gs_i)^{-1} \right]^{-1}}{Gs_i} \cdot Pi_i \qquad \delta T_i := Pi_i \cdot \frac{\left[(Gbraid_i)^{-1} + (Gs_i)^{-1} \right]^{-1}}{Gs_i \cdot Gbraid_i}$$

Results: (G in W/K, P in W, T in K)

$Ginsulator_i$	$Gboundary_i$	Gs_i	$Gbraid_i$	Pl_i	δT_i	T_i
$1.52 \cdot 10^{-4}$	$7.38 \cdot 10^{-6}$	$3.6 \cdot 10^{-6}$	$6.71 \cdot 10^{-10}$	$3 \cdot 10^{-14}$	$4.47 \cdot 10^{-5}$	$2 \cdot 10^{-2}$
$3.81 \cdot 10^{-3}$	$9.23 \cdot 10^{-4}$	$4.11 \cdot 10^{-4}$	$3.36 \cdot 10^{-9}$	$4.79 \cdot 10^{-14}$	$1.43 \cdot 10^{-5}$	$1 \cdot 10^{-1}$
$1.37 \cdot 10^{-1}$	$1.99 \cdot 10^{-1}$	$5.77 \cdot 10^{-2}$	$2.01 \cdot 10^{-8}$	$6.32 \cdot 10^{-15}$	$3.14 \cdot 10^{-7}$	$6 \cdot 10^{-1}$
$5.49 \cdot 10^{-1}$	1.59	$3.25 \cdot 10^{-1}$	$4.03 \cdot 10^{-8}$	$3.03 \cdot 10^{-14}$	$7.52 \cdot 10^{-7}$	1.2

No suprise: the heat sinking of the braids is trivial

Worksheet C.1b (page 2)

Coax, continued

Power from inner conductor

$rwire := \frac{1}{2} \cdot .005 \cdot 25.4 \cdot 10^{-3}$ $Lwire := 0.1$ $Awire := \pi \cdot rwire^2$ $Awire = 1.27 \cdot 10^{-8}$

(W)

$\kappa(T) := .075 \cdot T^{1.85}$ $Pi_i := \frac{Awire}{Lwire} \cdot \int_{T_i}^{T_i + 1} \kappa(T)\, dT$ This is using conductance of Nb-Ti

Pi_i
$4.66 \cdot 10^{-12}$
$7.73 \cdot 10^{-10}$
$4.83 \cdot 10^{-9}$
$1.68 \cdot 10^{-7}$

T_i
$2 \cdot 10^{-2}$
$1 \cdot 10^{-1}$
$6 \cdot 10^{-1}$
1.2

Very small

Heat sinking of inner conductor

$Ls := 25.4 \cdot 10^{-3}$ $rbraid := .001$

$\kappa insulator_i := 30 \cdot 10^{-3} \cdot (T_i)^2$

$Ginsulator_i := 2 \cdot \pi \cdot \kappa insulator_i \cdot \frac{Ls}{\ln\left(\frac{rbraid}{rwire}\right)}$

$Ai := 2 \cdot \pi \cdot rwire \cdot Ls$ $Ai = 1.01 \cdot 10^{-5}$

$Ao := 2 \cdot \pi \cdot rbraid \cdot Ls$ $Ao = 1.6 \cdot 10^{-4}$

$a := 1.43 \cdot 10^3$

$Gboundaryi_i := Ai \cdot a \cdot (T_i)^3$

$Gboundaryo_i := Ao \cdot a \cdot (T_i)^3$

$Gs_i := \left[(Ginsulator_i)^{-1} + (Gboundaryi_i)^{-1} + (Gboundaryo_i)^{-1} \right]^{-1}$ $Gwire_i := \frac{Awire}{Lwire} \cdot \kappa(T_i)$

$Gws_i := Gwire_i \cdot \frac{Lwire}{Ls}$ $Gx_i := \sqrt{Gs_i \cdot Gws_i}$

$Pl_i := \frac{\left[(Gwire_i)^{-1} + (Gx_i)^{-1} \right]^{-1}}{Gx_i} \cdot Pi_i$ $\delta T_i := Pi_i \cdot \frac{\left[(Gwire_i)^{-1} + (Gx_i)^{-1} \right]^{-1}}{Gx_i \cdot Gwire_i}$

Worksheet C.1b (page 3)

Results: (G in W/K, P in W, T in K)

Gs_i	Gws_i
$9.42\cdot10^{-8}$	$2.69\cdot10^{-11}$
$7.64\cdot10^{-6}$	$5.28\cdot10^{-10}$
$5.16\cdot10^{-4}$	$1.45\cdot10^{-8}$
$2.26\cdot10^{-3}$	$5.24\cdot10^{-8}$

$Ginsulator_i$	$Gboundaryi_i$	$Gboundaryo_i$	Gx_i	$Gwire_i$	Pl_i	δT_i	T_i
$6.95\cdot10^{-7}$	$1.16\cdot10^{-7}$	$1.83\cdot10^{-6}$	$1.59\cdot10^{-9}$	$6.83\cdot10^{-12}$	$1.99\cdot10^{-14}$	$2.91\cdot10^{-3}$	$2\cdot10^{-2}$
$1.74\cdot10^{-5}$	$1.45\cdot10^{-5}$	$2.28\cdot10^{-4}$	$6.35\cdot10^{-8}$	$1.34\cdot10^{-10}$	$1.63\cdot10^{-12}$	$1.21\cdot10^{-2}$	$1\cdot10^{-1}$
$6.25\cdot10^{-4}$	$3.13\cdot10^{-3}$	$4.93\cdot10^{-2}$	$2.74\cdot10^{-6}$	$3.69\cdot10^{-9}$	$6.5\cdot10^{-12}$	$1.76\cdot10^{-3}$	$6\cdot10^{-1}$
$2.5\cdot10^{-3}$	$2.5\cdot10^{-2}$	$3.94\cdot10^{-1}$	$1.09\cdot10^{-5}$	$1.33\cdot10^{-8}$	$2.05\cdot10^{-10}$	$1.54\cdot10^{-2}$	1.2

This looks good on paper: The question is, how good is the contact between the insulator and the metal in the coax? (Maybe good because the insulator thermally contracts onto the wire, and silver paint coats the outside.)

Heat sink conductances

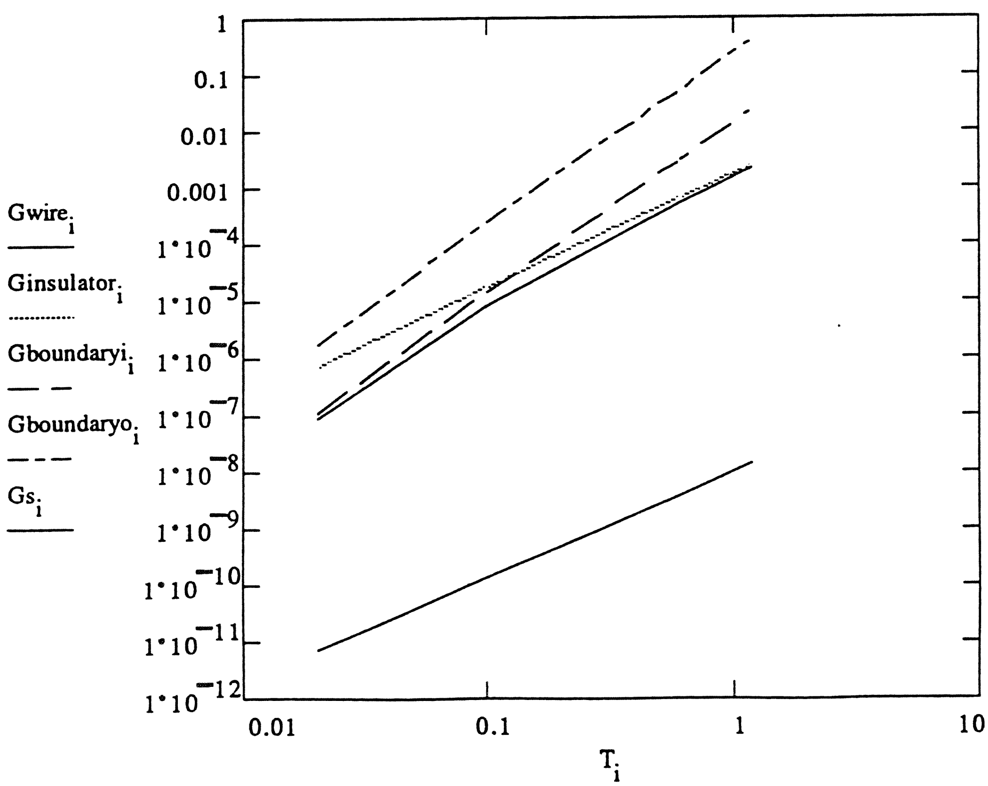

Worksheet C.1c (page 1)

Gate wires on 75 Fridge

(All units MKS)

Temperatures: $T_1 := .02$ $T_2 := 1.2$ $T_3 := 4$ $i := 1..2$

Wire heat loads

$Rwire_1 := .01$ $Rwire_2 := 1300$ $Rwire_3 := .01$ $i := 1..3$ $gwire_i := 24.5\cdot 10^{-9}\cdot\dfrac{1}{Rwire_i}$

$i := 1..2$ $Pi_i := \dfrac{gwire_{i+1}}{2}\cdot\left[(T_{i+1})^2 - (T_i)^2\right]$ Using Wiedeman-Franz

Pi_i (W)	T_i
$1.36\cdot 10^{-11}$	$2\cdot 10^{-2}$
$1.78\cdot 10^{-5}$	1.2

Heat sinks:

$Ls := .002$ $ro1 := .00125$ $ri1 := .001$ $\varepsilon := 6$ $\varepsilon o := 9\cdot 10^{-12}$

$$Cs := 2\cdot\pi\cdot\varepsilon\cdot\varepsilon o\cdot\left[\int_0^{.002}\frac{1}{\ln\left(\dfrac{ro1 + .5\cdot l}{ri1 + .5\cdot l}\right)}\,dl\right] \qquad Cs = 4.4\cdot 10^{-12}$$

Everywhere here
"o" refers to outer radius,
"i" refers to innerradius

$\kappa glue_i := 78\cdot 10^{-4}\cdot(T_i)^{1.8}$

$Ao := 2\cdot\pi\cdot\left(ro1\cdot Ls + \frac{1}{4}\cdot Ls^2\right)$ $Ao = 2.2\cdot 10^{-5}$

$Ai := 2\cdot\pi\cdot\left(ri1\cdot Ls + \frac{1}{4}\cdot Ls^2\right)$ $Ai = 1.88\cdot 10^{-5}$

$Gglue_i := Cs\cdot\dfrac{\kappa glue_i}{\varepsilon\cdot\varepsilon o}$

$a := 1.43\cdot 10^3$ $Gboundaryo_i := Ao\cdot a\cdot(T_i)^3$ $Gboundaryi_i := Ai\cdot a\cdot(T_i)^3$

$Gs_i := \left[(Gglue_i)^{-1} + (Gboundaryo_i)^{-1} + (Gboundaryi_i)^{-1}\right]^{-1}$ $Gwire_i := gwire_i\cdot T_i$

$Pl_i := \dfrac{\left[(Gwire_i)^{-1} + (Gs_i)^{-1}\right]^{-1}}{Gs_i}\cdot Pi_i$ $\delta T_i := Pi_i\cdot\dfrac{\left[(Gwire_i)^{-1} + (Gs_i)^{-1}\right]^{-1}}{Gs_i\cdot Gwire_i}$

Worksheet C.1c (page 2)

Results:

(G in W/K, P in W, T in K)

$Gglue_i$	$Gboundaryo_i$	$Gboundaryi_i$	Gs_i	$Gwire_i$	Pl_i	δT_i	T_i
$5.56 \cdot 10^{-7}$	$2.52 \cdot 10^{-7}$	$2.16 \cdot 10^{-7}$	$9.61 \cdot 10^{-8}$	$4.9 \cdot 10^{-8}$	$4.58 \cdot 10^{-12}$	$9.35 \cdot 10^{-5}$	$2 \cdot 10^{-2}$
$8.83 \cdot 10^{-4}$	$5.43 \cdot 10^{-2}$	$4.66 \cdot 10^{-2}$	$8.53 \cdot 10^{-4}$	$2.26 \cdot 10^{-11}$	$4.73 \cdot 10^{-13}$	$2.09 \cdot 10^{-2}$	1.2

The heat sinking is good

(Note: The gate wire coming out of the FET is probably not well heat sunk and may therefore put a fraction of mW on 1.2 K. This may increase the temperature of the wire at 1.2K, but Gsum is so much larger than Gwire that it will not result in substantial heat going down to 20 mK.)

Heat sink conductances

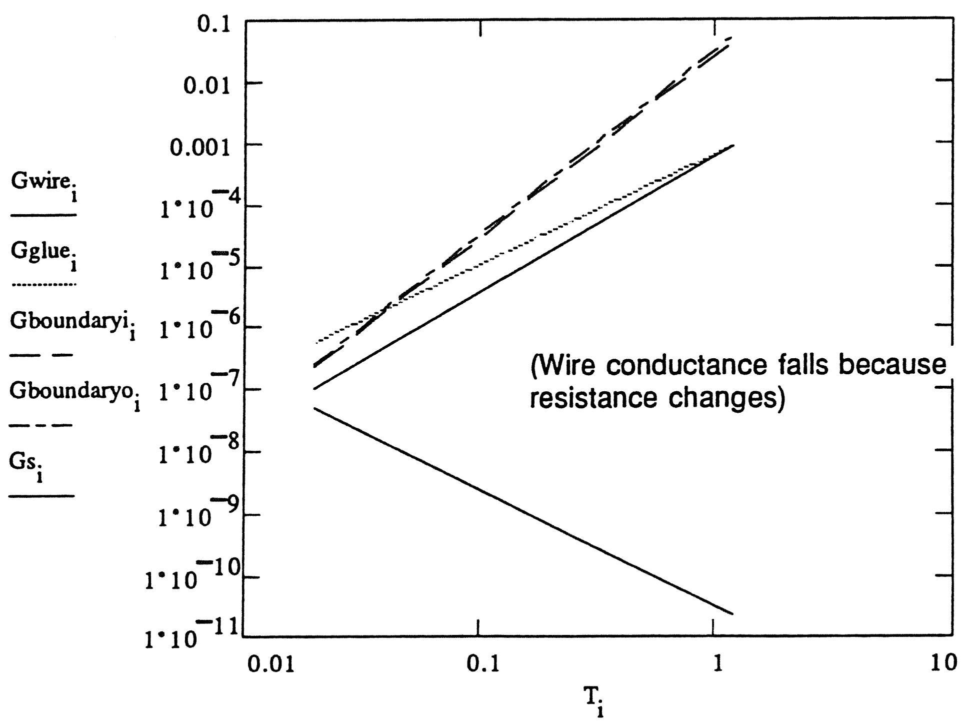

Appendix D: Microphonics

D.1) Characterization of the problem

The most difficult noise problem we have faced is that of microphonics (88). Microphonics is a term for electronic noise caused by vibrations of wires on a microscopic scale. The usual picture of this noise is that the capacitance between a line at voltage V and the ground is changed by the motion of the wire, inducing a charge $dQ = VdC$ on the signal line. In our case we observed this behavior, but also saw a much larger noise that was independent of V but also clearly caused by vibration. It seemed to be strongly correlated to the presence of insulators such as plastic near the gate wire. When materials with different work functions are in contact or close proximity a charge can be induced on the surface of each material. This is known as the triboelectric effect (89). On the surface of insulators this charge does not easily dissipate, and motion of the system apparently causes some of this charge to be injected onto the signal wire, either directly or capacitively.

Our problem is much more severe than is usually encountered because of the constraints (discussed in chapter 3) that force the FETs that serve as the front-ends of our amplifiers to be roughly 40 cm from the detector. Most of the microphonic pickup is encountered on the wire which runs from the gate of the FET to the detector. Usually this wire is as short as possible, often on the order of a millimeter instead of our 40 cm.

Characterizing microphoncis at room temperature can be accomplished much more quickly and easily than at low temperatures, though it is not an ideal way to attack the problem. For example, one can never be sure how similar the mechanical system is at room temperature and at low temperature, since, among other things, plastics harden and different materials contract by different amounts when cooled. Further, the Johnson noise of resistors is a factor of ≈120 smaller at 0.02 K than at 300 K, so that room temperature tests are much less sensitive than the actual experimental situation.

Nonetheless, we did test a number of configurations at room temperature. First and foremost we found that essentially any arrangement with insulators near the conductor, such as coaxial cable or insulated wire, is very bad. Even rigid objects such as long cylinders of solid epoxy with an embedded wire are quite microphonic. Different types of connector arrangements, especially those involving circuit board, had widely varying susceptibilities to microphonics, often in seemingly unpredictable ways.

It also appears as though most of the noise appears on the gate wire and at the FET, in both the ionization and charge measurements. The susceptibility of the gate wire makes sense, since microphonics is a current source, and the signal wire at the gate sees a very high impedance. The bias voltages, in contrast, are stiff (i.e., low impedance), as is the voltage at the source of the FET. The drain of the FET is susceptible to current noise, but much less so than the gate. (See the discussion of the amplifiers in appendix E.) The FET is presumably sensitive to microphonics because there is typically a ≈3.0 V difference between the drain and the gate. Vibrations in the FET change the drain-gate capacitance, inducing current on the gate.

We also tried to learn as much as possible while running the refrigerator. By far the dominant source of microphonics initially came from the flow of liquid helium through a regulating needle valve. Unlike single frequency vibrations at a few hundred Hertz typically found in a short stretched wire, this source produced a broad spectrum of frequencies and also a large number of discrete excitations at frequencies up to several tens of kHz. Unfortunately it is difficult to turn off this source since it is used to fill a continuously pumped 1.2 K chamber. By contrast, the flow of liquid helium 3 and helium 4 mixture through the main part of the dilution refrigerator does not seem to generate significant noise.

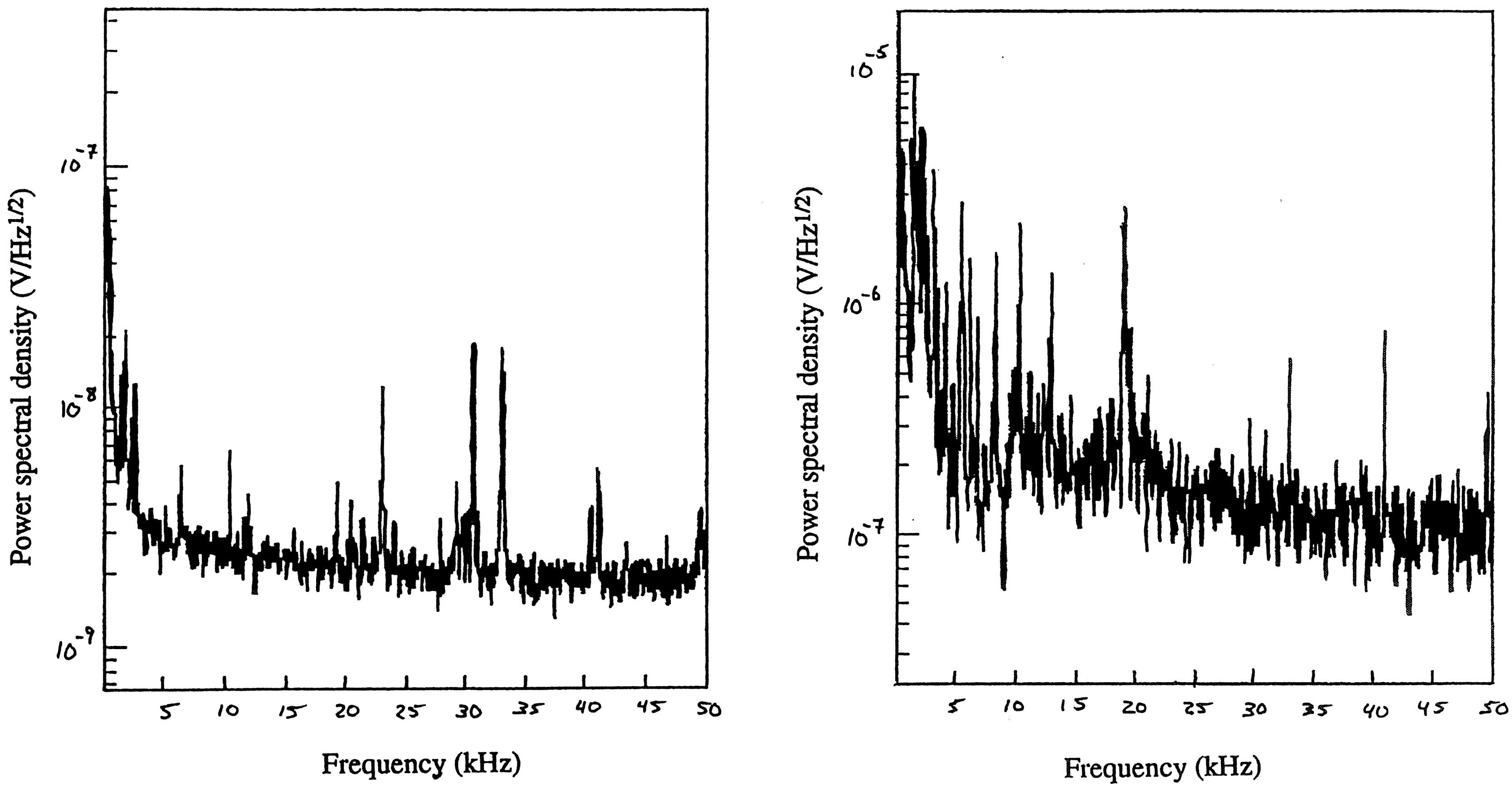

Figure D.1 The initial voltage noise power spectral density in (a) the phonon measurement and (b) the ionization measurement. Essentially all the features besides the flat noise level are due to microphonics, even at frequencies as high as 30 kHz.

Figure D.1 shows the microphonics we suffered from in both the phonon and ionization measurements with the first generation electronics setup in the refrigerator. The signal from events, for reference, is at a few Hz to a few hundred Hz in the phonon measurement, and has a characteristic frequency of ≈5 kHz in the charge measurement. The expected noise without microphonics (discussed in detail in appendix E), is ≈1 nV/Hz$^{1/2}$ in the phonon measurement and ≈200 nV/Hz$^{1/2}$ in the ionization measurement. Clearly the microphonics was the dominant noise by as much as several orders of magnitude at the signal frequencies at this time.

D.2) Mechanical decoupling

There are two different approaches we used to reduce this noise. The first was to try to reduce the transmission of vibrations from their source to the relevant parts of the electronic circuits. The other was to reduce the intrinsic sensitivity of the electronics to vibrations.

The idea behind mechanically decoupling is to concede that the refrigerator will be vibrationally noisy, and instead try to decouple the electronics from the refrigerator with a simple spring mounting system. (We also made an unsuccessful attempt to effecitively dampen the vibrations in the regulating needle valve, but abandoned this approach.) A harmonic oscillator of mass m which is driven at an angular frequency ω by a force of amplitude F_o oscillates at ω with an amplitude A given by

$$A = \frac{1}{m}\frac{F_o}{\omega^2 - \omega_o^2}$$

where ω_o is the natural resonant frequency of the system. The important point is that the amplitude decreases like $1/\omega^2$ for frequencies far above the resonance. The addition of a damping term does not change this basic behavior for $\omega \gg \omega_o$. In mechanical systems with macroscopic masses it is easy to attain resonant frequencies in the few Hz range, thus the we had hoped that with spring mounting our kHz microphonics should be severely attenuated.

Since only the gate wire and the FET itself seem to be susceptible to microphonic pickup, we built a system to hold the FET, gate wire and detector with springs alone. The resonant frequencies were all below about 10 Hz. The decoupling of the gate wire system and the detector itself proved to be of no value. We believe the problem is that high frequency vibrations travel along the metal of the coil of the spring itself without significant damping. The few Hz resonant frequency of the mechanical system, by contrast, only describes a macroscopic motion of the spring. It also proved difficult to keep the detector at 20 mK when it was free to move on springs.

However the spring mounting of the FET box did give a large reduction in microphonics noise. Presumably this was at least in part because the FET box happens to be mounted very near the regulating needle valves that are the dominant source of vibrations, and any amount of decoupling was useful. Another factor may be the intrinsic sensitivity of the FET to microphonics due to variations in the drain-gate capacitance, as mentioned above.

D.3 Low noise cabling

The other prong to our approach was to reduce the sensitivity of the system to vibrations. The FET itself is mounted on a fiberglass thermal standoff inside of 4 K box, as described in appendix C. We improved the mounting by tightly suspending the gate wire between the FET and a connector at 4 K, and by surrounding the gate wire by a metallic shield. Previously the gate wire had been varnished to the fiberglass post holding the FET.

Outside the FETs, we built "vacuum coax" cables that consist of thin (≈18 μm Ø) stainless steels wire stretched down the center of 3 mm Ø stainless steel tubes. The purpose of the tubes is to provide a shield against surrounding insulators and to prevent cross talk, not to form a coaxial transmission line. The wires are held at the ends with crimp sleeves which sit in brass holders. The technology for the crimping is adapted from wire chambers used in high energy physics. The brass piece is glued to a larger mount which holds the tubes. The glue joint is designed to optimize the trade-off between thermal conductance and capacitance to ground, as discussed in appendix C. Each heat sink has a capacitance of about 4 pF. The heat load of the thin wires is small enough that they run from a 1 K temperature stage near the FET to 20 mK without interruption. The tubes, by contrast, are heat sunk at 1 K, 600 mK, 100 mK and 20 mK.

With this arrangement there is no insulator near the gate wire except for the two small epoxy heat sinks at either end. This has two advantages. First, with insulators removed the microphonic noise is greatly reduced. Second, with this type of "coax" the insulator is vacuum which has a dielectric constant of 1, and the total capacitance is ≈4 pF/cable. The plastics used in normal coaxial cables, on the other hand, have a dielectric constant of about 5, and would thus have a capacitance of ≈20 for the same geometry.

At both ends of these rigid coaxial cables we need somewhat flexible connections a few inches long to go the FET box and to the detector. We first used "semi-rigid" coaxial cable from Malco (part number UT 34-95), which has an outer conductor made of a thin sheet of solid copper. We had hoped that the rigidity of this cable would minimize microphonic pickup, but we found it to be fairly bad.

Finally we learned from A.E. Lange and P.L. Richards of a different cable made by Malco that is purposefully designed to reduce microphonic noise (Malco "mini-noise cable", part number 250-3820-0000). It is basically a standard coaxial cable, but has graphite embedded on the outside of the insulator that separates the inner and outer conductors. The manufacturer does not explain how the cable works, but presumably the graphite (which is a mildly resistive electrical conductor) reduces the build up of charge between the insulator and the outer conductor on a microscopic scale. We found this cable to indeed have very little susceptibility to microphonic pickup. Unfortunately it has the normal large capacitance of any standard coaxial cable, and thus cannot replace the vacuum coax for most of the 40 cm from the FETs to the detector.

The final noise, with the spring mounted FET box, vacuum coax, and special coax end pieces is shown in figure D.2. There is clearly a dramatic improvement over figure D.1. At the lowest frequencies in both measurements, however, the excess noise is still due to microphonics.

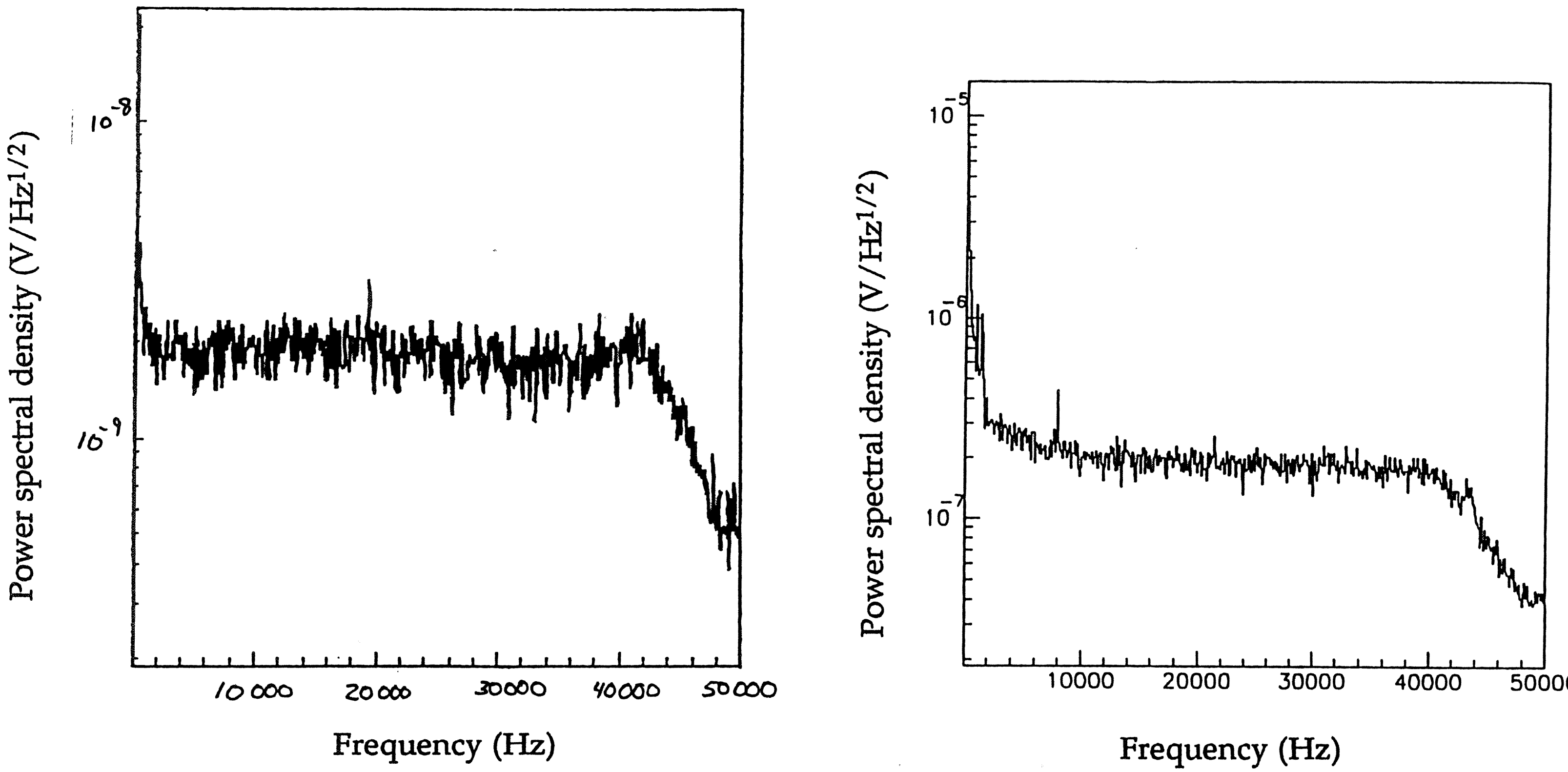

Figure D.2 The voltage noise power spectral density in (a) the phonon measurement and (b) the ionization measurement after the wiring had been rebuilt to reduce microphonics. The 1/f-like noise at lowest frequencies is the remaining microphonics.

Appendix E: Noise

The noise in both the phonon and charge measurements in principle can come from several sources: voltage and current noise in the amplifiers, Johnson voltage noise from the various resistors in the circuits, current noise from the detector in the charge measurement, and microphonic noise, which is the subject of appendix D. Here I will discuss each these noise sources in some detail, and briefly describe the amplifiers with an emphasis on their noise performance. Signal recognition in the face of these noise sources is the subject of appendix F.

E.1) Noise sources

Voltage noise is by definition a fluctuation whose exact time dependence, $\delta v(t)$, cannot be predicted. In many cases, however, the time average of the voltage noise squared,

$$\left\langle \delta v^2(t) \right\rangle \equiv \lim_{T\to\infty} \frac{1}{2T} \int_{-T}^{T} \delta v^2(t) dt, \qquad \text{E.1}$$

can be predicted. It is convenient to talk about the noise in terms of frequency components because it is often easier to analyze electrical circuits in the frequency domain.

The formalism of talking about noise in the frequency domain can be confusing, so we begin with some definitions. For an introductory reference, see Reif (69). To avoid convergence problems, we define

$$\delta v_T(t) = \begin{cases} \delta v(t) & -T < t < -T \\ 0 & \text{otherwise} \end{cases} .$$

The Fourier transform of $\delta v_T(t)$ is

$$\delta v_T(f) = \int_{-\infty}^{\infty} \delta v_T(t) e^{-i2\pi f t} dt$$

and the inverse transform is

$$\delta v_T(t) = \frac{1}{2\pi}\int_{-\infty}^{\infty} \delta v_T(\omega)e^{i\omega t}d\omega$$
$$= \int_{-\infty}^{\infty} \delta v_T(f)e^{i2\pi ft}df$$

We will also use the orthogonality result

$$\int_{-\infty}^{\infty} e^{i2\pi(f-f')t}dt = \delta(f-f').$$

With these definitions, equation E.1 becomes

$$\left\langle \delta v^2(t)\right\rangle = \lim_{T\to\infty}\frac{1}{2T}\int_{-\infty}^{\infty}\delta v_T^2(t)dt$$
$$= \lim_{T\to\infty}\frac{1}{2T}\int_{-\infty}^{\infty}\delta v_T(f)df\int_{-\infty}^{\infty}\delta v_T(f')df'\int_{-\infty}^{\infty}e^{i2\pi(f+f')t}dt$$
$$= \lim_{T\to\infty}\frac{1}{2T}\int_{-\infty}^{\infty}\delta v_T(f)df\int_{-\infty}^{\infty}\delta v_T(f')df'\delta(f+f')$$
$$= \lim_{T\to\infty}\frac{1}{2T}\int_{-\infty}^{\infty}\left|\delta v_T(f)\right|^2 df$$
$$= \lim_{T\to\infty}\frac{1}{T}\int_{0}^{\infty}\left|\delta v_T(f)\right|^2 df$$

We have used the fact that with $\delta v(t)$ real, $\delta v(f)=\delta v^*(-f)$, and so $|\delta v(f)|=|\delta v(-f)|$, and so, in the last equality, we can integrate only over positive quantities. Defining $e(f)$ as

$$e(f) \equiv \lim_{T\to\infty}\left|\frac{1}{\sqrt{T}}\int_{-T}^{T}\delta v(t)e^{-i2\pi ft}dt\right|$$
$$= \lim_{T\to\infty}\frac{1}{\sqrt{T}}\left|\delta v_T(f)\right| \qquad \text{E.2}$$

we then have

$$\left\langle \delta v^2(t)\right\rangle = \int_0^{\infty} e^2(f)df. \qquad \text{E.3}$$

The term $e^2(f)$ is known as the spectral power density, and has units of V^2/Hz. The total voltage noise in a circuit is found by calculating the effect of a noise source in the frequency domain, and then integrating the square of this power density over the effective bandwidth of the circuit.

The thermal energy in any resistor causes a fluctuating voltage, called Johnson noise, to appear across its ends. The spectral power density of this noise is

$$e^2(f) = 4kTR \qquad \text{E.4}$$

where T is the absolute temperature, R is the resistance and k is Boltzmann's constant. Note that this noise is flat in the frequency domain, or "white". A real resistor in a circuit is analyzed by replacing it with an ideal noiseless resistor configured in series with an ideal voltage source of magnitude $e(f)$. Alternatively, the resistor can be replaced by an ideal resistor configured in parallel with a current source of magnitude $e(f)/R$.

Devices such as FETs and bipolar transistors also have a voltage noise that arises in much the same way as Johnson noise. Our FETs behave as ideal noiseless devices with a source of voltage at the gate. This noise in general has two components, one that is flat in the frequency domain, and one whose power density has a $1/f$ shape. This noise is discussed in more detail below.

Current flowing through junctions in active elements such as the base current in a bipolar transistor or the leakage current in a vacuum tube has fluctuations known as "shot noise". This noise is also flat in the frequency domain with a spectral density given by

$$\delta I^2 = 2eI_o, \qquad \text{E.5}$$

where I_o is the DC current, e is the fundamental electric charge, and the units are A^2/Hz. This current is measured as a voltage noise in our circuit when it flows across a resistance such as the thermistor in the phonon measurement or the feedback resistor in the charge measurement. There is also a shot noise current on the gate of an FET, but it can arise from currents flowing both in and out of the gate, and so may be larger than the noise given by equation E.5. Note that ordinary currents in a resistive network do not have shot noise, as it arises from the discrete nature of charge flow in a semiconductor diode or in a vacuum tube.

Other noise sources include microphonics noise, which is the subject of appendix D, and an effect sometimes referred to as "excess noise" in resistors or "contact noise". This noise behaves as a fluctuation in the conductivity when current flows through a resistor made of a composite material, or through a poor contact. Typically it has a $1/f$

power spectral density. We have not seen this noise in our NTD thermistors at the sensitivity level of our electronics.

E.2) The voltage amplifier

Figure E.1*a* shows the main elements of voltage measurement with the different temperatures of the various components indicated, and with a greatly simplified schematic of the voltage amplifier. For a more thorough discussion of the amplifier the reader should refer to the paper by D. Yvon (38); here I try to discuss the amplifier in only enough detail to gain some insight into its noise.

First consider the amplifier in its quiescent state (input voltage fixed). The FET has current flowing from its drain to its source. (In actuality, electrons flow into the source and out of the drain, hence the names. The gate, drain and source of the FET are labeled G, D, and S in the figure.) The gate has a very high impedance, so to first order no current flows in or out of it. The basic action of the FET is to set a relationship between the gate-source voltage, V_{GS}, and the drain-source current, I_{DS}.

The transistor whose base is connected to the drain is configured as a "mirror CASCODE" and holds the drain voltage fixed. With the drain voltage and V^+ fixed, the current across R_D is fixed. The "amplifier" labeled Q is in reality a discrete component circuit which: a) in the quiescent state draws a small current (≈0.7 mA) on its input and sinks on its output the current from the source of the FET that flows across R_I; and b) acts as a high gain (>10^4) inverting current amplifier for changes to its input current. Except for the small current pulled by "Q" through the transistor, then, most of the fixed current across R_D flows between the drain and the source of the FET, fixing the voltage between the gate and source. Typically I_{DS}≈3 mA, the gate is within a few mV of ground, and the source is at 0.5-1.0 V. The quiescent output voltage is the source voltage minus the voltage drop across from the I_{DS} flowing across R_I.

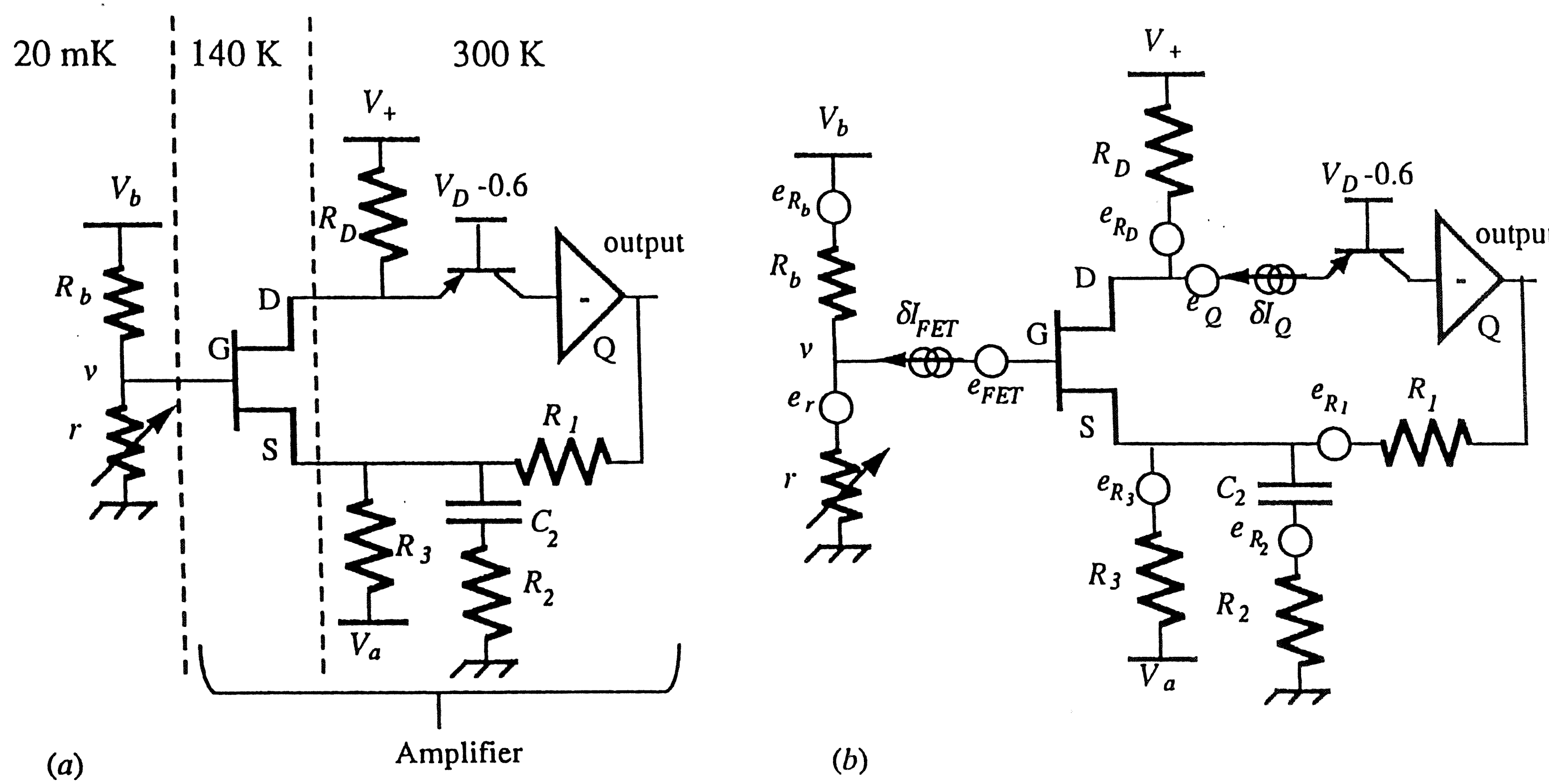

Figure E.1 Schematic view of the voltage circuit, (a), and potential noise sources, (b).

The resistor R_3 and the voltage V_a are included to deal with the problem that the gate source voltage changes when the FET is cooled from room temperature to 140 K. With the gate near ground, this means that the source voltage changes, which would change the output voltage if only I_{DS} were to flow across R_1. Such swings in the output voltage are prevented by essentially feeding very low frequency changes in the output voltage back to the voltage V_a. Thus this "auto-bias" circuit sources or sinks whatever current is needed to keep the output voltage fixed.

The signal we wish to measure is a change in the gate voltage. The basic action of an FET is to react to changes in V_{GS} by changing I_{DS} according to

$$\delta I_{DS}=g_m \delta V_{GS},$$

where g_m is called the transconductance. For the FETs we most often use in the voltage measurement $g_m \approx 1/40\ \Omega^{-1}$. If, for the moment, we consider the source voltage to be held fixed, then an increase in the gate voltage causes a positive change in the drain source current that comes at the expense of the quiescent current flowing into Q. In this open loop behavior, Q responds to this *decrease* in its input current by *increasing* its output current by a much larger amount. In actuality, though, for frequencies higher than $1/(2\pi R_2 C_2)$ the output current from Q flows across the feedback resistors R_1 and R_2 to raise the source voltage by precisely as much as the initial change in gate voltage. (R_3 does not play a role because it is much bigger than R_2, so $R_3 \| R_2 \equiv R_2$). In this process, with $\delta V_s = \delta V_G \equiv \delta v$, the output voltage changes by

$$\delta v_o = \frac{R_1 + R_2}{R_2} \delta v$$

so that the amplifier has a gain of

$$G = \frac{R_1 + R_2}{R_2}.$$

Currently R_1=990 Ω and R_2=10 Ω, so G =100. For frequencies slower than $1/(2\pi R_2 C_2)$ but faster than the response frequency of the autobias feedback, the gain is rolled off to $\approx R_1/R_3 \ll (R_1+R_2)/R_2$. At the lowest frequencies the autobias circuit holds the output fixed.

A note on the CASCODE transistor configuration: An alternative to having the drain voltage fixed by the transistor arrangement is to have one high gain voltage amplifier in place of this transistor and Q. In this case an input signal causes a change in the drain-source current, $\delta I_{DS}=g_m \delta V_{GS}$, that must flow across R_D. In the open loop this changes the drain voltage by $\delta V_{DS}=R_D g_m \delta V_{GS} \approx 75\, \delta V_{GS}$ for $R_D \approx 3$ kΩ. In the closed loop, ideally, the source voltage changes so that δV_{GS} is zero and so the behavior of the circuit is the same. However the open loop gain of the circuit will always begin to roll off at some high frequency. Without the CASCODE the drain voltage changes considerably with respect to the gate voltage as the open loop gain rolls off. With the CASCODE arrangement this does not happen. If the drain voltage changes by some factor times δV_{GS}, then the effective gate-drain capacitance is increased by the same factor. This extra capacitance on the gate rolls off the signal at high frequencies.

E.3 Noise in the voltage measurement

A number of potentially important noise sources in the voltage measurement are shown in figure E.1*b*. Voltage noise sources are indicated by a circle, and act as perfect voltage sources with zero impedance. Each noise source is analyzed separately by ignoring all other noise sources and assuming ideal behavior of all circuit elements. The total noise is found by adding the contribution of all the separate sources in quadrature. Note that in everything that follows we assume that we will integrate only over positive frequencies. If we integrate over all frequencies, then the noise sources, e, should be divided by $2^{1/2}$ in all results.

Because the FET ideally has no current into its gate the Johnson noise of the thermistor drives a noise current that must flow through the thermistor and load resistor. The bias voltage V_b and the ground are both fixed so that the total voltage drop over both resistors and the voltage source is zero. We take the current, δI, to flow from ground towards the bias, and take the polarity of e_r to be positive above (i.e., at v) and negative below (i.e., at the top of the thermistor). We then equate the voltage drops across the circuit as

$$\delta I r + e_r + \delta I R_b = 0\,.$$

The noise spectral density in v, e_v, then, is given by

$$\delta e_v = e_r - \delta I r = e_r\left(\frac{R_b}{r+R_b}\right) \cong e_r\,,$$

where the last approximate equality holds if $R_b \gg r$.

Similar reasoning shows that the Johnson noise of the bias resistor is

$$\begin{aligned}\delta e_v &= e_{R_b}\left(\frac{R_b}{r+R_b}\right) \\ &\cong e_{R_b}\frac{r}{R_b}\end{aligned}.$$

Note that by the definition of Johnson noise, equation E.4,

$$e_{R_b}\frac{r}{R_b} = e_r\sqrt{\frac{r}{R_b}}\,,$$

so the Johnson noise is dominated by the smaller of the two resistors. The reason for this is that with the bias voltage and ground both fixed, or at an "AC ground", the gate sees the parallel combination of the bias resistor and thermistor, which is approximately equal to the smaller resistance. Typically, at most $r \approx 1$ MΩ, which at 20 mK gives $e_r \approx 1.0$ nV/Hz$^{1/2}$.

The current noise of the FET causes a fluctuation in v given by

$$\begin{aligned}\delta e_v &= \delta I_{FET}\left(r^{-1} + R_b^{-1}\right)^{-1} \\ &\cong \delta I_{FET}\, r\end{aligned}.$$

The voltage noise of the FET directly appears as a noise in v since no current can flow into the gate, or

$$\delta e_v = e_{FET}.$$

This voltage noise is on the order of 1 nV/Hz$^{1/2}$. We think that the current noise is negligible our FETs are cooled to $\approx$140 K, but we have not carefully checked this.

One important aspect of the design of our amplifier is that the noise of the first active element, the FET, dominates all the other noise sources in the amplifier. There are two noise sources at the drain. The Johnson noise of the drain bias resistor, R_D, cannot change the drain voltage because of the action of Q, but instead it drives a current e_{RD}/R_D. The effect of this current can be understood by asking what equivalent change in the input voltage would cause this same change in the drain current through the action of the FET. The answer is $e_v=e_{RD}/(R_D g_m)$, so the equivalent noise of e_{RD} at the amplifier input is $e_{RD}/R_D g_m$. Typically $R_D \approx 3$ kΩ, so that $e_{RD} \approx 7$ nV/Hz$^{1/2}$, and $e_{RD}/(R_D g_m) \approx 0.06$ nV/Hz$^{1/2}$, far less than e_{FET}. The circuit represented by Q and the CASCODE transistor can be considered to have both a voltage noise e_Q, and a current noise δI_Q on the quiescent current drawn by Q. With the input voltage to Q fixed, e_Q changes the current drawn across R_D, thus it has the same effect as e_{RD}, which is negligible for the typical value of e_Q. The current noise in Q is generated internally by a Johnson noise from a resistor configured much like R_D. It thus has a negligible equivalent effect at the amplifier input for the same reason as for e_{RD}.

The Johnson noise of R_1 and R_3 are shorted by the Johnson noise of R_2 (since R_1=99xR_2, and $R_3 \approx R_1$) for the same reason that the noise of the bias resistor is shorted by the thermistor, as described above. The Johnson noise of R_2, on the other hand appears directly on the source of FET for frequencies higher than $1/(2\pi R_2 C_2)$. Since the basic action of the amplifier is to respond to changes in the gate-source voltage, this noise effectively appears at the input of the amplifier. To reduce this noise, we picked R_2=10 Ω which gives $e_{R2} \approx 0.4$ nV/Hz$^{1/2}$. The capacitor C_2 was chosen as large as practically feasible, C_2=300 μF, so that the roll-off frequency of the amplifier is about 50 Hz.

In summary, then, the important noise sources in the voltage measurement are the voltage noise of the FET, and in some cases the Johnson noise of the thermistor. The microphonics noise, δI_μ, is a current source at the amplifier input which flows across the

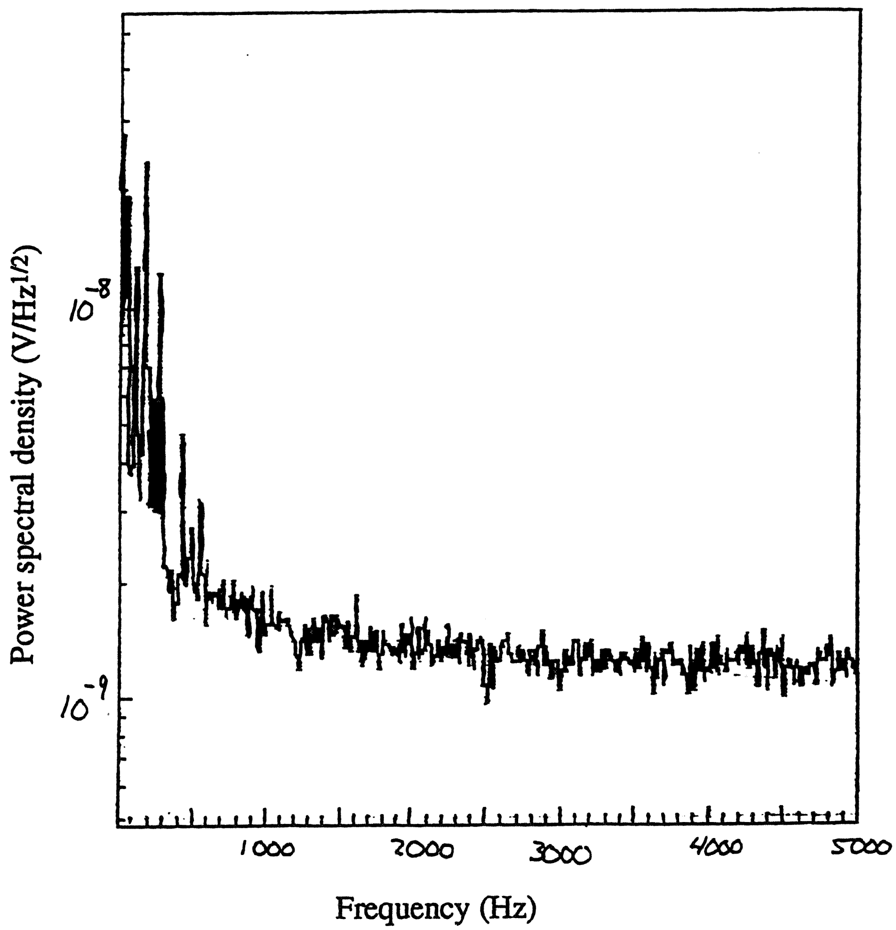

Figure E.2 Typical electronic noise in the phonon measurement.

parallel combination of the thermistor and bias resistor. At low frequencies this noise is quite high. Finally, for positive frequencies we can write

$$\delta e_v^2 = e_{FET}^2 + e_r^2 + \delta I_\mu^2 r^2. \qquad \text{E.6}$$

A typical noise spectrum is shown in figure E.2, in this case taken at 22 mK where $r \approx 1.7$ MΩ. The flat level of about 1.5 nV/Hz$^{1/2}$ is presumably from the FET and the thermistor Johnson noise. The spikes and overall rise at low frequencies is due to both microphonics and excess noise in the warm amplifier card because of inadequate filtering of the power supplies. Most of this noise has been suppressed in the new cards built by D. Yvon.

E.4) The charge amplifier

Figure E.3*a* shows the charge measurement with a simplified schematic of the charge amplifier. Again, for a full discussion of the amplifier, see the paper by D. Yvon. Just as for the voltage amplifier, the drain voltage fixed by the transistor in a mirror CASCODE arrangement. In conjunction with V_+, R_D then sets the I_{DS}, which in turn sets the gate source voltage, V_{GS}. Typically, again, $I_{DS} \approx 3$ mA, and $V_{GS} \approx -0.5$ V. (If the circuit were actually configured as in figure E.3*a*, this would mean the gate is at a negative voltage but connected directly to the detector. In reality the gate can be AC coupled to the detector as shown in figure E.3*c*, or the source can be held at $\approx +0.5$ V so that $V_G=0$.) The amplifier "A" is a discrete component circuit which acts as a high gain current-to-voltage amplifier. In its quiescent state it draws a small amount of current from the total current flowing across R_D.

The response to an event can be understood by imagining the gate voltage to undergo a small, positive change, as current from the detector charges the capacitance of the gate and detector. The FET responds to this by $\delta I_{DS} = g_m \delta V_{GS}$. Since the current across R_D is fixed, this change in current comes at the expense of the current into A. In

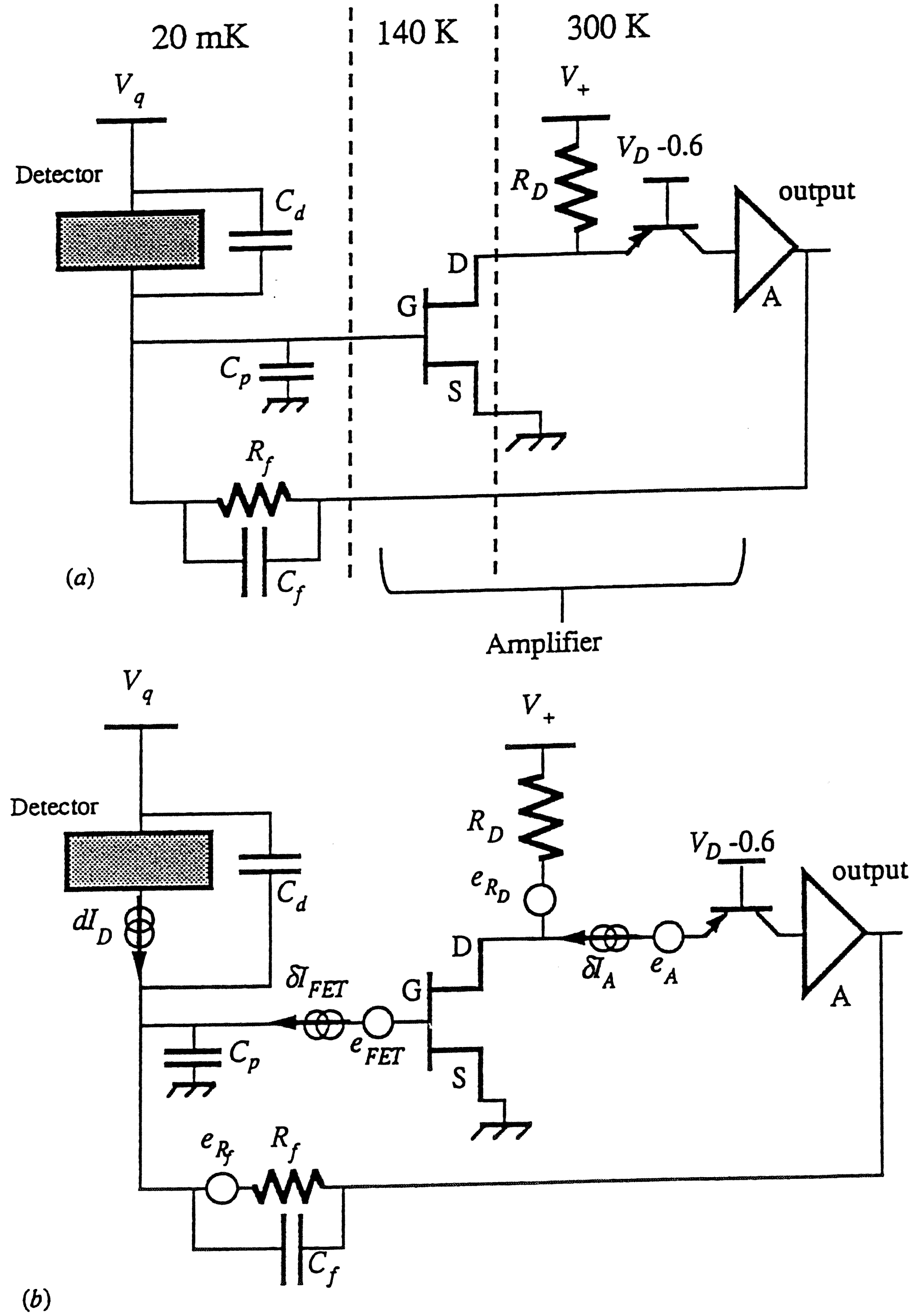

Figure E.3 Schematic of the charge measurement including simplified schematic of the charge amplifier (a) and noise analysis of the measurement (b).

the open loop situation, A responds with an enormous negative voltage on its output. With the feedback attached, however, this negative voltage allows the charge to flow across the feedback network, and not accumulate on the gate in the first place. The amplifier thus holds the gate voltage fixed by swinging its output voltage so that any current coming from the detector flows across the feedback network. Note that just as for the voltage amplifier, if the CASCODE circuit is not used on the drain, then the gate-drain capacitance effectively increases at high frequencies. As we shall show, this would cause an increase in the noise at high frequencies.

It will be useful in the discussion below to compare the noise in the frequency domain to the signal in the frequency domain. If in the time domain the current from the detector in an event is $I=Q\delta(t)$ where Q is the charge in coulombs, then in the frequency domain $I=Q$. Note that this assumes an infinitely fast rise time. The signal at the output of the amplifier is

$$v_o(f) = IZ_f = Q\frac{R_f}{1+i2\pi fR_fC_f}.$$

Defining

$$A(f) = \frac{R_f}{1+i2\pi fR_fC_f}, \tag{E.9}$$

the signal can be written

$$v_o = QA(f). \tag{E.10}$$

Since $A(f)$ has units of 1/resistance=capacitance/time, v_o has units of volts/time, as it should in the frequency domain.

E.5) Noise in the charge measurement

Figure E.3*b* shows a number of noise sources in the charge measurement. Since the charge measurement is a "transimpedance" measurement - it turns a current into a voltage - the noise is calculated at the output of the amplifier, not the input as is done for the voltage measurement. Another preliminary comment is that the that total capacitance at the gate is important for noise. The detector capacitance, C_D, and the parasitic capacitance C_p which includes the capacitances of the FET and gate wire, are both connected to fixed voltages. Since the noise is an AC signal for which a fixed, non zero voltage is equivalent to ground, these two capacitances act together as an input capacitance to the circuit, C_i=C_D+C_p. In all that follows we assume the amplifier has infinite gain, and thus its input remains strictly fixed. In reality at high frequencies this will not be true, and the noise will be somewhat different than that we obtain here.

The current noises from the detector, FET, and microphonics cannot flow across the input capacitance because this would change the gate voltage. Instead they must flow through the feedback network giving a noise at the output, e_o, equal to the current times Z_f, the feedback network impedance. This is

$$e_o^2 = \left(\delta I_D^2 + \delta I_{FET}^2 + \delta I_\mu^2\right)\left|\frac{R_f}{1+i\omega R_f C_f}\right|^2 . \qquad \text{E.11}$$

In the actual setup with the FET cooled to ≈140 K and the detector at 20 mK, we believe these current noise sources are negligible, but we have not carefully confirmed this. The microphonic current is typically not flat in the frequency domain but instead has a somewhat $1/f$-like component and several sharp features at frequencies below a few kHz.

The Johnson noise of the feedback resistor, similarly, drives a current that cannot flow across C_i, nor into the gate or across the detector. By charge conservation this current can then not flow to the output either, but must be in a closed loop around C_f and R_f. This implies that

$$e_{R_f} - \delta I R_f - \delta I \frac{1}{i\omega C_f} = 0.$$

With the gate voltage fixed the output noise is given by the sum of the voltage noise and the voltage drop across R_f, which gives

$$e_o^2 = e_{R_f}^2\left|\frac{1}{1+i\omega R_f C_f}\right|^2 . \qquad \text{E.12}$$

The voltage noise of the FET has a somewhat different effect from these noise sources since it appears between the gate, which is strictly fixed, and the point at which the feedback network connects to the "gate". The voltage at this point where the feedback network connects can in fact vary when driven by the noise source, and, if it does, will drive current across C_i. Since this current cannot flow into the gate, it must by charge conservation also flow across the feedback network, causing a variation in the output voltage. With Z_f the impedance of the feedback network and Z_i the impedance to fixed voltage at the gate of the FET,

$$e_o = e_{FET} + \delta I Z_f$$

where

$$\delta I = \frac{e_{FET}}{Z_i}.$$

Finally,

$$e_o^2 = e_{FET}^2 \left| 1 + \frac{Z_f}{Z_i} \right|^2 . \qquad \text{E.13}$$

If the detector is not AC coupled to the amplifier then Z_i is only due to the input capacitance. Figure E.4 shows the circuit used when the detector is AC coupled to the amplifier to allow simultaneous ionization and phonon measurements. The AC coupling has the effect of only allowing currents faster than R_bC_c to enter the amplifier. This rolloff is typically picked to be much slower than the signal, so that in all of the discussion above the coupling capacitor can be ignored. The bias resistor, however, has two effects.

The input impedance in E.13 now is due to the parallel combination of the input capacitance and R_b. The FET noise term can then be explicitly written as

$$e_o^2 = e_{FET}^2 \left| 1 + \frac{R_f}{R_b} \frac{1 + i\omega C_i R_b}{1 + i\omega R_f C_f} \right|^2$$
$$= e_{FET}^2 \left| \frac{R_b + R_f + i\omega R_b R_f (C_i + C_f)}{R_b(1 + i\omega R_f C_f)} \right|^2 \qquad \text{E.14}$$
$$= e_{FET}^2 \left| \frac{R_f}{(1 + i\omega R_f C_f)} \left(\frac{1}{R_f} + \frac{1}{R_b} + i\omega (C_i + C_f) \right) \right|^2$$

where C_i must now include the capacitance of the bias resistor, or $C_i = C_d + C_p + C_b$.

The bias resistor also has a Johnson noise. This noise drives a current that flows across R_b and C_c into the amplifier. With the gate voltage fixed the net voltage change between V_q and the gate is zero, or

$$-\delta I R_b + e_{R_b} - \delta I \frac{1}{i\omega C_c} = 0.$$

(This ignores current that flows across the detector capacitance, but this current is less than the current that flows across C_c by a factor $C_d/C_c \approx 15$ pF/5000 pF. The current that flows across the bias resistor stray capacitance is even smaller.) The current that flows onto the gate is then

$$\delta I = e_{R_b} \frac{i\omega C_c}{1 + R_b i\omega C_c},$$

which is simply a current e_{R_b}/R_b that is passed only at frequencies greater than $1/(2\pi R_b C_c) \approx 0.3$ Hz. We thus ignore the low frequency roll-off and find that output voltage from the bias resistor Johnson noise is

$$e_o = \frac{e_{R_b}}{R_b} \frac{R_f}{1 + i\omega R_f C_f}.$$

Using the definition of Johnson noise we finally arrive at

$$e_o^2 = e_{R_f}^2 \frac{R_f}{R_b} \left| \frac{1}{1 + i\omega R_f C_f} \right|^2. \qquad \text{E.15}$$

This noise has the exact same effect as the feedback resistor's Johnson noise, but is scaled by a factor (in e^2) of R_f/R_b.

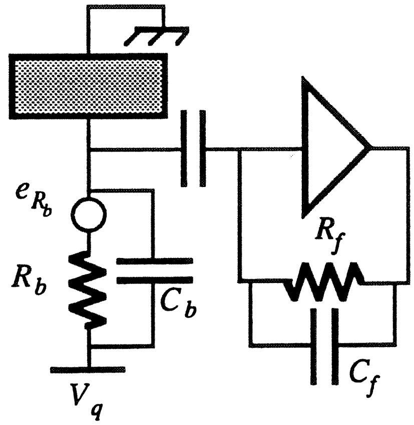

Figure E.4 Noise analysis of AC coupled charge circuit

The noise sources in the amplifier itself, just as for the voltage amplifier, have negligible effect. The Johnson noise of the R_D acts as a voltage noise on the drain, as does the voltage noise of A. As described above for the voltage amplifier, a voltage change at the drain is equivalent to a change voltage at the gate that has been divided by g_mR_D. With R_D=3 kΩ, $g_mR_D \approx 100$, and so both $e_{RD} \approx 7$ nV/Hz$^{1/2}$ and $e_A \approx 10$ nV/Hz$^{1/2}$ are negligible at the input compared to $e_{FET} \approx 1$ nV/HZ$^{1/2}$. The current noise from A directly causes a noise in I_{DS}, and is thus equivalent to a voltage noise at the gate of magnitude $\delta I_{FET}/g_m$. However δI_A is on the order of 1 pA/Hz$^{1/2}$ or even less, so this noise is also negligible.

The important noise terms from equations E.11 to E.15 can then be combined and written as

$$e_o^2 = |A(f)|^2 e_{FET}^2 \left\{ \left((C_i + C_f)^2 f^2 + \left(\frac{1}{R_f} + \frac{1}{R_b} \right)^2 \right) + 4kT\left(\frac{1}{R_f} + \frac{1}{R_b} \right) + \delta I_\mu^2 + \delta I_{FET}^2 + \delta I_D^2 \right\} \quad \text{E.16}$$

(current noise from FET, detector and microphonics

where the signal shape, $A(f)$, is defined in equation E.9. In figure E.5 we plot the total r.m.s. noise, e_o, and the r.m.s. contributions from the various pieces, with T=20 mK, R_f and R_b=100 MΩ, C_f=0.3 pF, C_i=60 pF, $e_{FET} \approx 1$ nV/Hz$^{1/2}$ and with the current noises

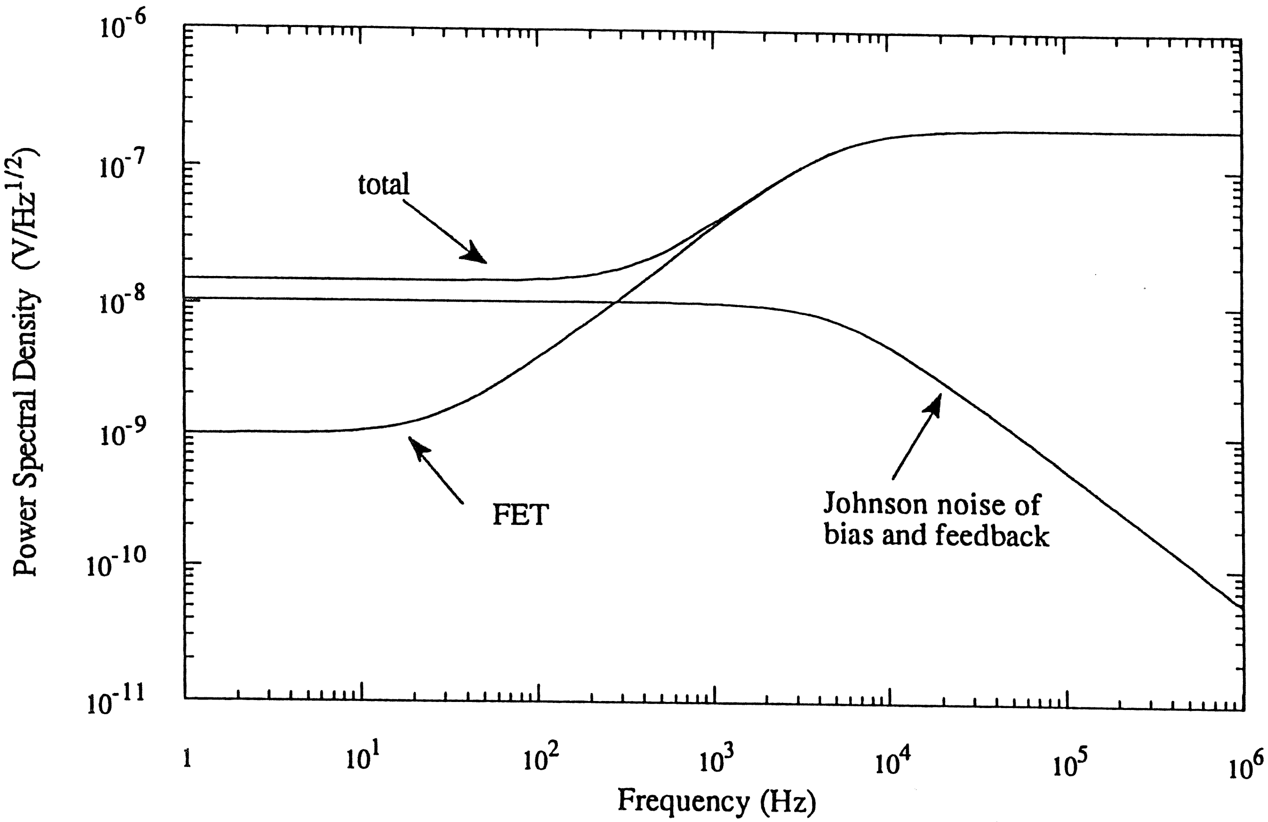

Figure E.5 Predicted noise in the charge measurement based on the circuit values discussed in the text.

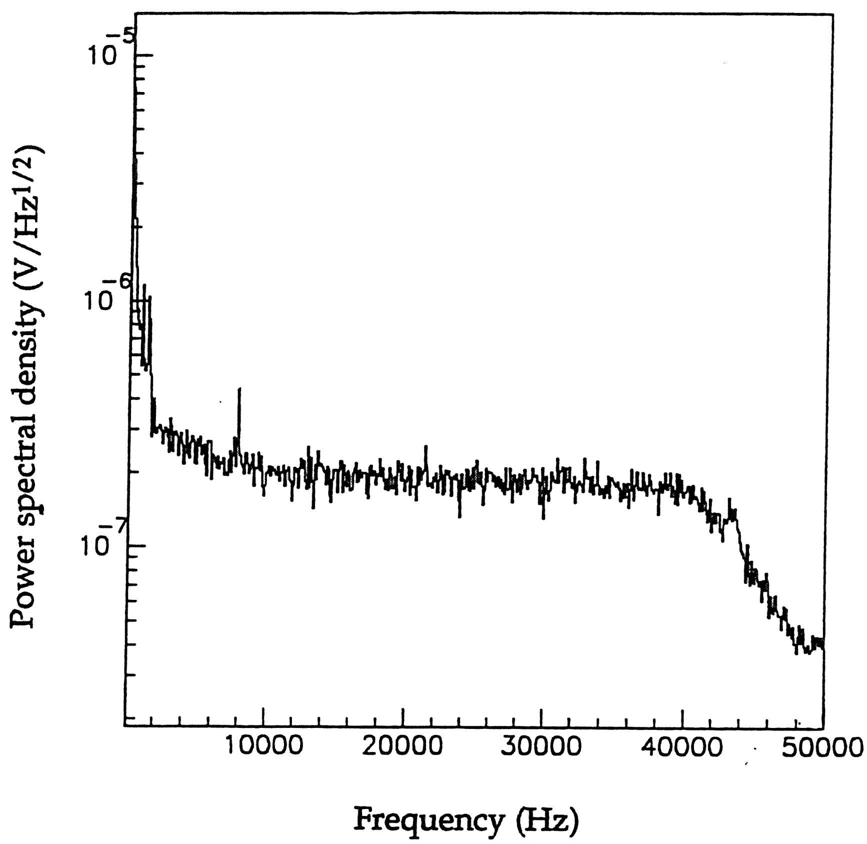

Figure E.6 Typical electronic noise in the ionization measurement.

taken to be zero. At frequencies well below $1/(2\pi R_f C_f)$ the Johnson noises dominates, while at high frequencies the FET noise dominates. The measured noise is shown in figure E.6, where the frequency scale is linear instead of logarithmic. This figure extends only to 50 kHz, and a steep anti-aliasing filter at 40 kHz has been employed. The flat noise continues at the same level out to the $\approx$ MHz roll-off frequency of the amplifier. The decrease in noise at low frequencies indicated in figure E.5 is not seen; to the contrary there is a large rise at frequencies below 2 kHz. We believe that this is mainly due to microphonics.

In appendix F we discuss the optimal filtering of signals and deduce the resolution expected with the noise given by equation E.16.

E.4) A quick note on FET Noise

The voltage noise of the FETs is one of the dominant noise sources in both measurements, and therefore one of the most important to reduce. This noise depends on several parameters. The variation with temperature is (90)

$$e_{FET}^2 = 4kT\frac{2}{3}\frac{1}{g_m}, \qquad \text{E.17}$$

which is essentially a Johnson noise with a resistance of $1/g_m$. The noise thus decreases as the temperature is decreased, but at some point the FET begins to freezeout and the noise increases dramatically. The temperature where this happens depends on the doping level of the FET, and for the FETs is at about 140 K. By equation E.17 this means the noise is a factor of $\approx\sqrt{2}$ below the room temperature noise. There is also a weaker decrease in the noise as the power dissipated by the FET, $I_{DS}V_{DS}$, is increased. In a full-scale dark matter experiment with many FETs there may well be a trade off between the tolerable heat load and the minimum FET noise. Finally, the noise decreases roughly as the inverse square root of gate-source capacitance, which, along with g_m, is basically determined by the geometry of the FET. In the charge amplifier the dominant noise is given by the FET noise times the input capacitance. Ideally the input capacitance should be dominated by the sum of the detector capacitance and the gate-source capacitance of the FET, with the parasitic capacitance on the cabling made very small. It is easy to show in this case that the lowest noise is obtained when the FET is selected so that the gate-source capacitance and detector capacitance are matched.

Appendix F: Optimal filtering

In this appendix we discuss the estimates of the signal amplitude for the ionization and phonon measurements. We do not attempt to explain underlying concepts of statistical analysis. For a more complete discussion the reader is referred to (91, 92).

The raw signals consist of a time series of the digitized voltages, $v(t_n)$. To a reasonable approximation, the events in our detector have a shape that is independent of the amplitude. We can then write

$$v(t_n)=as(t_n)+\sigma$$

where a is the amplitude of the underlying shape, $s(t_n)$ and σ is the noise in the measurement. The template $s(t_n)$ can be found by averaging many events that are carefully selected to be free of pathologies such as pile-up or clipping, or, alternatively, from a theoretical knowledge of the signal. The noise has been discussed in detail in appendix E. We seek a prescription for estimating a from $s(t_n)$ and $v(t_n)$ in the face of this noise.

F.1 Correlation of noise in the time domain

The noise is by definition a fluctuation in voltage that cannot be predicted. However in general the noise voltage at one point in time can be related to the noise voltage at another point of time. Let $\delta v(t)$ be the noise voltage. The correlation function for voltages separated by at time τ is

$$K(\tau)=\frac{1}{2T}\int_{-T}^{T}\delta v(t+\tau)\delta v(\tau)dt \quad .$$

If $\delta v(t)$ is completely uncorrelated between any two times, then $K(\tau)$ will clearly be zero. Following the argument in section 1 of appendix E, it is easy to show that $K(\tau)$ is related to the power spectral density of the noise by

$$K(\tau)=\int_0^\infty |e(f)|^2 e^{i2\pi f\tau}df \ . \qquad \text{F.1}$$

Note that if τ=0, we have

$$K(0)=\left\langle \delta v^2(t)\right\rangle=\int_0^\infty |e(f)|^2 df ,$$

which is consistent with the results in appendix E.

Equation F.1 shows that the correlation between the noise at any two times is intimately related to the behavior of the noise in the frequency domain. For instance, a microphonic excitation at one frequency is $e(f)=e_0\delta(f)$, and by equation F.1, $K(\tau)\approx e_o\cos(2\pi f\tau)$. The noise is correlated for as long as the oscillation is coherent. At the opposite extreme is white noise, or $e(f)$ independent of f. Suppose we have white noise that extends to a sharp cutoff frequency f_c. Equation F.1 becomes

$$K(\tau)=\frac{1}{2\pi\tau}\sin\left(2\pi f_c\tau\right). \qquad \text{F.2}$$

The first zeros of equation F.2 are at $\tau=\pm f_c/4$, and the noise is correlated on a time scale shorter than $f_c/2$. This result is directly related to the Nyquist theorem. Note that if $f_c\rightarrow\infty$, $K(\tau)\rightarrow\delta(\tau)$, and any two voltages at different times are completely uncorrelated.

F.2) Estimate of one amplitude in the frequency domain

In the standard method of estimating a parameter through the minimization of a "chi-square", the equations are much simpler if the errors on each measurement are independent. Since in general the noise is not flat in the frequency domain, and hence is correlated in the time domain, we construct the following chi-square in the frequency domain

$$\chi^2=\sum_{\mathrm{n}}\Delta f\frac{|v(f_{\mathrm{n}})-as(f_{\mathrm{n}})|^2}{\sigma^2(f_{\mathrm{n}})}.$$

Here $v(f_n)$ and $s(f_n)$ are the discrete Fourier transforms of $v(t_n)$ and $s(t_n)$, Δf is the frequency interval of the discrete transform, and the sum runs over frequencies. The noise at a given frequency is given by $\sigma(f_n)=e(f)$. The amplitude a is found by minimizing this chi-square with respect to a. We set

$$\frac{d\chi^2}{da}=\sum_{n}\Delta f\frac{-(v(f_n)-as(f_n))s^*(f_n)-s(f_n)\left(v^*(f_n)-as^*(f_n)\right)}{\sigma^2(f_n)}=0.$$

which gives

$$a=\frac{\sum_{n}\frac{\mathrm{Re}\left(v(f_n)s(f_n)\right)}{\sigma^2(f_n)}}{\sum_{n}\frac{|s(f_n)|^2}{\sigma^2(f_n)}} \quad . \qquad \text{F.3}$$

The term "optimal filter" now becomes clear: in the numerator the signal at each frequency, $v(f_n)$, is weighted by $s(f_n)/\sigma^2(f_n)$, so that frequencies with large signal to noise are emphasized.

The parameter a is not perfectly estimated because of the noise on each voltage measurement. A general theorem from statistics is that the error on a, or σ_a, is given by

$$\left(\sigma_a^2\right)^{-1}=\frac{1}{2}\frac{d^2\chi^2}{da^2}, \qquad \text{F.4}$$

which gives

$$\left(\sigma_a^2\right)^{-1}=\sum_{n}\frac{|s(f_n)|^2}{\sigma^2(f_n)}. \qquad \text{F.5}$$

F.3 Estimate of one amplitude in the time domain

Currently the noise in our measurements is basically flat in the frequency domain. In this case we can construct a chi-square in the time domain:

$$\chi^2=\frac{1}{\sigma^2}\sum_{n}\left(v(t_n)-as(t_n)\right)^2.$$

The noise on each sample, σ, is given by σ, is given by

$$\sigma^2=\int_0^\infty e^2 df.$$

If the bandwidth is taken to end abruptly at a frequency f_c, then $\sigma^2 = e^2 f_c$. Minimizing the chi-square we find

$$a = \frac{\sum_n v(t_n) s(t_n)}{\sum_n s^2(t_n)}, \tag{F.6}$$

If each sample is independent, then the error on a is given by the time-domain analog of equation F.4. It is possible to show that equation F.4 is equivalent to

$$\sigma_a^2 = \sum_n \left(\frac{\partial a}{\partial v(t_n)} \right)^2 \sigma^2(t_n).$$

In this formula the error on a is the error on each data point times the amount that each data point contributes to the estimate of a. Using equation F.6, this gives

$$\sigma_a^2 = \frac{\sigma^2}{\sum_n s^2(t_n)} . \tag{F.7}$$

Unfortunately, however, we usually sample our events faster than the Nyquist criterion, and so the errors on each sample are not independent, and equation F.7 does not correctly estimate the error on a. Note in particular that if we sample infinitely quickly, equation F.7 predicts that $\sigma_a \rightarrow 0$. We can approximately correct this formula by multiplying $\sigma_a{}^2$ by the ratio of dependent to independent samples.

F.4 General linear fit in the time domain

The fits we actually use on the ionization and phonon signals are slightly more complicated than the one above. The ionization is fit to an amplitude of a template event, plus an offset. That is, with the signal is fit to

$$f(t_n) = a_1 + a_2 s_2(t_n) \tag{F.8}$$

where $s_2(t_n)$ is the template signal. The coefficients a_1 and a_2 are found by minimizing

if $a_1 \neq 0$;

the chi-square

$$a_2 = \frac{\sum_n v_n S_n - \sum_n S_n \cdot \sum_m V_m}{\sum_n S_n^2 - \sum_n S_n \cdot \sum_m S_m}$$

$$\chi^2 = \frac{1}{\sigma^2}\sum_{n}\left(v(t_n) - f(t_n)\right)^2 \qquad \text{F.9}$$

with respect to a_1 and a_2. For the phonon signal we deal with event pileup by adding a falling exponential term, so that

$$f(t_n)=a_1+a_2s_2(t_n)+a_3s_3(t_n) \qquad \text{F.10}$$

where $s_2(t_n)$ is the template signal, $s_3(t_n)$ is given by

$$s_3(t_n) = e^{-\frac{t_n}{\tau}},$$

and the time constant, τ, is fixed.

Both equation F.8 and F.10 are linear in the fit amplitudes $\{a_i\}$, thus we then get a set of linear equations when the chi-square in equation F.9 is minimized with respect to all the $\{a_i\}$. Quite generally, with

$$f(t_n) = \sum_{i} a_i s_i(t_n)$$

and defining

$$A_{ij} = \frac{1}{\sigma^2}\sum_{n} s_i(t_n) s_j(t_n) \qquad \text{F.11a}$$

and

$$B_k = \frac{1}{\sigma^2}\sum_{n} v(t_n) s_k(t_n), \qquad \text{F.11b}$$

it is easy to show that the $\{a_i\}$ are given by

$$a_i = \sum_{k} A^{-1}_{ik} B_k. \qquad \text{F.11c}$$

A bit more algebra shows that the error on each a_i, assuming independent samples, is

$$\sigma^2_{a_i} = A^{-1}_{ii}. \qquad \text{F.11d}$$

Once again, however, if the samples are not independent, this error should be scaled by the ratio of dependent to independent samples.

The equations F.11 are all we need to perform the fit. The most time intensive computation is the inversion of the matrix A. Note however that A depends only on the template functions $\{s_i\}$, and so needs only to be evaluated once. The errors $\{\sigma_{ai}\}$ are also evaluated only from the $\{s_i\}$. In the data acquisition software documented in appendix H, the signals are fit online using this procedure.

F.5) Comparison with measured resolution

Ideally, we would fit in the frequency domain, and the estimation of errors would be unambiguous. Failing this, we can compare the crude estimate based on F.11d with the baseline noise in the measured spectra, which is discussed in chapter 6. In the fit by equation F.11 we need to know the noise on each sample. In the voltage measurement we have a power spectral density of $\approx$1.5 nV/Hz$^{1/2}$, and use a filter that has a corner frequency of 200 Hz, but not a sharp cutoff. If we choose 250 Hz as an approximate bandwidth, then σ=24 nV. With this 200 Hz filter, samples separated by less than 1/($\approx$400 Hz) should be uncorrelated, but we actually sample at 5 kHz. Thus the σ^2 in equation F.11d should be multiplied by roughly 12.5. In the charge measurement we have $\approx$200 nV/Hz noise and a shallow cutoff at 200 kHz. Using a bandwidth of 250 kHz we find σ=0.10 mV. Again samples are uncorrelated when separted by less than 1/($\approx$400 kHz), but we actually sample at 5 MHz, thus we multiply σ^2 by 12.5.

If the template event, s, is in units of voltage (e.g., if it is constructed from actual events), then a is unitless, and so is the error we estimate. The signals are then scaled by the calibration of the spectrum. In electron equivalent energy this means setting the 60 keV pulses to 60 keV. In electron equivalent energy units the numerically evaluated errors using the above numbers are σ= 425 eV in phonons, and σ= 620 eV in ionization. These numbers agree roughly with the 600 eV and 500 eV measured baselines.

Finally, it is interesting to consider a fit in the frequency domain. If we fit only for amplitude (and not the baseline or pulse-pileup), the variance on the amplitude can be calculated from the continuum limit of equation F.5, namely

$$\sigma_a^2 = \frac{1}{2\int_{-\infty}^{\infty}\left|\frac{A(f)}{e(f)}\right|^2 df}. \tag{F.12}$$

The factor of two arises from the fact that we integrate over positive and negative frequencies, yet use $e(f)$ to describe the noise.

To illustrate the method, we approximate our signals by an infinitely fast rise followed by a simple exponential fall, or

$$S(t) = \begin{cases} ae^{-s_o t} & t > 0 \\ 0 & t < 0 \end{cases}$$

where $s_o=1/\tau$, and τ is the fall time. The Fourier transform of this is

$$\begin{aligned} S(f) &= a\frac{1}{s_o + i2\pi f} \\ &= aA(f) \end{aligned}$$

where

$$A(f) = \frac{1}{s_o + i2\pi f}.$$

For phonons, the noise is flat in the frequency domain, and so the integral in equation E.7 is of the form

$$\int_{-\infty}^{\infty}\frac{dx}{a+bx^2} = \frac{\pi}{\sqrt{ab}} \tag{F.13}$$

with $a=s_o{}^2$ and $b=(2\pi)^2$. If the dominant noise is from the FET, so that $e_v=e_{\rm FET}$, we find

$$\sigma_a^2 = \frac{e_{FET}^2}{\tau}. \tag{F.14}$$

Using τ=0.05 sec and e_{FET}=1.5 nV/Hz$^{1/2}$, we find σ_a=6.7 nV. Our 60 keV signals have a pulse height, a, of 2.4 μV, so we scale σ_a by (60 keV/2.4 μV) and find an expected resolution of 167 eV. Part of the reason we do not actually attain such a low level is that we fit for three quantities at once, so the error on each is increased.

If the dominant noise is not that of the FET but is instead due to the intrinsic thermodynamic fluctuations in temperature and Johnson noise in the resistor, then the analysis is somewhat different. For an interesting discussion of this subject, see the papers by Mather and collaborators (47, 48).

The noise in the charge measurement is given by equation E.16, and the signal is given by equation E.9. Using these equations, the factor $A(f)$ scales out of the integral in equation F.12, and the integral is again of the form of equation F.13. We find directly that

$$\sigma_a^2 = e_{FET}(C_i + C_f)\left[e_{FET}^2\left(\frac{1}{R_f}+\frac{1}{R_b}\right)^2 + 4kT\left(\frac{1}{R_f}+\frac{1}{R_b}\right) + \delta I_\mu^2 + \delta I_{FET}^2 + \delta I_D^2\right]^{\frac{1}{2}}. \tag{F.15}$$

If we ignore the current noise, and take e_{FET}=1.5 nV/Hz$^{1/2}$, T=0.02 K, R_f=R_b=100 MΩ, C_i=80 pF, and C_f=0.4 pF, we find σ_a=26 e$^-$. The main reason this is considerably less than our current resolution is that we are dominated by microphonics at low frequencies, and thus cannot take advantage of the favorable signal to noise (apart from microphonics) at low frequencies.

Appendix G: Calculation of thermal pulses

G.1) Static equations

In this section we calculate the phonon pulses in the detector within the thermal model shown in figure 4.3. We first write down the thermal and electrical equations which describe the static situation. With V, v, R and r defined in figure 4.3, the electrical power on the electrons is

$$P_{ele} = \frac{v^2}{r} \tag{G.1}$$

where

$$v = V\frac{r}{R+r} = V\frac{R_{\parallel}}{R} \tag{G.2}$$

with parallel resistance $R_{//}^{-1}=r^{-1}+R^{-1}$. The current in the sensor is $i=v/r$. The resistance depends on the electron temperature as

$$r = R_o e^{\sqrt{\frac{\Delta}{T_e}}}. \tag{G.3}$$

The power flowing from the electrons to the phonons is

$$P_{e\varphi} = g_{e\varphi}(T_e^{\alpha} - T_{\varphi}^{\alpha}), \tag{G.4}$$

and the power flowing from the phonons to the heat sink is

$$P_{\varphi s} = g_{\varphi s}(T_{\varphi}^{\beta} - T_s^{\beta}). \tag{G.5}$$

In equilibrium the power flows must be conserved, and so $P_{ele}=P_{e\varphi}=P_{\varphi s}$.

To actually solve these equations to obtain an IV curve, it is easiest *not* to start with the bias voltage V. Instead specify the power, find the temperatures from equation G.4 and G.5, find r from equation G.3, and then compute v, i, and V from equations G.1 and G.2.

G.2 Linearized equations for perturbation with no electrical time constant

We must add one more basic idea to the static equations above in order to understand the dynamic behavior of the system, namely we need an equation of state relating the energy and temperature. If the energy in a system, E, changes in response to a net power on the system, $P=dE/dt$, we write

$$P = \frac{\partial E}{\partial T}\frac{dT}{dt} = C\dot{T} \qquad \text{G.6}$$

where

$$C \equiv \frac{\partial E(T)}{\partial T}$$

is the heat capacity, and we use the notation $dT/dt \equiv \dot{T}$.

We treat the complicated phonon physics of the event as consisting of a power $\delta P_e(t)$ on the electrons, and a power $\delta P_\varphi(t)$ on the phonons, whose form we shall specify later. In principle equations G.1-G.6 and these two powers completely determine the system, and we can solve for the signal $v(t)$. However it does not appear possible to obtain an analytical solution to these highly non-linear equations.

Instead we solve the equations to first order in a small perturbation in all variables. For the electrons equation G.6 becomes

$$C_e\delta\dot{T}_e = \delta P = \delta P_e + \delta P_{ele} - \delta P_{e\varphi}. \qquad \text{G.7}$$

where the input power is the sum of the electrical power, P_{ele}, the high energy phonons created by the event, P_e, and the power loss to the phonons, $P_{e\varphi}$. By equation G.4, this last term is

$$\begin{aligned}\delta P_{e\varphi} &= \alpha g_{e\varphi}T_e^{\alpha-1}\delta T_e - \alpha g_{e\varphi}T_\varphi^{\alpha-1}\delta T_\varphi \\ &\equiv G_{e\varphi}\delta T_e - G_{\varphi e}\delta T_\varphi\end{aligned} \qquad \text{G.8}$$

where we have defined the conductances $G_{e\varphi}$ and $G_{\varphi e}$.

In general we should include the capacitances in the electrical circuit in the computation of the pulses. However in E2 the electrical time constants are usually faster than all the other time scales, so we can greatly simplify the equations by treating the circuit as purely resistive. In this case the change in electrical power is

$$\delta P_{ele} = \delta\left(\frac{v^2}{r}\right) = \frac{2v}{r}\delta v - \frac{v^2}{r}\delta r.$$

The change in voltage is

$$\begin{aligned}\delta v &= \delta\left(V\frac{r}{R+r}\right) = V\frac{R}{(R+r)^2}\delta r \\ &= R_{\parallel}\frac{v}{r^2}\delta r,\end{aligned} \qquad \text{G.9}$$

and so

$$\begin{aligned}\delta P_{ele} &= \frac{v^2}{r^2}\left(2\frac{R}{R+r} - 1\right)\delta r \\ &= \frac{R-r}{R+r}\frac{v^2}{r^2}\frac{\partial r}{\partial T}\delta T_e.\end{aligned} \qquad \text{G.10}$$

Combing these equations we get

$$C_e\delta\dot{T}_e = \delta P_e + \frac{R-r}{R+r}\frac{v^2}{r^2}\frac{\partial r}{\partial T}\delta T_e - G_{e\varphi}\delta T_e + G_{\varphi e}\delta T_\varphi.$$

If we define

$$s_e = \frac{1}{\tau_e} = \frac{G_{e\varphi}}{C_e}\left(1 - \frac{R-r}{R+r}\frac{P_{ele}}{G_{e\varphi}}\frac{1}{r}\frac{\partial r}{\partial T}\right), \qquad \text{G.11}$$

which is basically the electron phonon decoupling time, $C_e/G_{e\varphi}$, but modified by thermal feedback, we can write

$$\delta\dot{T}_e + s_e\delta T_e - \frac{G_{\varphi e}}{C_e}\delta T_\varphi = \frac{1}{C_e}\delta P_e \qquad \text{G.12}$$

For phonons, equation G.6 is

$$C_\varphi\delta\dot{T}_\varphi = \delta P = \delta P_\varphi + \delta P_{e\varphi} - \delta P_{\varphi s}.$$

P_φ is the power from thermal phonons created by an event, $P_{e\varphi}$ is given by equation G.8, and the power flowing to the heat sink, $\delta P_{\varphi s}$, by equation G.5, is

$$\begin{aligned}\delta P_{\varphi s} &= \beta g_{\varphi s}T_\varphi^{\beta-1}\delta T_\varphi \\ &= G_{\varphi s}\delta T_\varphi,\end{aligned}$$

where we have defined the conductance $G_{\varphi s}$. Using this, we have

$$C_\varphi \delta\dot{T}_\varphi = \delta P_\varphi + G_{e\varphi}\delta T_e - G_{\varphi e}\delta T_\varphi - G_{\varphi s}\delta T_{\varphi s}.$$

If we define

$$s_\varphi = \frac{1}{\tau_\varphi} = \frac{G_{\varphi s}}{C_\varphi}, \qquad \text{G.13}$$

which is time constant of the crystal, we finally find

$$\delta\dot{T}_\varphi + \left(s_\varphi + \frac{G_{\varphi e}}{C_\varphi}\right)\delta T_\varphi - \frac{G_{e\varphi}}{C_\varphi}\delta T_e = \frac{1}{C_\varphi}\delta P_\varphi. \qquad \text{G.14}$$

We need now only solve equations G.12 and G.14 for δT_e, and can then use equation G.9 to directly get δv from δT_e with $\partial r/\partial T$ determined from equation G.3. It is easy to solve the differntial equations G.12 and G.14 if we take the Laplace transform of each. The Laplace transform of a function $f(t)$ is defined as

$$L(f(t)) = \tilde{f}(s) = \int_0^\infty f(t)e^{-st}dt.$$

After taking the transform of both equations we solve algebraically for $\delta\tilde{T}_e$ and then perform and inverse transform to find δT_e. We in fact need only the following transforms:

$$\begin{aligned} &L\left(e^{-s_o t}\right) = \frac{1}{s+s_o} \\ &L(\delta(t=0)) = 1 \\ &L\left(\dot{f}\right) = s\tilde{f}(s) - f(t=0). \end{aligned} \qquad \text{G.15}$$

Applying the transform to equations G.12 and G.14, we find

$$(s+s_e)\delta\tilde{T}_e - \frac{G_{\varphi e}}{C_e}\delta\tilde{T}_\varphi = \frac{1}{C_e}\delta\tilde{P}_e \qquad \text{G.16}$$

and

$$\left(s + s_\varphi + \frac{G_{\varphi e}}{C_\varphi}\right)\delta\tilde{T}_\varphi - \frac{G_{e\varphi}}{C_\varphi}\delta\tilde{T}_e = \frac{1}{C_\varphi}\delta\tilde{P}_\varphi. \qquad \text{G.17}$$

Multiplying equation G.16 by the coefficient of $\delta\tilde{T}_\varphi$ in equation G.17 we have

$$(s+s_e)\left(s+s_\varphi+\frac{G_{\varphi e}}{C_\varphi}\right)\delta\tilde{T}_e - \frac{G_{\varphi e}}{C_e}\left(\frac{G_{e\varphi}}{C_\varphi}\delta\tilde{T}_e + \frac{1}{C_\varphi}\delta\tilde{P}_\varphi\right) = \frac{1}{C_e}\left(s+s_\varphi+\frac{G_{\varphi e}}{C_\varphi}\right)\delta\tilde{P}_e$$

which can be immediately rearranged as

$$\delta\tilde{T}_e = \frac{1}{(s+s_e)\left(s+s_\varphi+\frac{G_{\varphi e}}{C_\varphi}\right)-\frac{G_{\varphi e}}{C_e}\frac{G_{e\varphi}}{C_\varphi}}\left\{\frac{G_{\varphi e}}{C_e}\frac{1}{C_\varphi}\delta\tilde{P}_\varphi+\frac{1}{C_e}\left(s+s_\varphi+\frac{G_{\varphi e}}{C_\varphi}\right)\delta\tilde{P}_e\right\}$$

G.18

We need to factor the denominator in order to perform an inverse transform. That is, writing the denominator as $s^2+2bs+c$, we would like to find s_1 and s_2 in

$$(s+s_1)(s+s_2)=s^2+2bs+c.$$

where by inspection

$$2b = s_e + s_\varphi + \frac{G_{\varphi e}}{C_\varphi}$$

and

$$c = s_e\left(s_\varphi + \frac{G_{\varphi e}}{C_\varphi}\right) - \frac{G_{\varphi e}}{C_\varphi}\frac{G_{e\varphi}}{C_e}.$$

Solving this we find that s_1 and s_2 are the roots of

$$s^2-2bs+c=0,$$

which is

$$s_1 = b+\sqrt{b^2-c} = b\left(1+\sqrt{1-\frac{c}{b^2}}\right) \qquad \text{G.19a}$$

and

$$s_2 = 2b - s_1. \qquad \text{G.19b}$$

For the case of $s_e \gg s_\varphi$, we can obtain a simple approximation for s_1 and s_2 as follows. We let

$$as_e = \frac{G_{e\varphi}}{C_e} \qquad \text{G.20}$$

so that, by equation G.11,

$$a = \frac{1}{1-\frac{R-r}{R+r}\frac{P_{ele}}{G_{e\varphi}}\frac{1}{r}\frac{\partial r}{\partial T}}.$$

We now can write

$$c = s_e\left(s_\varphi + \frac{G_{\varphi e}}{C_\varphi}(1-a)\right).$$

If $s_e \gg s_\varphi$ and $s_e \gg G_{e\varphi}$, and the thermal feedback term in a is small so that a is on order of unity, then

$$\frac{c}{b^2} = 4\frac{s_e\left(s_\varphi + \frac{G_{\varphi e}}{C_\varphi}(1-a)\right)}{\left(s_e + s_\varphi + \frac{G_{\varphi e}}{C_\varphi}\right)^2} \ll 1.$$

In which case

$$s_1 \cong 2b - \frac{c}{2b} \cong s_e + a\frac{G_{\varphi e}}{C_\varphi} \qquad \text{G.21a}$$

and

$$\begin{aligned} s_2 &\cong \frac{c}{2b} \cong s_\varphi + \frac{G_{\varphi e}}{C_\varphi}(1-a) \\ &\cong s_\varphi + \frac{G_{\varphi e}}{C_\varphi}\frac{R-r}{R+r}\frac{P_{ele}}{G_{e\varphi}}\frac{1}{r}\frac{\partial r}{\partial T}. \end{aligned} \qquad \text{G.21b}$$

The time constants are close to s_e and s_φ Moreover, since $\partial r/\partial T$ is negative and usually $R \gg r$, a is positive and $s_1 > s_e$ and $s_2 < s_\varphi$.

With the values of s_1 and s_2 known, we can finally find $\delta\tilde{T}_e$ with δP_e and δP_φ, specified. From equation G.9, we can then directly find $\delta\tilde{v}$ via

$$\delta v = i\frac{R_{\|}}{r}\frac{\partial r}{\partial T}\delta T_e$$

where the current $i = v/r$. Usually $R \gg r$ and so $R_{//}/r \cong 1$. The value of $\partial r/\partial T$ is found from equation G.3. We finally have

$$\delta\tilde{v} = i\frac{R_{\|}}{r}\frac{\partial r}{\partial T}\frac{1}{(s+s_1)(s+s_2)}\left\{\frac{G_{\varphi e}}{C_\varphi}\frac{\delta\tilde{P}_\varphi + \delta\tilde{P}_e}{C_e} + \left(s + s_\varphi\right)\frac{\delta\tilde{P}_e}{C_e}\right\}. \qquad \text{G.22}$$

G.3) Fast phonon energy deposition

One possibility is that the high energy phonons live for a time that is short compared to s_1 and s_2. In this case we write

$$\delta P_e = \eta E_o \delta(t) \qquad \text{G.23a}$$

and

$$\delta P_\varphi = (1-\eta) E_o \delta(t) \qquad \text{G.23b}$$

where E_o is the energy from the event, and η is less than one and describes how much energy makes its way to the electrons in the sensors. Using equations G.15, we have

$$\delta\tilde{v} = i\frac{R_\parallel}{r}\frac{\partial r}{\partial T}\frac{1}{(s+s_1)(s+s_2)}\left(s + s_\varphi + \frac{1}{\eta}\frac{G_{\varphi e}}{C_\varphi}\right)\frac{\eta E_o}{C_e}.$$

The inverse transform of $(s+s_1)^{-1}$ is known, so we factor

$$\frac{s+s_o}{(s+s_1)(s+s_2)} = \frac{1}{(s_1-s_2)}\left\{\frac{s_1-s_o}{s+s_1} - \frac{s_2-s_o}{s+s_2}\right\}$$

and, using equation G.15, find

$$\delta v(t) = i\frac{R_\parallel}{r}\frac{\partial r}{\partial T}\frac{\eta E_o}{C_e}\frac{1}{s_1-s_2}\left\{\left(s_\varphi - s_2 + \frac{1}{\eta}\frac{G_{\varphi e}}{C_\varphi}\right)e^{-s_2 t} - \left(\frac{1}{\eta}\frac{G_{\varphi e}}{C_\varphi} - (s_1 - s_\varphi)\right)e^{-s_1 t}\right\}$$

G.24

Note by equation G.21b, that the coefficient to the s_2 exponential is positive, and thus $1/s_2$ is always a fall time. The s_1 term, on the other hand, is a rise time only if

$$\frac{1}{\eta}\frac{G_{\varphi e}}{C_\varphi} > (s_1 - s_\varphi)\ ,$$

which is to say that most of the energy is deposited in phonons. On the other hand if most of the energy is deposited in the electrons, the signal rises abruptly and there are two fall times.

Finally, the limiting case of a purely calorimetric signal is η=0, for which eqution G.24 becomes

$$\delta v(t) = i\frac{R_\parallel}{r}\frac{\partial r}{\partial T}\frac{E_o}{C_e}\frac{G_{\varphi e}}{C_\varphi}\frac{1}{s_1-s_2}\left\{e^{-s_2 t} - e^{-s_1 t}\right\}. \qquad \text{G.25}$$

If, also, $s_1 \gg s_2$, this becomes

$$\delta v(t) = i \frac{R_{\parallel}}{r} \frac{\partial r}{\partial T} \frac{E_o}{C_\varphi} \frac{G_{\varphi e}}{G_{e\varphi}} a \left\{ e^{-s_2 t} - e^{-s_1 t} \right\} \qquad \text{G.24}$$

where a is defined in equation G.19.

The optimal bias we use is a compromise between three things. First, we would like to increase the current i, since the signal increases linearly with it. On the other hand increasing i heats the electrons. The small price we pay for this is that $\partial r/dT$ drops via equation G.3. The heavy price we pay is the term

$$\frac{G_{\varphi e}}{G_{e\varphi}} = \left(\frac{T_\varphi}{T_e} \right)^{\alpha-1}$$

in equation G.24. Since α is on the order of 5 or 6 this decreases very quickly for $T_e > T_\varphi$. The temperature rise of the phonon system is just E_o/C_φ, so if we were measuring the phonons in the system directly this term would be absent.

There is a simple explanation for this term. When the thermistor is biased the electrons are always hotter than the phonons, thus power always flows from the electrons to the phonons, and not the other way around. The only way in fact that the electrons know about the event (in this case where high-energy phonons do not couple directly to the electrons) is that the power flowing from the electrons to the phonons changes when T_φ changes, as seen by equation G.4. This disturbance from the equilibrium situation of power-out equals power-in causes the electrons to heat up. However if T_e is much higher than T_φ, then the power flowing to the phonons has scarcely any dependence on the phonon temperature.

G.4 Reverberating phonons

One possiblity is that phonons with energies of ≈1 meV live for some time in a pure semiconductor at 20 mK. We model this case as

$$\delta P_e(t) = \eta s_h E_o e^{-s_h t} \qquad \text{G.26a}$$

and

$$\delta P_{\varphi}(t) = (1-\eta)s_h E_o e^{-s_h t} \qquad \text{G.26b}$$

where η describes the partitioning of energy into the electrons and phonons, and τ_h=1/s_h is the lifetimfe of the phonons. Taking the transform of these (equation G.15), and using equation G.22, we have

$$\delta\tilde{v} = i\frac{R_{\parallel}}{r}\frac{\partial r}{\partial T}\frac{1}{(s+s_1)(s+s_2)(s+s_h)}\left(s+s_{\varphi}+\frac{1}{\eta}\frac{G_{\varphi e}}{C_{\varphi}}\right)\frac{s_h E_o}{C_e}.$$

We define

$$s_o = s_{\varphi} + \frac{1}{\eta}\frac{G_{\varphi e}}{C_{\varphi}},$$

and then after a bit of factoring, obtain

$$\begin{aligned}\delta v(t) = i\frac{R_{\parallel}}{r}\frac{\partial r}{\partial T}\Bigg\{&\frac{s_o-s_2}{(s_1-s_2)(s_h-s_2)}e^{-s_2 t}+\frac{s_h-s_o}{(s_h-s_2)(s_1-s_h)}e^{-s_h t} \\ &-\frac{s_1-s_o}{(s_1-s_2)(s_1-s_h)}e^{-s_1 t}\Bigg\}\frac{\eta E_o s_h}{C_e}.\end{aligned} \qquad \text{G.27}$$

Note that we in fact have three time constants in our pulses, and had expected that the middle one is s_h. If s_1>s_h>s_2, and

$$s_1 > \frac{1}{\eta}\frac{G_{\varphi e}}{C_{\varphi}} + s_{\varphi},$$

which means much of the energy goes into electrons, then s_1 is a rise time ands_h and s_2 are fall times.

G.5) Electrical pulsing

The first evidence for the hot electron effect came from electrical measurements of a thermistor. The method involves adding a small time depdendent signal δV to the bias voltage V. This changes v directly, but also changes the electrical power. We find, instead of equation G.9,

$$\delta v = \delta\left(V\frac{r}{R+r}\right) = V\frac{R}{(R+r)^2}\delta r + \frac{r}{R+r}\delta V$$
$$= R_{\parallel}\frac{v}{r^2}\delta r + \frac{R_{\parallel}}{R}\delta V \qquad \text{G.28}$$

The change in electrical power, instead of equation G.10, becomes

$$\delta P_{ele} = \frac{2v}{r}\delta v - \frac{v^2}{r}\delta r = \left(\frac{R-r}{R+r}\right)\frac{v^2}{r^2}\delta v + \frac{2v}{r}\frac{R_{\parallel}}{r}\delta V. \qquad \text{G.29}$$

We can easily calculate the temperature change of the electrons from the work we have done above if we treat the term in equation G.29 that does not appear in equation G.10 as a power on the electrons, δP_e, and use the fact tha δP_{φ}=0. We find

$$\delta\tilde{T}_e = \frac{1}{(s+s_1)(s+s_2)}\left\{s+s_{\varphi}+\frac{G_{\varphi e}}{C_{\varphi}}\right\}\frac{1}{C_e}2\frac{v}{r}\frac{R_{\parallel}}{R}\delta\tilde{V}.$$

Using equation G.28, we then find the voltage pulse in the frequency domain

$$\delta\tilde{v} = \left[2i^2\frac{R_{\parallel}}{r}\frac{\partial r}{\partial T}\frac{1}{C_e}\frac{1}{(s+s_1)(s+s_2)}\left\{s+s_{\varphi}+\frac{G_{\varphi e}}{C_{\varphi}}\right\}+1\right]\frac{R_{\parallel}}{R}\delta\tilde{V}.$$

If $\delta V(t)$ is a step of magnitude δV, we find

$$\delta v(t) = \left[2i^2\frac{R_{\parallel}}{r}\frac{\partial r}{\partial T}\frac{1}{C_e}\frac{1}{s_1-s_2}\left\{\frac{s_1-s_{\varphi}-\frac{G_{\varphi e}}{C_{\varphi}}}{s+s_1}e^{-s_1 t}+\frac{s_{\varphi}+\frac{G_{\varphi e}}{C_{\varphi}}-s_2}{s+s_1}e^{-s_2 t}\right\}+1\right]\frac{R_{\parallel}}{R}\delta V.$$

G.30

Note that we have the same time constants as for events, and both are fall times.

Appendix H: Documentaion of data acquisition and analysis code

This appendix consists of the documentation to the data taking and analysis code that is currently being used to take data in our group.

DARK EVENT Documentation

DATA TAKING and ANALYSIS STRATEGIES

The data acquisition system consists of the program DARK_EVENT, which takes data from a CAMAC crate and performs some analysis, and DARK_SORT, which performs essentially the same analysis as DARK_EVENT but on previously taken data. We also have PAW, a very powerful program (if perhaps a bit too big for PASTRO) from CERN. Additionally, you can easily access the data using fortran routines in a library and do your own analysis.

I suggest you do initial analysis with DARK_EVENT and DARK_SORT. These programs currently can compute the following for events: power spectra, pulse heights, slopes (i.e. linear approximations of rise and fall times), fits to template functions, and an estimate of the number of counts in a given time window. They also average events, and events with an arbitrary number of exponentials, and fit gaussians to peaks in a histogram. Finally, they have a built spectrum analyzer. If you write your own code, you may find, at the moment, that your analysis strategy is driven by the inability to easily make plots on PASTRO. Thus if you have new ideas about how to process events, you might want to write small programs with no plotting, and use my programs to look at the events. It is also quite easy to use the FTP utility with TELNET to transfer files to the Macintoshes. If you merely want to look at events you create (e.g., a predicted pulse shape), you can do this using the "analysis array" part of my programs.

When you want to do a statistical analysis of many events, you might consider PAW. PAW, for all its charms, does not really know how to think about time traces. Its forte is dealing with "Ntuples" - a set of N quantities for each of many events. So what you can do is use my code or your own to reduce a bunch of time trace events into a set of Ntuples and then use PAW to sort these Ntuples. You can sort arbitrary functions of the Ntuple parameters with arbitrary cuts (e.g. you could sort the ratio of two pulse heights vs the logarithm of a fall time with cuts on yet another parameter). If you like fitting things, PAW will put you in hog heaven. If you dislike PAW, my code can do some sorting, and is slowly but seemingly inexorably gaining more of the functions of PAW.

USING DARK_EVENT

I describe the following here:

A.) General comments on running DARK_EVENT and DARK_SORT.

B.) "Defining the data" - setting up a CAMAC crate for data taking, and specifying comments.

C.) Taking events.

D.) Writing events.

E.) Displaying events.

F.) Reducing and sorting events.

H.) Miscellaneous other functions: fitting, spectrum analysis, averaging, ...

I.) A note on names of things and comments

A.) General comments on running DARK_EVENT and DARK_SORT.

Types of Commands

DARK_EVENT and DARK_SORT use a combination of menus and global commands. Certain types of functions, such as setting up a module, or setting up a type of analysis is done only in a specific subroutine, and there is a different menu for each such subroutine. Hitting return in any routine gives you the menu for that routine. In addition, there are a number of global commands valid in all routines, such as commands to display data or list various things. "H", for help, summarizes these, and typing the first letter of any global command will give you a list of the possible commands of that type. DARK_EVENT and DARK_SORT have a nearly complete online help.

One important note is the use of COMICS routines. COMICS is a I/O software package developed by the TPC group that I have used almost exclusively to enter lists of numbers. You are given a list of names of parameters and the current values of these parameters. Hit ? to get an explanation of the meaning of the parameters. To change a value, type enough characters to uniquely describe the name of the parameter, followed by "=" or a space, the value and then a space of comma and then the next parameter name a value. If you want to know more, there is documentation for the comics routines floating around.

Listing information

Many of the parameters of a data taking or analysis session can be listed by typing two letter commands that start with 'L'. Type only 'L' to get a list of all the list commands. Some of the more useful list commands are 'LD', which lists information about the data channels, 'LR' and 'LS', which list the reductions and sorts scheduled, and 'LE', which lists information about a given event in memory, including the value of all reduced quantities for this event.

Default settings files

For all of the things that have to be set up - data channels, reduction and sorting of events, and displaying of data, there is a system to save all the settings. In each routine where setting up occurs (for example, the routine for setting up sorting is reached by typing 'SS' from the main routine), the command 'EW' writes all the setting in memory to a file on disk. You are prompted for a 7 letter name which becomes part of the file name. If you pick the name of an existing file, the program will either make you specifically agree to delete the old file, or cancel the command. The command 'ER' reads the settings from an existing file.

When the program is first run, a file with the name "default" is read in all of the various routines. You will find it convenient to save the settings you develop during a run in a file with a descriptive name, and also in the file with the name "default". Be aware, however, that other people will eventually overwrite the file named default.

Note also that the commands 'EW' and 'ER' only read in the settings that can be set in the subroutine you are currently in. For example, if you are busy setting up the waveshape recorders, and then type 'EW', nothing you have done to setup the creation of pulse height spectra will be saved by this action. Routines that have this "default file" system have a small note to this effect at the begin of their command menus.

B.) Defining the data.

General comments

Type 'SE' in the main program to "define events". This means setting up and giving comments for the waveshape recorder (WR), the transient recorder (TR), (and, in the future, any other modules) You can also specify where the modules are placed in the CAMAC rack ("configure the crate"). Set up of a module consists of specifying necessary data taking parameters, and of giving comments associated with the data taken by the module at hand.

Data Channels -

This is my name for the voltage vs. time traces that are taken by the WRs and the TRs. Data channels are created whenever a WR or TR module is setup to take data. 'LD' gives data channel info.

WR (LeCroy 6810 waveshape recorder) -

Each WR has 1,2 or 4 data channels. These channels all have the same size and timing, but different ranges, coupling, offset.

'C' sets up: # of channels per recorder, range, coupling, offset, etc. One tricky point is the "offset". You give the portion of the full range that will be below 0.0 volts, in terms of input voltage to the module, NOT the voltage referred to the front end of the amplifier.

'S' sets up timing: Each WR can have 1,2 or 3 time scales. Using two different frequencies f1 and f2, the allowed time structures are f1,f1,f1; f1,f2,f2; f1,f1,f2; f1,f2,f1. The first frequency change is always the trigger point, the second is some number of samples (>4) after the trigger which you give as the "frequency change sample". The WR also measures the time between triggers, you set the resolution for this measurement (essentially a clock speed) in the timing section also.

Commands starting with 'R' set up the trigger. There is external and internal triggering. Internal triggering is always from channel 1. For all triggering, you have to specify such things as the level, slope, etc. I have included a few complete trigger setups (RA,RB,RC) which give a certain type of trigger. Note that the scope's logic trigger out puts out a funny inverse TTL, be careful to set 'RB' for scope TTL and 'RA' for normal TTL. Otherwise you can specify all the settings needed by the trigger explicitly. The upper and lower trigger levels are used when you have a "hysterisis" mode trigger (refer to the WR manual for more information about this.) There is also the trigger position, which is entered as the fraction of the event (given in eighths) which occurs before the trigger.

The WR is a complicated beast, I can't really hope to completely document it here. For any information that I've left out here, try the manual (in file cabinet in 79 in CAMAC modules folder) or talk to me directly.

Transient Recorder -

The transient recorders are like the WR, but are faster: 32MHz max, and have only 8-bit resolution. The setup is far easier than for the WRs since there is only one time scale and a set voltage range. It also has only external triggers, and the program only accepts triggering (LAMS) from TR # 1. My guess is that at the moment this part of the code will not work, though it would be easy to get working if you want to use the TRs.

Crate configuring-

Here you specify the slots in the crate used by the modules.

C.) Automated data reduction and sorting

Reductions:

The overall structure of the automated analysis built into the code is shown in figure 1 below. Calculations are used to reduce the events to create what I call "reduced quantities". These reduced quantities can then be sorted into histograms which, for some reason, I call "sorts". This type of analysis is automated in the sense that once the user has set up what is to happen, it will then occur automatically on all events taken multiply (with the command 'TM', as described below), and the histograms will accumulate. This is in contrast to, for example, fitting events with exponentials, which must be done by hand for each event.

The subroutine where this analysis is scheduled is reached by typing 'SS' in the main routine. Reductions of events are scheduled by typing 'AR' to add a reduction. Reductions already scheduled can be modified with 'MRN', where N is the number of the reduction. 'XRN' deletes reduction N. The list of currently scheduled reductions is found by typing 'LR'.

Each reduction is based on a calculation and a data channel, and on a set of variables that must be specified. For example, the calculation "pulse height" will be performed on a given data channel and needs to have two time windows specified: the time window in which to search for a maximum and the time window over which to calculate a baseline. Thus four different times are specified as variables when the reductions is specified. Note that the same calculation can be used more than once at the same time. For example you might calculate the pulse height for phonons and ionization. Or you might calculate the pulse height in ionization with two different baseline time windows to see how the baseline affects the calculation. The calculations currently included in the code are listed by typing 'LC'.

Some calculations produce more than one answer, for example "Two Fit" finds an offset, an amplitude and the chisquare of the fit. For all calculations, even if there is only one output, the results of a given reduction of a data channel are called "reduced quantities", or RQs. Each RQ is specified by two numbers, the number of the scheduled reduction that created it, or R, and a second number, Q, which specifies the output from a given calculation. For example, when a reduction based upon the calculation "Two Fit" is scheduled, R will depend on how many reductions have already been scheduled. However the offset will always be Q=1, the amplitude Q=2, and the chisquare Q=3. These ideas are illustrated in table 1 which show explicitly what might go into scheduling several reductions.

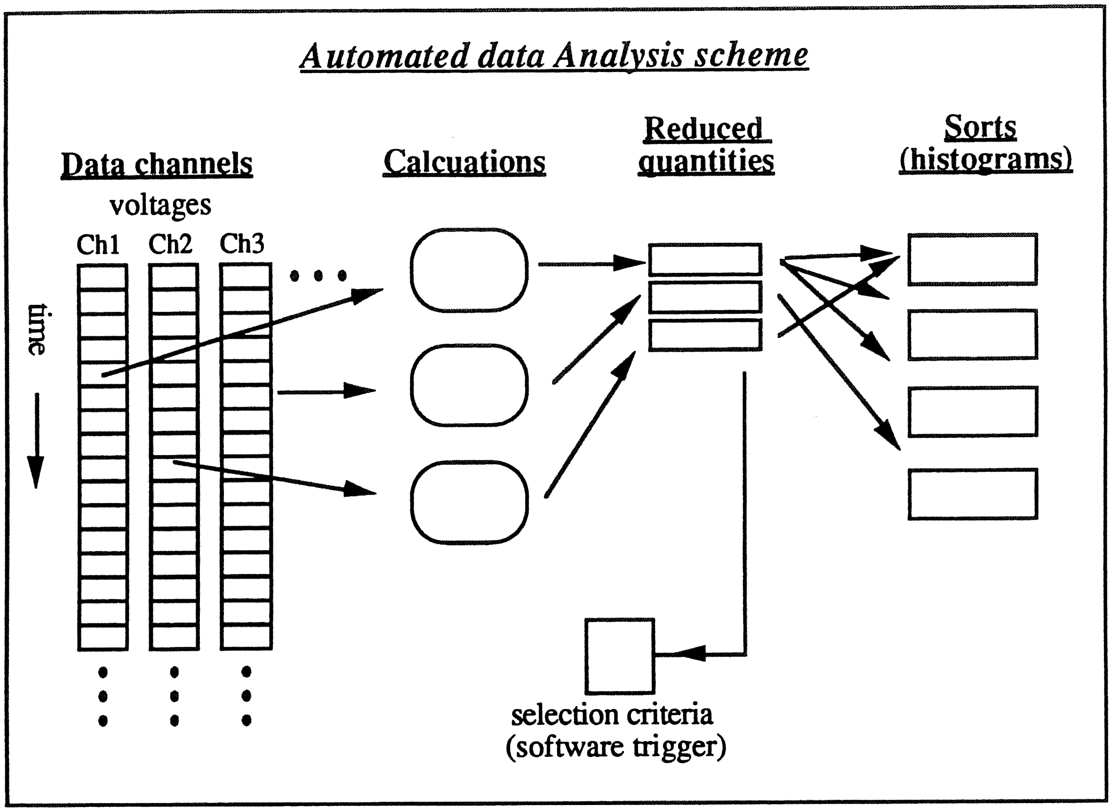

Figure 1 Architecture of automated data analysis structure

Table 1 Example of scheduled reductions

Reduction	Based on:			Result
	calculation	data channel	variable values	
1	1 (=pulse height)	2	T1=-10 mS T2=-5 mS T3=0 mS T4=15 mS	R1Q1 (=pulse height)
2	7 (=two fit)	2	File pointer=1	R2Q1 (=offset) R2Q2 (=amplitude) R2Q3 (=chisquare)
3	7 (=two fit)	1	File pointer=7	R3Q1 (=offset) R3Q2 (=amplitude) R3Q3 (=chisquare)

Sorts

Once the reductions are scheduled, they can be sorted. Both 1 and 2 dimensional sorts are allowed. To create a sort to add to the sort schedule type 'AS'; to modify an existing sort type 'MSN', where N is the number of the sort; 'XSN' deletes sort N. You must specify the R and Q values for each reduced quantity sorted, and a range of the values. Unfortunately the sorting ability is rather limited - only the direct RQ values can be sorted, not mathematical functions of these variables. You can set up cuts on various reduced quantities individually for each histogram. Cuts are setup in the routine reached by typing 'SC' in the reduction scheduling routine. Again, to add a cut type 'AC'; to modify a cut type 'MCN'; to delete a cut type 'XCN'. You will be asked to specify the RQ you want to cut on, the limits of the allowed values of this cut, and whether this cuts is to be an .AND. with other cuts or an .OR.. I am told that the .OR. does not work.

A note on template fits

The fits "two fit" and "three fit" are fits against templates. A template in principle can be constructed from theory if the events are well understood. So far we have only used templates made from averaging carefully selected clean events.

"Two fit" fits the event to a constant offset, plus an amplitude of the template.

"Three fit" fits the event to a constant offset, an amplitude of a falling exponential whose time constant is fixed, and the amplitude of the template. The falling exponential describes pile-up from previous events and should be set to the longest time constant in events.

To create a template, create a clean average event (use something like 10 or more events) either online or offline in the channel analysis routine. Dump this average event to disk using the analysis array (as described below). Then run the program

DARK_TEMPLATE.EXE. This program very simply takes the event in the ASCII file and spits out a new file with a name that is recognized by Dark_event or Dark_sort. It also asks you for the time window of the fit, the voltage noise on any given data sample, the energy corresponding to the template event, and for "three fit" the time constant in the falling exponential. This information is also written to its output file.

D.) Taking Data

There are two methods of data taking. One is to ask for a single event to be taken; the other is to run a detached subprocess that takes some specified number of events while the main program is free to display or analyze the data being collected by the subprocess.

Data taking commands start with a 'T'.

For either type of data taking, events are either triggered or randomly taken, which means the computer sends a LAM to the crate. An important note for random triggers: The WR modules will recognize the first trigger they get after the being armed. If you have chosen a random trigger but the event rate is higher than a few milliseconds between events, then you may get a real trigger before the computer sends a random trigger, so you can never be certain that a given "randomly" triggered events was actually randomly triggered.

Individual events can be taken from (almost) any routine by typing 'TT' for a triggered event or 'TR' for a random event. The subprocess can only be started in the main routine by typing 'TM'. When the spawned subprocess is running, you can do the following from any routine: 'TU' (update) gets the most recent event and updated sorts; 'TZ' allows you to reset trigger counters and sorts; 'TS' stops the spawned data taking. Note: if you do not specifically ask for the sorts to be reset when starting the subprocess, you will get a continuation of whatever was run last. If the sort definitions have changed, then the results can be garbage.

The flow of data when running the subprocess is shown in figure 2. The "selection criteria" in the figure refers to a system whereby the reduced quantities are be used to reject events. To setup selection criteria, type 'SS' in the routine where reductions and sorts are scheduled. Each selection criterion is specified by a reduced quantity and an allowed value range for this quantity. To add a criterion type 'AC'; to modify an existing criterion type 'MCN' where N is the number of the criterion; to delete a criterion type 'XCN'. The currently scheduled criteria are listed by typing the non-mnemonic command 'LL'. Each criterion requires an R and a Q value, the allowed limits for the cut, and whether this criterion is to be an .AND. with other criteria or an .OR.. (3/93. I am told that the .OR. does not work.)

Once you have scheduled selection criteria, then when taking multiple events all events that fail the cut are not written to disk, nor are they included in the sorting of histograms. The total number of hardware triggers is kept track of, however, and includes the rejected events. The total number of "good triggers" refers only to events that pass the software criteria. Note that even if an event fails the selection criteria, the raw data and the reduced data are brought to the main program by an update ('TU'). Included in the information you get by typing 'LE' is a marker indicating whether the event has passed the selection criteria.

If you have criteria scheduled and you take a single triggered event, the program will not return control to you until it has found a good event. This can be very powerful when searching for a certain type of event. Be careful however. Nothing prevents you from entering impossible criteria, and if you do and then type 'TT', the only escape is to crash the program (control-Y).

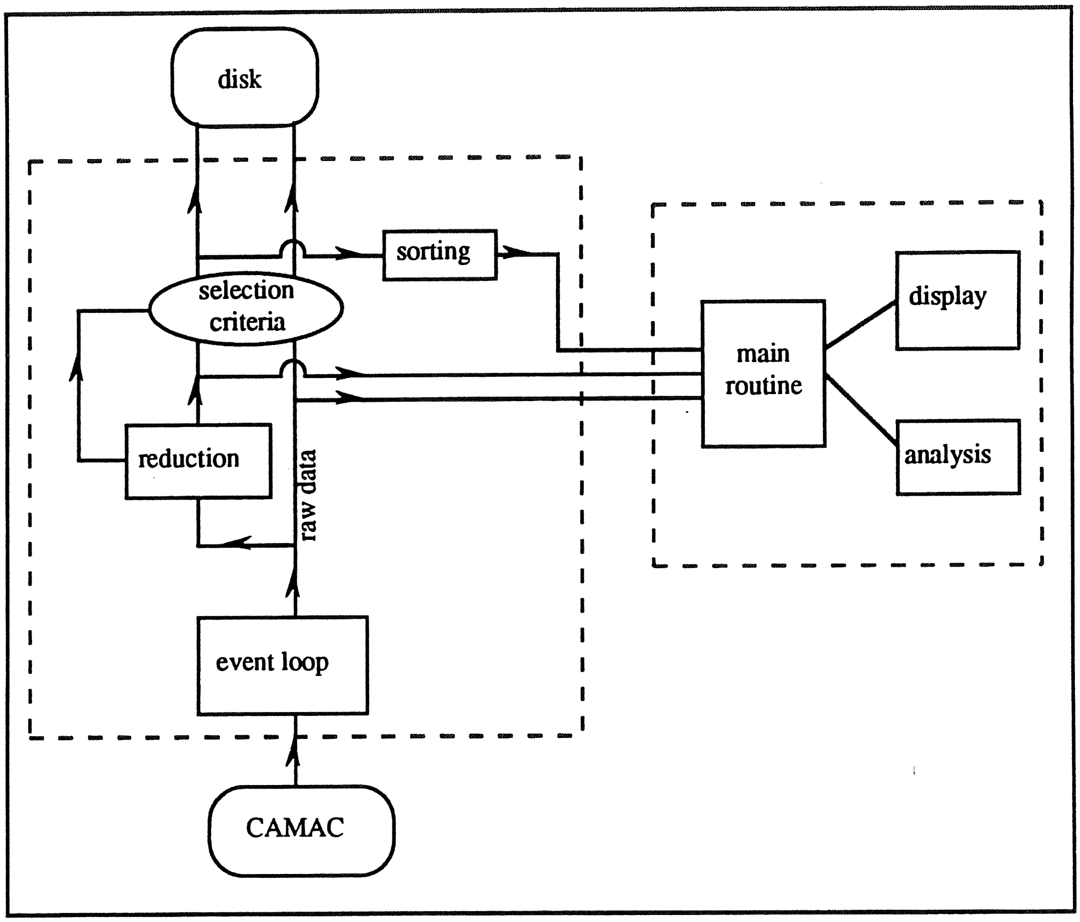

Figure 2 Flow of data when running the subprocess

E. Writing Data

There are two types of files: full data files, and RQ files which contain only an ntuple of Reduced Quantities (see sorting section) for each event. Full event files are have names like *Run15file73.dat,* where run 15 refers to the fridge run number and file 73 refers to the specific file during this run of the fridge. RQ files have two parts on disk, a header named *Run15file73_RQ.dat,* and a data section named *Run 15file73_RQ_data.dat.* The file numbers for the two types of files should be kept separate and both run from 1 to N - i.e., there should be both a *Run15file73.dat* and a *Run15file73_RQ.dat.*

To create a file type 'OO' in the main program only. When entering comments, remember that you have (or should have) already given comments about the specific data set when setting up the modules, and that these will stored in the file as well. Note that you may not have two data files with the same name. If you specify a name that already exists, the program will prompt you to pick a new name or ask you if you want to delete the old file.

Events are automatically written to disk if the subprocess is started and a file is open. When not running the subprocess, the current event in memory can be saved to the data file with 'OS'. (Note: nothing prevents you from writing the same event more than once or from writing blank events before you have taken data.) You can write a combination of events taken with the spawned subprocess and singly taken events. While an event file is open, you cannot change any data taking parameters, and you cannot get out of the program.

F.) Displaying Data

Data channels can be displayed in any subroutine. Displays options are set by typing 'SD' in the main program. Options that currently exist are the number of bins to display (note that you won't necessarily get the exact number of bins you choose), and the start and stop times, and log vs linear plots in voltage.

If you type 'WC' (or 'WS') followed by channel number, the same histogram that you would see displayed if you had typed 'DC' will be written to disk in HBOOK format. The program will prompt you for a file name.

A note on Default settings: Commands beginning with 'A' in the display setup menu give you default display settings (maximum time, sort ranges, etc.) Also, if you change the timing of the WR, let the program reset the display for you when coming out of the event definition subroutine.

A note on Scales: The zero of the time scale is the trigger time. Time is always in seconds. The voltage scale is always volts, and is the voltage as read by the module, divided by the user-specified amplifier gain.

A note on Baselines: You can have the program subtract a baseline from each time trace. The baseline is the average of samples from about 4 after the beginning to a few before the trigger. (I think the default is to subtract this baseline.)

G.) Miscellaneous other functions: fitting, spectrum analysis, averaging, ...

Fitting

Fitting commands are global and start with 'F'. Type 'F' to list current options. As of 3/93, spectra can be fit with gaussians, and events can be fit with an arbitrary number of exponentials. For the gaussian fits you specify the limits of the fit. Note that the limits of a previous fit are remembered, thus you need only type FS1 without limits to repeat a fit.

Fits to events area bit more complicated. The fit is for the amplitudes of a given number of exponentials with fixed time constants, and for the amplitudes *and* time constants of a given number of exponentials with floating time constants. Often the baseline is not easy to determine, especially in the thermal signal. Because of this there are a several different ways to find the baseline. In the fit command you specify something called "fit_type". If:

Fit_type=1, then the value you give for the baseline is used, and the time window for the baseline is ignored.

Fit_type=2, the baseline and the multiple exponentials are fit together in the fit time window, and the baseline time window is ignored.

Fit_type=3, the baseline is first found by a fit in the baselinetime window, and then the event is fit with this baseline fixed in the fit time window.

Fit_type=4, then baseline is fit in its window along with the amplitude of a falling exponential whose time constant is the last time constant enetered in the parameter list. The event is fit separately with this base and fall amplitude fixed. This is useful for events sitting on the tail of other events.

For data channel fits you can open a file which will save all the results of a fit. This file is in a format that Kaleidegraph (a plotting package on the Macintosh) can easily read. Note that the program prompts you explicitly to "dump" the results of a fit to this file, results are not dumped automatically.

Channel Analysis: Averaging, fitting residuals, writing ASCII files of events, + ?

In the routine reached by typing 'AC' in the main routine, you can do a number of things with events. One is to average events, which is either done on an event by event basis, or on a specified number of events taken (or read) and averaged on the fly. Note that the average event is stored separately in its own memory. To get this event into the data channels, you must type VTCN, where N is the channel in question. Offline, in dark_sort, I don't let you transfer the average array to the data channels, so instead put it in the analysis array.

The analysis array is a memory structure identical to the data channels that can be used for a variety of things. If you want to add some bizarre event transformation to the code, store the result here.

Events can be read into the code, or dumped to disk in a simple ASCII file using the analysis array. When reading or writing events to disk, you will be prompted for a name. The event will be put in a file that is (This name).ANA. The file consists of two rows of numbers, the first is the time and the second the voltage. The FORTRAN format of the I/O
statement is (1X,E20.13,1X,E20.13).

Another feature is subtraction of fits from events. This can currently only be done for fits performed within the reduction and sorting framework, not the simple exponential fitting. Type 'SCN' where N is the reduction number of the fit. The residual will be put into the analysis array of the channel associated with reduction N.

Spectrum Analyzer

Typing 'AZ' in the main routine gets you into the spectrum analyzer, which fourier transforms the data channels and then constructs the power spectral density in units of $V/Hz^{1/2}$. The power spectrum is stored in a separate memory structure which parallels the data channels - i.e., there is one power spectrum channel for each data channel. Type 'DPN' to view power spectrum "N".

A new power spectrum is created from a current data channel by typing 'ANN', where the second N refers to a data channel. With this command the existing power spectrum is overwritten. To combine the power spectrum of a current data to the existing power spectrum type 'ACN'. This correctly recomputes the average power spectrum. There is also a way to take (online) or read (offline) many events and automatically average the results.

The only real funniness is that you can specify a time window that is smaller than the full event size. This can be useful when you have some garbage in part of the time window. The power spectrum can also be integrated over any frequency range to obtain the r.m.s. variation of the voltage in the time domain.

H.) A note on names of things and comments

Comments

There are two types of comments written to the file - those associated with the data channels, and those about the file as a whole (entered when opening a new file). Often the only difference between two files is a change in a data channel that does not require change the module's settings. It is inconvenient wade through the module setup routine just to change one comment. I recommend therefore, that we adopt the following convention: When taking several files with the same module parameters but differing actual data channel conditions (e.g., bias), write "see file comments" in the module setup routine for the corresponding data channel comment, and then give the comment (e.g. "bias = 4.0 volts") in the file comments when opening the file.

In the comments you make when opening a file, I recommend the following: The run comment should describe the entire run and should *not* be changed within a run. This comment is intended to be used later merely to identify what run is what. File comments describe what is unique about this file - ideally what physics is intended in this measurement. Fridge comments give temperature or anything else of relevance. Device comments describe the device used for this file.

Names of things

It is easy to be confused about the names of data channels and reduced quantities. Data channel names should reflect only what distinguishes one channel from another, e.g. ions vs phonons, or ntd 1 vs ntd 2. Don't give the device name, since this is already contained in comments. (In the future, of course, this will change if we run more than one device at once.)

Reductions each have a name, and it should be different than the channel name. The channel name will always be identified anyway when you look at a reduction. Try to come up with a name that describes something unique about this reduction. Also, definitely make this name exactly 4 characters, no blanks. This makes things easier if you make a file outside of dark event.

GETTING DATA ON AND OFF OF TAPE

To write to tape you need an initialized tape mounted on the drive. To initialize a fresh tape, type "Initialize MUA0: label", where label is a 6 character name for the tape. To mount the tape, type "Mount/block=9000/rec=9000 MUA0: label".

Files created by DARK_EVENT are direct access and thus unfortunately cannot be put on tape directly. The programs WRITE_SEQ_FILE and READ_SEQ_FILE transform these direct access files (name = RUNXXXFILEXXX.DAT) to sequential files (name = RUNXXXFILEXXXSEQ.DAT) which can reside on tape or disk, and write the results directly to the tape. Sequential files written on disk (such as files created by an editor) can be transferred to tape using the VMS "copy" command.

If you need to put many files on tape, create a command file and run it as a batch job. Watch out. If you make a mistake, the only way to correct it is to erase the tape. Also, a tape with lots of data on it can take more than an hour to read.

In the following example I run WRITE_SEQ_FILE to write RUN69FILE3SEQ.DAT (and associated ...RQ_DATA.DAT) on tape.

$R WRITE_SEQ_FILE

Output on (T)ape or (D)isk? ==>>T

Run number, file number, Q for RQ files (O=quit) ==>>69,3,Q

A command file to write several files to tape would look like:

$MOUNT/BLOCK=9000/REC=9000..... MUA0: DKM009

$R WRITE_SEQ_FILE

T

69,1

69,2

69,3

69,1,Q

69,2,Q

0

$DIR/SIZE/DATE/OUTPUT='DKM009.LIS' MUA0:

$DISMOUNT MUA0:

Note that I took the directory at the end, with the result written to a file. You MUST do this every time you add to tape. You MUST also FTP a copy of the directory to the Mac in room 79, print out a copy, and file it in the folder labeled "Data Log".

DARK_SORT

DARK_SORT is very similar to DARK_EVENT, if you think of a data file as equivalent to the CAMAC crate (i.e., as black box that gives you data.) Simply type R.. to read events rather than T.. to take events. The routine reached via "AS" allows you to sort many events in an analogous way to 'TM'. Other things are the same as in DARK_EVENT.

There are a couple of subtleties, however. When you read in a full event file, the REDQ definitions you had when you took the data are part of the file and overwrite whatever you have currently defined. Once the file is read, you can delete or modify them or add new ones. The reason they are part of the data set is that they (potentially) form part of the software trigger. Sorting conditions, on the other hand, are not part of the data set. Note also that if you read in an RQ file, you cannot change REDQ definitions.

A final word: If you want to look at everything in the data header, write an output log file "OL". This creates a file with name RUNXXXFILEXXX.LOG.

WRITING YOUR OWN CODE

I have created a library with several routines that you should use to analyze DARK_EVENT files. The logical name of the library is dkm_event_lib. You must reference this library in your link statement when compiling (i.e., you must have a line reading dkm_event_lib/lib in your link command or options file).

There are two different types of routines available. I/O routines allow you to open the files and read (or write) events and other information from them. I strongly suggest you use my I/O routines, and not write your own. In addition, there are a number of functions I have written that you may find useful.

The source code is kept on Pastro in a VMS system called CMS (Code Management System). To look at the routine De_read_event.for, for example, type CMS, then "set lib dkm_event_cms", then fetch the routine with "Fetch element de_read_event.for". This will put a copy of the routine in the directory you are working in. You may find it necessary to look at "DE_DATA_DECLARATIONS.INC". This is also in the CMS library, and declares all the variables used in the data set.

IO Routines: use these to open and close files, and to read events

```
C*************
C**     SUBROUTINE DE_OPEN_EVENTFILE(FILE_ID, TYPE_FILE, FILE_NAME,
C**             VERSION, STATUS, ACCESS, NUM_EVENTS, IOERROR)
C**      FOR NEW (OLD) FILES - CREATES (OPENS) FILE, WRITES (READS) HEADER
C**       PARAMETERS:
C**             FILE_ID         = IDENTIFIES FILE (I*4)
C**             FILE_NAME       = NAME                  (CHAR*40)
C**             TYPE_FILE       = 1 - FULL DATA CHANNELS (I*4)
C**                               2 - RQ FILE (SEQ. ACCESS)
C**             VERSION         = VERSION #.
C**                                 FOR OLD FILES IS RETURNED.
C**                                 FOR NEW FILES THIS NUMBER IS USED, IF
C**                                   VALID. IF 0 IS GIVEN, THE LATEST
C**                                      VERSION IS USED. IF A NON ZERO
C**                                      INVALID VERSION IS GIVEN AN ERROR
```

```
C**                                   OCCURS
C**           STATUS          = 'NEW' OR 'OLD'(CHAR*3)
C**           SHARED          = 'SHARED' ALLOWS ACCESS BY MORE THAN ONE
C**                                PROCESS FOR OLD FILES ONLY.  ANYTHING
C**                                ELSE GIVES EXCLUSIZE ACCESS.   (CHAR*6)
C**           NUM_EVENTS = NUMBER OF EVENTS IN FILE - RETURNED
C**                                FOR OLD FILES,
C**                                WRITTEN FOR NEW FILES.  (NOTE: THIS IS
C**                                NOT NECESSARILY THE NUMBER OF
C**                                EVENTS IN ORIGINAL DATA SET) (I*4)
C**           IOERROR         = CONTAINS ERROR MESSAGE, = 0 IS O.K. (I*4)

C*************
C**      SUBROUTINE DE_CLOSE_EVENTFILE(FILE_ID,NUM_EVENTS) -  CLOSES
C**        EVENTFILES.
C**           FILE_ID                    - INDENTIFIES THE FILE (I*4)
C**           NUM_EVENTS  - IGNORED FOR OLD FILES
C**                              FOR NEW FILES, IF > 0,
C**                                THEN WRITTEN AS THE NUMBER OF
C**                                EVENTS IN THE FILE (I*4)

C*************
C**      SUBROUTINE DE_READ_EVENT(FILE_ID,EVENT_NUM,IOERROR)  --  READS
C**        EVENTS FROM DISK
C**                    FILE_ID - ID OF FILE TO READ FROM - PASSED
C**                              BY CALLER (I*4)
C**                    EVENT_NUM - # OF EVENT TO READ.  IS THE
C**                               # IN THIS FILE, NOT NECESSARILY
C**                               THE NUMBER OF THE EVENT IN THE
C**                               ORIGINAL DATA SET
C**                              FOR FULL EVENT FILES:
C**                                = 0  READS CURRENT EVENT, INCREMENTS
C**                                     EVENT POINTER
C**                                > 0  READS EVENT_NUM, DOES NOT INCREMENT
C**                                   EVENT POINTER  (I*4)
C**                              IGNORED FOR RQ FILES
C**                    IOERROR - 0=O.K. (I*4)

C*************
C**      SUBROUTINE DE_WRITE_EVENT(FILE_ID,EVENT_NUM,IOERROR)  --  HANDLES
C**        WRITING OF EVENTS TO DISK
C**                    FILE_ID - ID OF FILE TO WRITE TO - PASSED
C**                              BY CALLER (I*4)
C**                    EVENT_NUM - # OF EVENT TO WRITE.  IS THE
C**                               # IN THIS FILE, NOT NECESSARILY
C**                               THE NUMBER OF THE EVENT IN THE
C**                               ORIGINAL DATA SET
C**                              FOR FULL EVENT FILES:
C**                                = 0  WRITES CURRENT EVENT, INCREMENTS
C**                                     EVENT POINTER
C**                                > 0  WRITES EVENT_NUM, DOES NOT INCREMENT
C**                                   EVENT POINTER  (I*4)
C**                              IGNORED FOR RQ FILES
C**                    IOERROR - 0=O.K. (I*4)
```

Functions:

```
C*************
C**     FUNCTION DE_VOLTAGE(SAMPLE,TIME,CHANNEL) -- RETURNS THE VOLTAGE
C**       REFERED TO THE INPUT OF THE AMPLIFIER CHAIN FOR THE GIVEN
C**       CHANNEL, AND INPUT VOLTAGE OR TIME.
C**         SAMPLE    - USED IF NON ZERO (I*4)
C**         TIME      - USED ONLY IF SAMPLE = 0 (R*4)
C**         CHANNEL  - (I*4)

C*************
C**     FUNCTION DE_TIME(SAMPLE,CHANNEL) -- RETURNS THE TIME
C**       CORRESPONDING TO THE GIVEN SAMPLE FOR THE GIVEN CHANNEL
C**         SAMPLE  -  THE SAMPLE IN QUESTION (I*4)
C**         CHANNEL -  THE CHANNEL QUESTION (I*4)

C*************
C**     FUNCTION DE_SAMPLE(TIME,CHANNEL) -- RETURNS THE SAMPLE
C**       CORRESPONDING TO THE GIVEN TIME FOR THE GIVEN CHANNEL
C**       IF THE TIME IS OUT OF RANGE, THE CLOSEST VALID SAMPLE
C**       IS RETURNED
C**         SAMPLE    - (R*4)
C**         CHANNEL  - (I*4)

C*************
C**     FUNCTION DE_PEDESTAL(LOW_SAMPLE,HIGH_SAMPLE,CHANNEL) -- RETURNS THE
C**       PEDESTAL COMPUTED BY A SIMPLE AVERAGE OVER THE INPUT RANGE FOR THE
C**       GIVEN CHANNEL. (NOTE THAT THE RANGE IS FROM THE BEGINNING OF
C**       LOW_SAMPLE TO THE END OF HIGH_SAMPLE)
C**         LOW_SAMPLE      - START TIME IS LOWER EDGE OF THIS SAMPLE (I*4)
C**         HIGH_SAMPLE     - STOP TIME IS THE UPPER EDGE OF THIS
C**                               SAMPLE (I*4)
C**         CHANNEL                  - (I*4)

C*************
C**     FUNCTION DE_BIT_VOLTAGE(BIT_VALUE,CHANNEL) -- RETURNS THE VOLTAGE
C**       REFERED TO THE INPUT OF THE AMPLIFIER CHAIN FOR A GIVEN CHANNEL,
C**       CORRESPONDING TO A RAW DATA (BIT) VALUE.
C**         BIT_VALUE           - A RAW DATA VALUE (I*4)
C**         CHANNEL             - (I*4)
```

References

1. E. W. Kolb, M. S. Turner, *The Early Universe* (Addison-Wesley, Redwood City, California, 1990).

2. S. Tremaine, in *Physics Today* . (1992), pp. 28-36.

3. V. Trimble, *Ann. Rev. Astron. Ap.* **25**, 245 (1987).

4. V. C. Rubin, et. al., *Ap. J.* **238**, 471 (1980).

5. J. P. Hughes, *Astrophysics Journal* **337**, 21 (1989).

6. D. Merritt, *Astrophyics Journal* **313**, 21 (1987).

7. L. L. Cowie, M. Henriksen, R. Mushotzky, *Ap. J.* **317**, 593 (1987).

8. J. A. Tyson, F. Valdes, R. A. Wenk, *Astrophysics Journal Letters* **349**, L1 (1990).

9. A. Dressler, et al., *Ap. J. Lett.* **313**, L37 (1987).

10. A. Dressler, D. Lynden-Bell, D. Burstein, et. al., *Ap. J.* **313**, 42 (1987).

11. G. Goldhaber, C. Pennypacker, S. Perlmutter, 2nd NESTOR International Workshop (In Publication, Pylos, Greece, 1992),

12. A. Albrecht, P. J. Steinhardt, *Phys. Rev. Lett.* **48**, 1220 (1982).

13. A. Guth, *Phys. Rev.* **D23**, 347 (1981).

14. A. D. Linde, *Phys. Lett.* **129B**, (1983).

15. K. A. Olive, in *Science* . 1991), pp. 1194.

16. K. A. Olive, D. N. Schramm, G. Steigman, T. Walker, *Phys. Lett.* **B426**, (1990).

17. D. Denegri, B. Sadoulet, M. Spiro, *Review of Modern Physics* **62**, 1 (1990).

18. K. Griest, *Ap. J.* **366**, (1991).

19. B. Pazcinski, *Ap. J.* **304**, 1 (1986).

20. B. W. Lee, S. Weinberg, *Phys. Rev. Lett.* **39**, 165 (1977).

21. G. Smoot, C. Bennett, A. Kogut, E. Wright, et. al., *Ap. J. Lett.* **396**, L1 (1992).

22. M. Davis, G. Efstathiou, C. S. Frenk, S. D. M. White, *Nature* **356**, 489 (1992).

23. C. A. Hagman, Ph.D. Thesis, University of Florida (1990).

24. S. DePanfilis, et. al., *Phys. Rev. D* **40**, 3153 (1989).

25. J. R. Primack, D. Seckel, B. Sadoulet, *Ann. Rev. Nucl. Part. Sci.* **38**, 751-807 (1988).

26. J. Rich, D. L. Owen, M. Spiro, *Physics Reports* **151**, 241 (1987).

27. P. F. Smith, J. D. Lewin, *Physics Reports* **187**, 203 (1990).

28. D. O. Caldwell, et. al., *Phys. Rev. Lett.* **65**, 1305 (1990).

29. M. W. Goodman, E. Witten, *Phys. Rev. D* **30**, 272 (1984).

30. D. Reusser, et. al., *Phys. Lett.* **B235**, 143 (1991).

31. D. O. Caldwell, R. M. Eisberg, D. M. Grumm, et. al., *Phys. Rev. Lett.*, 510 (1988).

32. S. P. Ahlen, et. al., *Phys. Lett.* **B195**, 603 (1987).

33. J. Rich, M. Spiro, DPhPe, CEN-Saclay, (1987).

34. J. Lindhard, V. Nielsen, M. Scharff, P. V. Thomsen, *Kgl. Dan. Vidensk. Selk., Mat.- Phys. Medd.* **33**, (1963).

35. P. N. Luke, *J. Appl. Phys.* **64**, 6858 (1988).

36. N. J. C. Spooner, G. J. Homer, P. F. Smith, *Phys. Lett.* **B278**, 382 (1992).

37. N. Wang, Ph.D. Thesis, University of California, Berkeley (1991).

38. D. Yvon, et al., *In preparation*, (1993).

39. H. W. Ott, *Noise Reduction Techniques in Electronic Systems* (John Wiley & Sons, New York, 1988).

40. F. M. Rieke, A. E. Lange, J. W. Beeman, E. E. Haller, *IEEE Trans. on Nucl. Sci* **NS-36**, 946 (1986).

41. I. S. Park, Ph.D. Thesis, University of California, Berkeley (1988).

42. E. E. Haller, N. P. Palaio, M. Rodder, W. L. Hansen, E. Kreysa, in *Neutron Transmutation Doping of Semiconductor Materials* R. D. Larrabee, Eds. (Plenum, New York, 1984) pp. p1.

43. S. M. Grannan, A. E. Lange, E. E. Haller, J. W. Beeman, *Phys. Rev. B* **45**, 4516 (1992).

44. N. Wang, F. C. Wellstood, B. Sadoulet, E. E. Haller, J. Beeman, *Physical Review B* **41**, 3761 (1990).

45. A. L. Efros, B. I. Shkolvskii, *Electronic Properties of Doped Semiconductors* (Springer Verlag, New York, 1984).

46. T. F. Rosenbaum, K. Andres, G. A. Thomas, *Solid State Commun.* **35**, 663 (1980).

47. S. H. Moseley, J. C. Mather, D. McCammon, *J. Appl. Phys.* **56**, 1257 (1984).

48. J. C. Mather, *Appl. Opt.* **23**, 584 (1984).

49. W. E. Bron, Eds., *Nonequilibrium Phonon Dynamics* , vol. B125 (Plenum Press, 1985).

50. B. Cabrera, J. Martoff, B. Neuhauser, *Nucl. Inst. Meth.* **A275**, 97 (1988).

51. J. Wouters, et al., *Nuclear Instruments and Methods in Physics Research* **A311**, 215-218 (1991).

52. J. Wouters, Ph.D. Thesis, Katholieke Univeristeit Leuven (1989).

53. N. J. C. Spooner, A. Bewick, G. J. Homer, P. F. Smith, J. D. Lewin, *Phys. Lett.* **B273**, 333 (1991).

54. E. E. Haller, F. S. Goulding, in *Handbook on Semiconductors* E. E. Haller, F. S. Goulding, Eds. (North Holland, 1978).

55. P. R. Bratt, in *Semiconductors and Semimetals* R. K. Willardson, A. C. Beer, Eds. (Academic Press, New York, 1977), vol. 12, pp. 39.

56. E. E. Haller, *Infrared Phys.* **25**, 257-266 (1985).

57. N. M. Haegel, A. M. White, *Infrared Phys.* **29**, 915-923 (1988).

58. R. M. Westervelt, S. W. Teitsworth, *J. Appl. Phys.* **57**, 5457 (1985).

59. S. W. Teitsworth, *Applied Physics* **A48**, 127-136 (1988).

60. C. Kittel, H. Kroemer, *Thermal Physics* (W.H. Freeman, New York, 1980), vol. 2.

61. S. M. Sze, *Physics of Semiconductor Devices* (John Wiley & Sons, New York, 1981).

62. T. Shutt, et al., *Phys. Rev. Lett.* **69**, 3531 (1992).

63. A. H. Scott, H. L. Curtis, *Journal of Research of the National Bureau of Standards* **22**, 747 (1939).

64. S. C. Jain, D. J. Roulston, *Solid-State Electronics* **34**, 453-465 (1991).

65. Z. H. Levine, D. C. Allen, *Phys. Rev. B* **43**, 4187 (1991).

66. C. A. Klein, *IEEE Trans. on Nucl. Sci* **NS-15**, 214 (1968).

67. N. M. Haegel, J. W. Beeman, P. N. Luke, E. E. Haller, *Phys. Rev. B* **39**, 3677 (1989).

68. E. I. Gershenzon, G. N. Gol'tsman, A. P. Mel'nikov, *JTEP* **14**, 185 (1971).

69. F. Reif, *Fundamentals of Statistical and Thermal Physics* (McGraw-Hill, New York, 1965).

70. L. Reggiani, C. Canali, F. Nava, G. Ottaviani, *Phys. Rev. B* **16**, 2781 (1977).

71. V. N. Abakumov, V. I. Perel', I. N. Yassievich, *Soviet Phyiscs of Semiconductors* **12**, 1 (1978).

72. M. Lax, *Phys. Rev.* **119**, 1502 (1960).

73. T. Shutt, et al., *Phys. Rev. Lett.* **69**, 3452 (1992).

74. E. A. Lorch, *International Journal of Applied Radiation and Isotopes* **24**, 585-591 (1973).

75. A. R. Sattler, F. L. Vook, J. M. Palms, *Phys. Rev.* **143**, 588 (1966).

76. K. W. Jones, H. W. Kramer, *Phys. Rev. C* **4**, 125 (1971).

77. C. Chasman, K. W. Jones, H. W. Kraner, W. Brandt, *Phys. Rev. Lett.* **21**, 1430 (1968).

78. B. L. Dougherty, *Phys. Rev. A* **45**, 2104 (1992).

79. G. Gerbier, et. al., *Phys. Rev. D* **42**, 3211 (1990).

80. W. L. Hansen, E. E. Haller, G. S. Hubbard, *IEEE Trans. on Nucl. Sci* **NS27**, 247 (1980).

81. K. Greist, private communication. (1992).

82. O. V. Lounasmaa, *Experimental Principles and Methods Below 1 K* (Academic Press, London, 1971).

83. F. Pobell, *Matter and Methods at Low Temperatures* (Springer Verlag, Berlin, 1992).

84. W. A. Little, *Can. J. Phys.* **37**, 334 (1959).

85. G. K. White, *Experimental Techniques in Low Temperature Physics* (Clarendon, Oxford, 1979).

86. R. C. Richardson, E. N. Smith, *Experimental Techniques in Condensed Matter Physics at Low Temperatures* (Addison-Wesley, Redwood City, California, 1988).

87. C. Stanton, B.S. Thesis, University of California, Berkeley (1988).

88. A. Cummings, et. al., *IEEE Transactions on Nulcear Science Symposium Record* **1**, 209 (1990).

89. W. D. Greason, *Electrostatic Damage in Electronics: Devices and Systems* (John Wiley & Sons, New York, 1987).

90. P. Horowitz, W. Hill, *The Art of Electronics* (Cambridge, New York, 1989).

91. W. T. Eadie, D. Drijard, F. E. James, M. Roos, B. Sadoulet, *Statistical Methods in Experimental Physics* (North Holland, Amsterdam and London, 1971).

92. P. R. Bevington, *Data Reduction and Error Analysis for the Physical Sciences* (McGraw Hill, New York, 1969).

93. M. Mori, M. M. Nojori, Y. Oyama, A. Suzuki, et. al., *Phys. Lett. B* **270**, 89 (1991).